NASA
CP
2085
pt.1
c.1

NASA Conference Publication 2085
Part I

LOAN COPY:
AFWL TECHN
KIRTLAND AF
0099881
TECH LIBRARY KAFB, NM

Science and Technology of Low Speed and Motorless Flight

Proceedings of a symposium held at
NASA Langley Research Center
Hampton, Virginia
March 29-30, 1979

NASA | SSA

18 JAN 1979

TECH LIBRARY KAFB, NM

0099881

NASA Conference Publication 2085

Part I

Science and Technology of Low Speed and Motorless Flight

Perry W. Hanson, *Compiler*
NASA Langley Research Center

Proceedings of a symposium cosponsored by
NASA Langley Research Center and the
Soaring Society of America, and held at
NASA Langley Research Center, Hampton, Virginia
March 29-30, 1979

NASA

National Aeronautics
and Space Administration

Scientific and Technical
Information Office

1979

PREFACE

This NASA conference publication contains the proceedings of the Third International Symposium on the Science and Technology of Low Speed and Motorless Flight held at the NASA Langley Research Center, Hampton, Virginia, March 29-30, 1979. The symposium was cosponsored by the Langley Research Center (LaRC) and the Soaring Society of America (SSA). Oran Nicks, Deputy Director of the Langley Research Center, and James Nash-Webber, Massachusetts Institute of Technology and past chairman of the SSA Technical Board, were general cochairmen. Perry Hanson, NASA LaRC, was the symposium organizer and technical program chairman. Hewitt Phillips, NASA LaRC (Retired); Joseph Gera, NASA LaRC: and Robert Lamson, Chairman of the SSA Technical Board, served as chairmen for the technical sessions.

The purpose of the Symposium was to provide a forum for the interchange of information on recent progress in the science and technologies associated with low speed and motorless flight. Twenty-eight papers were presented in the areas of low speed aerodynamics, new materials applications and structural concepts, advanced flight instrumentation, sailplane optimal flight techniques, and self-launching and ultralight glider technology. This NASA conference publication contains these presentations and a paper, which was not presented, on proposed definitions for various categories of sailplanes and gliders.

The use of trade names or manufacturer's names in this publication does not constitute an official endorsement of such products or manufacturers, either expressed or implied, by NASA. The included papers are largely as submitted. The physical quantities, whether in the International System of Units (SI) or U.S. Customary Units, are retained as submitted by the authors.

CONTENTS

PREFACE iii

PART I

LOW-SPEED AERODYNAMICS

1. LOW-SPEED SINGLE-ELEMENT AIRFOIL SYNTHESIS 1
John H. McMasters and Michael L. Henderson

2. AN EXPLORATORY INVESTIGATION OF THE EFFECT OF A PLASTIC COATING ON THE PROFILE DRAG OF A PRACTICAL-METAL-CONSTRUCTION SAILPLANE AIRFOIL 33
Dan M. Somers

3. OPTIMUM TAIL PLANE DESIGN FOR SAILPLANES 65
Kay Mayland

4. THE EFFECT OF DISTURBANCES ON A WING 81
Richard Eppler

5. GENERATION AND BREAKDOWN OF AERODYNAMIC LIFT: PHYSICAL MECHANISM 93
Wolfgang Liebe

6. INTRODUCTION TO THE ARCOPTER ARC WING AND THE BERTELSEN EFFECT FOR POSITIVE PITCH STABILITY AND CONTROL 103
William D. Bertelsen

7. SOME NEW AIRFOILS 131
Richard Eppler

8. A COMPARISON OF THE AERODYNAMIC CHARACTERISTICS OF EIGHT SAILWING AIRFOIL SECTIONS 155
Mark D. Maughmer

9. LENGTH AND BURSTING OF SEPARATION BUBBLES: A PHYSICAL INTERPRETATION 177
John M. Russell

10. WING SHAPE OPTIMIZATION FOR MAXIMUM CROSS-COUNTRY SPEED, WITH MATHEMATICAL PROGRAMMING 203
Gunter Helwig

ADVANCED INSTRUMENTATION

11. FURTHER DEVELOPMENTS IN SIMPLE TOTAL ENERGY SENSORS 219
Oran W. Nicks

12. HOW ACCURATE IS NETTO 247
Stephen du Pont

13. THE APPLICATION OF MICROPROCESSOR TECHNOLOGY TO IN-FLIGHT COMPUTATIONS 267
Patricia L. Sawyer and Dan M. Somers

MOTORSOARERS

14. DESIGN OF PROPELLERS FOR MOTORSOARERS 285
E. Eugene Larrabee

PART II*

OPTIMAL FLIGHT TECHNIQUES

15. MINIMUM ALTITUDE-LOSS SOARING IN A SPECIFIED VERTICAL WIND DISTRIBUTION 305
Bion L. Pierson and Imao Chen

16. A STUDY OF COURSE DEVIATIONS DURING CROSS-COUNTRY SOARING 319
Steven M. Sliwa and David J. Sliwa

17. ON GLOBAL OPTIMAL SAILPLANE FLIGHT STRATEGY 355
G. Sander and F. X. Litt

18. BALANCE TRAINING OF THE EQUILIBRIUM ORGAN AND ITS EFFECT ON FLIGHT STRATEGY 377
K. -D. Eikemeier, H. -D. Melzig, N. Reicke, and W. Schmidt

19. A MONTE CARLO APPROACH TO COMPETITION STRATEGY 389
Michael P. Teter

STRUCTURES AND MATERIALS

20. A GENERAL METHOD FOR THE LAYOUT OF AILERONS AND ELEVATORS OF GLIDERS AND MOTORPLANES 399
Manfred Hiller

21. EXPERIMENTAL INVESTIGATION INTO THE FEASIBILITY OF AN "EXTRUDED" WING 419
Piero Morelli and Giulio Romeo

---

*Papers 15 to 28 are presented under a separate cover.

22. TREATMENT OF THE CONTROL MECHANISMS OF LIGHT AIRPLANES IN THE FLUTTER CLEARANCE PROCESS 437
Elmar J. Breitbach

23. ADVANCED COMPOSITES IN SAILPLANE STRUCTURES: APPLICATION AND MECHANICAL PROPERTIES 467
Dieter Muser

ULTRALIGHT SAILPLANES AND HANG GLIDERS

24. THE ULTRALIGHT SAILPLANE 485
J. H. McMasters

25. ANALYTICAL AND SCALE-MODEL RESEARCH AIMED AT IMPROVED HANG GLIDER DESIGN 505
Ilan Kroo and Li-Shing Chang

26. IMPROVEMENT OF HANG GLIDER PERFORMANCE BY USE OF ULTRALIGHT ELASTIC WING 523
Jerzy Wolf

27. EXPERIMENTAL STUDY OF THE FLIGHT ENVELOPE AND RESEARCH OF SAFETY REQUIREMENTS FOR HANG-GLIDERS 537
Claudius La Burthe

28. WIND TUNNEL TESTS OF FOUR FLEXIBLE WING ULTRALIGHT GLIDERS 557
Robert A. Ormiston

CONTEMPORARY SOARING NOMENCLATURE** 591
S. O. Jenko

ATTENDEES 595

**Paper not presented at symposium.

LOW-SPEED SINGLE-ELEMENT AIRFOIL SYNTHESIS

John H. McMasters and Michael L. Henderson

Boeing Commerical Airplane Co.

SUMMARY

Large quantities of experimental data exist on the characteristics of airfoils operating in the Reynolds number range between one and ten million, typical of conventional atmospheric wind tunnel operating conditions. Beyond either end of this range, however, good experimental data becomes scarce. Designers of model airplanes, hang gliders, ultralarge energy efficient transport aircraft, and bio-aerodynamicists attempting to evaluate the performance of natural flying devices are hard pressed to make the kinds of quality performance/design estimates taken for granted by sailplane and general aviation aerodynamicists. Even within the usual range of wind tunnel Reynolds numbers, much of the data is for "smooth" models which give little indication of how a section will perform on a wing of practical construction.

The purpose of this paper is to demonstrate the use of recently developed airfoil analysis/design computational tools to clarify, enrich and extend the existing experimental data base on low-speed, single element airfoils, and then proceed to a discussion of the problem of tailoring an airfoil for a specific application at its appropriate Reynolds number. This latter problem is approached by use of inverse (or "synthesis") techniques, wherein a desirable set of boundary layer characteristics, performance objectives, and constraints are specified, which then leads to derivation of a corresponding viscous flow pressure distribution. In this procedure, the airfoil shape required to produce the desired flow characteristics is only extracted towards the end of the design cycle. This synthesis process is contrasted with the traditional "analysis" (either experimental or computational) approach in which an initial profile shape is selected which then yields a pressure distribution and boundary layer characterisitics, and finally some performance level. The final configuration which provides the required performance is derived by cut-and-try adjustments to the shape.

Examples are presented which demonstrate the synthesis approach, following presentation of some historical information and background data which motivate the basic synthesis process.

INTRODUCTION

Since the dawn of human flight, enormous efforts have been expended on the design of efficient wings and their constituent airfoil sections. As such development became a race for ever increasing speed, the problems of

low-speed flight frequently became relegated to the status of "off-design" conditions, with performance requirements met by fitting "high speed" cruise airfoils with increasingly complex and sophisticated high-lift devices. During the past forty years, relatively little attention has been given to the development of "optimized" low-speed airfoils by other than academicians and "cut-and-try" experimenters.

While frequently outside the mainstream of modern commerical interest, the range of low-speed flying devices (characterized by generally low values of the scale parameters Reynolds and Mach number) covers an enormous portion of the feasible flight spectrum. To place the subsequent discussion in a proper global context, Figure 1 has been prepared to demonstrate quantitatively the relationships between low-speed flight vehicle size and performance and the sometimes arcane parameter, Reynolds number. While "low-speed" generally implies low Reynolds and Mach numbers, it is worth noting that recent interest in ultralarge transport aircraft has now expanded the low-Mach number flight Reynolds number range from that typical of small insects ($10 < Rn < 10^4$) through devices like huge wing-in-ground effect aircraft (ref. 1) which may have chord Reynolds numbers approaching one billion at flight speeds on the order of 100 m/s ($M \sim 0.3$). Even a "small" monster like the Boeing 747 (average wing chord approximately 10 m) becomes a low-speed aircraft during approach, with typical average Reynolds numbers for the wing of 40 million at $M \sim 0.2$.

To discuss the full range of problems associated with wing/airfoil design for the range of vehicles shown in Figure 1 would require several books. The present paper is limited to a discussion of two aspects of the overall problem:

1. A brief survey of historical trends in low-speed, single-element airfoil development, culminating in a review of the present state of the art in analytic design methodology.

2. A demonstration of the value of modern computational capabilities to, first, clarify the performance characteristics of several existing low-speed airfoil sections for which experimental data exist; and then show how one may proceed to "synthesize" a suitable section for a specific application from a desired specification of boundary layer/pressure distribution characteristics.

NOTATION

AR	Aspect ratio = $b/\bar{c} = b^2/S$
b	Wing span (m)
c	chord (m)
$\bar{c}$	Average chord = S/b (m)

C_d	Section drag coefficient
C_f	Skin friction coefficient
C_L	Wing lift coefficient = lift/qS
C_ℓ	Section lift coefficient
C_p	Pressure coefficient = $(p-p_\infty)/q_\infty$
C_m	Section pitching moment coefficient
H	Boundary layer form parameter $= \delta / \theta$
M	Mach number
p	Static pressure (N/m^2)
q	Dynamic pressure = $\frac{1}{2} \rho V^2$ (N/m)
Rn	Reynolds number = Vc/ν
S	Wing area (m^2)
t	Airfoil thickness (m)
V	Velocity (m/s)
v	Local velocity (m/s)
W	Weight (N)
x	Chordwise coordinate
z	Coordinate normal to chord

Greek symbols:

α	Angle of attack (degrees)
δ	Boundary layer displacement thickness = $\int_0^\infty \left(1 - \frac{v}{V_\infty}\right) dz$
ε	Section lift-drag ratio = C_ℓ / C_d
θ	Boundary layer momentum thickness = $\int_0^\infty \frac{v}{V_\infty}\left(1 - \frac{v}{V_\infty}\right) dz$
ν	Kinematic viscosity (1.46×10^{-5} m^2/s standard sea level)
ρ	Air mass density (1.225 kg/m^3 standard sea level)

Superscript:

( )*	indicates "design condition"

Subscript:

( )r recovery point or region

( )tr transition point or "trip" location

( )fp fair point (see Fig. 9)

( )TE trailing edge

$(\ )_\infty$ free-stream condition

( )u airfoil upper surface value

HISTORICAL PERSPECTIVE

To clarify the present status of low-speed airfoil development, it is of interest to briefly review the history of how we got from there to here. A map of the route is shown in Figure 2. It is important to note that well into the present century airfoil "design" was a largely empirical process, drawing its main inspiration from natural models (i.e., birds), and only partially clarified and systematized by recourse to potential flow theory (e.g., Joukowski airfoils). Elaborate testing programs at Göttingen and by the NACA, among others, guided by intuition, experience, and inviscid theory eventually lead to the accumulation of masses of data and subsequent publication of airfoil section catalogs to aid designers.

It was not until the mid-1930's that the influence of viscous "scale effects" was appreciated, and boundary layer theory well enough developed, to allow the qualitative incorporation of viscous flow concepts into the design of "low-drag" sections. The main upshot of these new considerations was the famous NACA 6-series "laminar flow" airfoils. The accumulated results of fifty years of empiricism culminating in the matrix of 6-series sections are covered extensively in the classic catalogs by Abbott and von Doenhoff (ref. 2), Riegels (ref. 3) and reports such as those by Jacobs and Sherman (ref. 4).

The preeminence of the 6-series sections (slightly altered on occasion to the taste of the individual designer) lasted for nearly twenty years, and these sections have only been overshadowed since the late 1950's by the emergence of the revolution ushered in by the computer. While the equations of advanced potential flow methods and viscous flow theory can be concisely written, it is quite another matter to routinely solve analytically the complex flow fields around even "simple" airfoils in a real fluid. Thus, until the advent of large computers, theory could only guide what remained a largely experimental development effort.

The wind tunnel is a marvelous tool for describing <u>what</u> happens, but seldom provides much guidance on <u>why</u> a particular event (e.g., boundary layer separation) occurs. To go beyond the level of "design by testing,"

practical quantitative solutions to the equations of viscous flow were required to supplement empirical experience.

The remarkable success of computer based methods in improving airfoil performance beyond the NACA 6-series level is well demonstrated in the catalog of Wortmann FX-series sections (ref. 5) and the reports and papers listed in refs. 6 and 7. Despite this new progress, designers without access to a computer of sufficient size, or those lacking a sophisticated background in theoretical aerodynamics and mathematics are still forced to rely on catalog data and outmoded "simplified" theory. With very few exceptions (notably ref. 8), available good catalog data is for "ideal" surface quality wind tunnel models operating in the range $7 \times 10^5 \leq Rn < 10^7$. As a summary of the preceding historical discussion, Figure 3 shows some representative airfoils sections used, or specifically designed for, various categories of low-speed aircraft during the last eighty years. The variety of shapes even within a given category is sometimes bewildering.

LOW-SPEED AIRFOIL DESIGN

The general principles of low-speed, single-element airfoil design in light of modern theory have been discussed in detail by several authors, notably Wortmann (ref. 9-11), Miley (ref. 12) and Liebeck (ref. 13). A brief review is presented here in Appendix A.

Whether one is designing a new airfoil section or attempting to select one from a catalog, it is important that all the relevant criteria are kept clearly in mind. The author's list is as follows:

Basic Airfoil Selection/Design Criteria

1. Basic Operating Conditions (superscript * indicates design point):

   a. Lift Coefficient Range $\left(0 \leq C_{\ell_{\substack{min \\ drag}}} \leq C_\ell^* \leq C_{\ell_{max}}\right)$

   b. Reynold Number Range $\left(Rn_{min} < Rn^* < Rn_{max}\right)$

   c. Mach Number Range $\left(0 \leq M^* < M_{crit}\right)$

2. Airfoil Characteristics Desired (Priorities to be established for each specific application):

   a. Low Drag (e.g., absolute minimum drag at C_ℓ^*, "low" drag over operating C_ℓ range).

   b. High Lift (e.g., absolute $C_{\ell_{max}}$, moderate $C_{\ell_{max}}$ with "gentle" stall).

c. Pitching Moment (e.g., positive moment for flying wing applications, low negative moment to minimize horizontal tail trim loads or aeroelastic effects on wing).

3. Practical Constraints:

a. Required thickness-chord ratio and/or required local structural thickness.
b. Anticipated surface quality (e.g., skin joints or slat/airfoil junctions which might force boundary layer transition).

High-Lift/Low Drag Design

From the preceeding list it can be seen that the airfoil selection/design process is complex and this partially accounts for the wide variety of section shapes shown in Figure 3, each intended to strike some particularly beneficial compromise between often conflicting requirements. It is seldom possible to state categorically that a particular section is the "best" one even for a given type of aircraft.

Within the overall low-speed performance spectrum, however, one is generally forced to bias the selection/design toward achievement of either: (a) low-drag, or (b) high-lift. No general rules can be given for how much "high-lift" one can achieve with a "low-drag" section or vice versa, although clues are beginning to emerge from modern viscous flow theory. General guidelines for good design can be formulated, and these are briefly reviewed in Appendix A.

It should be noted that the NACA 6-series airfoils are basically "low drag" sections. Their long reign is due more to the fortuitous fact that they scaled well with Mach number, rather than providing the long runs of laminar flow which was the original design objective. Only in the special case of applications to sailplane wings was the original objective met, practical construction and operational problems (bugs, paint, rivets, dimples, etc.) tending to abort the "laminar flow" behavior in other applications. None of the 6-series sections can be categorized as "high-lift" airfoils.

Empirical Data

With the preceeding list of airfoil selection/design criteria in mind, one can consult the various catalogs to see if a suitable section exists. Data from these standard sources (e.g., Refs. 2-5, 7, 8) is summarized in global terms in Figure 4.

Within the range of Reynolds number for which large quantities of data exist, a diligent searcher can find some apparently curious anomalies - specifically the "spectacular" Liebeck sections (ref. 13). That the Liebeck sections achieve the high-lift performance shown is no longer in

serious question, nor are the reasons such performance is achieved. What remains unclear is the nature of the trade-offs in section characteristics which are available between the "feasible upper bound" represented by the Liebeck sections and the "top-of-the-line" conventional sections within the shaded bands shown in Figure 4.

As a prerequisite to discussion of systematic methods for evaluation of these trade-offs, some appreciation of the parameters of boundary layer theory as they relate to airfoil performance is required. Figures 5 through 8 show some examples of the boundary layer characteristics of several familiar sections and the relationships between this data; and the more traditional display of global performance data, section geometry and pressure distributions is discussed in detail in Appendix B.

AIRFOIL SYNTHESIS

To advance beyond an empirically based approach to airfoil selection, or to consider the prospect of tailoring airfoil sections to a specific application, it is necessary to understand the difference between a design approach based on "analysis" as contrasted with one based on "synthesis." The synthesis (inverse) approach to airfoil design begins with the boundary layer characteristics as they effect the pressure distribution and ultimately define and limit the performance of a section in every way. The airfoil shape is derived last in this process, and is that physically realizable contour which provides the desired flow characteristics. Synthesis is almost the direct opposite to the traditional "empirical" (analysis) approach wherein one begins with a shape which yields a pressure distribution and a set of boundary layer characteristics, and thus initial values of lift, drag and moment. Performance requirements are finally met by trial and error modification of the shape. Whether these modifications are made to a wind tunnel or computer model, the basic process is one of iterative cut-and-try until the solution "converges."

AN INVERSE AIRFOIL DESIGN TECHNIQUE

While the possibility of synthesizing an airfoil has been recognized for many years, it has only been possible to implement satisfactory inverse methods (based on modern boundary layer theory) since the advent of the computer. Synthesis approaches have been employed by Wortmann (ref. 9) and more recently by Liebeck (ref. 13). A very general technique for airfoil synthesis (applicable to both single- and multi-element section components) has recently been developed by Henderson (ref. 14), based on proven integral boundary layer techniques described largely in Schlichting (ref. 15). While the specific techniques used in the overall program may seem almost old fashioned, the program has proven to be very satisfactory in practice and is quite a powerful tool for both single and multi-element airfoil synthesis (particularly when coupled with the

methods described in ref. 16). Details of the method are described in reference 14, and only the basic elements are listed here for reference.

Elements of an Inverse Boundary Layer Analysis and Design Technique

Component	Theory (ref. 15 except *)
Laminar Boundary Layer	Polhausen
Laminar Separation	Polhausen
Laminar Separation Bubble	Henderson (empirical)*
Transition	Granville
Turbulent Boundary Layer	Momentum integral Power law velocity profile Garner's eqn. for form parameter Ludwieg-Tillman eqn. for wall shear stress
Turbulent Separation	$H > 3.0$
Compressibility Corrections	Karman-Tsien*
Profile Drag	Squire and Young

Utilizing the methodology outlined above, it becomes possible to implement the airfoil design process shown in Figure 9. Once an "optimized" viscous flow pressure distribution and linear theory airfoil shape have been determined, the powerful methods described by Henderson in reference 16 (which also account for separated flows) are applied to arrive at the final airfoil geometry which yields that pressure distribution, and final analytic performance predictions are made.

Several points in this synthesis process need to be clarified. For example, any "airfoil" shape will produce a unique pressure distribution. The converse is not generally true. In order to assure that an initial "designed" pressure distribution will result in a closed, non-reentrant airfoil shape, an upper surface pressure distribution is designed free of geometrical constraints, and a lower surface pressure distribution is defined as that which will result in a section with an NACA 00XX thickness form. This yields a total pressure distribution which will result in a realizable airfoil of desired thickness. This initial lower surface pressure distribution and its corresponding boundary layer characteristics are usually poor. In the initial stage, however, it is the upper surface which is being optimized, and it is a simple matter to subsequently reconfigure the lower surface (guided by the preliminary result) to a more desirable form as indicated in Figure 9.

The program allows a rather arbitrary specification of upper surface recovery region form parameter (H) variation as a primary input. Thus one can systematically study the effect of this important parameter easily and in some detail before proceeding to more detailed design calculations. This feature will be demonstrated shortly. The significance of various form parameter variations is discussed in Appendix B.

The most difficult parameter to specify correctly at the outset is the trailing edge pressure coefficient. This parameter has a very powerful effect on the design lift level a theoretical section will achieve, and to date the determination of its final "correct" value has generally required an iterative approach. The problem is discussed at some length by Liebeck (ref. 13).

Probably the weakest part of the theoretical performance estimation procedure is calculation of profile drag. In principle, at the final stage in the design cycle one can integrate the total pressure and skin friction drag components and arrive at a total profile drag coefficient. Experience to date with viscous flow programs which accurately predict pressure distributions and hence lift and pitching moments gives generally less accurate drag estimates. This is due primarily to the fact that drag is usually two orders of magnitude lower than lift, and whereas errors in lift computations are small with a good pressure distribution predictor, errors in pressure integration (particularly in the leading edge region) tend to be on the same order as pressure drag values. Thus for simplicity, the present state of the art is to rely on the method of Squire and Young (ref. 15) for total drag prediction and, in the present case, a supplementary calculation of skin friction drag to provide a clarification of the magnitude of this component within the total drag value. This procedure has been found to be reasonably adequate, at least for purposes of comparing the drags of single-element sections. While absolute values of Squire and Young drag may sometimes be questionable, anyone experienced with the pecularities of two-dimensional wind tunnel testing (particularly at high-lift values) must realize the magnitude of the error band in "good" experimental drag data.

SOME RESULTS

To indicate the use of the above methodology, two examples have been chosen to demonstrate several aspects of the influence of Reynolds number on airfoil characteristics. Figure 10 demonstrates the results obtainable from a parametric study of the influence of variations of recovery point location and Reynolds number on a family of sections with simple roof-top pressure distributions (cf. Fig. 9), and a common specified exponential form factor variation in the recovery region. The principal observations to be made in this example are the significant difference in "optimum" recovery point between sections designed (for

high lift-drag ratios) at two million and thirty million Reynolds number, and the ultimate desirability of designing to full-scale Reynolds number conditions (i.e., 30×10^6 in this case) to achieve maximum performance, despite the fact that such results may appear inferior to those obtained from a design optimized at wind tunnel conditions when both are tested at low Reynold numbers.

Figure 11 shows the effect of a systematic variation of recovery region form parameter on the shape and characteristics of three airfoils designed to the same lift coefficient level at a Reynolds number of five-hundred thousand. The performance characteristics of these sections are summarized in Figure 12, and clearly show the trades available in lift, drag, pitching moment and stall break from different specifications of recovery region characteristics.

The results shown in Figure 12 are generally nonobvious and are of some interest in view of the discussion in Appendix B and the fact that relatively little modern experimental data exists for sections designed specifically for this low value of Reynolds number. The stall behavior of the three sections can be understood on the basis of the discussion in Appendix B regarding the correlation between boundary layer form parameter (H) variation and upper surface separation progression.

A more subtle and remarkable aspect of the results shown in Figure 12 is that the net Squire-Young drag of all three sections at the design point lift coefficient is nearly the same. The rate at which the drag rises between the design point and maximum lift coefficients will be different, however, reflecting the way in which flow separation progresses on the three sections as stall is approached. The example calculations also show the relative values of upper surface recovery region (turbulent) skin friction coefficient relative to the total upper surface profile drag coefficient. Although the highly concave recovery pressure distribution of Airfoil C (which approaches a Stratford type recovery, c.f. Appendix B) shown in Figure 11 has the lowest skin friction coefficients, it also has the highest rate of growth (and final trailing edge value) of boundary layer momentum thickness. Thus while Airfoil C has the lowest skin friction drag it has the highest pressure drag and in the overall balance, all three sections exhibit similiar net profile drag values. This effect is not limited to the low Reynolds number case shown. As Reynolds number increases, the pressure drag becomes the increasingly dominant drag term, and minimization of the recovery region turbulent skin friction coefficient by employing a Stratford type recovery becomes increasingly less satisfactory.

CONCLUDING COMMENTS

A review of the history and present state of the art of low-speed single-element airfoil design has been presented, leading to a description of a powerful new inverse boundary layer scheme which can be used to synthesize an airfoil section tailored to the requirements of a

specific aircraft. The basic intent of this paper has been to provide background and motivation for this alternative approach to airfoil design, as contrasted with the more traditional "design by experiment/analysis" approach to the problem. Along the way (Appendix B) it has been possible to clarify the performance characteristics of sections of quite different geometry and design objectives, and indicate the influence of Reynolds number on both "low-drag" and "high-lift" sections. Several examples of parametric analyses using the "synthesis" methodology have been presented which only hint at the potential of these new techniques.

It has been shown that airfoil design (even when limited to very low Mach numbers and single-element sections) is a hugely complex problem to which no single "best" solution exists even for a single specialized category of aircraft type. On the other hand, it is clearly possible to derive a section biased and optimized to the taste of an individual aerodynamicist with a great deal more intelligence than was possible less than a decade ago. Much work still needs to be done, however, to finally free the hang glider designer from reliance on his present very slender catalog of airfoil candidates.

REFERENCES

1. McMasters, J. H. and Greer, R. R., "Large Winged Surface Effect Vehicles," in Jane's Surface Skimmers - Hydrodoils and Hovercraft, 1975-76, Ray McLeavy, ed. NY: Franklin Watts (for Janes Yearbook: London), 1975, pp. 425-33.

2. Abbott, I. H. and von Doenhoff, A. E., Airfoil Sections, NY: Dover, 1959.

3. Riegels, F. W., Airfoil Sections, London: Butterworth, 1961.

4. Jacobs, E. N. and Sherman, A., "Airfoil Section Characteristics as Affected by Variations of the Reynolds Number," NACA TR 586, 1937.

5. Althaus, D. Stuttgarter Profil Katalog I, Stuttgart University, 1972.

6. McMasters, J. H., "Low-Speed Airfoil Bibliography," Tech. Soaring, Vol. 3, No. 4, Fall 1974, pp. 40-42.

7. Hoerner, S. F. and Borst, H. V., Fluid-Dynamic Lift, Hoerner Fluid Dynamics, P.O. Box 342, Brick Town, N.J. 08723, 1975.

8. Schmitz, F. W., Aerodynamik des Flugmodells, Trans: N 70-39001, Nat. Tech. Info. Service, Springfield, Va., Nov. 1967.

9. Wortmann, F. X., "Experimental Investigations on New Laminar Profiles for Gliders and Helicopters," Ministry of Aviation Translation TIL/T.4906, March 1960 (Avail. ASTIA, Arlington, Va.) (Z. Flugwiss, Vol. 5, No. 8, 1957, pp. 228-48).

10. Wortmann, F. X., "Progress in the Design of Low Drag Airfoils," in Boundary Layer and Flow Control, G. V. Lachmann, London, 1961, pp. 748-70.

11. Wortmann, F. X., "A Critical Review of the Physical Aspects of Airfoil Design at Low Mach Number," in Motorless Flight Research - 1972, J. L. Nash-Weber, ed, NASA CR 2315, Nov. 1973.

12. Miley, S., "On the Design of Airfoils for Low Reynolds Numbers," AIAA Paper No. 74-1017, September 1974.

13. Liebeck, R. H., "Design of Subsonic Airfoils for High Lift," Journal of Aircraft, Vol. 15, No. 9, September 1978, pp. 547-61.

14. Henderson, M. L., "Inverse Boundary Layer Technique for Airfoil Design," Proceedings NASA Advanced Technology Airfoil Research (ATAR) Conference, March 1978.

15. Schlichting, H., Boundary Layer Theory, NY: McGraw-Hill, 1960.

16. Henderson, M. L.: Inverse Boundary Layer Technique for Airfoil Design. Advanced Technology Airfoil Research, Volume I, NASA CP-2045, Pt. 1, 1978, pp. 383-397.

17. McGhee, R. J. and Beasley, W. D., "Low Speed Aerodynamic Characteristics of a 17-Percent Thick Airfoil Section for General Aviation Applications," NASA TN D-7428, 1973.

18. Wortmann, F. X., "The Quest for High Lift," AIAA Paper No. 74-1018, September, 1974.

19. Loftin, L. K., Jr., and Bursnall, W. J., "The Effects of Variations in Reynolds Number Between 3.0×10^6 and 25.0×10^6 Upon the Aerodynamic Characteristics of a Number of NACA 6-Series Airfoil Sections," NACA TR 964, 1946.

20. Stratford, B. S., "The Prediction of Separation of the Turbulent Boundary Layer," Jour. Fluid Mech., Vol. 5, January 1959, pp. 1-16.

APPENDIX A: BASIC AIRFOIL DESIGN

The purpose of this appendix is to provide a brief tutorial review of some of the principles of airfoil design. The discussion follows that of Wortmann (ref. 11), Miley (ref. 12) and Liebeck (ref. 13).

All practical airfoils will carry some lift loading (whether high, low, or moderate) at some desired operating condition, and this will be characterized by generation of some peak level of negative pressure coefficient on the upper surface of the section, followed by recovery to near free-stream conditions at the trailing edge. The pressure loading on the lower surface will depend on factors like required maximum section thickness, establishment of favorable pressure gradients for low-drag at the section design lift level, and the requirements of satisfactory "off-design" performance at low section lift coefficients. At some point on both surfaces of the contour, the initial run of laminar boundary layer flow will transition to turbulent flow, the particular transition points being strongly dependent on the Reynold number, the form of the pressure distribution (or the profile shape which generates it), the surface quality of the section, and the free-stream turbulence level. All other factors being equal, the natural transition point will move forward on the profile as Reynolds number increases.

At this point there is a parting of the ways as one seeks either high-lift, or low-drag performance at low-to-moderate lift coefficients. To achieve low-drag, the longest possible runs of laminar flow are desired on both surfaces of the section followed by an orderly transition to thin turbulent boundary layer flow as the pressure recovers to trailing edge conditions; and separation is to be avoided like the plague.

In the high-lift case, attention mainly focuses on the upper surface. As in the low-drag case laminar flow is sought, together with high negative pressures over the forward portion of the section. The problem in the high-lift case is not necessarily to delay the onset of turbulent flow, but rather to cause an orderly transition at some optimum point to a healthy thin turbulent boundary layer over the pressure recovery region to allow the flow to decelerate from the high peak values reached on the forward portion without significant separation. The "optimum" high-lift upper surface pressure distribution will thus be constructed to produce the highest possible loading on the forward portion of the profile, consistent with the recovery capability of the turbulent boundary layer beginning at an "optimum" transition point. At low Reynolds numbers, getting rid of laminar flow at the recovery point and avoidance of large scale laminar separation become a major consideration.

A major constraint on the high-lift section is the character of the stall break; all things being equal, a gradual stall progressing from the trailing edge is desired. It should also be noted that the bulk of "good" high-lift sections achieve their maximum lift coefficients after upper surface (trailing edge) separation has begun. Controlled laminar separation bubbles may even be tolerated if they lead to orderly transition to turbulent flow in the pressure recovery region and do not burst before trailing edge separation is well developed.

In the high-lift case, the lower surface pressure distribution will be tailored in much the same fashion as in the low-drag case, although the

lower surface pressure distribution can be made to produce a significant portion of the net lift and/or alter the pitching moment characteristics. This factor and the influence of various forms of upper surface distribution on section pitching moment coefficients are indicated in Figures 9 through 12 and in Appendix B.

APPENDIX B: SOME RELATIONSHIPS BETWEEN AIRFOIL PERFORMANCE AND BOUNDARY LAYER CHARACTERISTICS

While most aerodynamicists have some appreciation of the section geometric parameters (e.g. thickness, camber, leading edge radius, trailing edge angle) which may influence performance, relatively few have a corresponding "feeling" for the fundamental parameters of boundary layer theory (e.g. form parameter, momentum thickness), and how these parameters are influenced by scale effects. The purpose of this appendix is to provide a brief evaluation of the boundary layer characteristics of several representative airfoils, and a description of how these parameters relate to the more familiar presentations of pressure distributions and global performance characteristics. An understanding of the connection between boundary layer behavior, pressure distribution, and section geometry as they influence performance is essential to success in the synthesis approach to design.

The performance characteristics of four familiar sections are shown in Figure 5. Two of these sections (the NACA 63_3-018 and Wortmann FX 61-184) have been designed primarily for low-drag, and the other two (the FX 74-CL6-140 and Liebeck L1003) for high-lift. These sections actually represent something of a continuum in that the NACA section is a classic "minimum drag" shape while the Liebeck is a pure "high-lift" section. The Wortmann FX 61-184 (ref. 5, 11) is a classic 1960 vintage sailplane section designed for "low-drag" over a "wide" range of lift coefficients, with a compromise struck between absolute low drag, thickness, and a very benevolent stall behavior at a moderate maximum lift coefficient.

The FX 74-CL6-140 (ref. 18) on the other hand, represents an attempt to design a section with the same level of maximum lift coefficient as the Liebeck, but with a biased compromise again being struck between thickness, maximum lift, wide "drag bucket" and satisfactory stall characteristics. All four sections are quite different in shape, and in the absence of detailed information on the types of pressure distribution and boundary layer characteristics (including an evaluation of the post-separated flow region) one is provided only superficial clues to why each of these sections exhibits such different performance characteristics.

As an aside, the influence of flow separation on the performance of a section and the importance of accurately modeling this effect in a theoretical design exercise have been graphically demonstrated by Henderson (ref. 16). Figure 6 shows an experimental lift curve for the NASA GA(W)-1 section (ref. 17) in comparison with theoretical

calculations made with increasingly sophisticated analytical techniques. For this particular section, Figure 6 shows that modeling the attached boundary layer flow remains inadequate in predicting the variation in lift with angle of attack beyond 75% of the final maximum lift coefficient value. The full theory developed by Henderson (ref. 16), which models both the boundary layer and separation, provides excellent predictions however. This improved methodology (which extends to multielement sections) represents a major, and so far unique, advance in computational capability.

To better understand the differences in performance and shape between the sections shown in Figure 5, it is necessary to evaluate in detail the pressure distributions and boundary layer parameter (specifically the form parameter, H) variations for each section. Example data for the NACA 63_3-018 (ref. 19) at 2° angle of attack (within the drag bucket of the section) are shown in Figure 7 for three widely different Reynolds numbers. The classic 6-series aft-end shape corresponds to a roughly linear rise in the recovery region pressure distribution, and consequent form parameter (H) variation shown. The influence of Reynolds number on the location of the point of natural transition is indicated, and clearly shows the difficulty of achieving long runs of laminar flow as Reynolds number increases.

As shown in Figure 11, the shape and magnitude of the form parameter (the ratio of boundary layer displacement thickness to momentum thickness) variation in the pressure recovery region of the airfoil correlate in general with the shape of the pressure distribution in this region. The specification of recovery region form parameter variation is one of the central inputs in the Henderson inverse method described previously. As discussed in Schlichting (ref. 15), laminar separation occurs when H reaches 3.5 and turbulent separation begins when H exceeds about 3.0. The influence of the H-factor variation on airfoil stall behavior will be discussed presently.

Wortmann (refs. 9-11) has argued that there are advantages to a "concave" recovery pressure distribution (with near constant value of recovery region form parameter) for drag reduction, compared to the linear or convex pressure distributions associated with earlier profiles, including many of the Göttingen/Joukowski airfoils (c.f. Figure 3). The basic principles of the design of Wortmann's sailplane and related sections (including the FX 61-184) with concave pressure rises have been thoroughly discussed in references 9 through 11, and by Miley (ref. 12). These references also discuss the importance of properly contouring both the upper and lower surfaces of low-drag profiles.

Turning attention to the high-lift airfoils cases, it is interesting to compare the pressure distributions and boundary layer characteristics of the Wortmann FX 74-CL4-140 (ref. 18) and Liebeck L1003 (ref. 13) shown in Figure 8, and contrast this data with that for the NACA 63_3-018 in Figure 7.

The Liebeck sections are of great theoretical interest for several reasons. Members of the family apparently approach the upper limit of lift coefficient achievable with a single-element section without mechanical boundary layer control. The sections also exhibit commendably low drag coefficients in the region of the design lift coefficient and low pitching moments. In exchange for these desirable characteristics, the stall behavior is wretched and the undersurface separates at rather high (positive) lift coefficients, thus limiting "high-speed" performance. This latter factor can be partially ameliorated by use of a camber changing trailing edge flap; however, the abrupt stall behavior is a fundamental characteristic of the basic family.

The Liebeck sections have been theoretically designed by the previously described synthesis process, in this case by use of a Stratford recovery region pressure distribution (ref. 20) to establish the maximum level of negative pressure on the upper surface "roof top" region of the section. The Stratford recovery region pressure distribution is that which, for a turbulent flow, results in a boundary layer which is everywhere equally close to separation. Thus, to within the accuracy of the Stratford formulation, the recovery region boundary layer is either completely attached or completely separated - there is no (theoretical) middle ground. This factor accounts for the very abrupt stall behavior of the sections. Thus, by reliance on the Stratford distribution, Liebeck generated the single class of high lift sections which can be "optimized" and analyzed without recourse to explicit partially separated flow calculations. Herein lies the success Liebeck had in designing to very much higher lift coefficients and section lift-drag ratios than had once been thought possible for a single-element section. The resulting shapes and pressure distributions for Liebeck sections are entirely non-obvious and the prospects of happening on them by "cut-and-try" were remote. This example provides a strong motivation for use of inverse methods.

The experimental verification of the predicted performance of the Liebeck sections, and by extension the validation of the Stratford theory, apparently opens a whole new prospect in high-lift airfoil design. However, the inability of Liebeck's methodology to account for partially separated flows, and the resulting formal reliance on the Stratford distribution, severely circumscribe the range of sections which can be designed. The possible trade-offs in performance between the Liebeck sections and the range of conventional sections shown in Figure 4 remain obscure.

The result of a highly sophisticated attempt to design such an "intermediate" airfoil, which trades some drag and thickness for a better stall behavior, while acheiving the same high-lift level, is represented by the Wortmann FX 74-CL(X)-140 pair discussed in ref. 18. Referring to Figure 8, one sees that the Liebeck and Wortmann pressure distributions are quite different, although both have "concave" distributions in the recovery region. Where Liebeck uses a well defined "instability" region as described by Miley (ref. 12) to achieve orderly transition to

turbulent flow in the recovery region, Wortmann forces the formation of a "well-behaved" thin laminar separation bubble which acts as a passive boundary layer trip.

Reviewing the performance curves for the Wortmann and Liebeck high-lift sections shown in Figure 5, one sees the consequences of the two approaches to the design problem. Looking at the resulting airfoil shapes and pressure distributions in Figure 8, one sees little in common between the two sections however. To see how "equally" high-lift coefficients are generated by two such dissimilar sections, one must refer to the details of the boundary layer characteristics for the two airfoils.

For both the Liebeck and Wortmann sections, recovery begins at about 40% of the chord aft of the leading edge. Prior to this, the "laminar H" for the Liebeck section is nearly constant through the instability region, falling abruptly to an initial "turbulent" value as the flow transitions. By contrast, on the Wortmann section the laminar H rises abruptly prior to transition until a value of H for laminar separation is reached, following which a "short bubble" is formed leading to transition and turbulent reattachment at the beginning of the recovery region.

Once into the recovery region, the turbulent form parameters on the Liebeck section rise rapidly to an initially high value and then begin a further very gradual linear rise to a point just short of the trailing edge. This recovery region form parameter variation is characteristic of a Stratford imposed pressure distribution.

On the Wortmann section, the turbulent form parameter does not jump initially, but rises instead from its starting value behind the laminar bubble at a nearly identical rate to that of the Liebeck/Stratford, until it hooks upward at the end. The result is again a generally concave pressure distribution on the recovery portion of the Wortmann section.

Comparison of these form parameter variations for two very different "looking" sections clarifies much of the difference in stall behavior between the sections. On the Liebeck section, as angle of attack is increased beyond the "design" value (design lift coefficient equal to 1.8), the recovery region form parameter level is shifted progressively upward until a value of approximately 3.0 is reached, at which point turbulent separation begins. With the Liebeck/Stratford recovery pressure distribution, the form parameter level is almost constant across the bulk of the recovery region. Thus, if nothing else (a laminar short bubble for example) interferes, the whole recovery region becomes "critical" with respect to separation at nearly the same time, and an abrupt stall subsequently occurs. By contrast, the recovery region form parameter on the Wortmann section does not reach so uniform a critical level as angle of attack is increased towards stall. This is reflected in the more gradual stall break for the Wortmann section. The existence of the short bubble ahead of the recovery point on the Wortmann section

throughout this approach to stall clouds the issue of how the stall progresses, and the critic will note that the stall behavior is not that much better than the Liebeck. That the stall progresses non-catastrophically (at least initially) from the trailing edge is indicated (c.f. Fig. 5) by the creeping drag rise as stall is approached and entered.

The preceeding examples are intended to be illustrative of a few well known sections and demonstrate some specific trends. The results shown are not necessarily typical of wide classes of sections and the possible ranges of form parameter variation and pressure distribution are enormous. These limited examples do, however, demonstrate the level of detailed analysis which modern theory can provide, and the necessity of delving this deeply into detail in order to understand differences and similarities between airfoils with different shapes and global performance characteristics, and finally to design an optimized profile for a given application. Obviously, much more could and should be said on these topics. In addition, much needs to be said regarding the problems of "optimizing" both upper and lower surface contours, and the influence on drag of form parameter variation, boundary layer momentum thickness, transition point, etc. All of these investigations require a technique by which the important variables of the problem can be varied in an orderly and systematic fashion, particularly as a function of Reynolds number. Such a technique has been described in this paper.

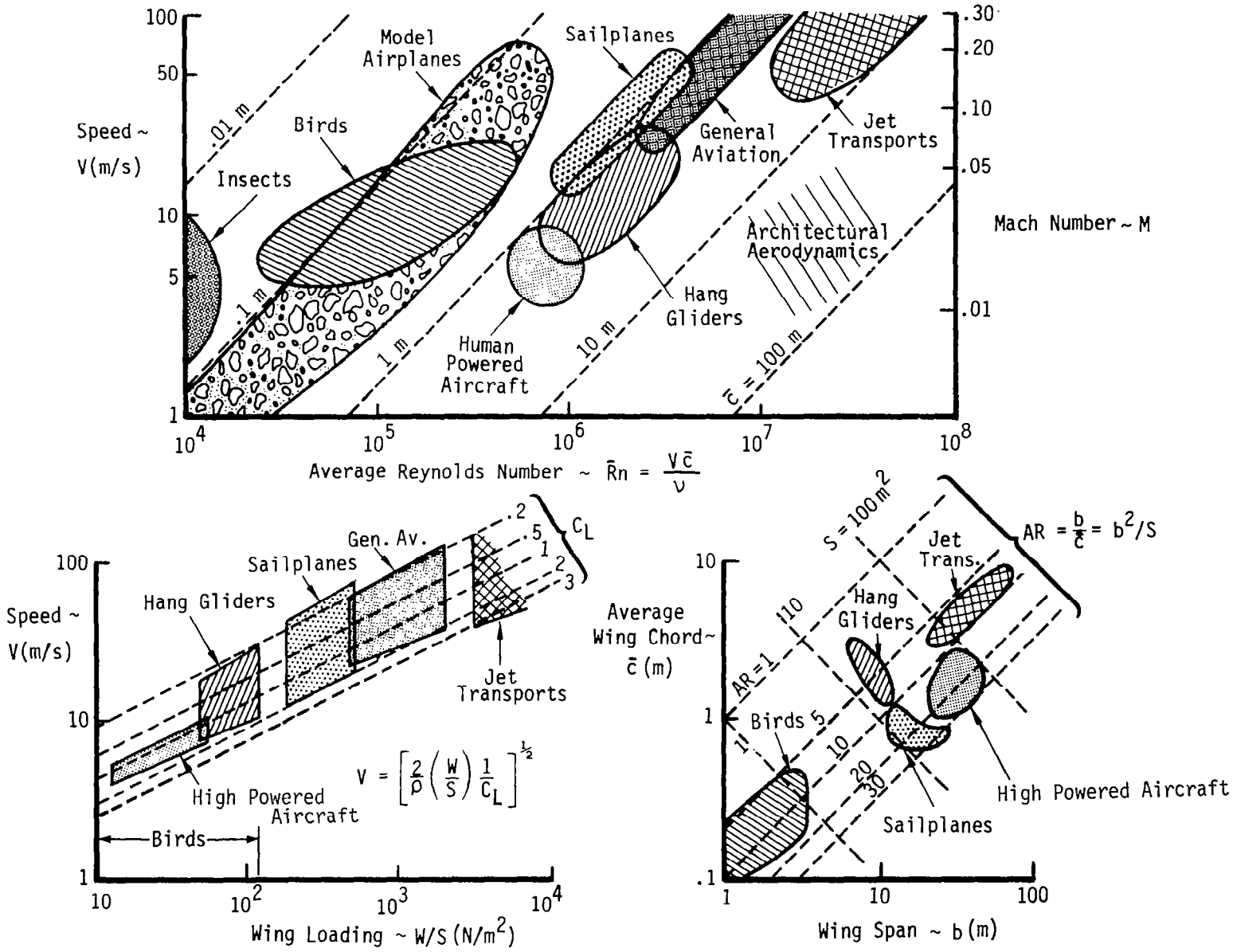

FIGURE 1 A GUIDE TO THE REGIONS OF LOW-SPEED FLIGHT AT STANDARD SEA LEVEL CONDITIONS

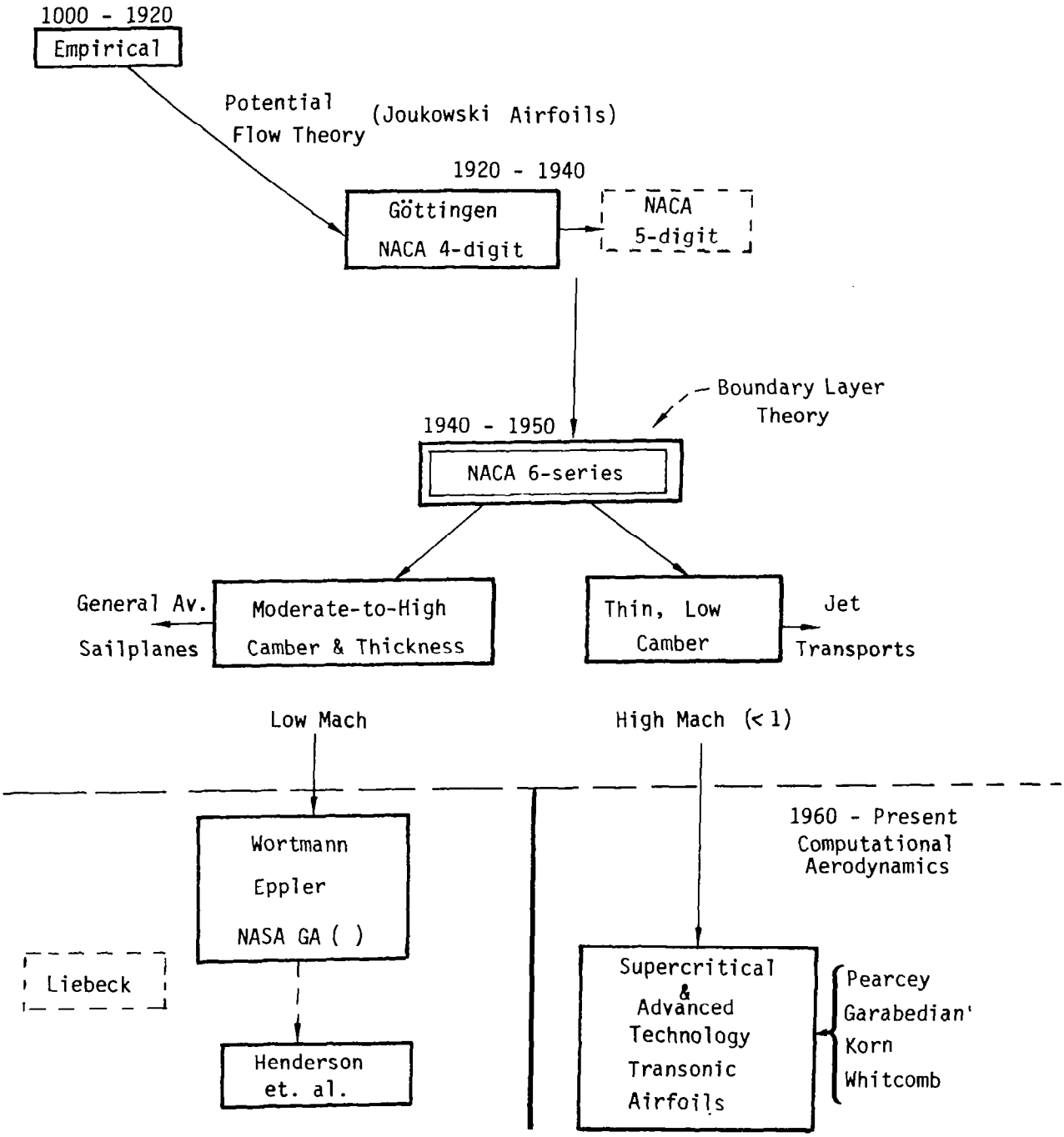

FIGURE 2 SINGLE ELEMENT AIRFOIL EVOLUTION

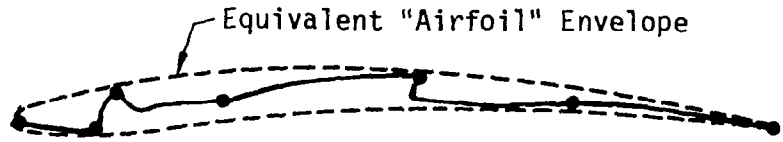

Crane Fly (c = .004 m)

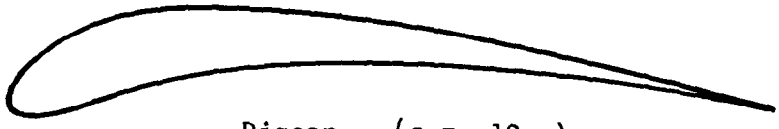

Pigeon (c = .10 m)

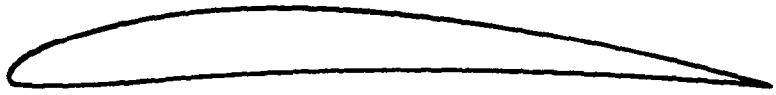

NACA 6409

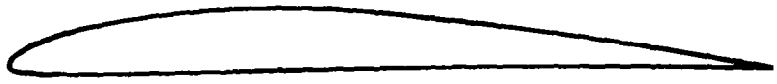

Eppler 387

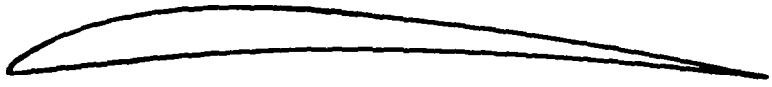

Benedek 6356 b

Jedelsky EJ-75

FIGURE 3a SOME VERY LOW-SPEED AIRFOILS

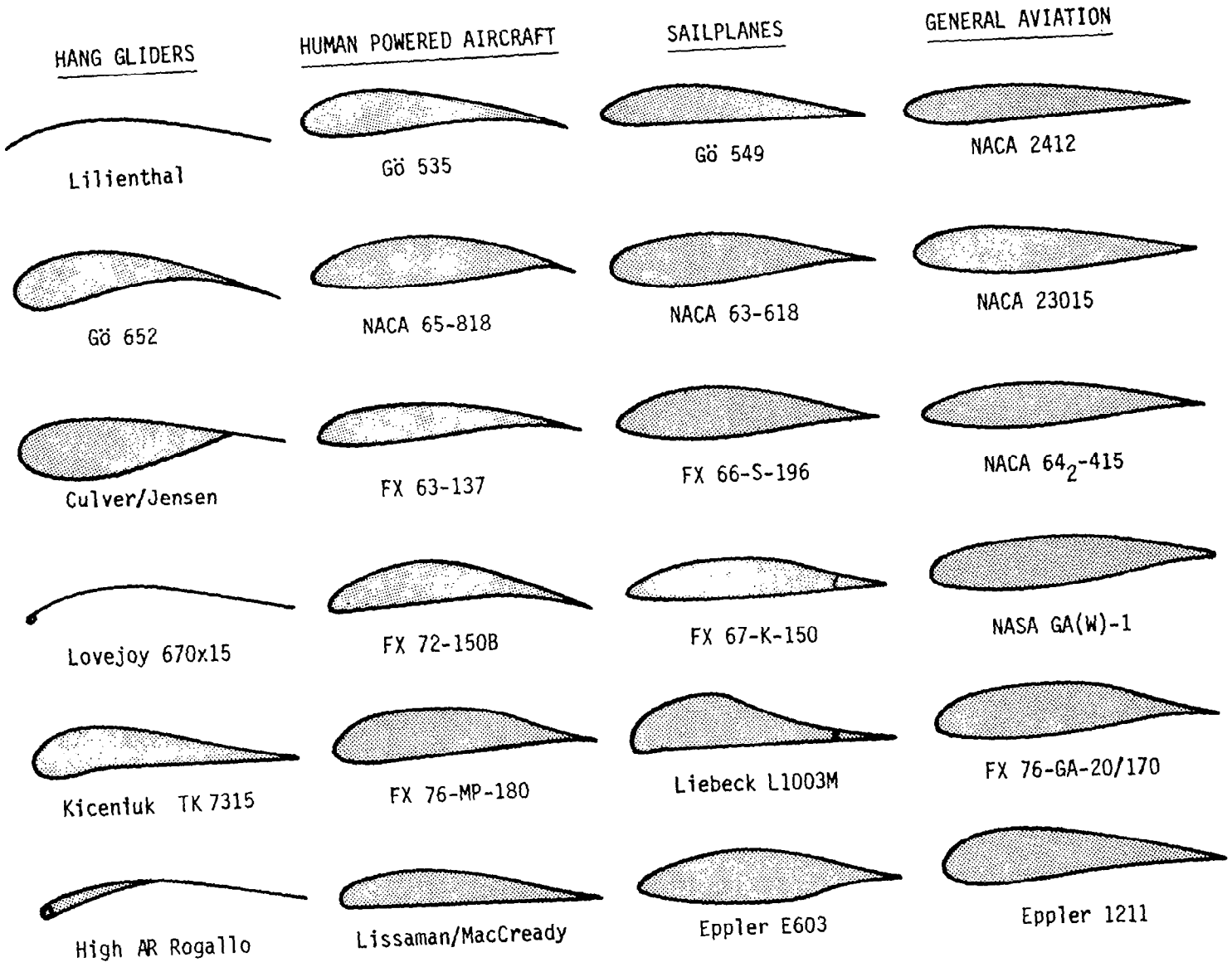

FIGURE 2b REPRESENTATIVE LOW-SPEED AIRFOIL SECTIONS

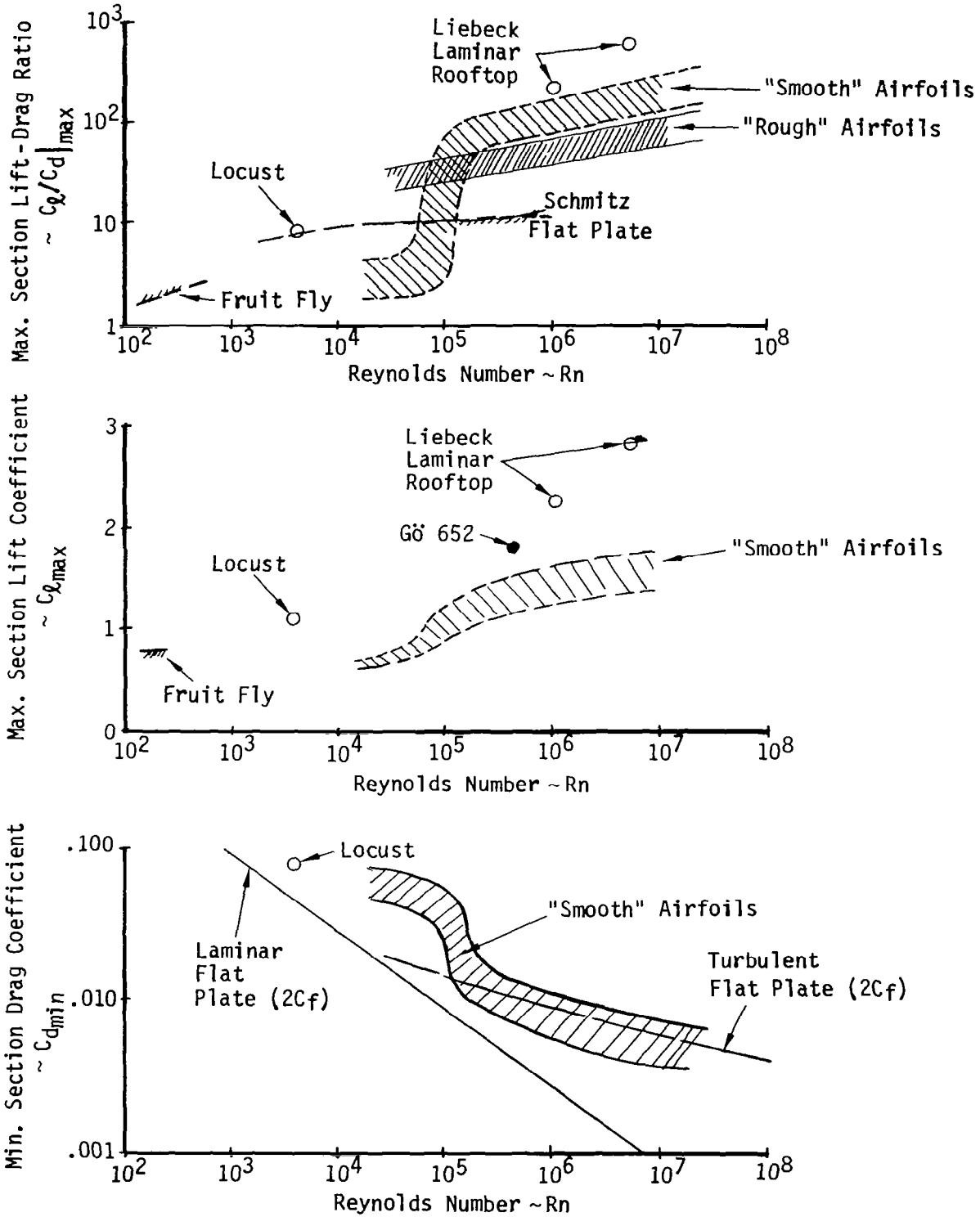

FIGURE 4 EMPIRICAL SURVEY OF LOW-SPEED SINGLE ELEMENT AIRFOIL DATA

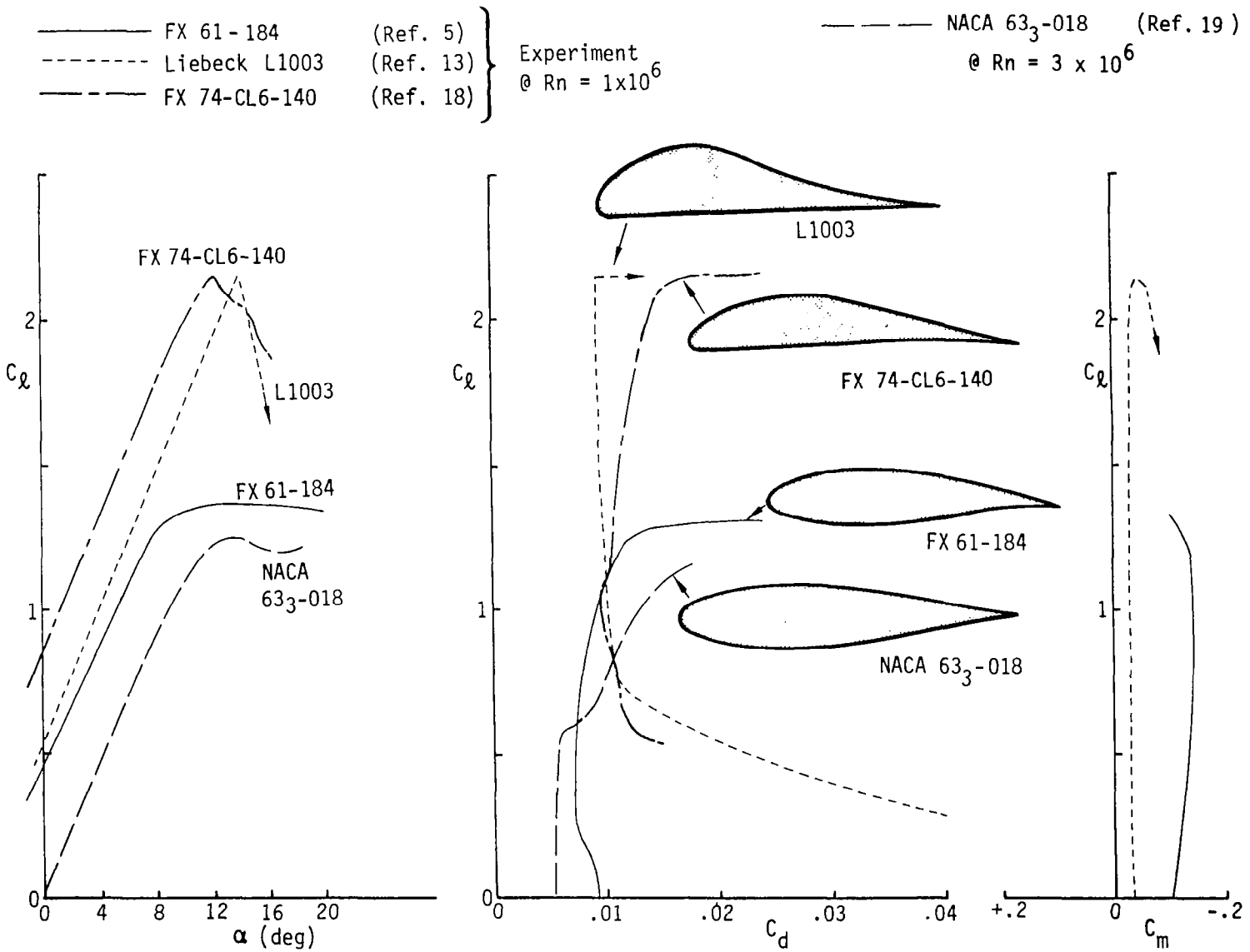

FIGURE 5 - COMPARISON OF PERFORMANCE CHARACTERISTICS OF SEVERAL AIRFOILS

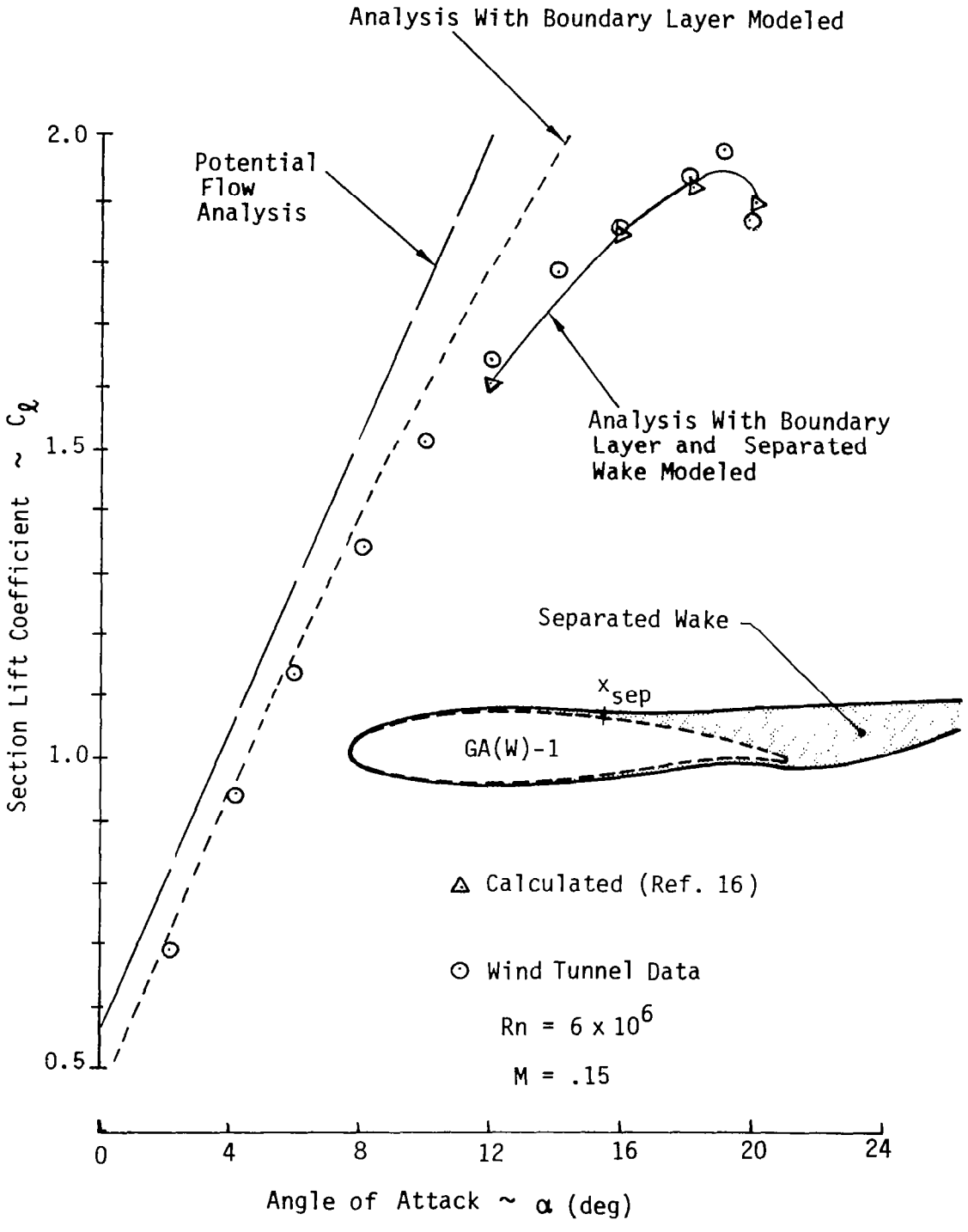

FIGURE 6. TEST THEORY COMPARISONS FOR NASA GA(W)-1 AIRFOIL

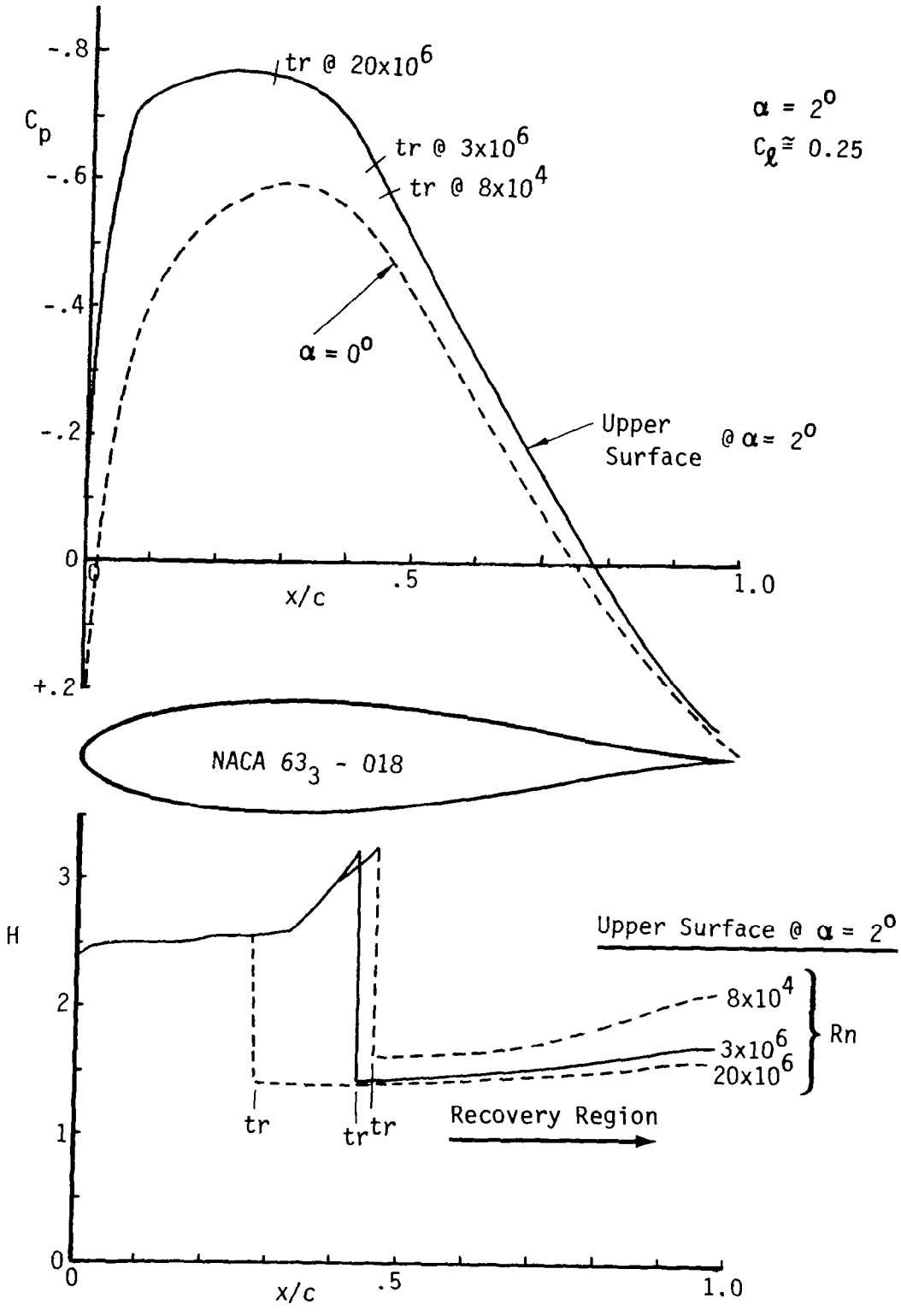

FIGURE 7 - PRESSURE DISTRIBUTION AND BOUNDARY LAYER CHARACTERISTICS OF THE NACA 63_3 - 018 AT SEVERAL REYNOLDS NUMBERS

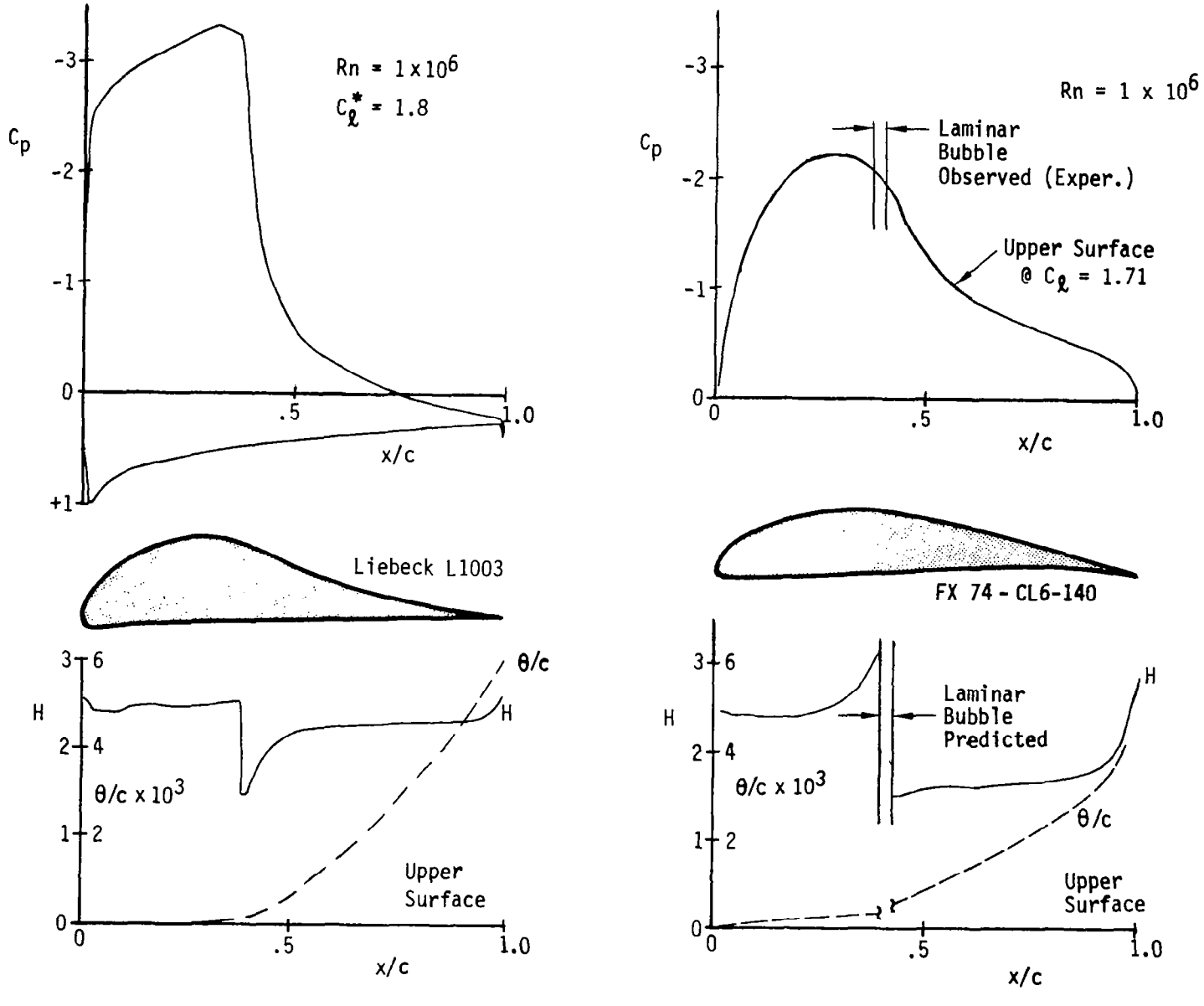

FIGURE 8 - COMPARISON OF LIEBECK AND WORTMANN HIGH-LIFT AIRFOILS

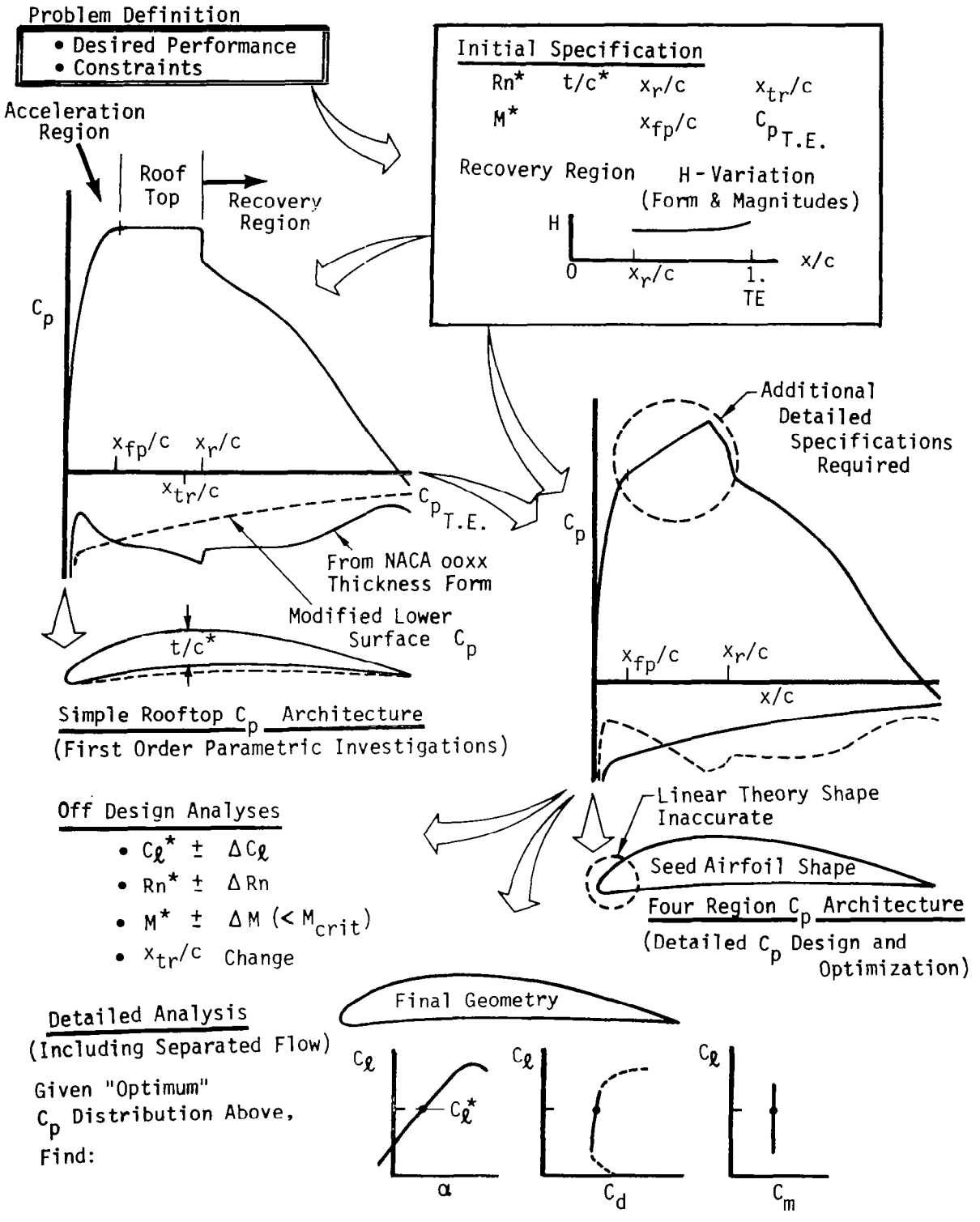

FIGURE 9 GENERAL AIRFOIL DESIGN PROCEDURE

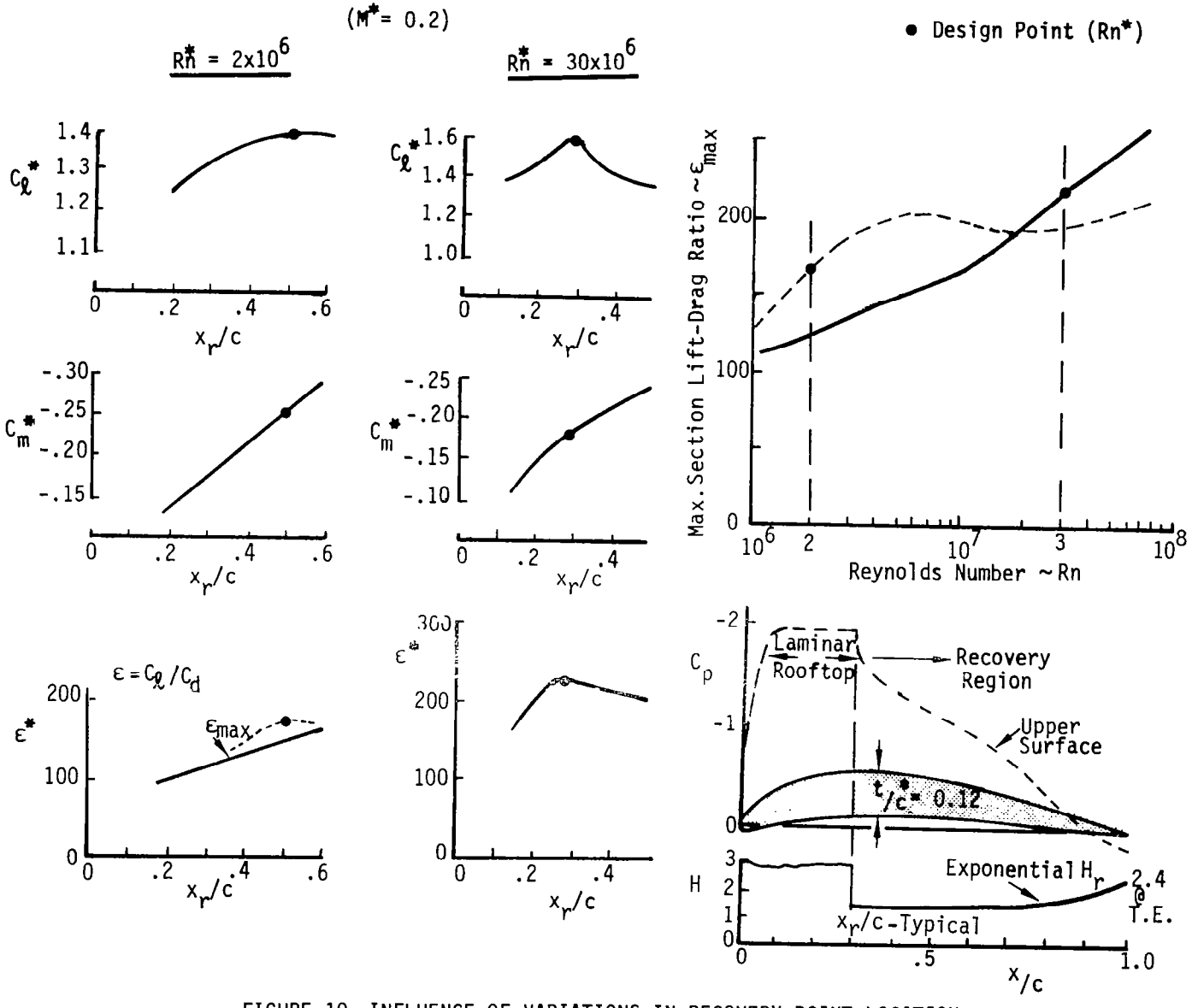

FIGURE 10 INFLUENCE OF VARIATIONS IN RECOVERY POINT LOCATION AND REYNOLDS NUMBER ON A FAMILY OF ROOF-TOP AIRFOILS

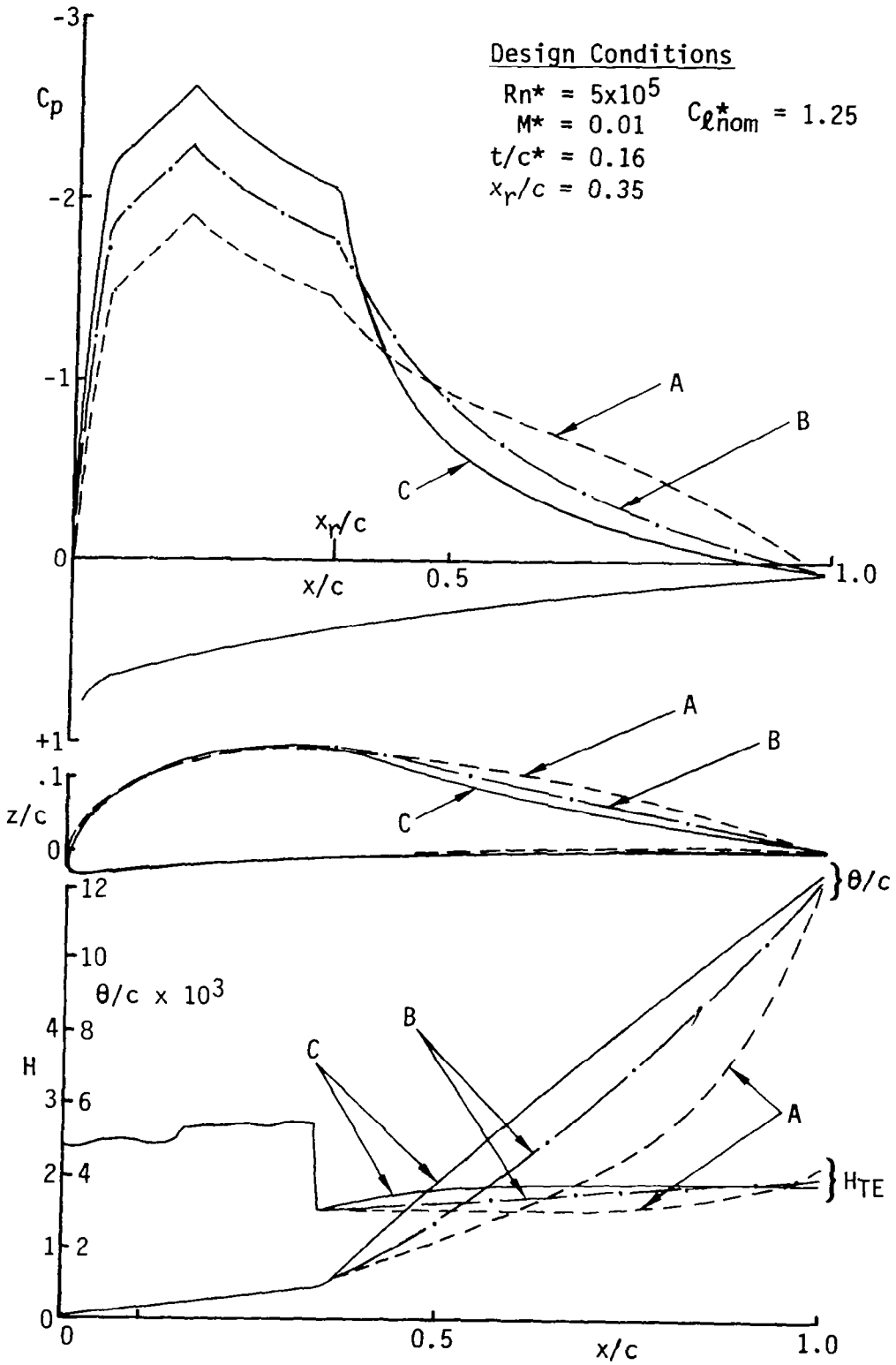

FIGURE 11 THREE AIRFOILS DESIGNED FOR THE SAME LIFT COEFFICIENT AT Rn = .5 × 10^6

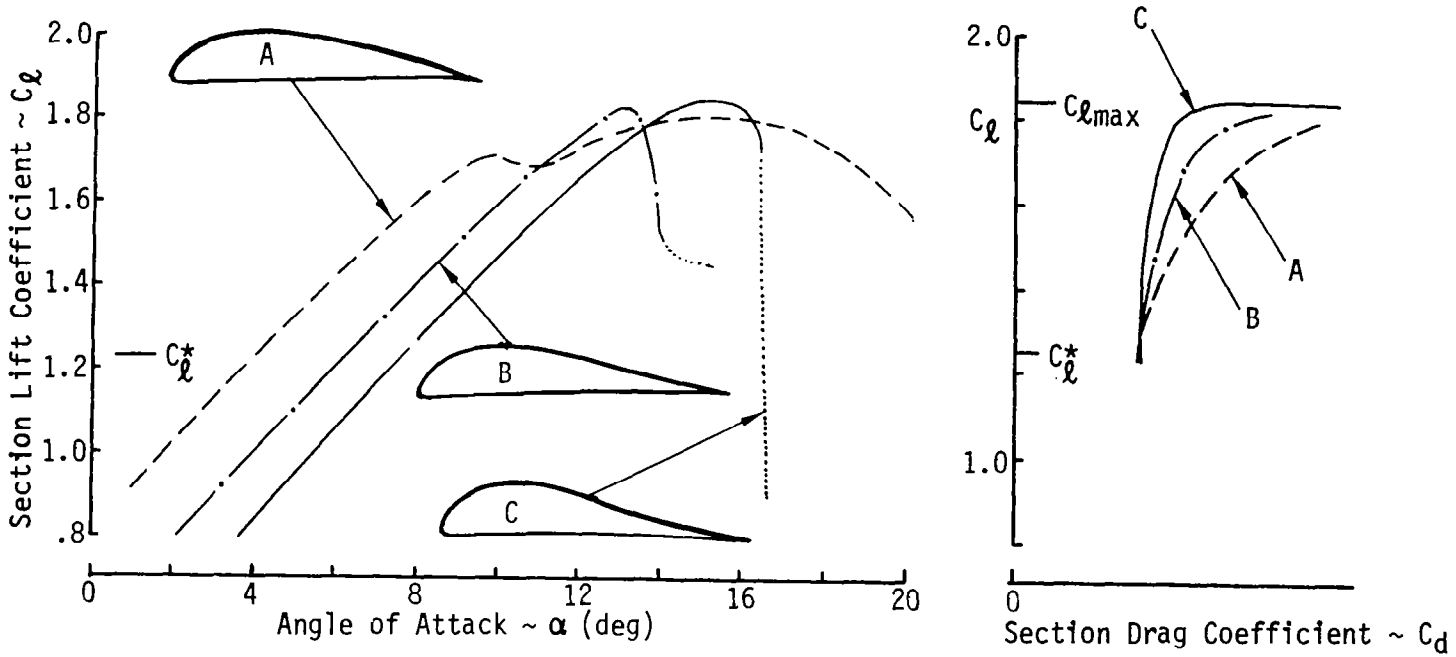

Design Conditions

$Rn^* = 5 \times 10^5$
$M^* = 0.01$
$t/c^* = 0.16$
$x_r/c = 0.35$
Nom. $C_\ell^* = 1.25$

Air foil	H_r var.	H_{TE_u}	C_ℓ^*	C_m^*	ε^*	$C_{\ell max}$	$C_{d_u}^*$	$C_{f_{r_u}}^*$
A	Exponent	2.20	1.21	-0.152	105	1.79	0.0112	0.0073
B	Linear	1.99	1.22	-0.061	104	1.82	0.0112	0.0056
C	Constant	1.92	1.24	-.004	103	1.83	0.0114	0.0041
	Recovery Region						Squire & Young	Recovery Region

FIGURE 12 AERODYNAMIC CHARACTERISTICS OF AIRFOILS SHOWN IN FIGURE 11

AN EXPLORATORY INVESTIGATION OF THE EFFECT OF A PLASTIC COATING ON THE PROFILE DRAG OF A PRACTICAL-METAL-CONSTRUCTION SAILPLANE AIRFOIL

Dan M. Somers
Langley Research Center

SUMMARY

An exploratory investigation was performed in the Langley low-turbulence pressure tunnel to determine the effect of a plastic coating on the profile drag of a practical-metal-construction sailplane airfoil. The model was tested with three surface configurations: (1) filled, painted, and sanded smooth; (2) rough bare metal; and (3) plastic-coated. The investigation was conducted at Reynolds numbers based on airfoil chord of 1.1×10^6, 2.2×10^6, and 3.3×10^6 at a constant Mach number of 0.10.

The results indicate that, at all three Reynolds numbers, the order of the drag values of the three surface configurations, starting with the highest drag, was: filled, painted, and sanded smooth; rough bare metal; and plastic-coated.

INTRODUCTION

Research on advanced technology airfoils has received considerable attention over the past several years at the Langley Research Center. As part of this overall research program, the present investigation was conducted to determine the effect of a plastic coating on the profile drag of a practical-metal-construction sailplane airfoil. Accordingly, a two-dimensional wind-tunnel model was constructed by an American sailplane manufacturer employing the same sheet-metal fabrication techniques used in constructing the corresponding production wing. Three surface configurations were investigated: (1) as received (filled and painted); (2) bare metal; and (3) plastic-coated. The plastic-coating procedure is described in detail in reference 1. The airfoil, which corresponds to the FX 67-K-170/17 airfoil designed by F. X. Wortmann, is representative of state-of-the-art laminar airfoils having variable geometry (in this case, a plain flap). The experimental section characteristics of the FX 67-K-170/17 airfoil are reported in reference 2.

The investigation was performed in the Langley low-turbulence pressure tunnel (ref. 3). The profile-drag coefficients of the three configurations were obtained at Reynolds numbers based on airfoil chord of 1.1×10^6, 2.2×10^6, and 3.3×10^6 at a constant Mach number of 0.10. The geometric angle of attack varied from -5° to 10°. The results have been compared with data from reference 2.

SYMBOLS

C_p	pressure coefficient
c	airfoil chord, cm (in.)
c_d	section profile-drag coefficient, $\int_{wake} c_d' \, d\left(\frac{h}{c}\right)$
c_d'	point drag coefficient (ref. 4)
c_l	section lift coefficient
c_m	section pitching-moment coefficient about quarter-chord point
d	surface-waviness-gage reading, cm (in.)
h	vertical distance in wake profile, cm (in.)
M	free-stream Mach number
R	Reynolds number based on free-stream conditions and airfoil chord
s	arc length from leading edge, cm (in.)
x	airfoil abscissa, cm (in.)
z	airfoil ordinate, cm (in.)
α	angle of attack, deg

MODEL, APPARATUS, AND PROCEDURE

Model

The constant-chord wind-tunnel model was constructed by an American sailplane manufacturer employing the same sheet-metal fabrication techniques used in constructing the corresponding tapered production wing. The structure consisted of a spar and four stringers to which a 0.81 mm (0.032 in.) skin was flush-riveted. In addition, four ribs were flush-riveted to the skin at 30.48-cm (12.00-in.) intervals spanwise. The model had a chord 66.47 cm (26.17 in.) and a span of 91.44 cm (36.00 in.). A plain lower-surface-hinged flap having a chord of 0.17c was fixed at 0° deflection (fig. 1). The flap gap was sealed with tape along the lower surface. No orifices were installed in the model.

Three surface configurations were investigated (fig. 2). Configuration 1 (as received) (fig. 2(a)) had a factory finish - a painted epoxy primer (filler) -

which had been sanded to insure an aerodynamically smooth surface. Configuration 2 (bare metal) was obtained by chemically removing the paint and primer. (See fig. 2(a).) The surface of configuration 2 (bare metal) was very rough because it had been mechanically roughened at the factory to provide a good bonding surface for the epoxy primer (fig. 3(a)). A plastic film was then bonded to the metal of configuration 2 (bare metal) to obtain configuration 3 (plastic-coated) (figs. 2(b) and 3(b)). It should be noted that the rough surface of configuration 2 (bare metal) can be seen through the plastic film and adhesive of configuration 3 (plastic-coated) (fig. 3(b)). The thickness of the plastic film was approximately 0.1 mm (0.005 in.) whereas the adhesive averaged about 0.25 mm (0.010 in.) in depth. The thickness of the plastic film and the adhesive together was nearly equal to that of the paint and filler as illustrated in figure 2(c). Configuration 1 (as received) and the FX 67-K-170/17 airfoil are compared in figure 2(d). The coordinates of the three configurations together with those of the FX 67-K-170/17 airfoil are listed in table I.

A relative waviness survey was made at the midspan of configuration 3 (plastic-coated). (See fig. 4.) A surface-waviness gage as described in reference 5 was used. The distance between the feet of the gage was approximately 6.4 cm (2.5 in.).

Wind Tunnel

The Langley low-turbulence pressure tunnel (ref. 3) is a closed-throat, single-return tunnel which can be operated at stagnation pressures from 10.13 to 1013 kPa (0.1 to 10 atm) with maximum tunnel-empty test-section Mach numbers of 0.46 and 0.23, respectively. The minimum unit Reynolds number is approximately 0.66×10^6 per meter (0.20×10^6 per foot) at a Mach number of about 0.10, whereas the maximum unit Reynolds number is approximately 49×10^6 per meter (15×10^6 per foot) at a Mach number of 0.23. The test section is 91.44 cm (3.000 ft) wide by 228.6 cm (7.500 ft) high.

Hydraulically actuated circular plates provide positioning and attachment for the two-dimensional model. The plates, 101.6 cm (40.00 in.) in diameter, are flush with the tunnel sidewalls and rotate with the model. The model ends were mounted to rectangular model-attachment plates as shown in figure 5.

Wake-Survey Rake

A fixed, wake-survey rake (fig. 6) was cantilevered from the tunnel sidewall at the model midspan and approximately 0.9 chords downstream from the trailing edge of the model. The wake rake employed 91 total-pressure tubes, 0.152 cm (0.060 in.) in diameter, and 5 static-pressure tubes, 0.318 cm (0.125 in.) in diameter. The total-pressure tubes were flattened to 0.102 cm (0.040 in.) for a length of 0.61 cm (0.24 in.) from the tips of the tubes. Each static-pressure tube had four flush orifices located 90° apart, 8 tube diameters from the tip of the tube in the measurement plane of the total-pressure tubes.

Instrumentation

Measurements of the wake-rake pressures were made by an automatic pressure-scanning system. Basic tunnel pressures as well as the wake-rake pressures were measured with variable-capacitance precision transducers. Geometric angle of attack was measured by a calibrated digital shaft encoder driven by a pinion gear and rack attached to the circular plates. Data were obtained by a high-speed data-acquisition system and were recorded on magnetic tape.

Tests and Methods

The airfoil was tested at Reynolds numbers based on the airfoil chord of 1.1×10^6, 2.2×10^6, and 3.3×10^6 at a Mach number of 0.10 over an angle-of-attack range from -5° to 10°. For several test runs, the upper surface of configuration 3 (plastic-coated) was coated with oil to determine the location as well as the nature of the boundary-layer transition from laminar to turbulent.

Section lift coefficients and pitching-moment coefficients about the quarter-chord were determined with the viscous-flow airfoil method of reference 6 because no orifices were installed in the model. Section profile-drag coefficients were computed from the wake-rake total and the wake-rake static pressures by the method of reference 4.

Standard low-speed wind-tunnel boundary corrections (ref. 7), approximately 2 percent of the measured coefficients, have been applied to the drag data.

DISCUSSION

Pressure Distributions

The theoretical chordwise pressure distributions at the approximate limits of the laminar low-drag range are shown in figure 7. At an angle of attack of 0° ($c_l = 0.5$) which corresponds to the lower limit of the laminar low-drag range, a favorable pressure gradient was predicted on the upper surface to about $x/c = 0.40$ whereas a zero pressure gradient was predicted on the forward portion of the lower surface. As angle of attack was increased, the calculated pressure gradient on the lower surface became more favorable whereas that on the upper surface became less favorable. At an angle of attack of 6° ($c_l = 1.2$), the upper limit of the low-drag range, a favorable pressure gradient was predicted to about $x/c = 0.60$ on the lower surface whereas a zero pressure gradient was predicted on the forward portion of the upper surface. Between the lower and upper limits of the laminar low-drag range, favorable pressure gradients were predicted on the forward portions of both surfaces.

Section Characteristics

The section characteristics of the three configurations are shown in figure 8 and tabulated in table II. The lift and drag coefficients of the FX 67-K-170/17 airfoil are shown for comparison, having been interpolated from the data of reference 2, which were obtained at Reynolds numbers of 1.0×10^6,

1.5×10^6, 2.0×10^6, and 2.5×10^6. As previously mentioned, both the lift and pitching-moment coefficients of the three configurations were generated by the theoretical method of reference 6, which appears to give excellent agreement with experiment where no trailing-edge separation is present (ref. 8). Accordingly, the c_l - versus - α and the c_l - versus $-c_m$ portions of figure 8 are entirely theoretical whereas the c_l - versus $-c_d$ portion consists of the theoretical lift coefficient plotted against the experimental drag coefficient. No quantitative measure of maximum lift coefficient is possible because of a lack of separation modelling in the theory of reference 6.

The mechanism of boundary-layer transition from laminar to turbulent on this airfoil at these Reynolds numbers is a laminar separation bubble as shown in figure 9 and illustrated in the sketch below.

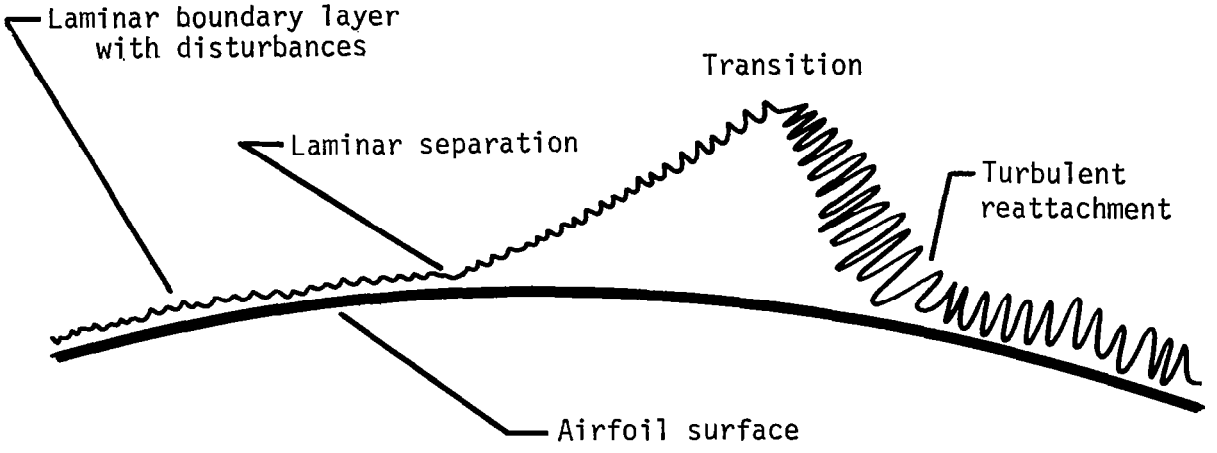

The bubble was caused by a slight adverse pressure gradient immediately downstream of the minimum pressure on the upper surface. (See fig. 7.) This slight adverse gradient was a design feature of the airfoil, as discussed in reference 9.

The section characteristics at a Reynolds number of 1.1×10^6 are shown in figure 8(a). The drag of configuration 1 (as received) was the highest, the drag of configuration 2 (bare metal) lower, and the drag of configuration 3 (plastic-coated) the lowest. The drag coefficients interpolated from the data of reference 2 for the FX 67-K-170/17 airfoil fell between those for configurations 1 (as received) and 2 (bare metal).

One possible explanation for the above order, based upon an understanding of laminar separation bubbles and the data presented in references 9-11, follows. The lower drag coefficients of configurations 2 (bare metal) and 3 (plastic-coated) have been attributed to reductions in the size of the laminar

separation bubble on the upper surface of the airfoil. These reductions were probably caused by two different mechanisms. For configuration 2 (bare metal), introduction of additional disturbances into the laminar boundary layer by the roughness of the surface (fig. 3(a)) apparently did not cause premature transition because they were too small. Once the laminar boundary layer had separated, however, the disturbances would grow rapidly, resulting in transition and, finally, turbulent reattachment. These additional disturbances, therefore, probably reduced the distance between laminar separation and transition (i.e., a shorter bubble). For configuration 3 (plastic-coated), introduction of disturbances into the laminar boundary layer by the waviness of the surface apparently affected the length of the laminar separation bubble as did the disturbances caused by the roughness of configuration 2 (bare metal) with an even shorter bubble for configuration 3 (plastic-coated). The waviness of the configuration 3 (plastic-coated) surface (fig. 4) was probably caused by hand application of the plastic film on very thin sheet metal.

The section characteristics at Reynolds numbers of 2.2×10^6 and 3.3×10^6 are shown in figures 8(b) and 8(c), respectively. The drag of configuration 1 (as received) was again the highest, the drag of configuration 2 (bare metal) was lower, and the drag of configuration 3 (plastic-coated) was again the lowest. The drag coefficients interpolated from the data of reference 2 for the FX 67-K-170/17 airfoil were higher than those for configuration 1 (as received) at a Reynolds number of 2.2×10^6. The explanation for these results is probably the same as that for a Reynolds number of 1.1×10^6.

Results similar to those described above have been reported by other investigators. A substantial drag reduction was obtained by using a trip wire to eliminate the laminar separation bubble on the upper surface of an airfoil (ref. 9). Reductions in the sizes of the laminar separation bubbles on two different airfoils through the introduction of disturbances by roughness and trip wires were reported in references 10 and 11, respectively.

SUMMARY OF RESULTS

An exploratory investigation was performed in the Langley low-turbulence pressure tunnel to determine the effect of a plastic coating on the profile drag of a practical-metal-construction sailplane airfoil. The model was tested with three surface configurations: (1) filled, painted, and sanded smooth; (2) rough bare metal; and (3) plastic-coated. The resulting data have been compared with data for the design airfoil (Wortmann FX 67-K-170/17) from another low-turbulence wind tunnel. The investigation was conducted at Reynolds numbers based on airfoil chord of 1.1×10^6, 2.2×10^6 and 3.3×10^6 at a constant Mach number of 0.10.

At all three Reynolds numbers, the drag of the filled, painted, and sanded smooth configuration was the highest, followed by the drag of the rough bare metal configuration, and finally the drag of the plastic-coated configuration.

REFERENCES

1. Beasley, William D. and McGhee, Robert J.: An Exploratory Investigation of the Effects of a Thin Plastic Film Cover on the Profile Drag of an Aircraft Wing Panel. NASA TM 74073, 1977.

2. Althaus, D.: MeBergebnisse aus dem Laminarwindkanal des Instituts für Aerodynamik und Gasdynamik der Universität Stuttgart. Stuttgarter Profilkatalog I, Institut für Aerodynamik und Gasdynamik der Universität Stuttgart, 1972.

3. Von Doenhoff, Albert E. and Abbott, Frank T., Jr.: The Langley Two-Dimensional Low-Turbulence Pressure Tunnel. NACA TN 1283, 1947.

4. Pankhurst, R. C. and Holder, D. W.: Wind-Tunnel Technique. Sir Isaac Pitman & Sons, Ltd. (London), 1952.

5. Braslow, Albert L.; Burrows, Dale L.; Tetervin, Neal; and Visconti, Fioravante: Experimental and Theoretical Studies of Area Suction for the Control of the Laminar Boundary Layer on an NACA 64A010 Airfoil. NACA Rep. 1025, 1951.

6. Smetana, Frederick O.; Summey, Delbert C.; Smith, Neill S.; and Carden, Ronald K.: Light Aircraft Lift, Drag, and Moment Prediction - A Review and Analysis. NASA CR-2523, 1975.

7. Allen, H. Julian; and Vincenti, Walter G.: Wall Interference in a Two-Dimensional-Flow Wind Tunnel, With Consideration of the Effect of Compressibility. NACA Rep. 782, 1944. (Supersedes NACA WR A-63.)

8. Somers, Dan M.: Experimental and Theoretical Low-Speed Aerodynamic Characteristics of a Wortmann Airfoil as Manufactured on a Fiberglass Sailplane. NASA TN D-8324, 1977.

9. Wortmann, F. X.: Experimental Investigations on New Laminar Profiles for Gliders and Helicopters. TIL/T.4906, British Minist. Aviat., March 1960.

10. Hurley, D. G.: The Downstream Effect of a Local Thickening of the Laminar Boundary Layer. Aeronautical Research Laboratories (Australia) Aerodynamics Note 146, July 1955.

11. Harris, K. D.: The Effect of Transition Wires on the Pressure Distributions over a N.A.C.A. 63A215 Aerofoil Section. The College of Aeronautics (Cranfield), Technical Note 41, 1956.

TABLE I.- AIRFOIL COORDINATES

(a) Configuration 1 (as received)

[c = 66.4827 cm (26.1743 in.)]

Upper surface		Lower surface	
x/c	z/c	x/c	z/c
0.000000	0.000000	0.000000	0.000000
.000004	-.000042	-.000008	-.000038
.000497	.004443	.000500	-.002048
.000993	.005651	.001001	-.003026
.001490	.006827	.001490	-.003805
.001987	.007721	.002017	-.004489
.002980	.009452	.002988	-.005391
.003973	.011133	.003992	-.006185
.004982	.012722	.004986	-.006839
.006980	.015611	.006980	-.007943
.009968	.019389	.009968	-.009360
.014957	.024635	.014950	-.011274
.019939	.029055	.019932	-.013127
.029907	.036658	.029907	-.015611
.039879	.043390	.039879	-.017712
.049843	.049549	.049850	-.019515
.059814	.055214	.059814	-.021063
.069782	.060498	.069786	-.022427
.079754	.065381	.079754	-.023680
.089725	.070080	.089725	-.024677
.099693	.074363	.099689	-.025735
.119633	.082123	.119636	-.027550
.149540	.092274	.149540	-.029773
.199386	.106295	.199386	-.032016
.249225	.116867	.249237	-.033212
.299087	.124687	.299080	-.034221
.348922	.130342	.348922	-.035031
.398773	.133142	.398769	-.035500
.448627	.132928	.448623	-.034924
.498466	.129925	.498470	-.033602
.548301	.124095	.548313	-.031749
.598163	.114696	.598159	-.028734
.648017	.101921	.648006	-.024612
.697845	.086738	.697852	-.020153
.747699	.070241	.747703	-.015389
.797538	.053824	.797546	-.010468
.847392	.037896	.847392	-.006823
.897247	.026320	.897231	-.001941
.947089	.012975	.947085	.001242
.967025	.008638	.967029	.000455
.976997	.006629	.976993	-.000317
.986964	.004569	.986964	-.001035
1.000000	.001486	.999828	-.001284

TABLE I.- AIRFOIL COORDINATES - Continued

(b) Configuration 2 (bare metal)

[c = 66.4670 cm (26.1681 in.)]

Upper surface		Lower surface	
x/c	z/c	x/c	z/c
0.000000	0.000000	0.000000	0.000000
.000050	..000000	.000046	.000000
.000520	.003604	.000501	-.002109
.000994	.004632	.001376	-.004330
.001490	.005568	.001494	-.004548
.001987	.006370	.001987	-.005381
.002992	.008117	.002992	-.006496
.003986	.009749	.003990	-.007184
.004987	.011342	.004979	-.007819
.006955	.014227	.006993	-.008931
.009966	.018075	.009966	-.010433
.014957	.023238	.014949	-.012508
.019944	.027568	.019936	-.014132
.029914	.035069	.029918	-.016730
.039884	.041807	.039892	-.018832
.049855	.047856	.049858	-.020552
.059832	.053542	.059836	-.022061
.069799	.058827	.069810	-.023364
.079777	.063746	.079784	-.024564
.089747	.068255	.089747	-.025627
.099721	.072543	.099724	-.026723
.119661	.080262	.119665	-.028489
.149579	.090385	.149583	-.030694
.199434	.104536	.170547	-.042151
.249292	.115190	.249288	-.033166
.299162	.123020	.299154	-.034683
.349005	.128653	.348997	-.035532
.398871	.131511	.398886	-.036090
.448726	.131064	.448745	-.035731
.498592	.128087	.498603	-.034404
.548443	.122191	.548443	-.032326
.598297	.112702	.598312	-.029295
.648171	.099874	.648167	-.024966
.698014	.084599	.698010	-.020380
.747876	.067773	.747865	-.015947
.797735	.051677	.797735	-.011487
.847589	.036457	.847593	-.007341
.897455	.024645	.897436	-.003424
.947314	.012198	.947314	-.000910
.967254	.007417	.967262	-.000657
.977243	.005583	.977232	-.000703
.987290	.002939	.987271	-.000734
.999889	.000046	1.000000	-.000378

TABLE I.- AIRFOIL COORDINATES - Continued

(c) Configuration 3 (plastic-coated)

[c = 66.4860 cm (26.1756 in.)]

Upper surface		Lower surface	
x/c	z/c	x/c	z/c
0.000000	0.000000	0.000000	0.000000
-.000023	.000061	.000997	-.002124
.000508	.005108	.001494	-.003266
.001016	.006449	.002006	-.003973
.001494	.007664	.002995	-.005058
.001998	.008607	.003985	-.005891
.002991	.010017	.004989	-.006582
.003988	.011522	.006984	-.007683
.004978	.012978	.009963	-.009077
.006972	.015935	.014964	-.011136
.009960	.019904	.019935	-.012817
.014960	.025111	.029898	-.015369
.019938	.029356	.039873	-.017470
.029898	.036943	.049844	-.019213
.039858	.043674	.059815	-.020710
.049844	.049772	.069786	-.022085
.059811	.055414	.079746	-.023235
.069783	.060671	.089713	-.024339
.079746	.065634	.099696	-.025417
.089725	.070222	.119634	-.026991
.099688	.074432	.149544	-.029302
.119634	.082168	.199369	-.031399
.149540	.092517	.249228	-.032599
.199377	.106561	.299069	-.033432
.249221	.117101	.348917	-.034211
.299069	.125105	.398742	-.034830
.348905	.130603	.448593	-.034547
.398749	.133323	.498441	-.033069
.448593	.132983	.548282	-.031124
.498445	.130102	.598122	-.028175
.548285	.124181	.647985	-.024259
.598130	.114786	.697806	-.019388
.647981	.102202	.747666	-.014789
.697818	.087146	.797510	-.010208
.747654	.070237	.847350	-.006284
.797518	.053909	.897179	-.002124
.847346	.038440	.947042	.000004
.897194	.027927	.967015	.000531
.947046	.014960	.976944	.000604
.966985	.010823	.986923	.000714
.976956	.008496	1.000000	.001108
.988837	.005998		
.999924	.003687		

TABLE I.- AIRFOIL COORDINATES - Concluded

(d) FX 67-K-170/17 airfoil

Upper surface		Lower surface	
x/c	z/c	x/c	z/c
0.00000	0.00000	0.00000	0.00000
.00107	.00653	.00107	-.00217
.00428	.01292	.00428	-.00514
.00961	.02012	.00961	-.00815
.01704	.02765	.01704	-.01057
.02653	.03487	.02653	-.01321
.03806	.04309	.03806	-.01580
.05156	.05158	.05156	-.01827
.06699	.06011	.06699	-.02062
.08427	.06856	.08427	-.02282
.10332	.07685	.10332	-.02490
.12408	.08490	.12408	-.02682
.14645	.09263	.14645	-.02856
.17033	.09994	.17033	-.03011
.19562	.10677	.19562	-.03146
.22221	.11305	.22221	-.03261
.25000	.11870	.25000	-.03354
.27866	.12365	.27866	-.03425
.30866	.12783	.30866	-.03474
.33928	.13119	.33928	-.03499
.37059	.13370	.37059	-.03501
.40245	.13526	.40245	-.03480
.43474	.13571	.43474	-.03435
.46730	.13490	.46730	-.03365
.50000	.13274	.50000	-.03272
.53270	.12919	.53270	-.03155
.56526	.12429	.56526	-.03012
.59755	.11808	.59755	-.02844
.62941	.11063	.62941	-.02654
.66072	.10208	.66072	-.02437
.69134	.09263	.69134	-.02187
.72114	.08259	.72114	-.01896
.75000	.07233	.75000	-.01572
.77779	.06229	.77779	-.01236
.80438	.05287	.80438	-.00913
.82967	.04437	.82967	-.00625
.85355	.03689	.85355	-.00386
.87592	.03040	.87592	-.00197
.91573	.01991	.91573	-.00037
.94844	.01201	.94844	-.00124
.97347	.00631	.97347	-.00105
.99039	.00243	.99039	-.00044
.99893	.00027	.99893	-.00005
1.00000	0.00000	1.00000	0.00000

TABLE II.- SECTION CHARACTERISTICS

(a) $R \approx 1.1 \times 10^6$, $M = 0.10$

c_l	α, deg	c_d	c_m
Configuration 1 (as received)			
-.020	-5.05	.0130	-.0978
.080	-4.13	.0117	-.0986
.199	-3.07	.0109	-.1043
.294	-2.09	.0101	-.1055
.412	-1.05	.0082	-.1087
.530	-.00	.0086	-.1120
.650	1.07	.0086	-.1152
.755	2.02	.0084	-.1178
.867	3.07	.0084	-.1203
.974	4.12	.0080	-.1224
1.072	5.12	.0082	-.1231
1.190	6.18	.0079	-.1270
1.297	7.13	.0075	-.1310
1.410	8.22	.0078	-.1345
1.512	9.27	.0079	-.1366
1.602	10.24	.0090	-.1390
Configuration 2 (bare metal)			
-.060	-5.12	.0126	-.0906
.035	-4.21	.0117	-.0925
.162	-3.04	.0110	-.0950
.260	-2.11	.0101	-.0965
.363	-1.03	.0073	-.0980
.477	.01	.0069	-.1003
.585	.99	.0072	-.1023
.694	1.99	.0074	-.1045
.803	3.03	.0072	-.1067
.915	4.07	.0076	-.1091
1.026	5.13	.0078	-.1122
1.139	6.14	.0082	-.1157
1.255	7.21	.0077	-.1195
1.357	8.19	.0071	-.1224
1.441	9.19	.0076	-.1232
1.543	10.27		-.1247
Configuration 3 (plastic-coated)			
-.090	-5.10	.0123	-.0848
.022	-4.08	.0110	-.0870
.130	-3.10	.0100	-.0894
.230	-2.05	.0090	-.0913
.345	-1.04	.0072	-.0940
.465	.02	.0066	-.0967
.575	1.03	.0068	-.0992
.685	2.04	.0070	-.1015
.795	3.06	.0068	-.1035
.898	4.05	.0068	-.1052
1.010	5.10	.0071	-.1082
1.120	6.11	.0072	-.1118
1.233	7.12	.0069	-.1153
1.340	8.16	.0069	-.1172
1.425	9.16	.0074	-.1187
1.522	10.17	.0115	-.1210

TABLE II.- Continued

(b) $R \approx 2.2 \times 10^6$, $M = 0.10$

c_l	α, deg	c_d	c_m
Configuration 1 (as received)			
-.020	-5.05	.0096	-.0979
.090	-4.05	.0095	-.1006
.204	-3.02	.0090	-.1037
.307	-2.06	.0083	-.1062
.420	-1.04	.0059	-.1093
.538	.01	.0057	-.1127
.655	1.03	.0057	-.1159
.770	2.06	.0056	-.1193
.885	3.09	.0060	-.1223
.995	4.09	.0062	-.1250
1.105	5.13	.0064	-.1275
1.220	6.19	.0064	-.1292
1.305	7.14	.0065	-.1303
1.400	8.20	.0067	-.1345
1.505	9.32	.0093	-.1365
1.600	10.29	.0224	-.1392
Configuration 2 (bare metal)			
-.067	-5.14	.0103	-.0905
.037	-4.20	.0096	-.0927
.170	-3.00	.0094	-.0955
.281	-1.96	.0085	-.0977
.378	-1.01	.0063	-.0996
.487	-.02	.0056	-.1020
.613	1.04	.0056	-.1054
.727	2.08	.0054	-.1078
.839	3.05	.0056	-.1096
.936	4.07	.0060	-.1113
1.039	5.10	.0063	-.1132
1.154	6.15	.0066	-.1164
1.260	7.17	.0062	-.1190
1.352	8.26	.0084	-.1220
1.442	9.30		-.1232
1.527	10.18		-.1250
Configuration 3 (plastic-coated)			
-.089	-5.08	.0098	-.0848
.025	-4.06	.0092	-.0874
.140	-3.03	.0088	-.0899
.246	-2.03	.0082	-.0922
.360	-1.00	.0061	-.0950
.473	.01	.0053	-.0977
.590	1.05	.0053	-.1008
.708	2.08	.0053	-.1038
.817	3.06	.0055	-.1065
.930	4.10	.0057	-.1087
1.035	5.15	.0057	-.1100
1.143	6.18	.0058	-.1120
1.247	7.15	.0058	-.1152
1.333	8.17	.0061	-.1175
1.417	9.16	.0107	-.1193
1.518	10.18		-.1215

TABLE II.- Concluded

(c) $R \approx 3.3 \times 10^6$, $M = 0.10$

c_l	α, deg	c_d	c_m
Configuration 1 (as received)			
-.027	-5.09	.0084	-.0977
.090	-4.03	.0081	-.1007
.542	-.02	.0050	-.1130
.657	1.00	.0050	-.1164
.775	2.02	.0050	-.1197
.893	3.08	.0053	-.1230
1.005	4.08	.0055	-.1260
1.111	5.09	.0060	-.1288
1.207	6.11	.0063	-.1307
1.293	7.13	.0060	-.1295
1.389	8.14	.0076	-.1330
1.487	9.15	.0093	-.1365
1.595	10.25		-.1395
Configuration 2 (bare metal)			
-.067	-5.14	.0093	-.0906
.053	-4.06	.0085	-.0932
.158	-3.12	.0084	-.0955
.275	-2.09	.0078	-.0980
.394	-.99	.0066	-.1008
.498	.01	.0050	-.1030
.610	1.00	.0049	-.1058
.737	2.07	.0047	-.1094
.849	3.09	.0049	-.1116
.950	4.09	.0052	-.1127
1.060	5.17	.0057	-.1150
1.160	6.12	.0058	-.1170
1.255	7.19	.0056	-.1185
1.340	8.18	.0099	-.1210
1.437	9.23		-.1237
1.533	10.23		-.1255
Configuration 3 (plastic-coated)			
-.099	-5.14	.0089	-.0847
.025	-4.06	.0081	-.0875
.138	-3.05	.0079	-.0910
.248	-2.05	.0075	-.0926
.367	-1.00	.0061	-.0955
.477	.02	.0046	-.0983
.596	1.04	.0048	-.1015
.710	2.03	.0047	-.1045
.827	3.06	.0047	-.1074
.942	4.10	.0050	-.1102
1.052	5.10	.0053	-.1130
1.150	6.14	.0058	-.1130
1.245	7.16	.0057	-.1149
1.328	8.18	.0073	-.1170
1.420	9.19	.0308	-.1195
1.523	10.19	.0799	-.1219

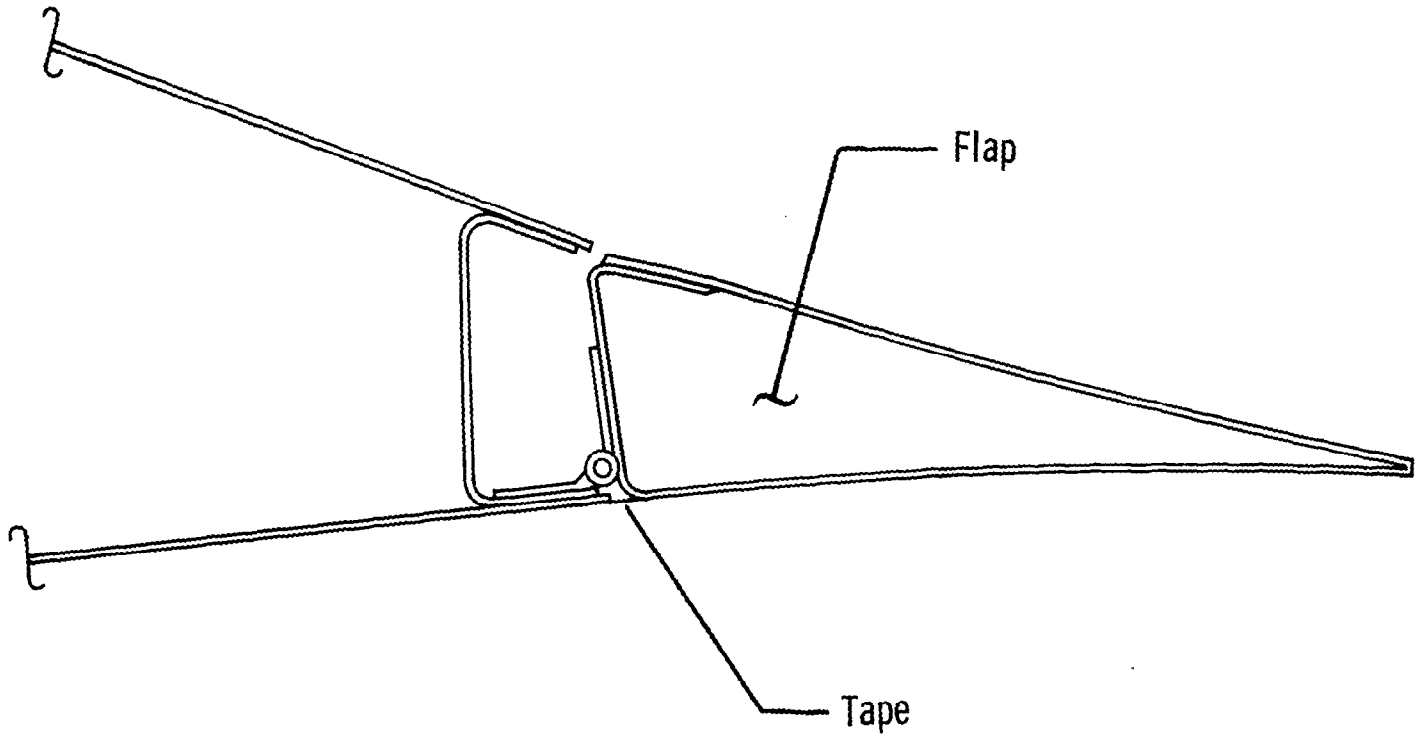

Figure 1.- Flap geometry.

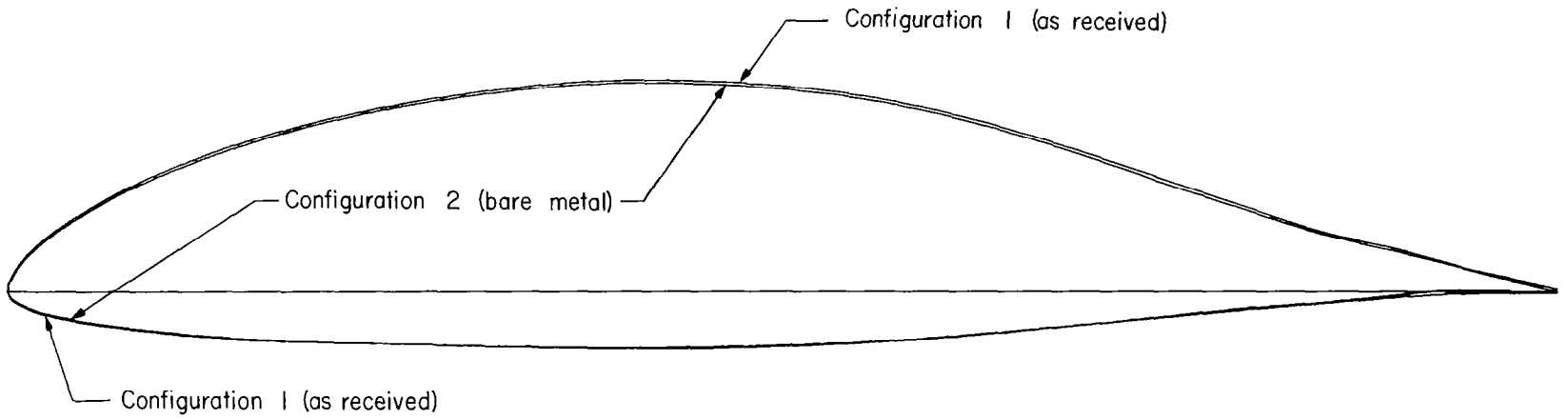

(a) Configurations 1 (as received) and 2 (bare metal).

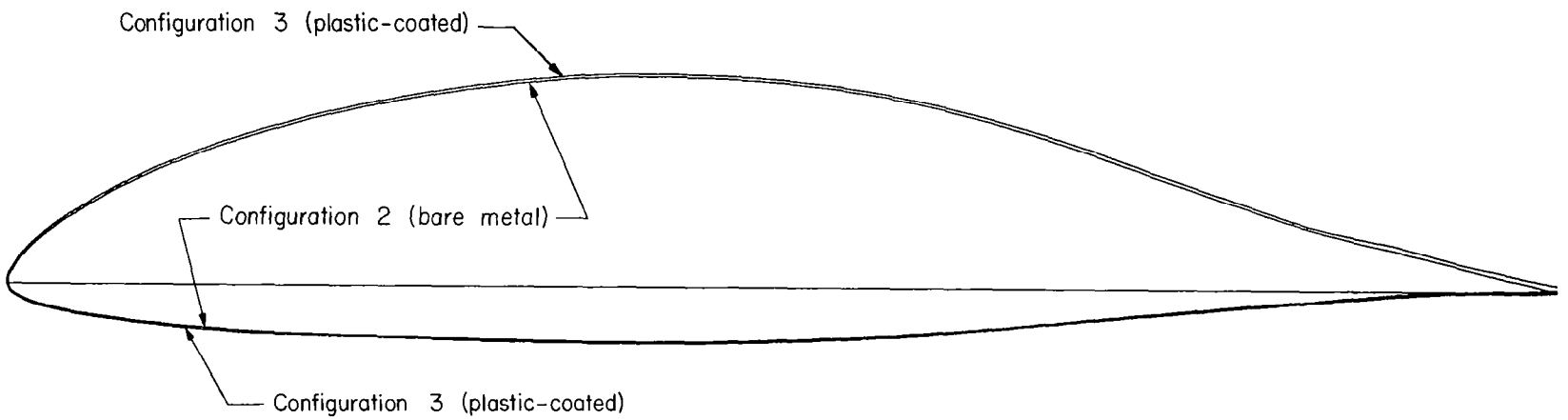

(b) Configurations 2 (bare metal) and 3 (plastic-coated).

Figure 2.- Comparisons of configurations 1 (as received), 2 (bare metal), 3 (plastic-coated), and FX 67-K-170/17 ordinates.

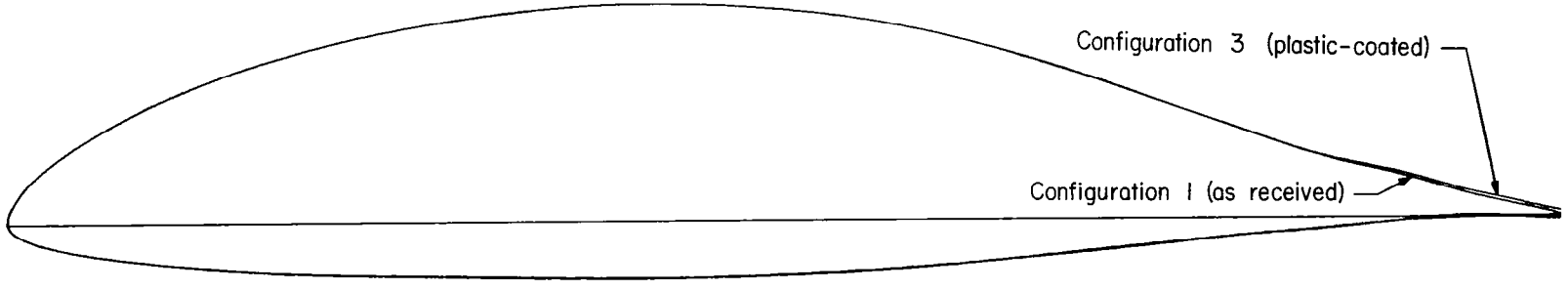

(c) Configurations 1 (as received) and 3 (plastic-coated).

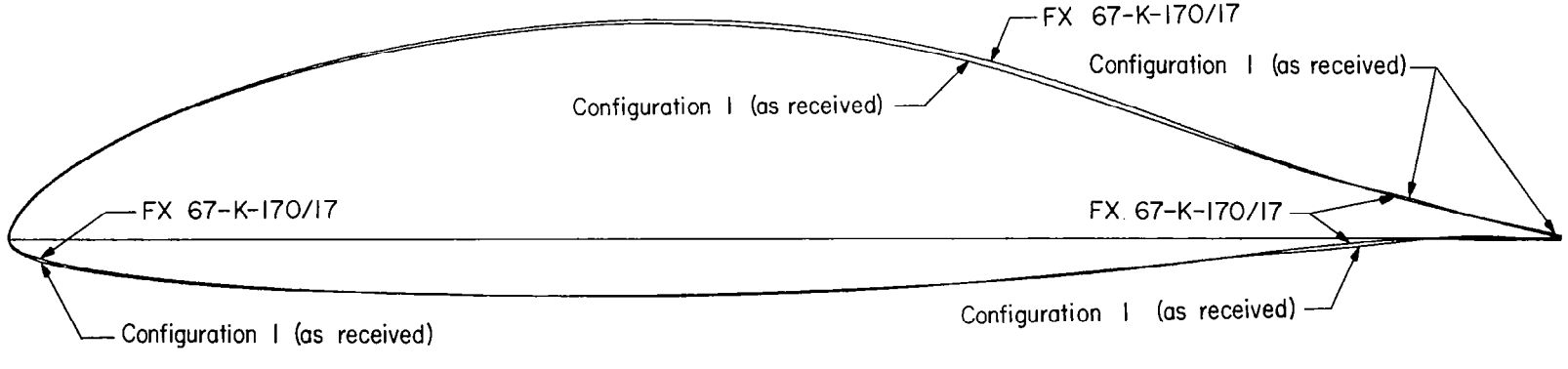

(d) Configuration 1 (as received) and FX 67-K-170/17.

Figure 2.- Concluded.

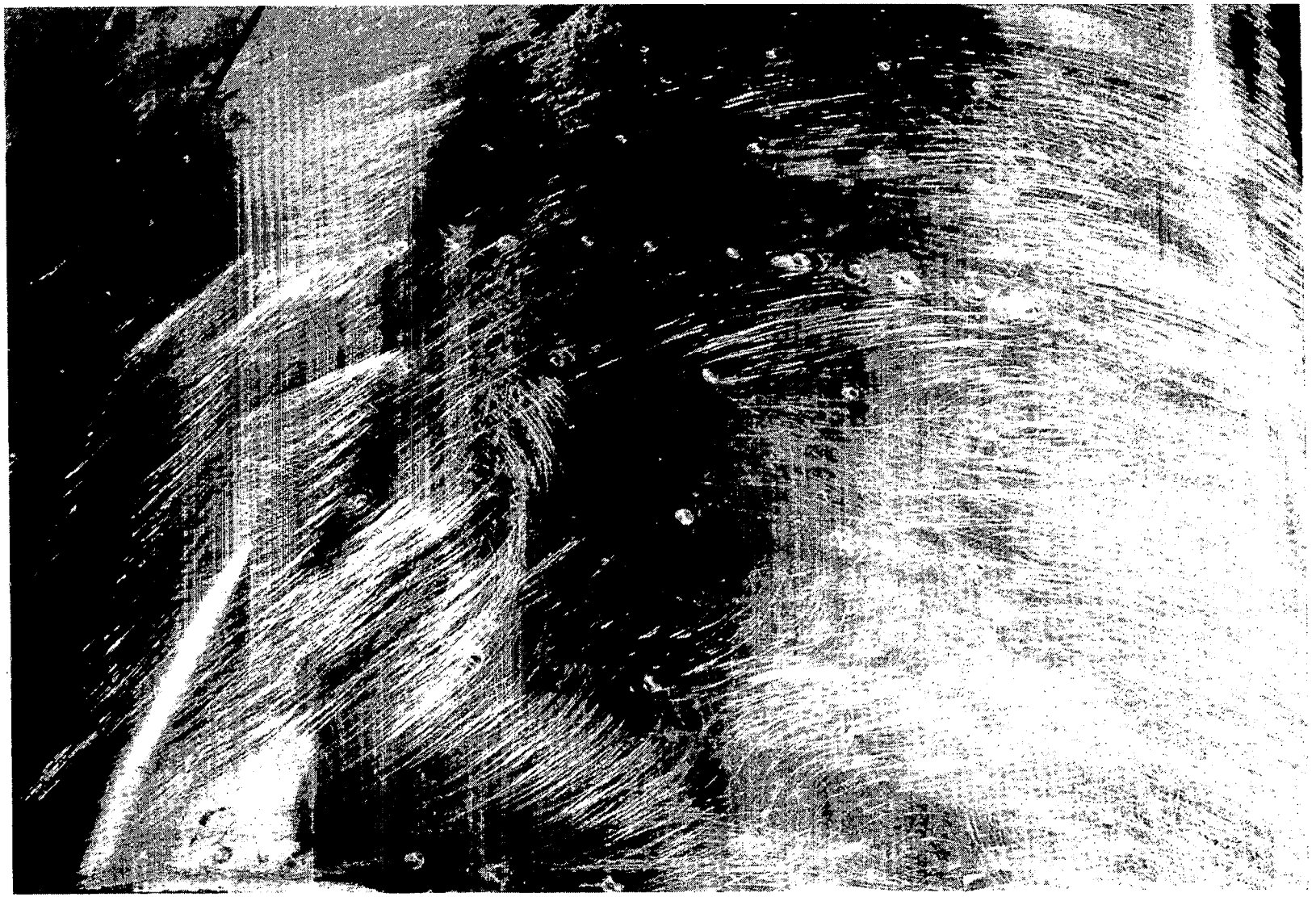

(a) Configuration 2 (bare metal).

Figure 3.- Surfaces of configurations 2 (bare metal) and 3 (plastic-coated).

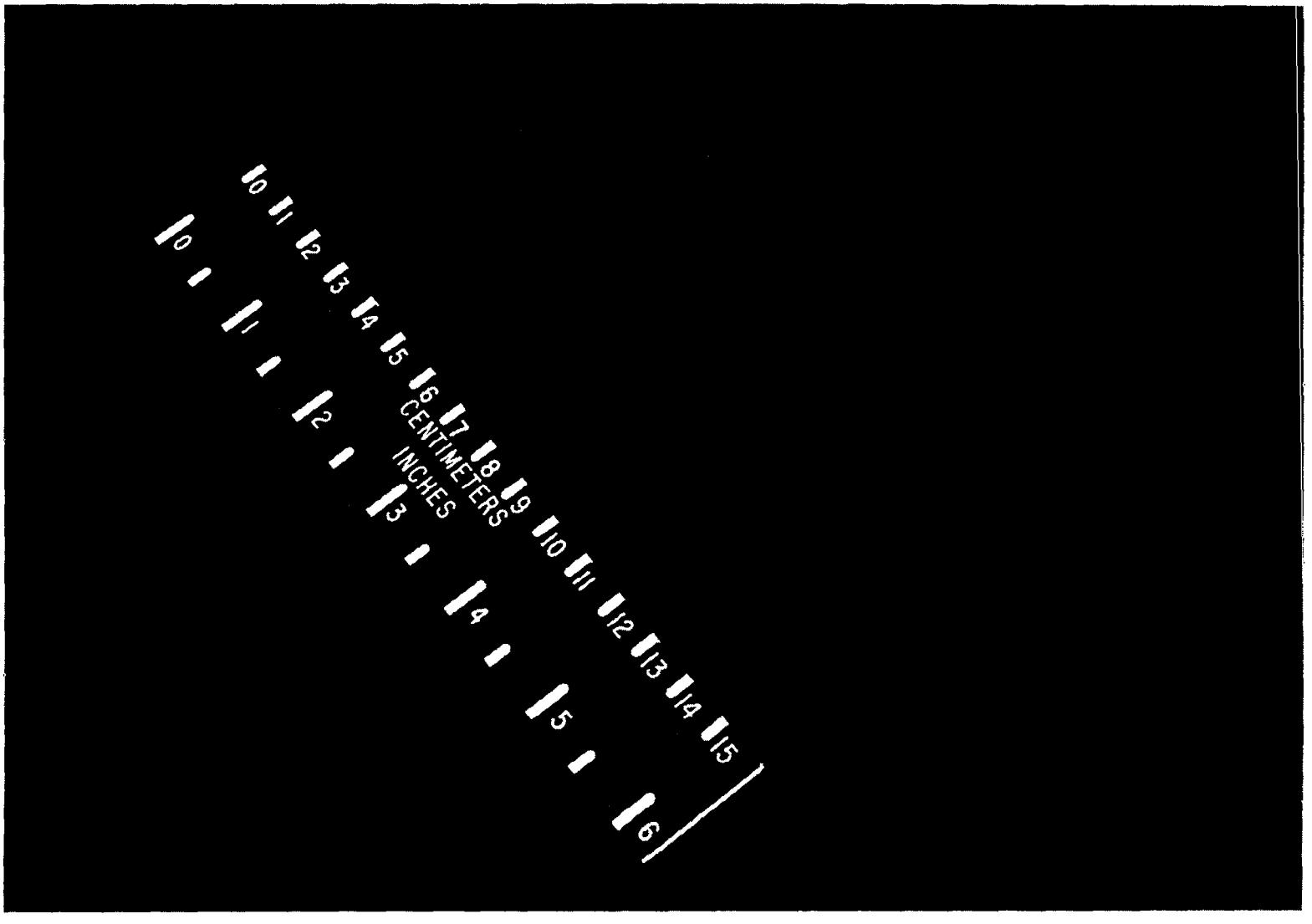

(b) Configuration 3 (plastic-coated).

Figure 3.- Concluded.

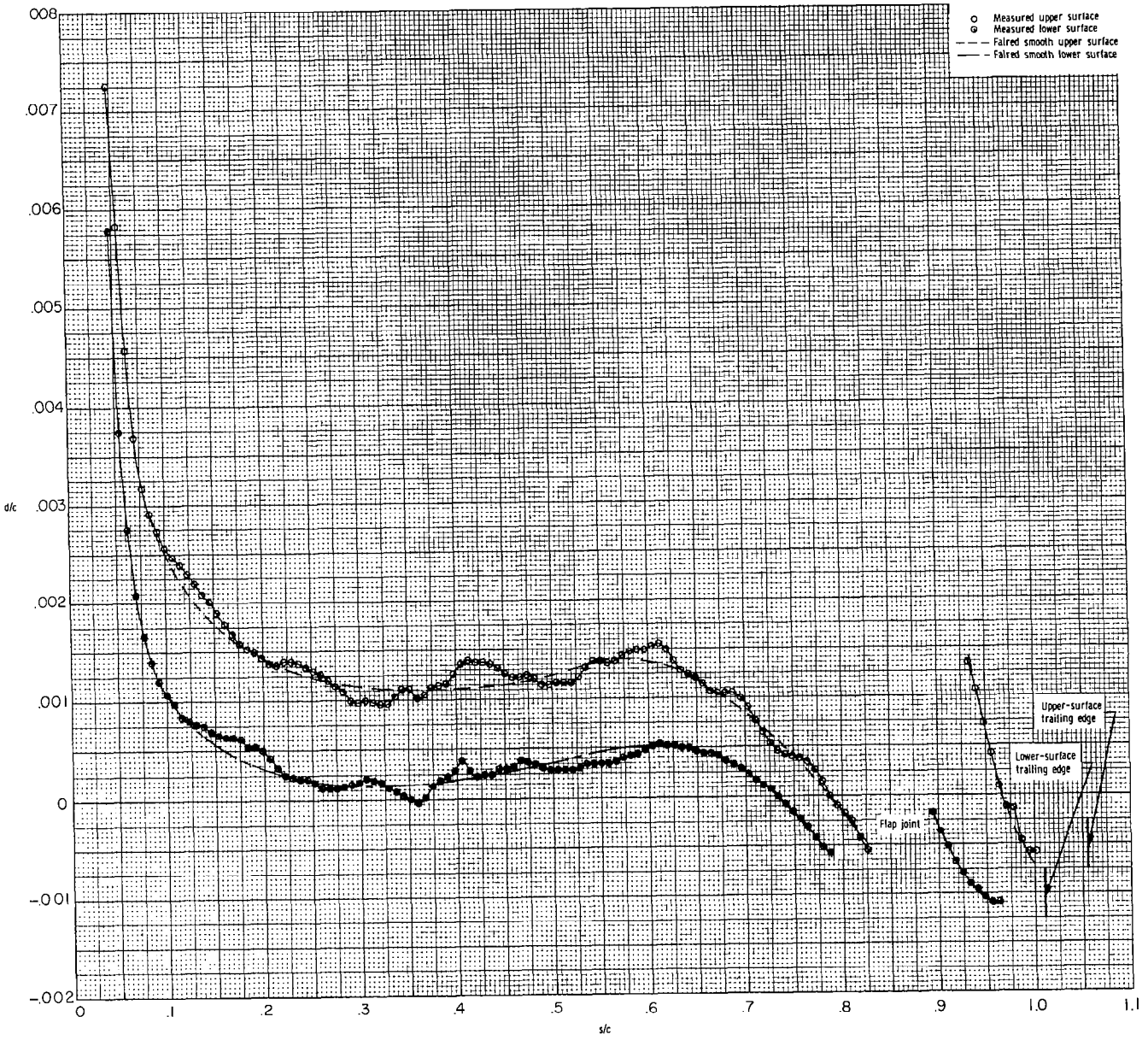

Figure 4.- Surface waviness of configuration 3 (plastic-coated).

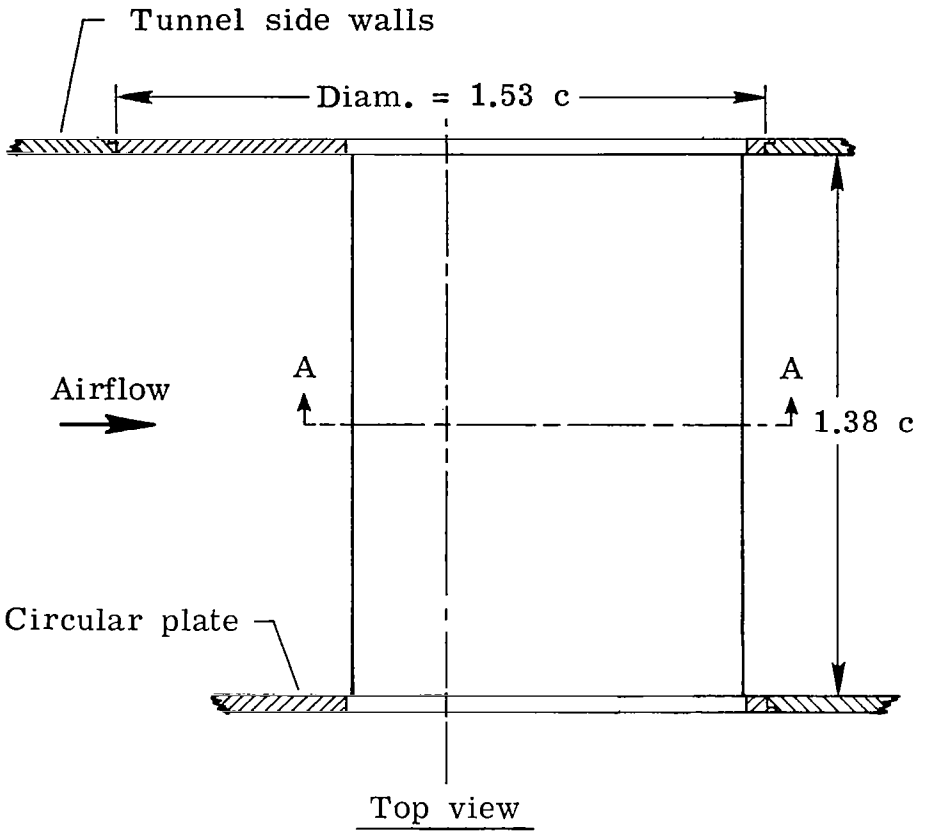

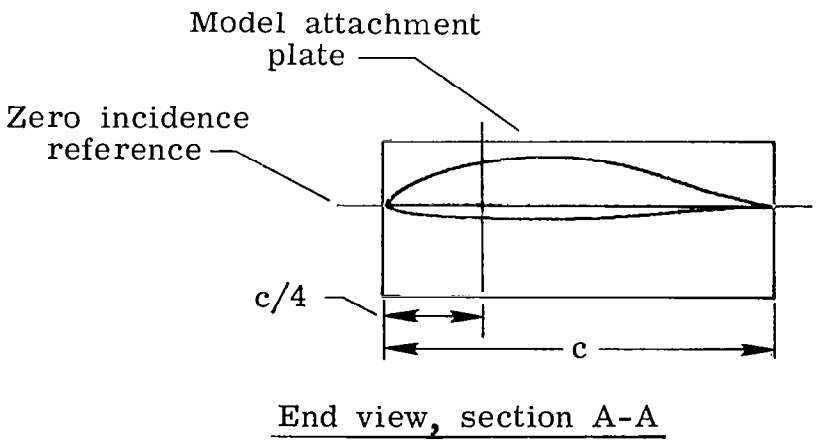

Figure 5.- Airfoil model mounted in wind tunnel. All dimensions are in terms of model chord, c = 66.47 cm (26.17 in.).

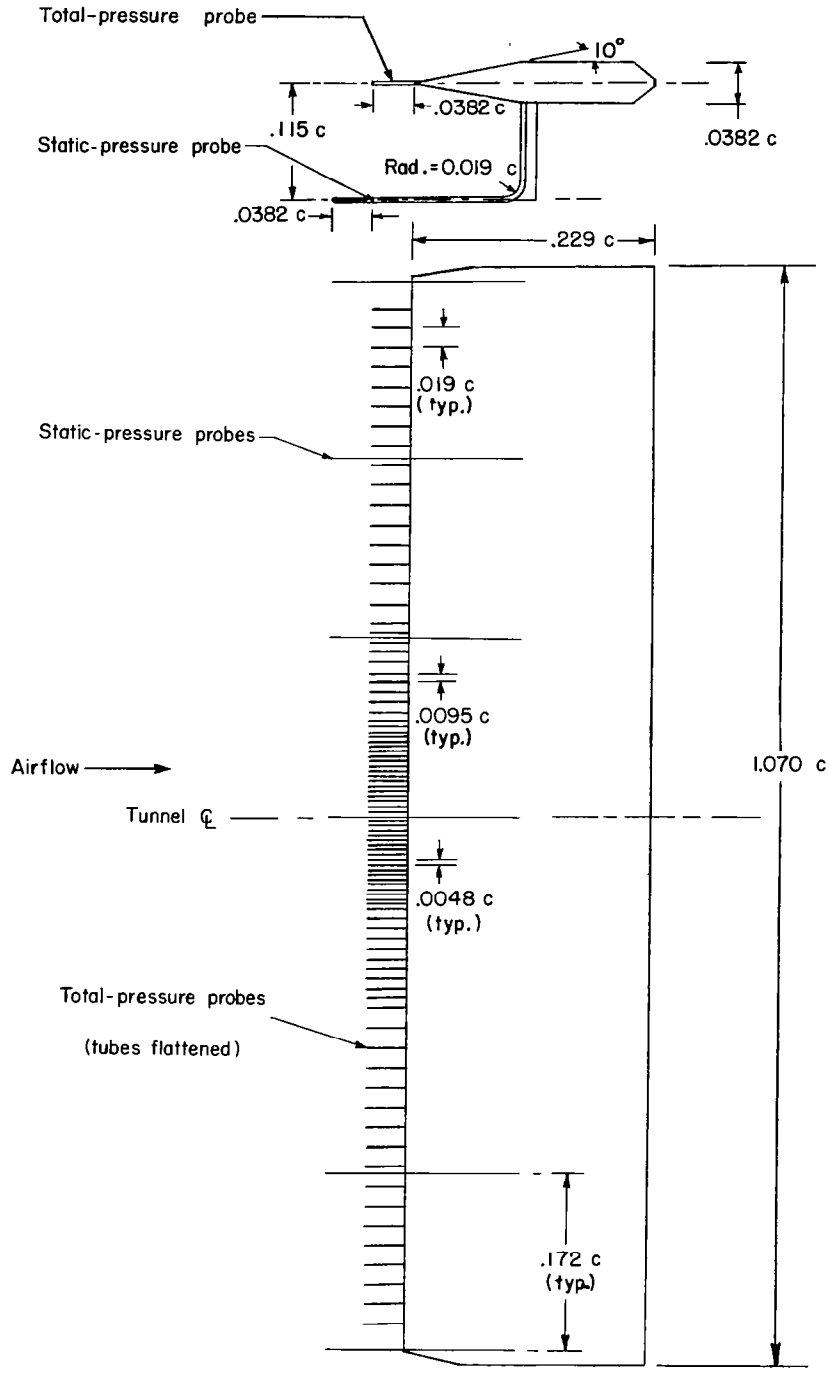

(a) Drawing of wake-survey rake. All dimensions are in terms of model chord, c = 66.47 cm (26.17 in.).

Figure 6.- Wake-survey rake.

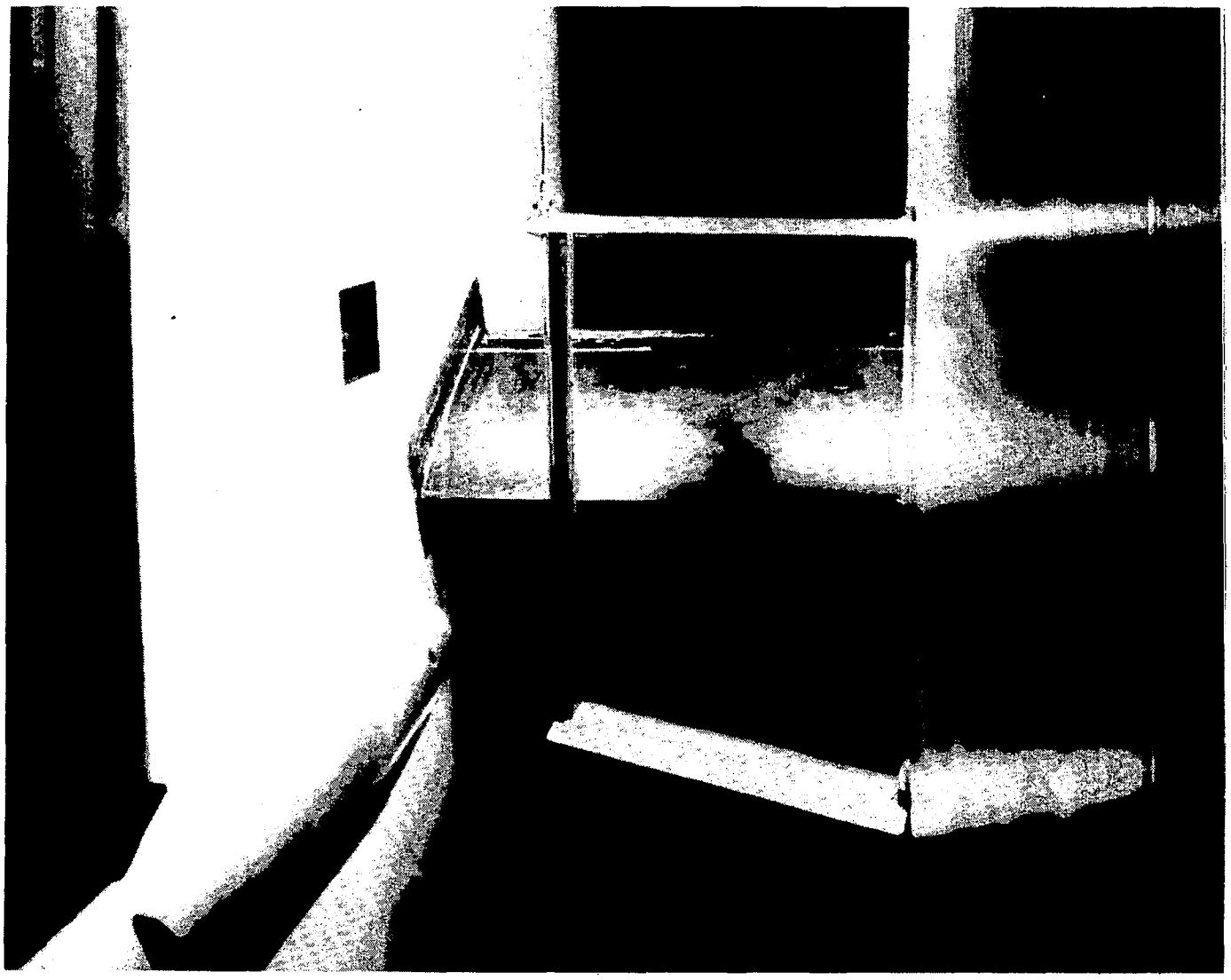

(b) Photograph of wake-survey rake in the Langley low-turbulence pressure tunnel.

Figure 6.- Concluded.

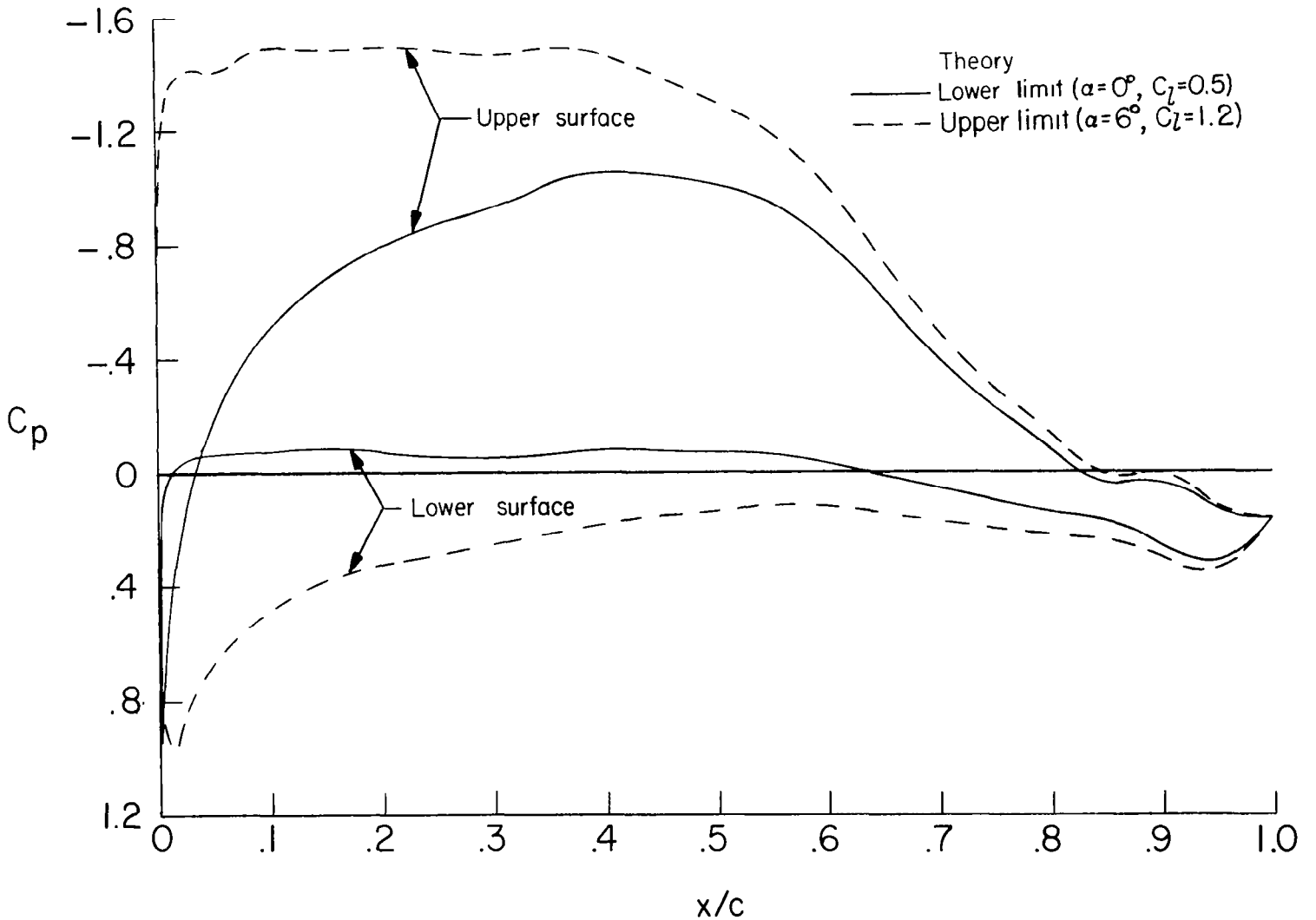

Figure 7.- Theoretical chordwise pressure distributions for configuration 1 (as received) at lower and upper limits of laminar low-drag range for $R = 2.2 \times 10^6$ and $M = 0.10$.

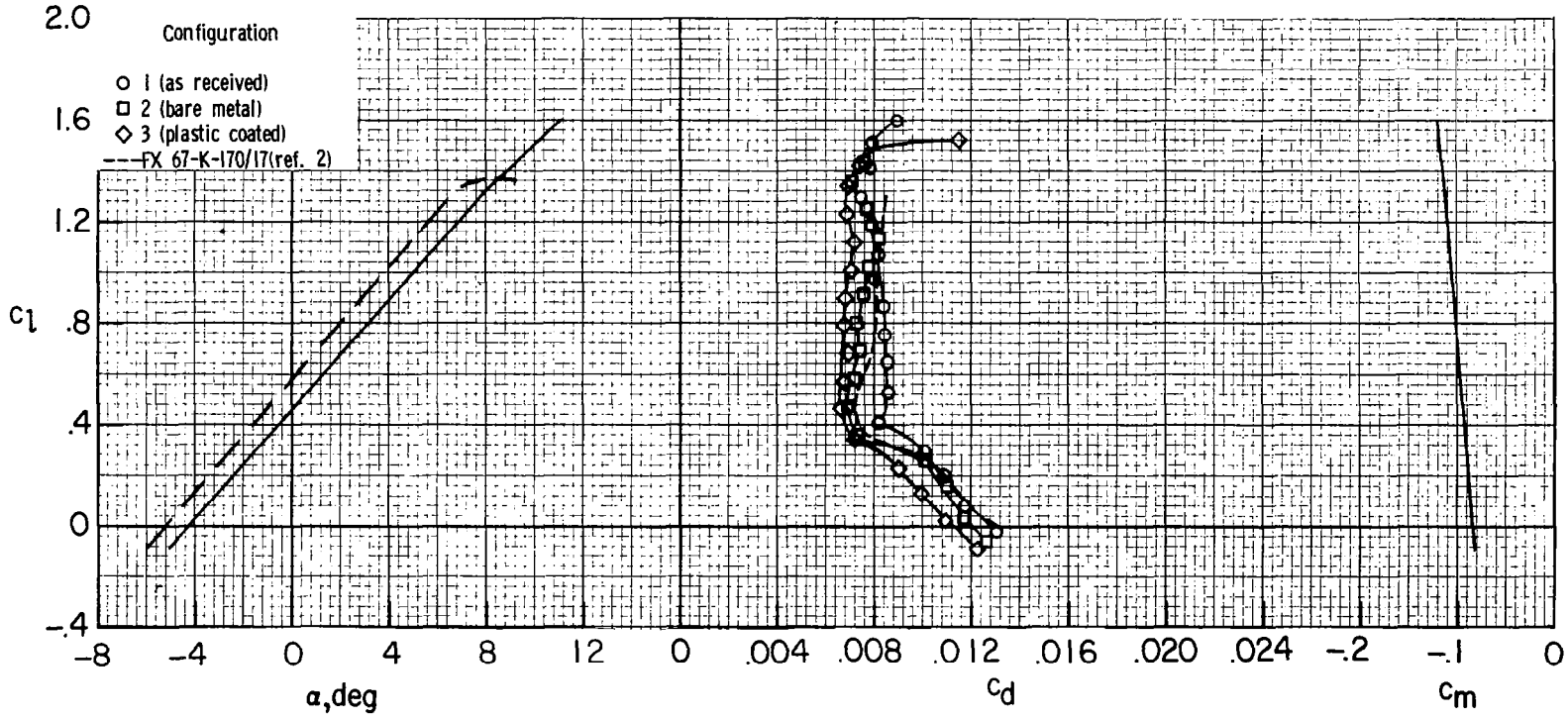

(a) $R = 1.1 \times 10^6$; $M = 0.10$.

Figure 8.– Comparisons of section characteristics of configurations 1 (as received), 2 (bare metal), 3 (plastic-coated), and FX 67-K-170/17 airfoil.

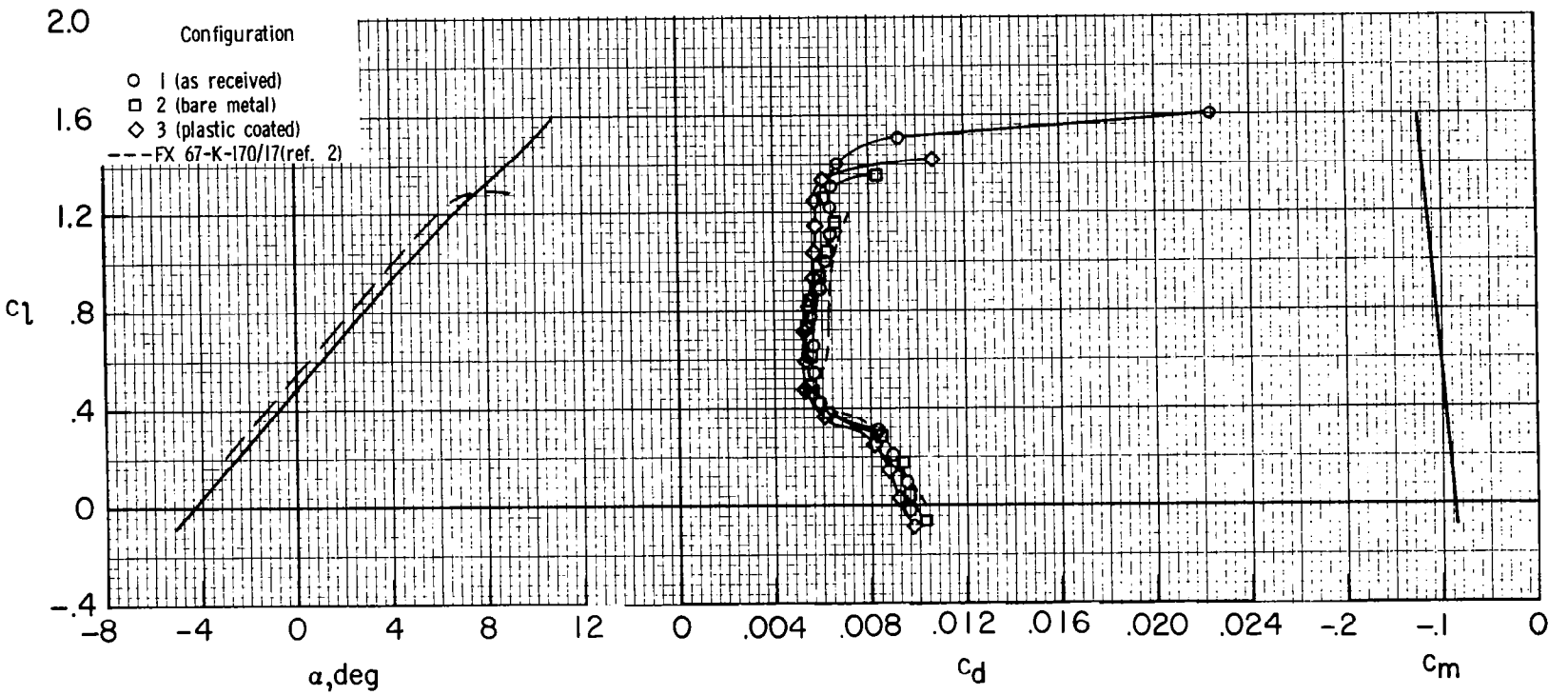

(b) R = 2.2 × 10^6; M = 0.10.

Figure 8.- Continued.

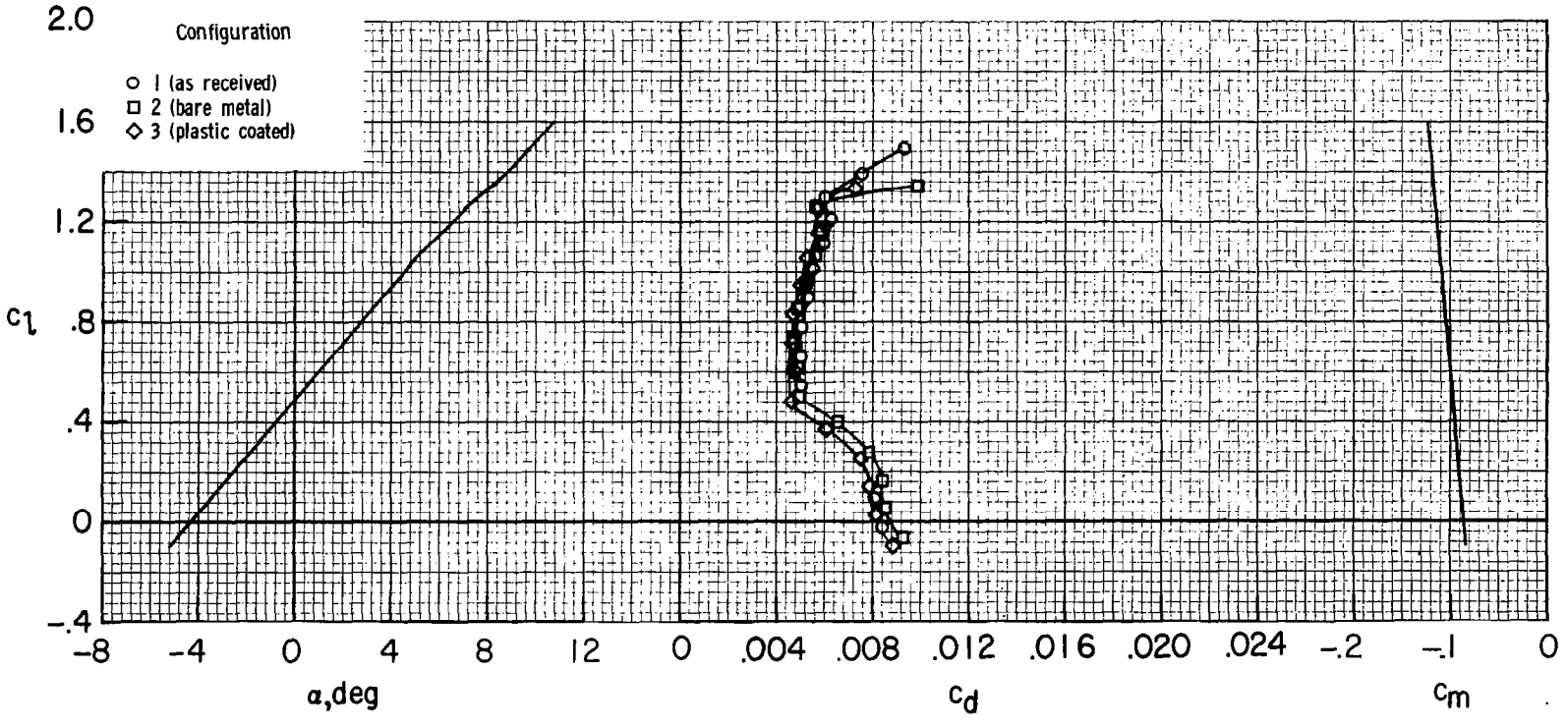

(c) $R = 3.3 \times 10^6$; $M = 0.10$.

Figure 8.- Concluded.

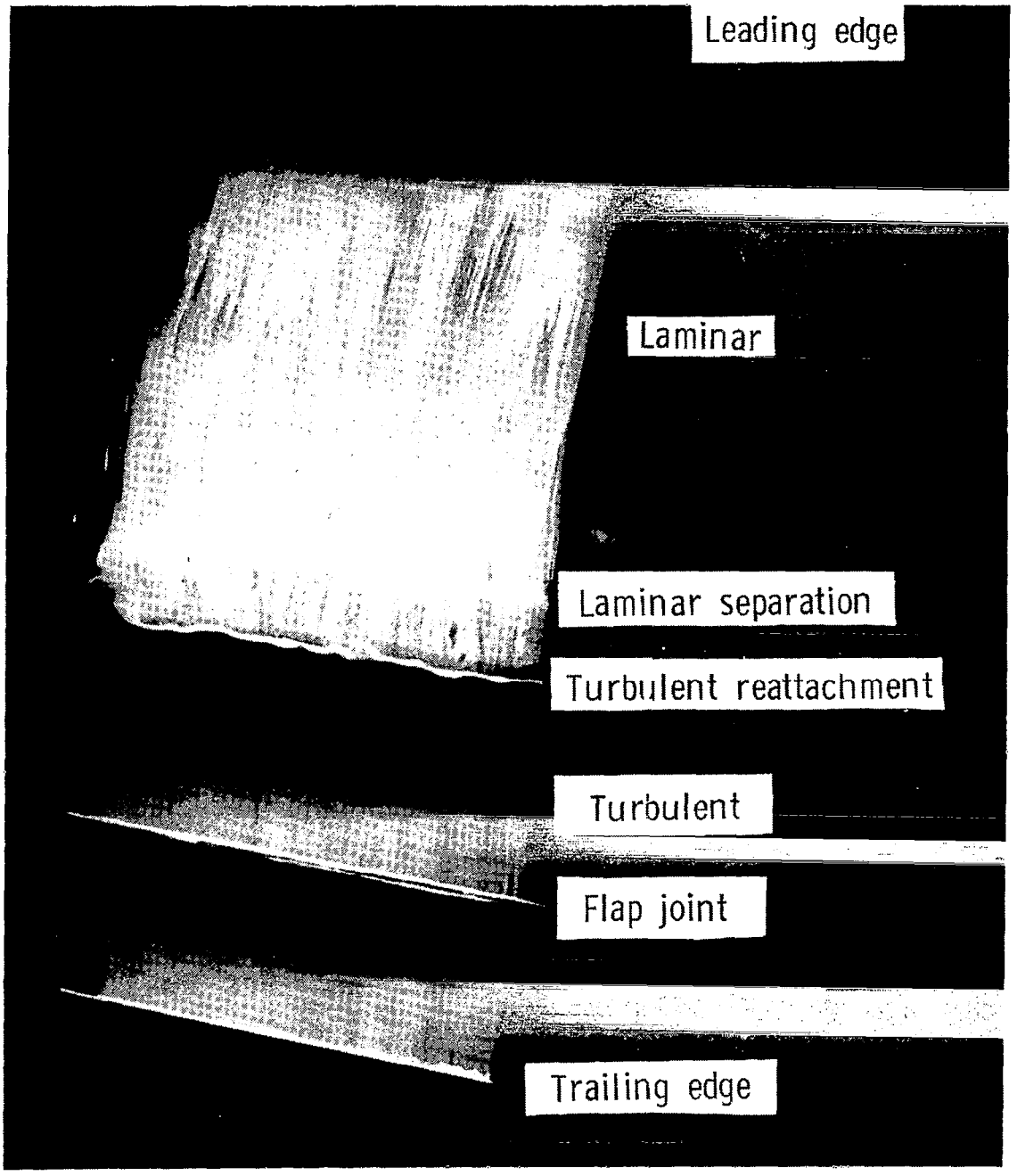

(a) $R \approx 1.1 \times 10^6$, $M = 0.07$, and $\alpha = 0^\circ$.

Figure 9.- Oil flow photographs of upper surface of configuration 3 (plastic-coated).

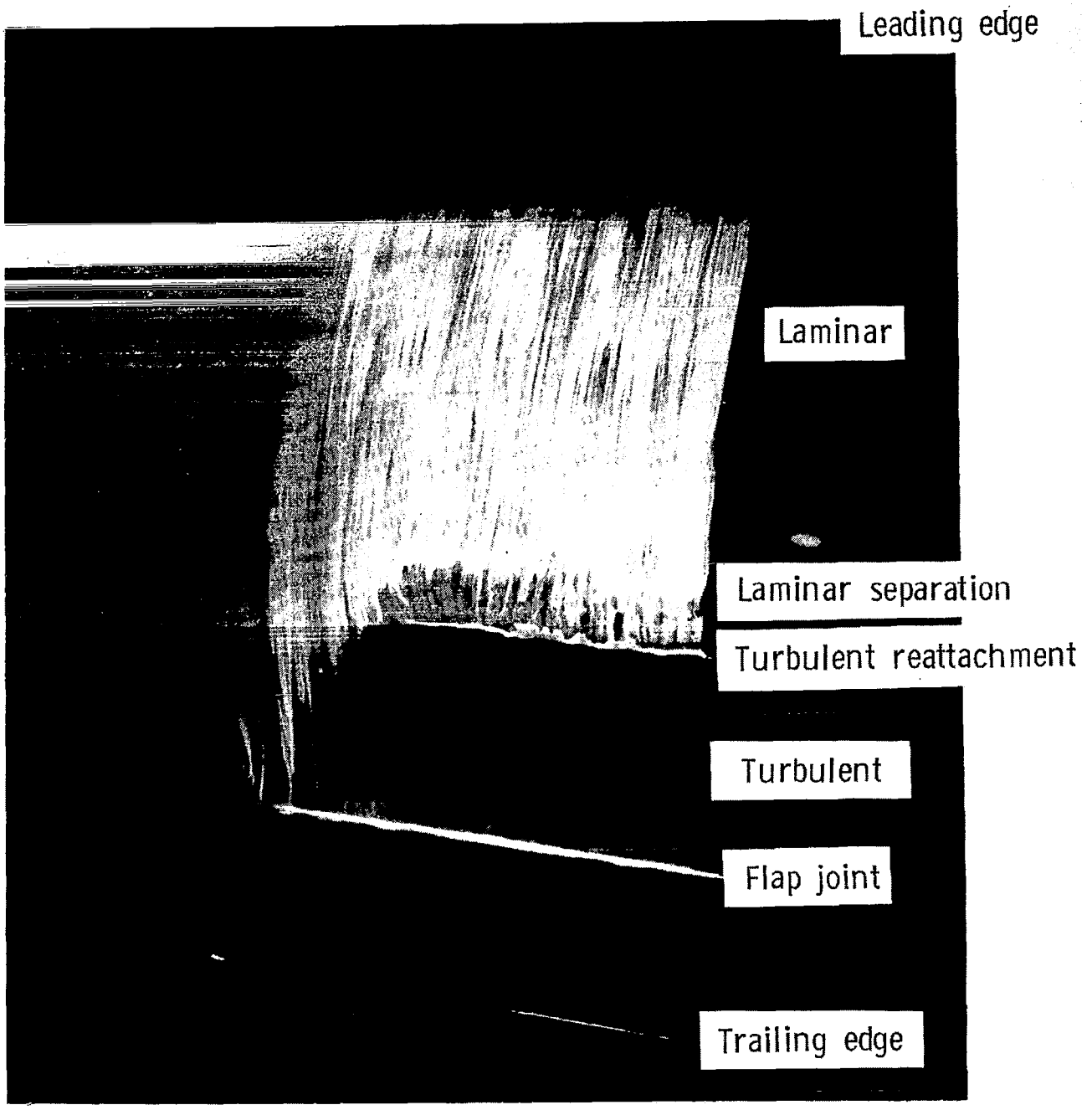

(b) $R \approx 1.5 \times 10^6$, $M = 0.10$, and $\alpha = 0^\circ$.

Figure 9.- Continued.

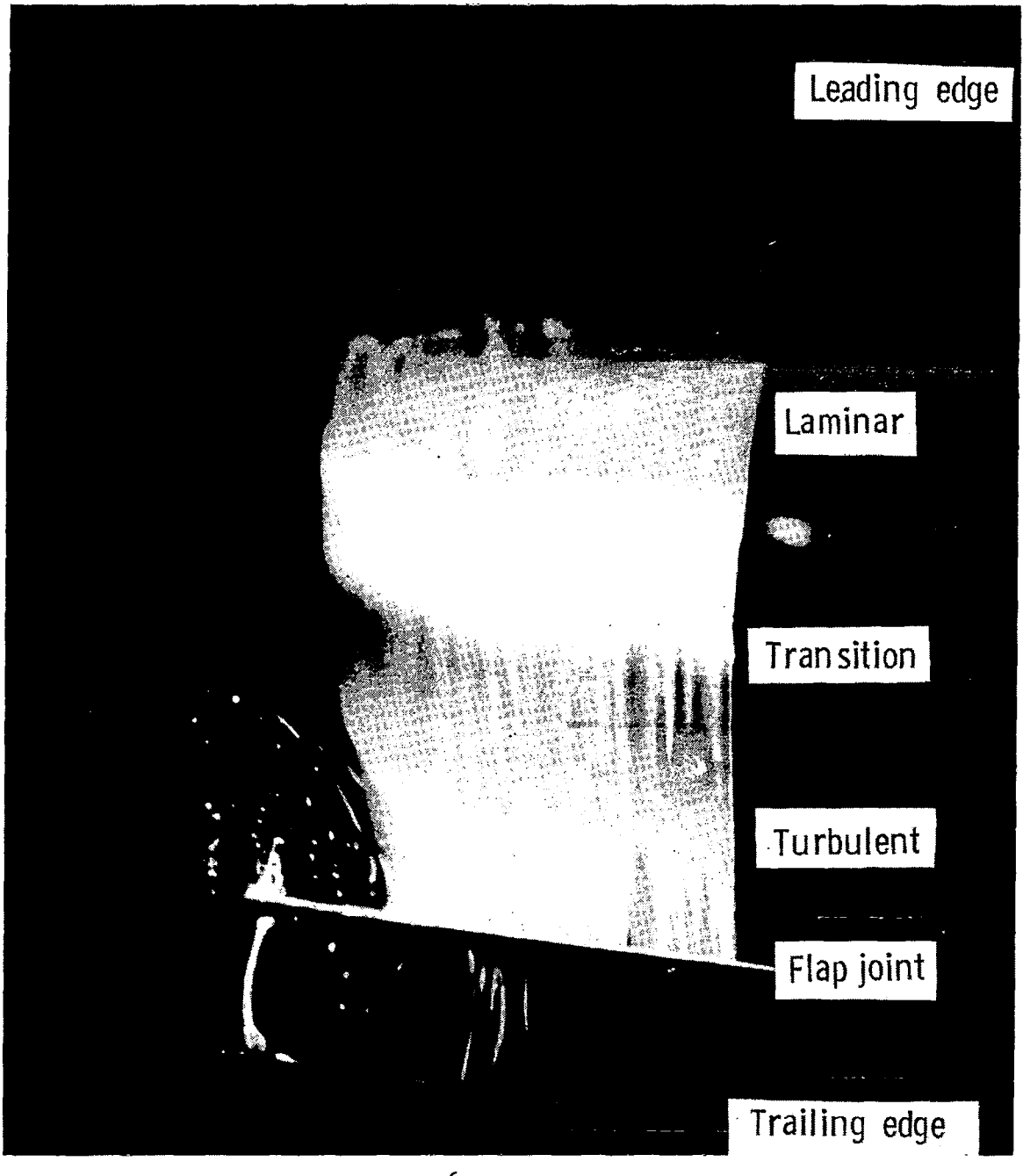

(c) $R \approx 1.5 \times 10^6$, $M = 0.10$, and $\alpha = 7^{\circ}$.

Figure 9.- Continued.

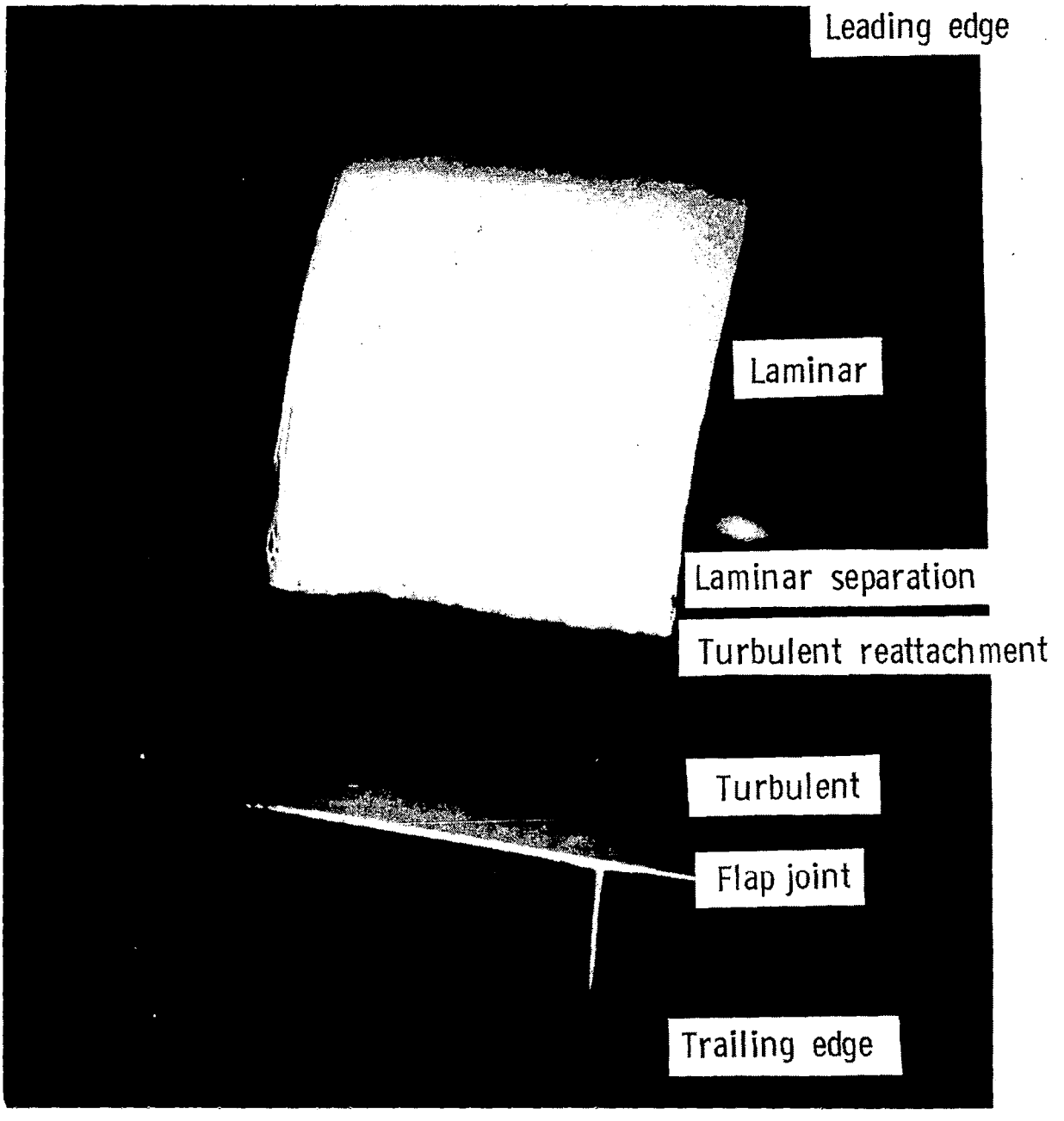

(d) $R \approx 2.5 \times 10^6$, $M = 0.16$, and $\alpha = 0^\circ$.

Figure 9.- Concluded.

OPTIMUM TAIL PLANE DESIGN FOR SAILPLANES

Kay Mayland
Technische Hochschule Darmstadt

SUMMARY

Classical drag equations in a modern version have been used to calculate the influence of tail modifications on the drag of a standard class sailplane. The profile drag which depends on the Reynolds number is included in the calculations. Minimum drag is compared with real drag for two lift coefficients.

Some results have no clear tendency but low tail area and relatively low tail aspect ratio give some advantages. Optimum and real lift ratios between wing and tail plane are compared for the original sailplane.

INTRODUCTION

Since the energy crisis in 1973 there is a lot of interest in reducing the trimmed drag of airplanes (Refs. 1-5). One contribution to the trimmed drag is the wing/tail interference drag. This interference drag had been interpreted as a component of the tail lift vector due to local downwash angle at the tail position. Sachs (Refs. 6, 7, 8, 9) has shown that this interpretation is not correct. The exact method is to calculate the interference drag with the aid of the downwash angle at downstream infinity. This new explanation corresponds to the well-known biplane theory of Prandtl and Munk (Ref. 10) which was also used in some new papers (Refs. 4, 11, 12). This theory in the modern version was used in this paper to show the relation between optimum and real load distributions between wing and tail.

Another purpose of this paper is to show the influence of tail plane design on total drag. It is important that the addition of the Reynolds number dependent profile drag has great influence on the optimum design.

All calculations are performed for a standard class sailplane.

SYMBOLS

Values are given in SI units.

AR	aspect ratio
b, b_t	wing span, tail span, m
C_D	drag coefficient
C_D^*	drag coefficient (tail profile drag + total induced drag)
C_L	lift coefficient
C_m	pitching moment coefficient
$\bar{c}$	mean aerodynamic chord, m
D	drag, N
g	acceleration of gravity, m/s^2
h, h_{wb}, h_t	distance in chord lengths from leading edge of wing to c.g., wing-body aerodynamic center, tail
k_{wb}, k_t	induced drag factor for wing-body, tail
L	lift, N
m	mass, kg
$\bar{q}$	dynamic pressure, N/m^2
Re	Reynolds number
S, S_t	wing and tail area, m^2
ε	downwash angle
ε_∞	downwash angle at downstream infinity
ε^*	downwash factor, $\varepsilon_\infty = \varepsilon^* k_{wb} C_{L_{wb}}$
μ	span ratio b_t/b
σ	interference factor

Subscripts:

min	minimum
o	zero lift
opt	optimum
t	tail
wb	wing-body

BASIC RELATIONS

The following fundamental relations were used, assuming that the aerodynamics are linear and that the dynamic pressure ratio is $\bar{q}_t/\bar{q} = 1$:

$$C_L = C_{L_{wb}} + C_{L_t} \frac{S_t}{S} \tag{1}$$

$$C_m = C_{mo_{wb}} + C_{L_{wb}} (h - h_{wb}) - C_{L_t} \frac{S_t}{S} (h_t - h) = 0 \tag{2}$$

$$C_m = C_{mo_{wb}} + C_L (h - h_{wb}) - C_{L_t} \frac{S_t}{S} (h_t - h_{wb}) = 0 \tag{2a}$$

$$C_D = C_{Do_{wb}} + k_{wb} C_{L_{wb}}^2 + \frac{S_t}{S} (C_{Do_t} + k_t C_{L_t}^2 + \varepsilon_\infty C_{L_t}) \tag{3}$$

The last term within the round brackets of the drag equation (3) is the wing/tail interference drag. The derivation was given by Sachs and shall not be repeated here. This interference drag is the product of the tail lift and the downwash angle at downstream infinity and corresponds to the one given by Prandtl but the new expression is much easier to use in calculations. The downwash angle at downstream infinity may be expressed as (Ref. 13)

$$\varepsilon_\infty = \varepsilon^* k_{wb} C_{L_{wb}} \qquad (\varepsilon^* = 0 - 3) \tag{4}$$

The downwash factor $\varepsilon^* = 1$ corresponds to a rectangular, $\varepsilon^* = 2$ to an elliptic and $\varepsilon^* = 3$ to a parabolic spanwise lift distribution of the wing.

Influence of Reynolds number

Wortmann (Ref. 14) has designed and measured a lot of excellent profiles for sailplanes. The wind tunnel test results are published in the "Stuttgarter Profilkatalog". Figure 1 shows some test results demonstrating the influence of Reynolds number on profile drag for several profiles. The solid lines are according to the relations used in this paper for calculating the influence of Reynolds number:

$$C_{Do_{wb}} = \frac{0.009}{Re_{wb}^{0.3}} \qquad \text{Re in millions} \qquad (5)$$

$$C_{Do_t} = \frac{0.007}{Re_t^{0.3}}$$

These relations are only valid for the above mentioned profiles and for a special Reynolds number range.

Real lift ratio

For balance in equilibrium flight ($C_m = 0$) equations (1) and (2) can be solved for the lift ratio between tail and wing

$$\left.\frac{L_t}{L_{wb}}\right|_{\substack{C_L=\text{const}\\ C_m=0}} = \frac{C_{L_t}\,\frac{S_t}{S}}{C_{L_{wb}}} = -\frac{\frac{C_{mo_{wb}}}{C_L} + (h - h_{wb})}{\frac{C_{mo_{wb}}}{C_L} + (h - h_{wb}) - (h_t - h_{wb})} \qquad (6)$$

This lift ratio depends on fixed quantities and on the parameters, total lift coefficient and c.g. position. It is possible to eliminate the c.g. position by considering the stability requirement. The static margin may be expressed as

$$\frac{\partial C_m}{\partial C_L} = (h - h_{wb}) - \frac{(C_{L_\alpha})_t}{C_{L_\alpha}}\,\frac{S_t}{S}\,(h_t - h_{wb})\left(1 - \frac{\partial \varepsilon}{\partial \alpha}\right) < 0 \qquad (7)$$

Solving equation (7) for $(h - h_{wb})$ and combining this with equation (6) gives the following equation:

$$\left.\frac{L_t}{L_{wb}}\right|_{\substack{C_L=\text{const}\\ C_m=0}} = -\frac{\dfrac{C_{mo_{wb}}}{C_L} + \dfrac{\partial C_m}{\partial C_L} + \dfrac{(C_{L_\alpha})_t}{C_{L_\alpha}}\dfrac{S_t}{S}(h-h_{wb})\left(1-\dfrac{\partial\varepsilon}{\partial\alpha}\right)}{\dfrac{C_{mo_{wb}}}{C_L} + \dfrac{\partial C_m}{\partial C_L} + \dfrac{(C_{L_\alpha})_t}{C_{L_\alpha}}\dfrac{S_t}{S}(h-h_{wb})\left(1-\dfrac{\partial\varepsilon}{\partial\alpha}\right)-(h_t-h_{wb})} \tag{8}$$

Regarding equation (8) it is possible to say that the real load distribution between tail and wing depends on several fixed values and on the parameters, stability margin and total lift coefficient.

Optimum load Distribution

Prandtl has published the optimum tail/wing lift ratio in his biplane theory (Ref. 10):

$$\left(\frac{L_t}{L_{wb}}\right)_{opt} = \frac{\mu - \sigma}{\frac{1}{\mu} - \sigma} \qquad \text{with } \mu = \frac{b_t}{b} \tag{9}$$

The interference factor σ has to be taken out of diagrams (Ref. 6). Therefore it is easier to use the following relations. Comparing Prandtl's equation for the interference drag

$$D_{Int} = \frac{2\,\sigma}{\pi\,\bar{q}}\,\frac{L_t\,L_{wb}}{b_t\,b} \tag{10}$$

with equation (3) it is possible to rewrite equation (9) as

$$\left(\frac{L_t}{L_{wb}}\right)_{opt} = \frac{1-\frac{\varepsilon^*}{2}}{\left(\frac{b}{b_t}\right)^2 - \frac{\varepsilon^*}{2}} \tag{11}$$

The optimum tail lift may be either positive or negative depending on the downwash factor ε^*. Only an elliptic spanwise lift distribution over the wing requires zero tail lift. The combination of equations (6) and (11) gives the optimum c.g. position

$$(h - h_{wb})_{opt} = -\frac{C_{mo_{wb}}}{C_L} + \frac{1-\frac{\varepsilon^*}{2}}{1+\left(\frac{b}{b_t}\right)^2 - \varepsilon^*}(h_t - h_{wb}) \tag{12}$$

and the optimum stability margin

$$\left(\frac{\partial C_m}{\partial C_L}\right)_{opt} = (h - h_{wb})_{opt} - \frac{(C_{L_\alpha})_t}{C_{L_\alpha}} \frac{S_t}{S} (h_t - h_{wb})\left(1 - \frac{\partial \varepsilon}{\partial \alpha}\right) \qquad (13)$$

The minimum induced drag was also given by Prandtl and may be rewritten in the following equation

$$C_{Di_{min}} = k_{wb}\, C_L^2 \left[1 - \frac{\left(1 - \frac{\varepsilon^*}{2}\right)^2}{1 + \left(\frac{b}{b_t}\right)^2 - \varepsilon^*} \right] \qquad (14)$$

The term in the brackets demonstrates the decreasing induced drag of the wing/tail combination compared with the wing alone.

NUMERICAL RESULTS

Optimum c.g. position

All calculations are performed with the data set of a typical standard class sailplane; see table 1.

The pilot of this airplane wants to know whether he can reach good performance by choosing the correct c.g. position. In figure 2 the equations (8) and (11) are evaluated. It is easy to see that the optimum load distribution depends on the downwash factor ε^* but not on the lift coefficient C_L while the real lift ratio has inversed dependencies. The downwash factor is normally not known exactly; therefore it is not easy to reach exact conclusions from figure 2. A more accurate way is to evaluate the equation (13); see figure 3. It is easy to see that the optimum stability margin for lift coefficients $C_L > 0.4$ is obtained by a normal (stable) c.g. position. This statement is valid for downwash factors between 1 and 2. Good performance for a wide range of lift coefficients will therefore be obtained by choosing a medium or forward c.g. position. Only high speed flight requires aft c.g. positions.

Tail modifications

While the pilot of a sailplane is interested in the optimum c.g. position, the sailplane designer is interested in the tail design to meet stability requirements and to achieve good performance. For a fixed wing geometry it is possible to vary two main parameters: tail area and tail span. It is important not to

evaluate the parameter variations only by regarding the total induced drag because the tail profile drag will also change. Therefore the criterion is the sum of both the total induced drag and the tail profile drag (equation 5)

$$C_D^* = C_{Di} + C_{Do_t} \frac{S_t}{S} \tag{15}$$

The induced drag is calculated as in equation (3) with the lift coefficients obtained from the real load distribution (equation 8). The stability margin is assumed to be $\partial C_m/\partial C_L = -0.15$, and the downwash factor is assumed to be $\varepsilon^* = 1$. (The calculations were also performed for $\varepsilon^* = 2$; the tendencies correspond to $\varepsilon^* = 1$.) The real drag coefficient is compared with the theoretical minimum drag coefficient using equation (14) for the minimum induced drag.

In figure 4 this drag coefficient is plotted versus the tail span with constant tail m.a.c. for two lift coefficients. Parameter in this diagram is the tail profile drag at Re = 10^6. The minimum induced drag ($C_{Do_t} = 0$) is decreasing with increasing tail span but the higher profile drag due to increasing tail area is predominant. It is suitable to design the tail with the minimum possible area to satisfy stability requirements.

Assuming a minimum tail area of 1 m^2, another question is, what span or what AR_t is optimum? There are two effects:

- With increasing tail span the minimum induced drag of the complete sailplane is decreasing
- Increasing tail span means decreasing Reynolds number resulting in increasing tail profile drag.

In figure 5 it is shown that the superposition of these two effects results in no clear tendency. With increasing profile drag the Reynolds number effect becomes predominant. Assuming a tail profile drag coefficient of $C_{Do_t} = 0.01$ at $Re_t = 10^6$ a reduction of tail span from 2.4 m (original value) to perhaps 2.0 m will give some little advantages.

The differences between minimum and real drag coefficients are generally small; only low total lift coefficients ($C_L = 0.2$) require high tail downloads (see figure 2) resulting in greater differences.

Wing and tail modifications

The wing geometry is included in the variations. The only restrictions are now a wing span of 15 m and a total area (wing +

tail) of 11 m^2. To simplify the calculations it is assumed that wing and tail have the same profile drag at Re = 10^6. It is suitable to regard the drag or the drag areas directly rather than the drag coefficient:

$$\frac{D_o}{\bar{q}} = C_{Do}\ S = (C_{Do})_{Re=10^6} \left(\frac{S}{Re^{0.3}} + \frac{S_t}{Re_t^{0.3}}\right) \tag{16}$$

$$\frac{D_{i_{min}}}{\bar{q}} = k_{wb}\ C_L^2\ S \left[1 - \frac{\left(1 - \frac{\varepsilon^*}{2}\right)^2}{1 + \left(\frac{b}{b_t}\right)^2 - \varepsilon^*}\right]$$

$$= \left(\frac{m\ g}{\bar{q}\ b}\right)^2 \frac{1}{\pi} \left[1 - \frac{\left(1 - \frac{\varepsilon^*}{2}\right)^2}{1 + \left(\frac{b}{b_t}\right)^2 - \varepsilon^*}\right] \tag{17}$$

Figure 6 shows the total profile drag area (equation 16) plotted versus the ratio of tail area to total area. For normal tail aspect ratios between 3 and 6 the total profile drag will increase with increasing tail area due to decreasing medium Reynolds number of the total area.

The combination of equations (16) and (17) gives the minimum total drag D_{min} which is plotted versus the ratio of tail area to total area in figure 7. The trends are clear: the lowest possible drag is obtained with low ratios of tail area to total area.

CONCLUSIONS

The influences of c.g. position and of tail plane design on the performance of a standard class sailplane have been shown. One important result is that the optimum c.g. position is for a wide range of lift coefficients within the normal c.g. range. The calculations for the tail plane design have shown that the reduction of induced drag due to higher tail span is less important than the influence of profile drag. Low tail area and relatively low tail aspect ratio will give some advantages. It is remarkable that the best standard class sailplanes of today have a tail area of $S_t \approx 1\ m^2$ and a tail aspect ratio of $AR_t \approx 5$ while older sailplanes have for example $S_t = 1.5\ m^2$ and $AR_t = 6$.

REFERENCES

1. S.E. Goldstein and G.P. Combs: Trimmed drag and maximum flight efficiency of aft tail and canard configurations. AIAA Paper 74-69 (1974).

2. F.H. Lutze, Jr.: Trimmed drag considerations. J. Aircraft 14 (1977), pp. 544-546.

3. F.H. Lutze, Jr.: Reduction of trimmed drag. In: NASA CR-145 627 (1975), pp. 307-318.

4. E.E. Larrabee: Trim drag in the light of Munk's stagger theorem. In: NASA CR-145 627 (1975), pp. 319-329.

5. J. Roskam: Some comments on trim drag. In: NASA CR-145 627 (1975), pp. 295-305.

6. G. Sachs: Leitwerksauslegung und künstliche Stabilität. Dornier-Bericht 77/16 A (1977).

7. G. Sachs: Optimale Leitwerksauslegung für Flugzeuge künstlicher Stabilität. Zeitschrift für Flugwissenschaften Heft 1, 1978, pp. 1-10.

8. G. Sachs: Einfluß des Leitwerks auf die Flugleistungen. Institut für Flugtechnik der Technischen Hochschule Darmstadt, IFD-Bericht 2/77, 1977.

9. G. Sachs: Minimum Trimmed Drag and Optimum C.G. Position. J. Aircraft 15 (1978), pp. 456-459.

10. L. Prandtl: Tragflügeltheorie. 2. Mitteilung. Nachr. Ges. Wiss. Göttingen, Math.-phys. Kl. 1919, pp. 107-137.

11. E.V. Laitone: Ideal tail load for minimum aircraft drag. J. Aircraft 15 (1978), pp. 190-193.

12. McLaughlin: Calculations and comparison with an ideal minimum of trimmed drag for conventional and canard configurations having various levels of static stability. NASA-TN-D-8391, May 1977.

13. H. Schlichting und E. Truckenbrodt: Aerodynamik des Flugzeuges, 2. Band. Springer-Verlag, Berlin/Heidelberg/New York 1969.

14. F.X. Wortmann and D. Althaus: Stuttgarter Profilkatalog, Institut für Aerodynamik, Universität Stuttgart, 1972.

15. F. Thomas: Grundlagen für den Entwurf von Segelflugzeugen. DFVLR-Bericht IB 154-78/8, November 1976.

TABLE 1.- DATA SET OF A TYPICAL SAILPLANE

[Reference 10]

Mass, kg	300
Wing:	
Span, m	15
Area, m^2	10
Mean aerodynamic chord, m	0.67
Aspect ratio	22.5
Pitching moment coefficient, zero lift	-0.1
Horizontal tail:	
Span, m	2.4
Area, m^2	1.0
Aspect ratio	5.76
Distance between wing and tail aerodynamic centers, m	3.85
Stability margin	-0.15

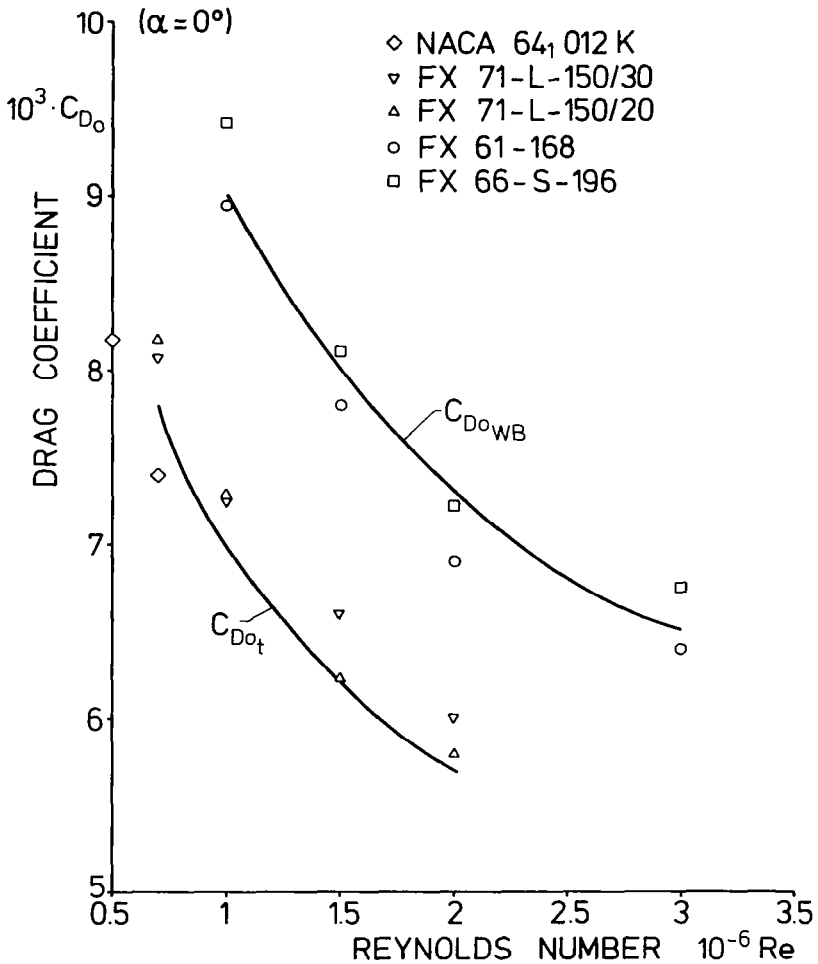

Fig. 1: Influence of Reynolds number on profile drag

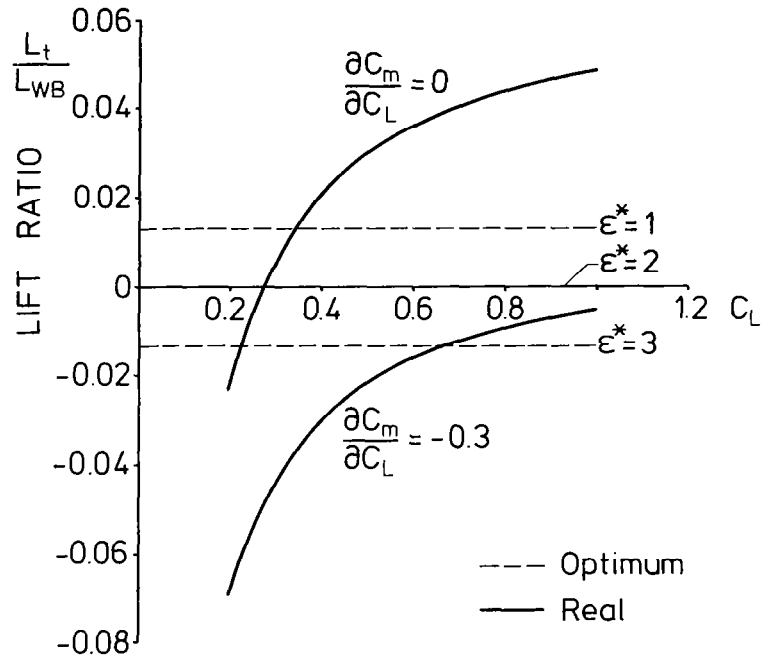

Fig. 2: Lift ratio between wing and tail

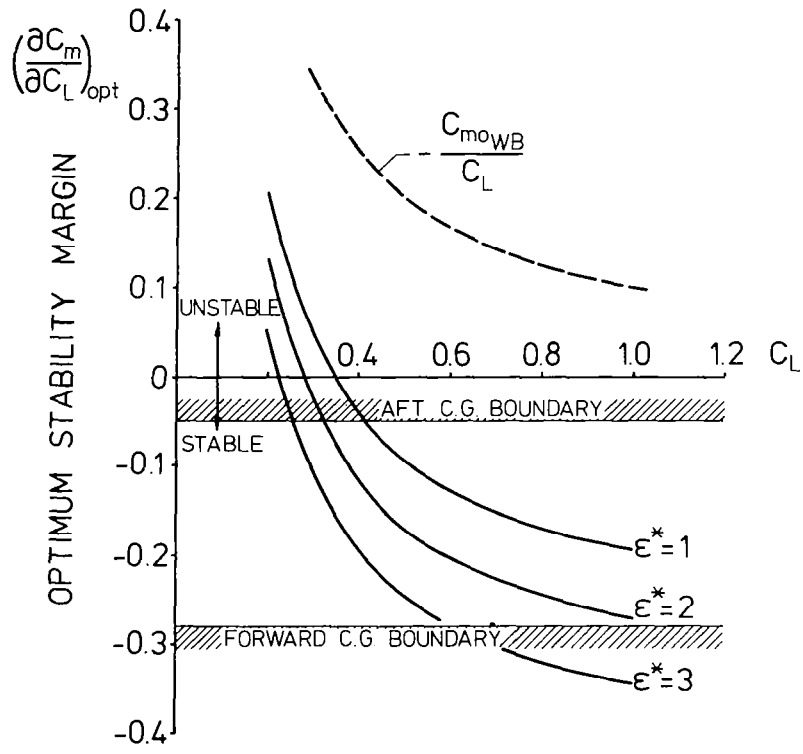

Fig. 3: Optimum stability margin

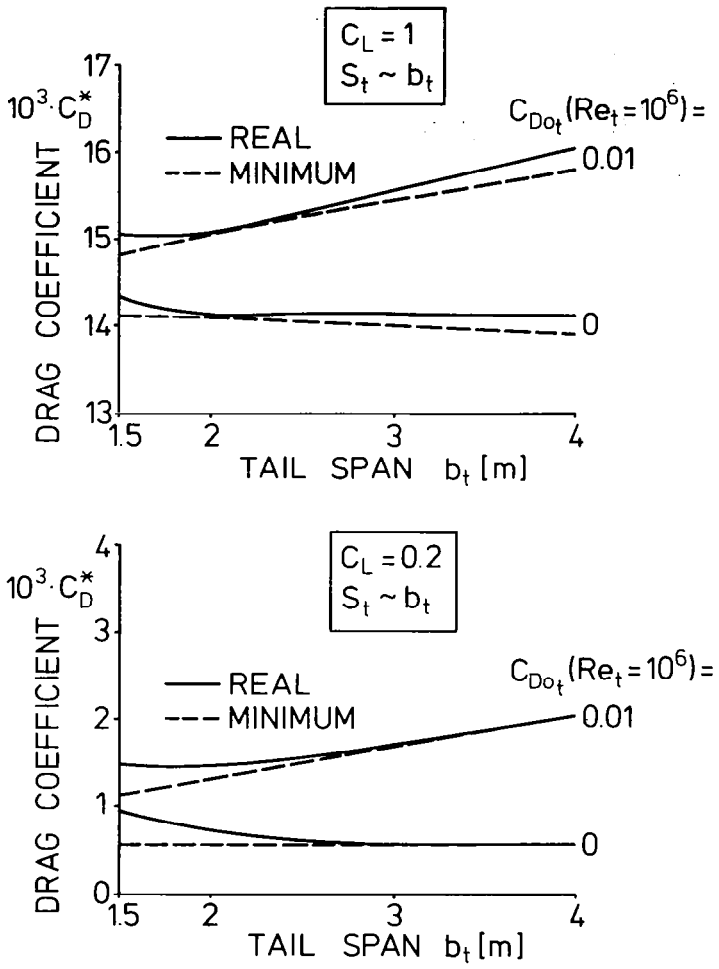

Fig. 4: Variation of tail span and area

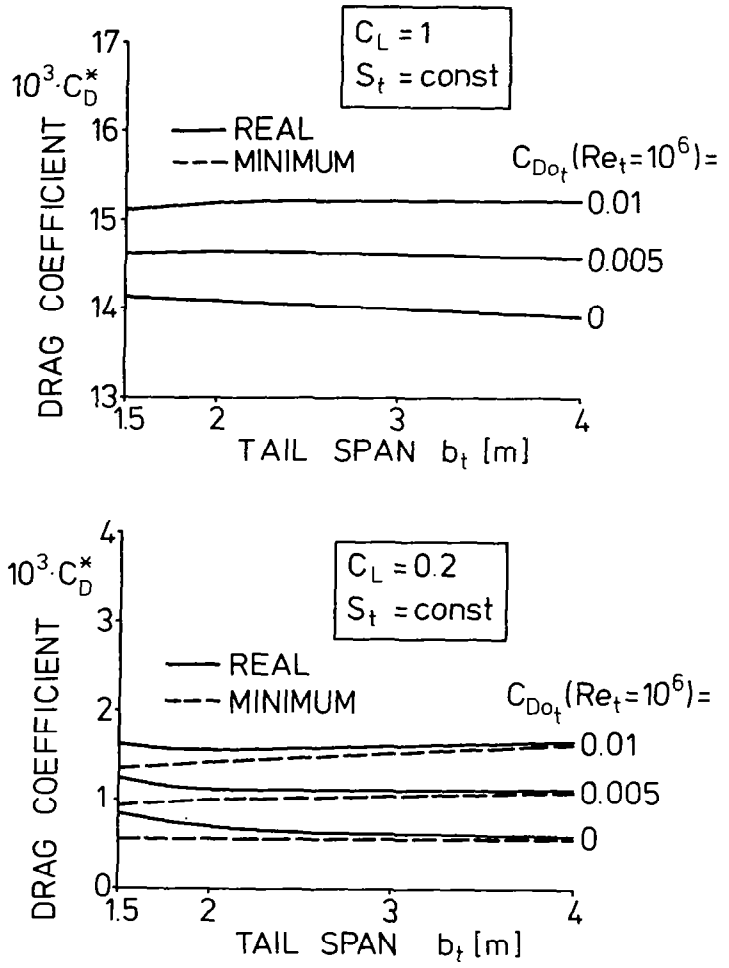

Fig. 5: Variation of tail span, tail area = const.

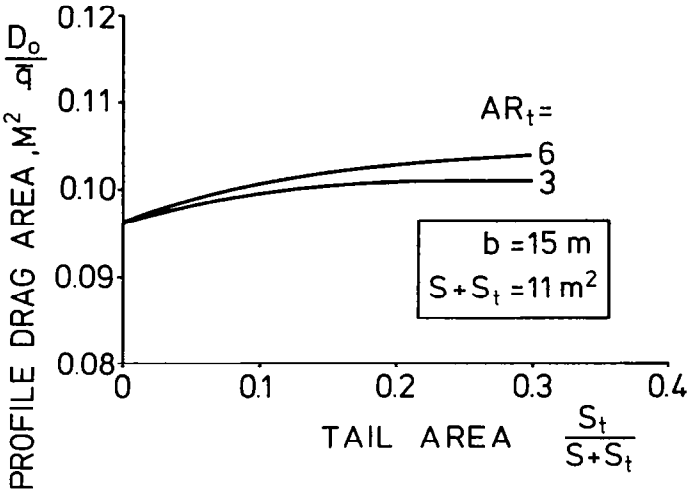

Fig. 6: Profile drag area versus tail area

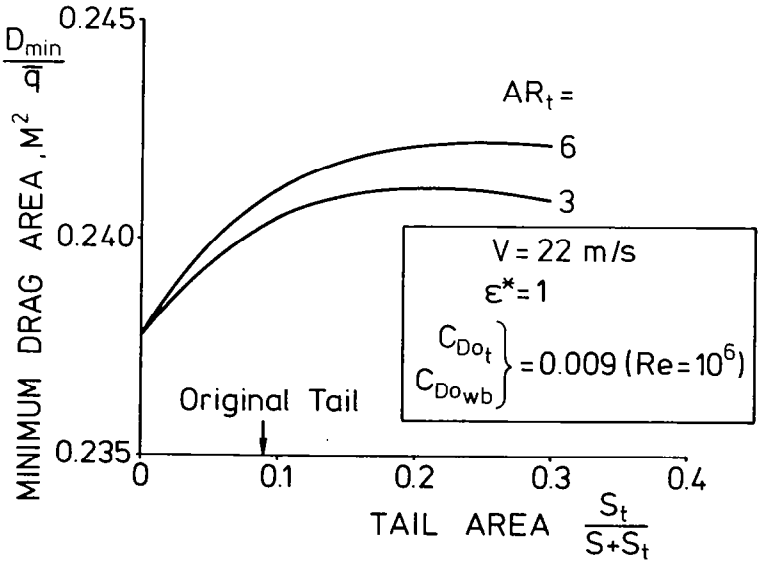

Fig. 7: Minimum drag area versus tail area

THE EFFECT OF DISTURBANCES ON A WING

RICHARD EPPLER
UNIVERSITAT STUTTGART
STUTTGART, WEST GERMANY

SUMMARY

Disturbances such as flap and aileron hinges and poorly faired spoilers were simulated in a computer wind tunnel. The total drag of a single roughness element does not depend only on the size of that element. Its position on the wing has a surprisingly strong effect. In particular, a roughness element on the convex side of a deflected flap or aileron causes a very substantial increase in drag. Very few experimental data are available for comparison. Good agreement with experiment can be achieved, however, by adapting a fictive "step size." The correlation between the real roughness-element size and the drag increase remains to be determined. Simple, fundamental experiments are suggested which will allow a theoretical estimation of the drag increase due to roughness elements.

INTRODUCTION

Disturbances on a wing due to flap and aileron hinges, variable chord arrangements, poorly faired spoilers, etc. become more significant as airplanes become more efficient. In other words, as the profile drag decreases, so must the parasitic drag. Performance differences between airplanes of the same type and performance differences between similar types have been measured several times. These differences indicate that some airplanes have parasitic drag due to seemingly insignificant details. It is necessary to investigate such details in the sense of Bruce Carmichael's study "What Price Performance?" (ref. 1). As long as we spend lots of money on variable chord concepts, we should at least be sure to take every opportunity to realize less expensive performance improvements. One such improvement could be the reduction of disturbances connected with flap and aileron hinges and with spoiler gaps and steps. These two-dimensional disturbances usually occur at wing positions where the boundary layer is already turbulent. Because there is very little experimental information on such disturbances, a theoretical disturbance model has been developed. It yields relative effects and indicates which simple, fundamental experiments are necessary to obtain a method for the estimation of the absolute amount of these effects.

THE DISTURBANCE MODEL

The boundary-layer flow in the region surrounding a two-dimensional disturbance of height h perpendicular to the wall is shown in figure 1. The velocity $u(y)$ in the boundary layer at $y = h$ is called u_h. It is plausible that the influence of the disturbance will depend mainly on h and u_h. This influence will be evident several step heights downstream (fig. 1). As long as h is not too large, the velocity $u(y)$ depends only on the wall shear stress τ_o. This was shown by Ludwieg and Tillman (ref. 2) and reconfirmed by Kader and Yaglom (ref. 3). A good approximation for $u(y)$ is

$$\frac{u(y)}{u_\tau} = a \log \frac{y u_\tau}{\nu} + b \tag{1}$$

where ν is the kinematic viscosity, $u_\tau = \sqrt{\frac{\tau_o}{\rho}}$ is the wall shear-stress velocity, and ρ is the density; a ($\approx$5) and b ($\approx$6.5) are constants. For use in a boundary-layer computation method, it is better to transform equation (1) by means of the local skin-friction coefficient $C_f = \frac{\tau_o}{\rho U^2}$ into

$$\frac{u(y)}{U} = \sqrt{C_f}\left[2.17 \ln \left(\sqrt{C_f}\,\frac{U}{U_\infty} R \frac{y}{L}\right) + 6.5\right] \tag{2}$$

where U is the local potential-flow velocity, $R = \frac{U_\infty L}{\nu}$ is the overall Reynolds number of the flow, U_∞ is the free-stream flow velocity, and L is the reference length which, for a wing, is the chord length c.

As long as this approximation is valid for u_h, the influence of the disturbance will depend only on the local disturbance Reynolds number

$$R_h = \frac{u_h h}{\nu}$$

It is even plausible that the displacement thickness δ_1 will change linearly with R_h. This means that the distance between the undisturbed and disturbed velocity distributions is proportional to $u_h h$. The same is approximately true for the momentum thickness δ_2 and the energy thickness δ_3. Therefore, the model to be used assumes that δ_2 is increased by a value.

$$\Delta\delta_2 = ku_h h \tag{3}$$

as a result of a disturbance of height h. It can be shown that the additional assumption

$$\Delta\delta_3 = \Delta\delta_2 \tag{4}$$

is also reasonable provided u_h is not too large. The most difficult problem is determining the value of the proportionality constant k. The value of this constant will depend on the precise shape of the disturbance. It should not be too difficult to obtain accurate values for k from simple experiments. Such experiments have been planned by F. X. Wortmann and D. Althaus of the Institut für Aerodynamik und Gasdynamik at the Universität Stuttgart.

If the boundary layer is laminar at the position of the roughness element, the computation predicts transition at that position.

DISTURBANCES ON A WING

A value of $k = 0.15$ was used in equation (3) as a rough approximation for a simple roughness element like a trip wire. A computer program was used to evaluate the effects of disturbances on a wing. Given the airfoil shape, the program computes the velocity distributions corresponding to the various input angles of attack. For all velocity distributions, boundary-layer computations are performed for the different input Reynolds numbers. Disturbances can be specified at up to two different positions on each surface of the airfoil.

Several examples illustrate the capabilities of this disturbance model. For the first example, one disturbance of height $h = 1$ mm was introduced at various positions along the upper surface of airfoil E603. The velocity distributions for various lift coefficients c_l are shown in figure 2. The roughness element was introduced at three different chordwise positions; $x/c = 0.4$, $x/c = 0.6$, and $x/c = 0.81$. The theoretical polars at $R = 1 \times 10^6$, which corresponds roughly to low-speed flight in a sailplane, and $R = 3 \times 10^6$, which corresponds to high-speed flight in a sailplane, are presented in figure 3. The results clearly indicate that the potential-flow velocity at the position of the roughness element has a strong influence on the drag. The additional drag nearly always increases with lift coefficient as does the local velocity. The polar for the most forward disturbance, however, has a different character. At $c_l \approx 1.1$, the most upstream roughness element has less influence than the more downstream ones. By looking into the details, it was determined that not only the potential-flow velocity, but also the skin-friction coefficient at the position of the roughness element has a strong influence.

If transition occurs in an adverse pressure gradient and the roughness element is shortly behind this transition, the turbulent boundary layer will not be fully developed at the position of the roughness element and the effect on the drag will, therefore, be quite small. Of course, the effect on the drag will be quite large if the roughness element shifts the transition point toward the leading edge.

These results are entirely theoretical. It is, of course, desirable to obtain a correlation between theory and experiment. It would be easy to perform wind-tunnel experiments which correspond to this example. As previously mentioned, these experiments are planned but have not yet been performed.

Experimental data applicable to this problem are rare. There have been many experiments concerning the influence of roughness elements on transition, but few on the effects of roughness elements on a boundary layer which is already turbulent. One such experiment was performed in 1971 by D. Althaus in a low-turbulence wind tunnel at the Universität Stuttgart. In that test, the polars of an airfoil (FX 62-K-153/20) with a conventional, center-hinged flap (gap sealed) were measured first. Then, the polars were determined for the same airfoil with a so-called "Elastic Flap" (ref. 4). These experiments are valuable for evaluating the theory because the two models differed only by the radius of the arc between the forward portion of the airfoil and the flap and by the single step (roughness element) which is a part of every flap hinged in the conventional manner.

The envelopes of the polars for both configurations are shown in figure 4. Each envelope was obtained by plotting the lowest drag coefficients for the various flap deflections at a given lift coefficient. This means that the drag coefficients for zero or negative (up) flap deflections are used for low lift coefficients and the drag coefficients for positive (down) flap deflections are used for high lift coefficients. Thus, the envelope is defined by the data for the optimal flap deflections. The differences between the two curves is quite small for the lower lift coefficients and surprisingly large for the higher lift coefficients.

For some time, no explanation could be found for this apparent anomaly. After introducing the disturbance model into the computer program, however, it was not difficult to analyze these two configurations theoretically. The velocity distributions for the FX 62-K-153/20 airfoil (ref. 5) using the original coordinates are shown in figure 5. Not unlike many Wortmann airfoils, the coordinates are not smooth. The velocity distributions show irregularities, the worst one occurring at the leading edge on the lower surface. In the practical use of this airfoil and for the wind-tunnel model, these irregularities have probably been smoothed out. Therefore, it was reasonable to smooth the coordinates before

proceeding with further computations. The boundary-layer method is very sensitive to such irregularities, especially with regard to the prediction of transition. The velocity distributions for the smoothed airfoil with 0° and 10° flap deflection are shown in figure 6. The differences between the two flap configurations (plain and elastic) are evident only on the upper surface in the region around the hinge. The elastic flap causes a much lower suction peak at the hinge than the normal, plain flap. Moreover, the plain flap introduces a certain, single roughness element at that point. It was not possible to specify the height h of the roughness element in the disturbance model directly from the step height at the hinge. Instead, several different values for h were tried. The theoretical results for $h = 0.6$ mm at $R = 1 \times 10^6$ and 3×10^6 are shown in figure 7. Interestingly, the theory shows exactly the same phenomenon as the experiment. At 0° flap deflection, the differences between the two flap configurations are small, and at 10° deflection, the same roughness element causes a considerable drag penalty for the plain flap. For positive flap deflection, the roughness element is located precisely at the position of the suction peak, which means that it is in a region of high potential-flow velocity. Also, the increased favorable pressure gradient for the plain-flap configuration ahead of the element causes an increase in wall shear stress which further amplifies the drag penalty. For 0° flap deflection, the potential-flow velocity and the wall shear stress are much lower at the position of the roughness element, which explains the small difference for this case.

Some of the experimental data from figure 4 are included in figure 7. The drag penalties predicted by the theory agree well with the experiment. It must be emphasized that the absolute value of the drag penalty is not the significant result. This value was achieved by selecting the right value for h. The ratio between the drag differences with and without flap deflection, however, must be pointed out as a fundamental result which agrees well with experiment. This result, of course, has practical applications and can eventually explain some of the performance differences between similar airplanes. The order of magnitude of these drag differences should not be neglected in performance calculations.

The maximum lift coefficient and its decrease due to the roughness element were not predicted as well as the drag penalty. It should be noted, however, that the wind-tunnel results for maximum lift coefficient must be suspect. The wind tunnel used has a closed, rectangular test section with the model spanning the tunnel from wall to wall. The lift coefficient is determined by measuring the pressures along the top and bottom tunnel walls. Thus, these measurements yield the average c_l over the span of the model. Note also that the span is roughly equal to the chord. Accordingly, any separation at the juncture of the tunnel wall and the model influences the measured lift coefficient considerably.

CONCLUSIONS

Single roughness elements have been theoretically modeled. The data from a previously run experiment on a flapped airfoil with and without a disturbance at the hinge was used for comparison. The drag penalty predicted by the theory and measured in the experiment was large enough to account for performance differences between similar airplanes. It must be concluded, therefore, that more effort should be spent on dealing with this phenomenon. Some simple experiments should be performed to support the theory. More attention should be paid to the roughness elements on airplanes which originate near spoilers and near flap and aileron hinges.

REFERENCES

1. Carmichael, B. H.: What Price Performance? Soaring, vol. 18, no. 3, May - June 1954, pp. 6-10.

2. Ludwieg, H.; and Tillman, W.: Investigations of the Wall-Shearing Stress in Turbulent Boundary Layers. Ing.-Arch., vol. 17, no. 4, 1949, pp. 288-299.

3. Kader, B. A.; and Yaglom, A. M.: Similarity Treatment of Moving-Equilibrium Turbulent Boundary Layers in Adverse Pressure Gradients. J. Fluid Mech., vol. 89, part 2, Nov. 28, 1978, pp. 305-342.

4. Althaus, D.; and Eppler, R.: Airfoils With a New Hinge for Ailerons and Flaps. Motorless Flight Research, 1972. NASA CR-2315, 1973, pp. 205-217.

5. Althaus, D.: MeBergebnisse aus dem Laminarwindkanal des Instituts für Aerodynamik und Gasdynamik der Universität Stuttgart. Stuttgarter Profilkatalog I, Institut für Aerodynamik und Gasdynamik der Universität Stuttgart, 1972.

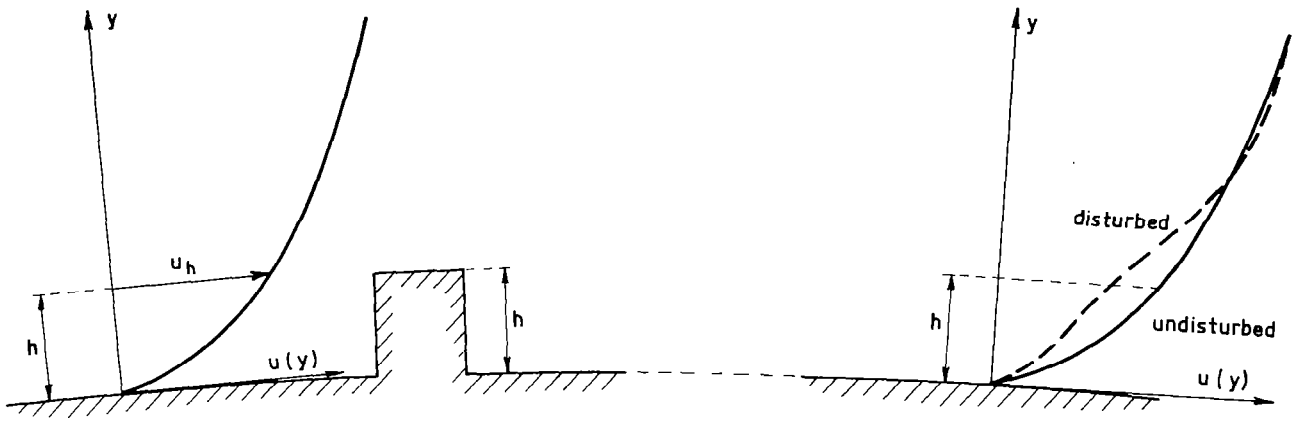

Figure 1.- Influence of disturbance on flow in boundary layer.

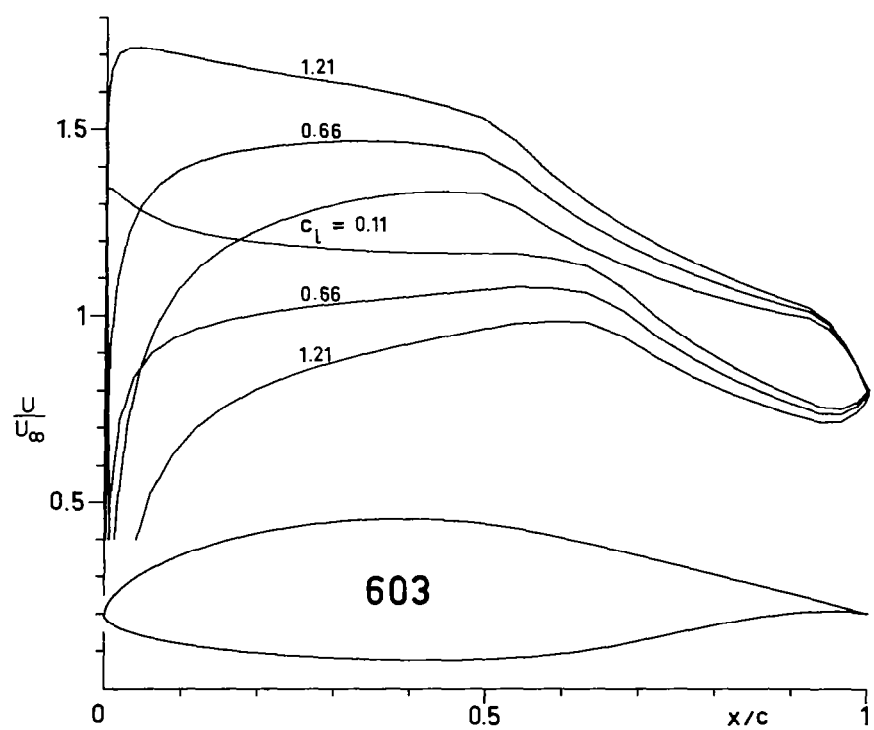

Figure 2.- Velocity distributions of airfoil E603.

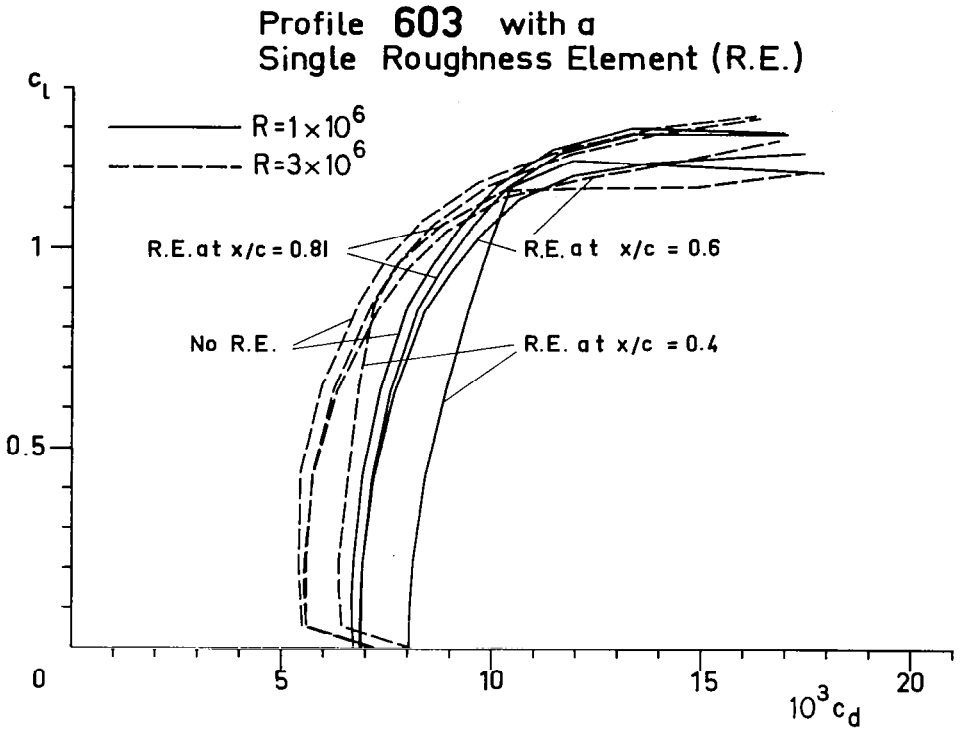

Figure 3.- Theoretical polars for airfoil E603.

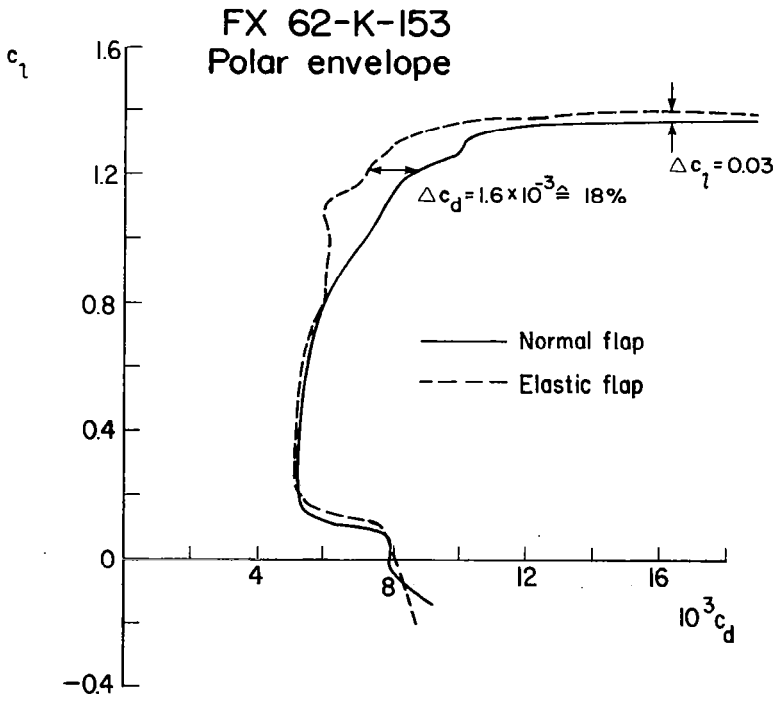

Figure 4.- Experimental envelope for FX 62-K-153/20 airfoil.

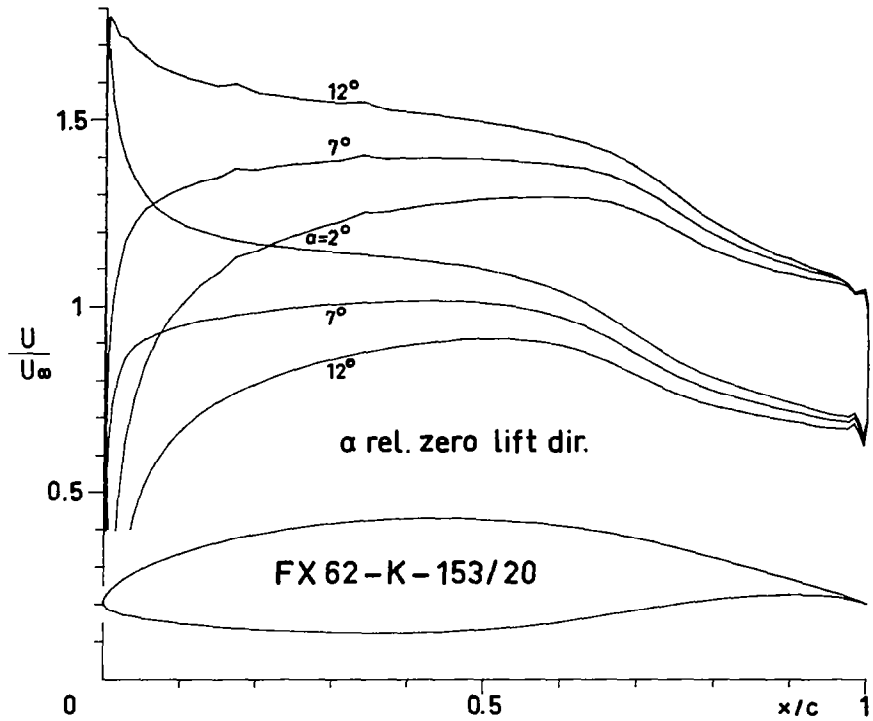

Figure 5.- Velocity distributions for FX 62-K-153/20 airfoil; original coordinates.

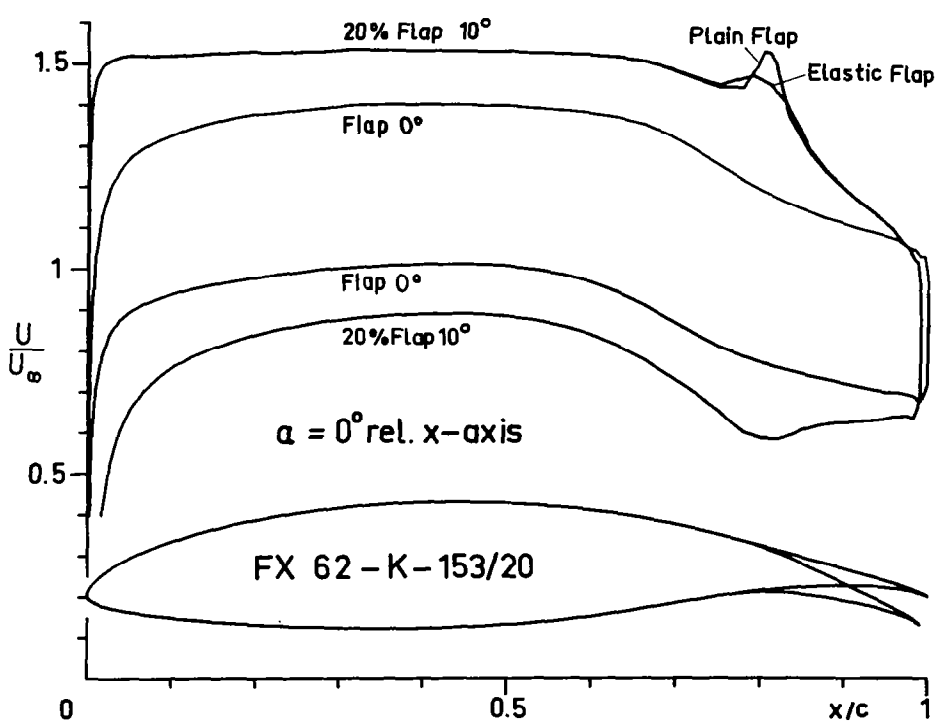

Figure 6.- Velocity distributions for FX 62-K-153/20 airfoil; smoothed coordinates.

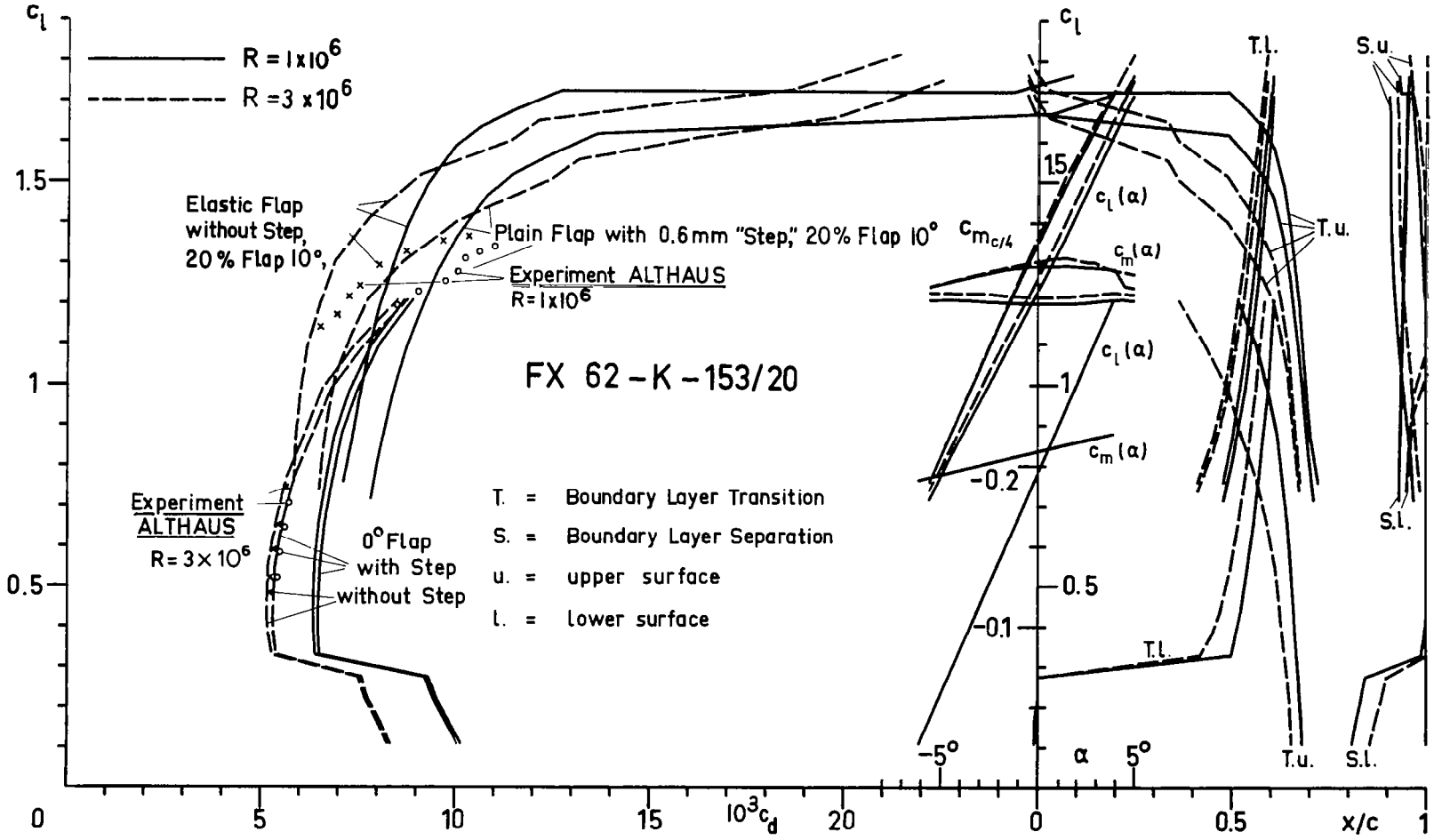

Figure 7.- Theoretical and experimental polars for FX 62-K-153/20 airfoil.

GENERATION AND BREAKDOWN OF AERODYNAMIC LIFT:

PHYSICAL MECHANISM

Wolfgang Liebe
Techn. University Berlin

INTRODUCTION

At high angles of attack the condition of attached flow is dependent upon the balance between forces on the leading edge and on the trailing edge of the wing. In the case of low-speed flight the wing operates at the upper limit imposed by this balance. In order to calculate and possibly influence this limit, a detailed understanding of the physical mechanism is required. We do know how to generate lift forces and we are able to calculate their magnitude as well as their distribution along the wing span. We do not know, however, the real physical mechanism of lift generation.

THOMSON'S THEOREM

The lift force is a result of circulation, i.e., a net flow around the airfoil. A differential pressure results with a corresponding force perpendicular to the main flow; this lift force is proportional to the airspeed and to the intensity of the circulatory flow. In order to discuss the problem of lift generation, attention has to be focussed on the circulation itself.

We learn from standard literature (refs. 1 and 2) the way circulation is produced: A layer of separation arising at the trailing edge coils up to a starting vortex. According to Thomson's theorem (ref. 3) the circulation along a closed flow path situated in a homogeneous inviscid fluid remains constant with time. Consequently the formation of the starting vortex requires the generation of an opposite circulatory flow. Since the total circulation is zero to begin with, the magnitude of the opposite circulatory flow is such as to compensate the starting vortex. Hence the starting vortex gives rise to a superimposed additional velocity of the fluid particles in the vicinity of the wing surface.

At this point one may have difficulties realizing the logical sequence of events. Of course there are no doubts about the validity of Thomson's theorem. The application of this theorem, however, does not explain the physical origin of additional forces acting on the fluid particles. Presently we need some kind of electrodynamic "far field effect" to explain this fluid dynamics problem.

FLOW AROUND THE TRAILING EDGE

The fluid particles pass the trailing edge with extremely high and localized velocities, especially during the early phase of the motion. Figure 1 illustrates the corresponding flow pattern and the resulting low pressure zone. Static pressure differences are produced in the vicinity of the trailing edge. As a result more and more of the flow close to the surface moves towards the low pressure region even against the main flow. The "depression zone" is filled up by spirally moving particles forming a vortex sink. With increasing vortex diameter the flow velocity around the trailing edge decreases. This in turn reduces the suction and the transport of material towards the sink will decay as shown in figure 2. Finally the vortex reaches a critical size which is characterized by zero suction and vanishing flow around the trailing edge. At this moment the vortex is free; it separates from the wing surface (fig. 3).

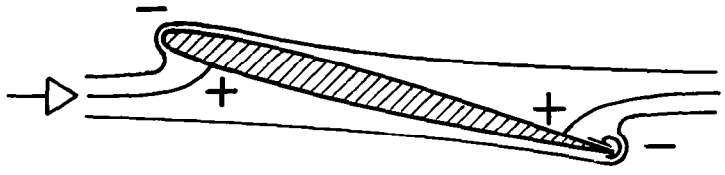

Figure 1.- Suction head at the trailing edge.

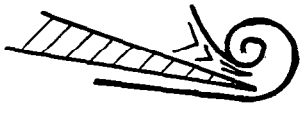

Figure 2.- Accumulation in a vortex sink.

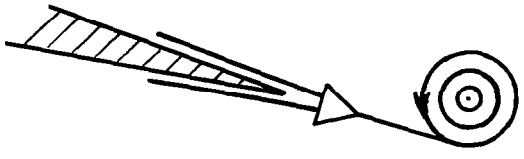

Figure 3.- Separation of vortex.

As soon as the starting vortex drifts away, the condition of attached flow is attained. Smooth flow is established all the way down to the trailing edge. A combined local suction and material transport mechanism has been able to initiate a circulation. "Far field effects" are no longer required.

VORTEX ROLL

Filling up the suction zone is characterized by the formation of a typical flow pattern which generates what may be called a vortex roll. The intermittent phenomena taking place at the wing surface can be simulated by a continuous source-sink mechanism as shown in figure 4.

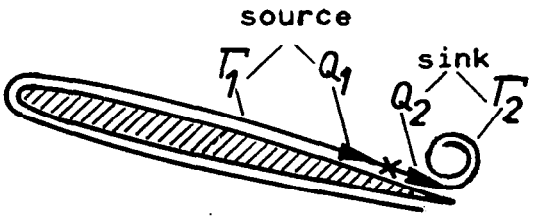

Figure 4.- Source-sink mechanism.

The mass flow $Q_1\rho$ discharging from the source equals the one $Q_2\rho$ entering the sink at any instant of time. Continuity of the incompressible flow requires (dots denote partial differentiation with respect to the time)

$$dQ_1 + dQ_2 = \dot{Q}_1\, dt + \dot{Q}_2\, dt = 0 \tag{1}$$

In addition to this the stimulated circulation Γ is directly proportional to the volume flow according to

$$dQ = -S\, d\Gamma \tag{2}$$

The quantity S represents the active span of the wing.

Combining equations (1) and (2) yields

$$d\Gamma_1 + d\Gamma_2 = \dot{\Gamma}_1\, dt + \dot{\Gamma}_2\, dt = 0 \tag{3}$$

which indicates that flow continuity and the proportionality (2) are reflecting the relevant physical phenomena at the wing; in particular, equation (3) satisfies Thomson's theorem at any instant of time.

Finally at a time T the formation of the vortex roll is terminated which is characterized by

$$\Gamma_{1_T} + \Gamma_{2_T} = 0 \tag{4}$$

Consequently a circulation around the wing has been built up, having the same magnitude but different orientation from the final vortex roll drifting away.

LIFT

The lift force at the wing can be directly calculated from the properties of the vortex roll. According to Kutta's theorem the fluid velocity V produces a lift force F at the active wing span S of

$$F = \Gamma\, \rho\, V\, S \tag{5}$$

Γ represents the steady state circulation around the airfoil, which according to equation (4) is replaced by $-\Gamma_{2_T}$. Following figure 5 the vortex-roll circulation Γ_{2_T} is

$$\Gamma_{2_T} = -\pi D W \tag{6}$$

where the quantity D represents the final diameter of the vortex roll and W is the local fluid velocity passing the trailing edge.

Therefore the lift force is

$$F = \pi D W \rho V S$$

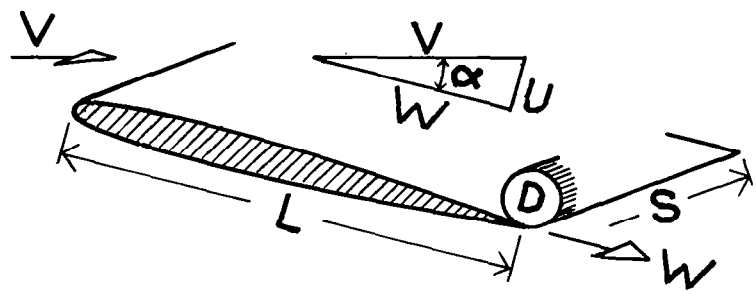

Figure 5.- Properties of wing and vortex roll.

Mechanical similarity requires a simple proportionality between geometry and velocity ratios as shown in figure 5:

$$(D/L) = m(U/W) = m \tan \alpha \tag{7}$$

Herein L is the wing chord and U is the transverse velocity component at the trailing edge according to the angle of attack α. The factor m is a dimensionless coefficient.

With the relations,

$$D = m L \tan \alpha$$

$$W = \cos \alpha V$$

it is possible to calculate the lift force

$$F = m \pi L \tan \alpha V \cos \alpha \rho V S = m \pi \sin \alpha \rho V^2 S L$$

or specializing for small angles of attack α (wing area $S L = A$),

$$F = 2 \pi m \alpha (\rho/2) V^2 A$$

For the lift coefficient C_A one obtains

$$C_A = \frac{F}{(\rho/2)V^2A} = 2\,\pi\,m\,\alpha \tag{8}$$

Experiments indicate that the dimensionless coefficient m is close to 1.0 so that the following approximation is justified:

$$C_A \approx 2\,\pi\,\alpha$$

THE TRAILING-EDGE MECHANISM

The condition of attached flow dominates just after separation of the starting vortex. This condition, however, is not stable since dissipation and other effects are disturbing the flow. Consequently, the fluid again passes the trailing edge causing suction, which is able to correct for the disturbance. This mechanism at the trailing edge continuously and effectively maintains the condition of attached flow. The sharper the edge is, the more effective the mechanism is.

At high angles of attack, however, a counteracting effect is initiated at the leading edge.

BREAKDOWN

Usually the leading edge is rounded; nevertheless similar processes take place as at the trailing edge. High fluid velocities are accompanied by strong suction. Local backflow is initiated in the boundary layer, but no vortex roll can be formed in the front. This is not due to rounding of the leading edge but to the fact that the front depression zone has no direct contact with a region of significantly higher static pressure which is able to fill a vortex roll. With increasing angle of attack there is an increasing static pressure gradient from the front to the back of the upper wing surface. But the boundary layer is able to resist a major backflow. So in spite of this pressure gradient, the front low pressure zone remains isolated.

As far as this isolation is concerned, there is a fundamental difference between the processes at the leading edge and those at the trailing edge. In the case of the back depression this zone is being rapidly filled from a very close reservoir, the high pressure stagnation zone. In the case of the front region the low pressure is continuously maintained since there is no high static pressure reservoir available which could form and fill a vortex roll.

At high angles of attack the pressure gradient along the upper surface rises considerably; this changes the situation drastically: The thickness of the boundary layer increases, giving rise to a backflow at the wing surface. This reverse wedge flow expands from the back and reaches the front depression

zone. At the moment of contact a rather violent inflow takes place towards the centre of the zone. A flow unbalance results since the depression zone takes in more material than the main flow is able to deliver. As a consequence the low pressure region is filled very fast, which in turn leads to a rapidly growing vortex roll. Finally the flow separates as indicated in figure 6.

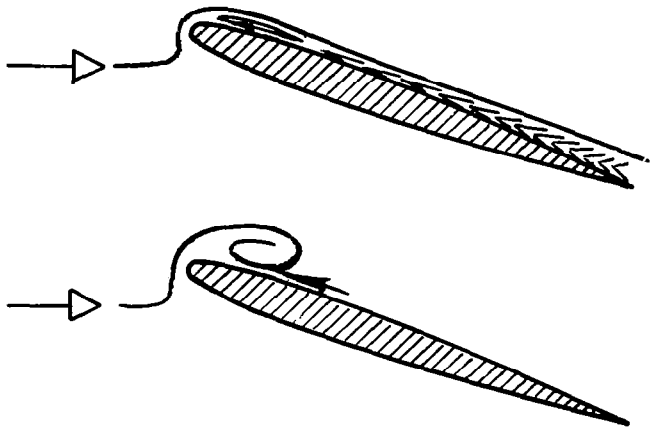

Figure 6.- Above: Expanding reverse flow.
Below: Contact - the flow separates.

These phenomena now correspond directly to what has previously been described as happening at the trailing edge, except for one important difference: There is a net flow around the airfoil which reduces the circulation and causes lift breakdown.

It has been shown that flow separation is not only initiated by static pressure rise and friction; a third condition has to be satisfied: The condition of contact between the low pressure zone with regimes at a higher static pressure.

COUNTERMEASURES

The range of steady lift generation could be extended if one were able to prevent contact of flow from the trailing edge with the front depression. One device for this purpose is shown in figure 7.

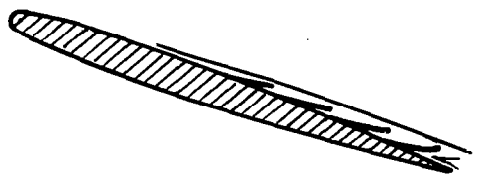

Figure 7.- Pockets at the upper surface.

Such "pockets" at the upper wing surface are well known from the wings of birds. At high angles of attack the backflow in the boundary layer causes these elastic elements to raise. This way the expansion of the backflow is effectively stopped; contact is prevented and lift breakdown is delayed.

The outlined principle is not yet in use in aeronautics, but it has proven successful in biotechnics (fig. 8). So far only one case is known where such a pocket-type device has been tested on a stalling airplane — with good results.

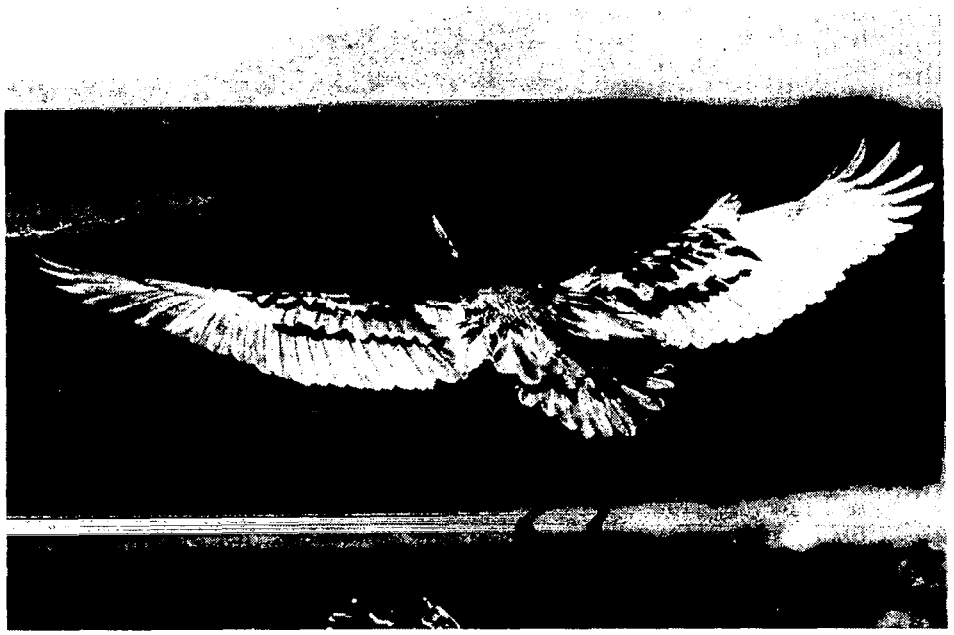

Figure 8.- Heron during approach for landing.
(G. Rueppell, Vogelflug, Kindler 1975)

Up to now only two-dimensional flow conditions were considered. In real situations lift breakdown mostly starts locally somewhere along the wing span. Localized lift breakdown, however, being limited to a short part of the span may lead to a three-dimensional flow. Now the low pressure zone in the vicinity of the local breakdown fills up from separated regions causing sideways inflow of material. At high angles of attack that sideways influx rapidly propagates to the wing tip. Like a chain reaction the lift collapses all of a sudden along the whole wing as shown in figure 9.

As a countermeasure an effective device has been suggested: The boundary layer fence. A simple shroud is mounted on the wing in order to protect the outer part of the wing against infiltration. Thin threads have been fastened to the wing surface to make the flow pattern visible during flight (fig. 9). The fence does prevent sideways contact and subsequent lift collapse.

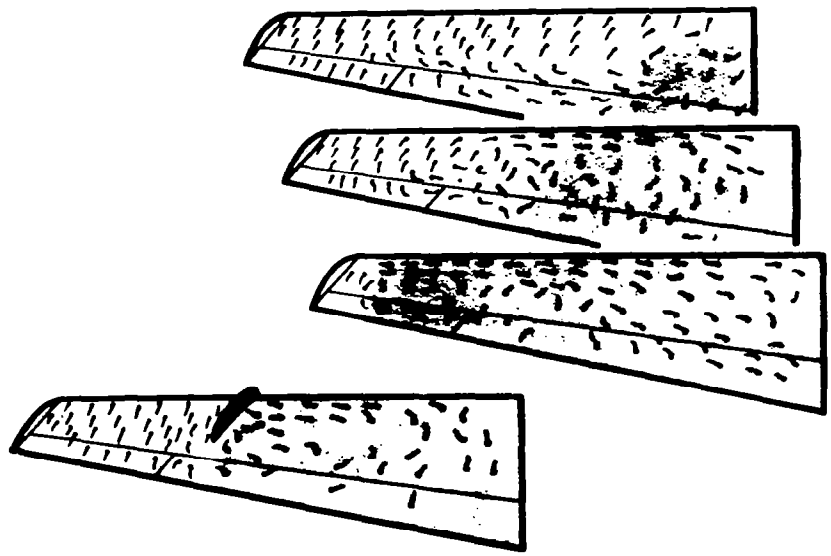

Figure 9.- Flow pattern on a stalling airplane. Right: Sideways influx rapidly propagating to the wing tip. Left: A fence protects the outer part against infiltration.

Quite frequently the boundary layer fence is used in conjunction with sweptback wings. Sweepback means shifted airfoils which is accompanied by sideways pressure gradients. Thus the low pressure zone is filled sooner from the adjacent side, causing not only reduced lift but also unfavorable pitching moments. These inherent effects can be prevented by fences.

WING FLAPPING

The outlined extremely high velocities around the trailing edge can be provoked by a transverse motion of this edge relative to the main flow, for example by moving a trailing edge periodically up and down. Corresponding vortex rolls are generated and material is absorbed from the boundary layer, thus reducing its thickness. The reverse wedge flow decreases and again lift breakdown is delayed.

The volume flow due to wing flapping can be calculated from the following relation:

$$Q_f = 2\ \pi^3\ k^2\ \rho_0^2\ n^3\ \frac{r^2 S\ L^2}{V^2} \tag{9}$$

where

Q_f volume flow due to flapping

k dimensionless coefficient

n flapping frequency

ρ_0 angular amplitude of flapping

r radius of moving edge

S span of active wing

L wing chord

V fluid velocity

The material taken out from the boundary layer is accelerated backwards by flapping, which as a reaction produces wing propulsion. The thrust attained in this manner is negligibly small in gases; in high density fluids it is possible to produce significant propulsive forces by this technique.

SUMMARY

A contribution has been given to an old problem: The explanation of the generation of aerodynamic lift. New physical models are described which provide a better understanding of the phenomena involved. The suggested viewpoint leads to new technological implications. The formation of both a starting vortex and a circulation can be conceived as the filling of a vortex sink at the trailing edge. Fluid is absorbed by the vortex, which causes it to expand to a vortex roll. The lift force can be calculated from the properties of the vortex roll.

Once the starting vortex drifts away, the condition of attached flow is attained. With increasing angle of attack this condition is disturbed by low pressure close to the leading edge. Finally this depression zone fills from the back of the wing, which induces a countercirculation and lift breakdown.

Filling requires the low pressure region to have contact with flow regimes of higher static pressure. Flow separation caused by filling of the vortex at the leading edge can be influenced by anti-contact devices such as pockets or fences.

A periodic flow can be superimposed around the wing by a forced oscillatory motion of the trailing edge. The periodic formation and separation of small vortex rolls reduce the drag or even produce propulsion.

REFERENCES

1. Prandtl, L.: Strömungslehre, Vieweg, 1965, pp. 46-47.
2. Tietjens, O.: Strömungslehre I, Springer, 1960, p. 496.
3. Thomson, W.: On Vortex Motion. Edinburgh, 1869.

INTRODUCTION TO THE ARCOPTER ARC WING AND THE BERTELSEN EFFECT FOR POSITIVE PITCH STABILITY AND CONTROL

William D. Bertelsen
Bertelsen, Inc.

SUMMARY

Studies in the realm of low-speed and motorless flight have traditionally produced the most creative approaches to the problem of flight. The problem is the same today as always, namely, the search for higher performance with complete safety. Towards that end a brief report is offered on a new wing design, new in geometry, construction, and flight characteristics. This report includes preliminary wind tunnel data on a three-dimensional model as well as some full-scale man-carrying test results. There are photos of all phases of the experiments and some figures which serve to illustrate the Bertelsen Effect, a unique focus of aerodynamic forces in the arc wing system which allows the attainment of high lift coefficients with the maintenance of pitch stability and control.

INTRODUCTION

The name "Arcopter" comes from a combination of the Latin word "arc" for segment of a circle with the Greek "pteron" for wing. The name thus embodies the basic geometric configuration of the device. In this case the arc refers not to any chordwise airfoil curvature but to a regular spanwise curvature describing an arc like a rainbow over the lateral pitching axis of the system. From antiquity the arch has been an element of structural design and it has come to be a symbol of strength and simplicity. This paper introduces the arc wing configuration as a novel aeronautical device which embodies certain valuable aerodynamic properties in a light-weight, self-constituted physical unit of inherent strength and simplicity.

ABBREVIATIONS AND SYMBOLS

Values are given in both SI and U.S. Customary Units. The measurements and calculations were made in U.S. Customary Units.

VTOL	vertical takeoff and landing
m.p.h.	miles per hour
R.P.M.	revolutions per minute
C.L.	center of lift
C.G.	center of gravity
a.c.	aerodynamic center
L	lift, kg (lbs.)
D	drag, kg (lbs.)
T	thrust, kg (lbs.)
W	weight, kg (lbs.)
α	angle of attack, degrees
x'	lift moment arm, m (ft.)
z	drag moment arm, m (ft.)
c	wing chord length, m (ft.)
V	velocity, m/sec (ft/sec)
C_L	coefficient of lift
C_D	coefficient of drag
C_{Mac}	moment coefficient about a.c.
C_{Mcg}	moment coefficient about C.G.

INVENTION OF THE ARC WING

The VTOL Design Problem

In the 1950's the National Advisory Committee for Aeronautics (NACA) recognized the usefulness of the helicopter because of its ability to operate from very small bases. The advantages to be gained with an airplane that incorporated both the small-field capabilities of the helicopter and the high-speed potential of conventional airplanes became readily apparent (ref. 1). One possible means of achieving these advantages was seen to be an engine/

propeller combination capable of providing static thrust in excess of gross weight. Lift for vertical takeoff could then be obtained by deflecting the propeller slipstream downward by means of large-chord wing flaps, retractable for high-speed cruising flight. Accordingly, an investigation of various wing/flap configurations was conducted in the 7- by 10-foot tunnels at the Langley Aeronautical Laboratory in an effort to develop relatively simple arrangements that could deflect propeller slipstreams downward for vertical takeoff. References 1, 2, and 3 present the characteristics of slotted, sliding, and plain flaps, respectively.

The slotted-flap configuration was effective in achieving a slipstream turning angle corresponding to a rotation of the effective thrust vector upward about 73°, with the ratio of resultant force to thrust varying from about 1.00 nearest the ground to about 0.86 out of the ground effect region. With this configuration it was concluded that vertical takeoff could be made with an initial attitude of 17° and at airplane weights up to 90 percent of the total propeller thrust.

Similar results were achieved with the plain flap configuration, but only after the installation of auxiliary vanes which greatly complicated the arrangement. The slotted-flap configuration, while seen as somewhat simpler, had the disadvantage of exhibiting rather large diving moments, caused partly by the fact that as the flaps extended they moved appreciably rearward and the effective axis of the redirected slipstream was relatively far behind the quarter-chord point of the wing. For the same turning angle the diving moments associated with the slotted-flap configurations were found to be approximately twice as large as the diving moments for the configurations with plain flaps and two auxiliary vanes. However, the process of retracting and storing the two auxiliary vanes necessary on the plain flap system was seen to present serious mechanical problems, nearly prohibitive to the design of a practical, high-speed VTOL aircraft.

Subsequent investigation of the Ryan VZ-3RY VTOL prototype (ref. 4) under the auspices of the new National Aeronautics and Space Administration in 1959 underscored the serious limitations of the conventional approach to the design of double-slotted flaps for VTOL applications. While the aircraft could take off vertically, longitudinal stability was said to be impossible to realize below 46 km/hr (29 m.p.h.) with the existing center of gravity location. Pitch control in hover and transition was difficult and critical even with a complicated jet-reaction control located in the tail.

In summary, the experiments established (1) that VTOL capabilities are possible with slipstream deflection by means of conventional, large-chord, double-slotted flap arrangements and (2) that, because of the large diving moments associated with extended

double-slotted flaps, a VTOL using such an arrangement may be longitudinally trimmed and controlled in either the hovering mode or the transitional mode but not in both, at least not by simple means. A VTOL aircraft should be stable and controllable in hover, transition, and high-speed cruise. Conventional tail surfaces are totally ineffective at zero forward speed and almost ineffective in transition. The NACA-NASA studies of the 1950's indicated that an unconventional approach would be required to meet the VTOL design challenge.

The Arcopter VTOL

The Arcopter wing system was the direct result of the efforts of Dr. William R. Bertelsen to develop a slotted flap configuration for deflecting a propeller slipstream through the large turning angles required for vertical takeoff without the deleterious diving moments or complexity which accompanied the NACA experiments. The cited NACA technical notes touch on the importance of the center of gravity location in analysis of VTOL wing and flap pitching characteristics.

In the Arcopter system it is proposed that if an aircraft extends single or multi-element flaps and/or slats for high lift or slipstream deflection, then those flaps should rotate, while extending, about an area in which the center of gravity lies, so that the summation of flap resultant forces converges at all times in the vicinity of the center of gravity. Each flap may be considered in such regard as an entity with its own force focus coinciding with the others near the center of gravity. The center of gravity is preferably below the center of lift of the airfoil combination in order to effect stability regardless of the attitude of the aircraft with respect to gravity. The concentration of wing forces, coupled with flap and wing slot augmentation, all converging about the center of gravity of the aircraft, thus comprises an engineering principle called the Bertelsen Effect.

Figure 1 shows how multi-element flaps might be arranged to take advantage of this principle in a VTOL of the deflected slipstream type. It can be seen that if flaps B and C retract and extend by pivoting on a radius centered at the C.L./C.G. focal point there will be little or no diving moment at any flap setting. The aircraft can therefore make the transition from hover to flaps-up cruise smoothly and predictably. Because of the focus of flap resultant force through the C.G. area, the system does not depend on propeller thrust to achieve longitudinal trim in any mode. Forces remain balanced at all power settings including power off, affording an extra measure of safety in controlling a power-off descent. The full lifting capability of the wing system can be utilized in all modes without the usual loss in effec-

tive lift coefficient owing to negative tail loads. The need for such negative loads is effectively eliminated in the Arcopter system.

Figure 1 diagrams the general arrangement of wing and flap elements around the center of gravity. It is left to specify the most practical physical form to be taken by an aircraft which is to employ the Bertelsen Effect. It has been established that multi-element slotted flaps of large chord can deflect a propeller slipstream through the large turning angles required for vertical takeoff (ref. 1). Reference 5 suggests the effectiveness of large end plates in augmenting flap efficiency as regards the ratio of resultant force to thrust, especially in ground effect. The Arcopter system proposes a synthesis of the wing and end plates into a spanwise, semicircular arc as being the most efficient configuration for confining and deflecting the slipstream of one large-diameter propeller or two dual-rotating propellers on a single thrust axis. At the same time the necessary rotational motion of arc-shape flap elements can be easily achieved, owing to the convenient coincidence of element pivot points on an axis across the diameter of the arc. This location and coincidence of wing element pivots substantially simplifies the mechanism for flap actuation.

Figures 2-6 are photos of the Arcopter VTOL flying model which was built to demonstrate the Arcopter design principle and the Bertelsen Effect. Figure 2 shows the arc wing and flap elements fully extended. Such arched structure is inherently strong while being light in weight. Because of the great tensional strength of the arch structure, there is no longer a design requirement for thickness in the structure of the main wing. Airfoils can be chosen without regard for structural considerations. The wing and flaps on the model are constructed of molded Plexiglas sheet. Aluminum tubes attached to the model are for handling and serve no aerodynamic function. Figure 3 shows the complete VTOL model in a three-quarter front view, flaps fully extended. Simple canard control vanes have been included in the slipstream to counteract propeller torque and provide positive three-axis control at all speeds including zero and reverse. It can be seen that any residual diving moment can be dealt with by increasing incidence on the horizontal canards in such a way as to contribute to the overall slipstream-turning and lift effectiveness of the system.

Figure 4 is a direct front view showing shortness of the wingspan. If a single thrust axis is to be used on an Arcopter VTOL, the wingspan should be somewhat less than the diameter of the prop or rotor. Short span saves weight and reduces drag in high-speed cruise. The tubular diametric spar visible in figure 4 is oversized for rough handling. Figure 5 shows a side view of the Arcopter VTOL in high-speed cruise configuration with flaps retracted. Thin flap segments easily nest in the main arc wing

after simple rotational motion, pivoting about the diametric axis through the wing tips at the point where the tightening nut attaches the handle. A glow plug engine drives the propeller via an extended shaft to help maintain proper C.G. location. Viewed from the top (fig. 6) the arc wing is seen to have an elliptical planform, and therefore a near-ideal lift distribution.

The Arcopter VTOL model was demonstrated (in and out of ground effect) in hover, in slow flight fore and aft, for control effectiveness, etc., in the 7- by 10-Foot Tunnel at Langley Aeronautical Laboratory on January 23, 1958. As a solution to the VTOL design problem, the Arcopter offers a simpler, safer alternative to the helicopter through implementation of the Bertelsen Effect. But the invention of the arc wing as an element in itself, an arch-tension structure with centralized force focus, offers possible solutions to a variety of aeronautical design problems, especially those where lightness of weight and structural simplicity are prime considerations.

THE ULTRA-LIGHT ARCOPTER WING

As indicated previously, the arc wing may be considered in multi-element combinations, as in the VTOL discussion, or each element may be considered separately as an entity with its own centralized force focus. Figure 7 represents the Bertelsen Effect as it applies to a single-element arc wing. It shows how lift force acts in a direction perpendicular to imaginary lines tangent to each point along the semicircular arc wing span. The magnitude of a local lift force through the point of tangency is proportional to the local wing chord length and angle of attack. On an arc wing with an elliptical planform, the greatest lift will develop near the crown of the arch where the wing chord length is greatest. The vector L represents the relative magnitude and direction of lift force acting on this point with respect to the lift forces which act simultaneously on every other point along the span. Because the arc wing is a semicircle as viewed from the front, it becomes clear that all lift forces, regardless of magnitude, aim through a common point at the geometric center of the arc. This point is the true center of lift in the Arcopter system.

On the right in figure 7 is a side view of the arc wing focus. This side view shows how lift and drag forces interact at each local section center of pressure to focus a resultant force directly through the geometric center of the wing arc. If the aircraft C.G. is also located near this point, the vector sum of the forces is zero, and there is no pitching moment about the C.G. The longer broken lines denote the outline of the arc wing leading and trailing edges as seen from the side. Vector R' has the same magnitude and direction as the resultant R and acts through

the same point. R' is simply a restatement of the resultant R for convenience in graphically adding R to the weight W and thrust T.

Structure of the Ultra-Light Arc Wing

It was decided to design and build a single-element arc wing to analyze its aerodynamic properties, including lift, drag, and static pitch stability. The basic simplicity and tension strength of the arc geometry implied that an ultra-light structure could be devised which could support a very large wing area. Intuitively, the semicircular shape is suited for confining high pressure air underneath the wing surface by effectively restricting spanwise flow. If the wing were properly designed, the lift force created by the free stream should stretch a single- or double-surface fabric membrane into an efficient airfoil curve without the necessity for any rib structure whatsoever, at a great saving of weight, cost, and complexity.

The ultra-light, adjustable-camber arc wing evolved during numerous experiments with models, kites, wind tunnel tests, full-scale force tests, and finally, man-carrying, powered, free-flight tests. The wing is essentially a fabric tension structure utilizing the dynamic force of the air to stretch the wing fabric on the bias, thus maintaining a single-surface airfoil curve. (See figure 8.) An aluminum tube forms the basic arch inside the fabric cuff at the wing's leading edge. This aluminum (or fiber glass) arch is anchored in sockets at opposite ends of a rigid tubular spar. This arch and spar assembly forms a "D" shape unit which has proven extremely rugged and damage resistant on test craft of every size. The sail is patterned after the elliptical planform of the Arcopter VTOL flap elements, with maximum chord length at the crown of the arch.

Maximum chord length was specified arbitrarily to be one-third the length of the wingspan for all size test aircraft, fixing the aspect ratio at about 3.9 to 1. The wing fabric itself is non-porous urethane-coated nylon weighing 88 g/m^2 (2.6 oz/yd^2). There is no continuous rigid structure shaping the wing sail except for the arch tube in the leading edge. At zero airspeed the fabric droops limply from the arch. The only other members required for proper shape in flight are a number of rigid tubes or sticks which extend between the leading and trailing edges of the wing at various stations on the span. The length of each of these chordwise members is adjustable, making it possible to change airfoil camber between flights. Shortening the tube increases the camber. The tubes are all double hinged at their leading-edge point of attachment to allow the sail to hang down at zero forward speed. Nylon webbing straps are sewn to the leading and trailing edge of each wing tip to transfer flight loads to the spar. The trailing edge webbing straps also serve an important pitch control

function to be discussed later.

The preceding description of the ultra-light arc wing structure is brief but complete. It is a supremely simple structure with few parts, but its arc configuration and adjustable-camber surface enable it to develop respectable lift coefficients. At flying speed all waviness and wrinkles disappear as the fabric stretches to its cambered airfoil contour without the use of ribs or battens. The natural load distribution of the arc configuration seems to prevent fluttering of the trailing edge without the need for battens. Also contributing to efficiency is the elimination of the usual fuselage junction losses which disturb most wing mid-sections. The device shown in figure 8 can be built to almost any size without complicating the design. The arc wing photographed in figures 8-10 has a wingspan of 3 m (10 ft.). This unit was used extensively to develop structural design and fabrication techniques, as well as to study pitch stability and control in tethered flight.

Pitch Stability and Control

As apparent in figures 8-10 the Arcopter wing has inherent positive static pitch stability in flight without the addition of auxiliary stabilizing surfaces which most aircraft require. This stability is largely independent of airfoil section characteristics. Any airfoil section can be employed on an arc wing according to performance requirements. Moreover, the angle of attack at which the wing stabilizes can be completely controlled by varying the tension in the trailing edge of the wing. This is easily accomplished by tightening or loosening the nylon webbing strap which anchors the wing fabric to the spar at the trailing edge.

Figure 11 shows the full-size Arcopter wing built to carry a man. Wingspan of this unit is 7.3 m (24 ft.). Clearly visible at the wingtip trailing edge is a steel cable attached to the nylon anchor strap. When the cable is connected to a trim tab crank or control stick, the pilot can control the wing's pitch attitude in flight. Pulling on the cable causes the wing to stabilize at a higher angle of attack. Releasing tension causes the wing to pitch down to a more shallow angle of attack. Recovery from a completely luffed condition resulting from negative angles of attack can be made at once by pulling on the cable. Continuing to draw the trailing edge down results in stabilization at extremely high angles of attack, upwards of 40°. Experience has shown that at high angles of attack the arc wing behaves like a parachute and cannot be stalled in the normal sense. Releasing some tension on the trailing edge produces immediate wing response, restabilizing it at some lower angle of attack. Total cable travel required for the whole flight range is only about 15 cm (6 in.).

Center of Gravity Location

As in the case of the Arcopter VTOL, the pitch stability and control behavior of the ultra-light arc wing is primarily related to the location of the center of gravity with respect to the vector sum of all aerodynamic forces acting on the wing. Figure 12 is a representation of wing and low C.G. location which is somewhat like the arc wing situation. Values can be assigned to the lift moment arm x' and the drag moment arm z for each angle of attack to be considered. The value of x' is taken to be negative when the C.G. lies ahead of the aerodynamic center (a.c.). The value of z is taken to be positive when the C.G. is below the a.c. The formula in figure 12 is developed in reference 6 to express the pitching moment about the C.G. when the C.G. location and relative forces are known. Positive values of C_{Mcg} indicate tendency to pitch up and negative values indicate tendency to pitch down.

Using the formula, a family of curves of C_{Mcg} versus angle of attack can be developed to predict the basic pitch stability characteristics of a conventional wing with a C.G. located 1.5 chord lengths below the section a.c. Figure 13 is such a plot using coefficient values of an NACA 23012 wing of aspect ratio 6. The angle of attack corresponding to a pitching moment of zero is called the "trim point". The slope of the curve at the trim point is an indication of the static pitch stability of the system; the more negative the slope, the more statically stable the wing. Aft movement of the C.G. results in a trend toward increased stability at higher angles of attack.

Figure 13 is a hypothetical case not meant to represent the exact behavior of an arc wing, but it does indicate the large influence C.G. location has on static pitch stability. Minor adjustments in C.G. location might be made accordingly which would enable an arc wing to use any airfoil section and yet retain a zero pitching moment about the C.G. at the design lift coefficient. When the C.G. is fixed, minor shifts in the focal position of the force vectors (from changes in trailing edge tension) give total pitch control on the ultra-light arc wing.

Preliminary Wind Tunnel Tests

Through the cooperation of the late Dr. H.S. Stillwell, then head of the University of Illinois Department of Aeronautical and Astronautical Engineering, a brief series of tests were conducted on a single-element arc wing of ultra-light construction in the university's 1.5-m by 1.5-m (5 ft. by 5 ft.) low-speed wind tunnel in 1973 and 1975. The 1975 data is included in figures 14 and 15. Figure 16 shows the model installed inverted in the test facility. Wingspan was 1.2 m (4 ft.). The model was of the same construction in all respects as described previously, including the wing

fabric of non-porous urethane nylon, sewn to allow some bias stretch.

Several problems combined to interfere with the accuracy of the test results. In the first place, the model was perhaps too large for the tunnel. Secondly, the smooth airfoil camber which characterizes all the larger arc wings failed to develop on the small wind tunnel model. Thirdly, during the course of the testing, the tunnel screens were discovered to be dirty, thus creating extra turbulence. The screens were removed for the tests labeled "MAX" and MED" camber in figures 14 and 15. This raised the tunnel Reynolds number based on mean geometric chord from about 0.24×10^6 to 0.32×10^6. Nevertheless data was taken and tabulated for values of C_L, C_D, and C_{Mcg} for three varying degrees of airfoil camber, the extremes of which can be seen in figures 17 and 18. Because of inability of the fabric to stretch naturally into airfoil camber on the small model, it had to be induced by bending the three most central chordwise tubes.

The lift and drag measurements indicated disappointing performance by the model compared with expectations based on experience with the large arc wings in the field. However the maximum value of C_L did show increase with increasing camber as might be expected. One interesting result was that the wing never reached the stalling point in any of the tests. Limitations of tunnel balance apparatus precluded investigation of very high angles of attack, but it can be seen in figure 14 that the wing with maximum camber did not stall even after a 29° increase in attack angle, beginning at C_L of about 0.23.

The pitching moment data (fig. 15) taken about the horizontal spar shows a negative slope, indicating a degree of positive static pitch stability, in all three tests. Increasing airfoil camber appears to produce greater positive (nose-up) values of the C.G. moment coefficient at low angles of attack. Positive moments remain near the maximum even in the vicinity of the zero-lift angle. Unfortunately, angles of attack below the zero-lift angle were not investigated. The pitching moment data implies that the arc wing will retain a measure of positive static stability about the C.G. no matter what airfoil curvature is employed. Increased camber seems to have a favorable effect on static stability.

Piloted Tests of the Full-Scale Arc Wing

By 1976 the 7.3 m (24 ft.) span Arcopter wing was ready for limited flight testing with a pilot aboard. The wing itself, as shown previously in figure 11, of projected area 13.9 m^2 (150 ft^2), was fitted to a heavy-duty tricycle landing gear for auto towing.

In addition, a unique annular rudder-elevator provided yaw control and contributed to pitch control (fig. 19). Like the wing, the "ring tail" is a light-weight tension structure with a circular rigid hoop inside the fabric cuff at the leading edge. In the same manner as the wing, the tail design provides a maximum of effective area with a minimum of structure.

The auto-tow tests of the Arcopter "sailplane" were very limited, intended only to gauge the minimum flying speed at gross weight. On one such experiment observed by Dr. Stillwell, the wing lifted a total of 170 kg (375 lbs.) at 10.7 m/sec (24 m.p.h.). No drag measurements could be made, but the low-speed lifting potential of the full-scale wing was substantiated. Some pilotless tethered flying was also conducted in moderate wind of 8.9 m/sec (20 m.p.h.), as shown in figure 20. Empty weight was 107 kg (235 lbs.). These tethered flights indicated the wing to be so stable in pitch at moderate to high angles of attack that the ring tail could not effect any visible change in pitch attitude. Subsequently all pitch control was accomplished by regulating trailing edge tension according to the method described earlier.

In an attempt to come as close as possible to full-scale flight conditions for the purpose of measuring drag on the Arcopter sailplane, a trailerized mobile force balance was constructed in 1977. The complete airframe, including pilot, was mounted on an articulated steel pylon via a ball-and-socket joint at the aircraft C.G. (figs. 21, 22). The airframe was thus free to pivot about three axes, making it possible to check out control systems as well as to monitor and record airspeed and drag values from calibrated pressure gauges connected to small hydraulic cylinders. Cylinder pressure, being a function of the total drag, was continuously recorded on movie film, as was airspeed from a boom-mounted pitot tube. It was also intended to measure lift with the trailer apparatus but the lift balance failed to function in the predicted manner.

Good drag data was obtained by towing the rig on smooth blacktop. The aircraft was set to stabilize at an angle of attack of 13-15° so a plot could be made of drag versus airspeed. Two days of testing produced the data presented in figure 23. On a number of test runs the arc wing itself was removed from the rest of the airframe in order to measure and compare drag on pilot and supporting structure alone. The resulting figures could then be subtracted from the total drag to gain a more meaningful idea of the drag on the wing as a separate entity. The drag figures obtained on the Arcopter sailplane were low enough to suggest that a very small engine would be sufficient to propel the aircraft and pilot in flight, without necessitating an increase in wingspan.

Besides facilitating drag measurement, the mobile force balance made it possible to safely observe the behavior of the 7.3 m

arc wing at speed. The ball-and-socket coupling at the C.G. allowed the entire aircraft adequate freedom to pitch, roll, and yaw. Test runs were made with and without the ring tail at various speeds in an attempt to ascertain general handling qualities and control responses. The following conclusions were drawn concerning stability: 1. Without the ring tail, the arc wing has only neutral static yaw stability. 2. The arc wing has positive static pitch stability over a wide angle of attack range, with or without the ring tail. 3. The arc wing is neutral in roll stability, but gets increasingly positive as the C.G. is lowered below the center of lift focus. There is no damping in roll. To effect roll control, the arch structure was hinged on wingtip "toggles" to enable the pilot to shift the entire wing and center of lift to the right and left relative to the C.G., but response was sluggish and inconsistent. Pilot weight shift did produce a slow but sure response without adverse yaw.

The Powered Ultra-Light Arcopter B-1A

The experiments conducted with the Arcopter sailplane were important, but certainly not exhaustive. The relative merits of the differing degrees of camber available in the adjustable-camber wing were not explored. But it was proven that the 7.3-m arc wing can carry significant pay loads at low speed. Some evidence was obtained also that power requirements for takeoff are low even with a fairly short wingspan. Piloted flights, powered by a small engine, now more certainly establish the efficiency of the ultra-light arc wing as a lifting device.

The powered Arcopter B-1A was built using the same size wing and tail surface but with a simpler structure supporting the pilot in a prone position on a steel cable anchored at the wingtips. While being lighter and more streamlined, this design has the added advantage of being collapsible for car-top transport. Before installation of the power system and landing gear, the new airframe made piloted tethered flights as a foot-launched hang glider (fig. 24). Empty weight of this configuration, including pilot harness and ring tail, is only 39.9 kg (88 lbs.). Flights out of ground effect were made with a wind of 8.9 m/sec (20 m.p.h.) sustaining a gross weight of 104 kg (230 lbs.), indicating a lift coefficient of 1.5. Angle of attack at the maximum chord station was 13° with respect to the horizon as measured from other photos. The attainment of lift coefficients near 2.0 seems a reasonable possibility, given a modest increase in angle of attack.

The Arcopter B-1A (figs. 25-28) has now made successful short flights, out of ground effect, under its own power with a pilot aboard. Gross weight was 147 kg (325 lbs.). The nucleus of the power system is a small 2-cycle engine of 134 cm^3 (8.2 in^3) dis-

placement which drives two opposite-rotating pusher propellers, each 1.07 m (42 in.) in diameter (fig. 27). A maximum of 45 kg (100 lbs.) static thrust is available at 6500 engine shaft R.P.M. for takeoff and climb. Minimum takeoff airspeed is about 10 m/sec (22.3 m.p.h.).

Future Experiments

Flight testing of the Arcopter B-1A has only just begun, and experiments will continue. More investigation is warranted because the first flights of the B-1A show that the Arcopter wing configuration offers a maximum of performance from a minimum of structure, with possible aeronautical utility ranging from ultralight sport flying to high-speed VTOL transportation.

REFERENCES

1. Kuhn, Richard E.; and Draper, John W.: Investigation of Effectiveness of Large-Chord Slotted Flaps in Deflecting Propeller Slipstreams Downward for Vertical Take-Off and Low-Speed Flight. NACA TN 3364, 1955.

2. Kuhn, Richard E.; and Spreeman, Kenneth P.: Preliminary Investigation of the Effectiveness of a Sliding Flap in Deflecting a Propeller Slipstream Downward for Vertical Take-Off. NACA TN 3693, 1956.

3. Kuhn, Richard E.; and Draper, John W.: An Investigation of a Wing-Propeller Configuration Employing Large-Chord Plain Flaps and Large-Diameter Propellers for Low-Speed Flight and Vertical Take-Off. NACA TN 3307, 1954.

4. James, Harry A.; Wingrove, Rodney C.; Holzhauser, Curt A.; and Drinkwater, Fred J. III: Wind-Tunnel and Piloted Flight Simulator Investigation of a Deflected-Slipstream VTOL Airplane, the Ryan VZ-3RY. NASA TN D-89, 1959.

5. Kuhn, Richard E.: Investigation of Effectiveness of a Wing Equipped With a 50-Percent-Chord Sliding Flap, a 30-Percent-Chord Slotted Flap, and a 30-Percent-Chord Slat in Deflecting Propeller Slipstreams Downward for Vertical Take-Off. NACA TN 3919, 1957.

6. Dommasch, Daniel O.; Sherby, Sydney S.; and Connolly, Thomas F.: Airplane Aerodynamics. New York: Pitman Publishing Corporation. Third Edition, 1961.

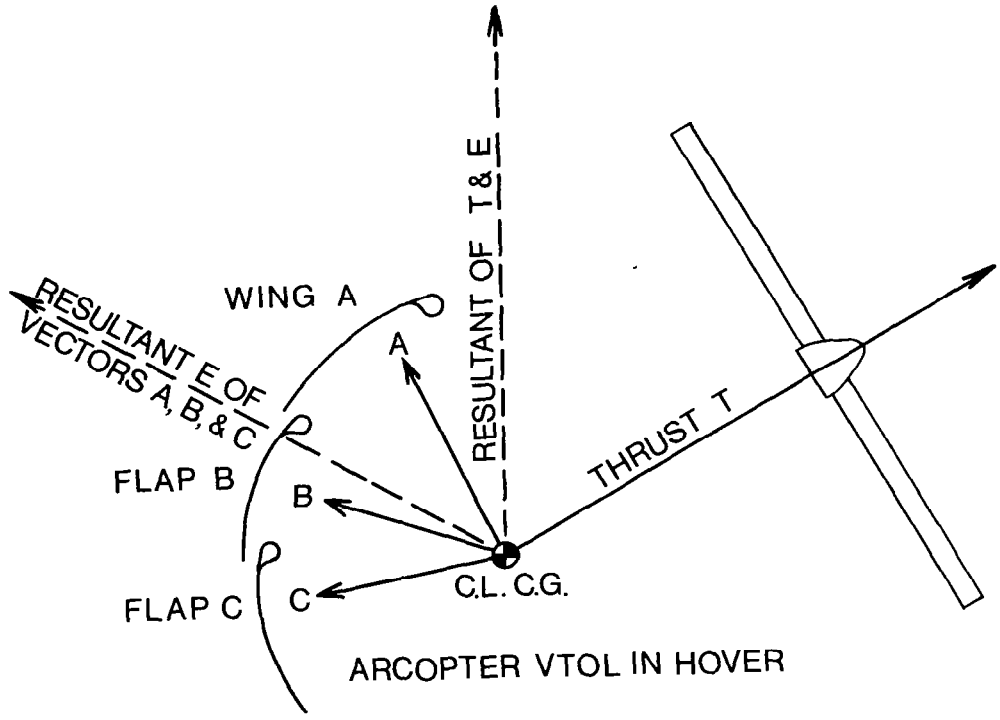

Figure 1.- The Bertelsen Effect, multi-element focus.

Figure 2.- Arcopter VTOL model, flaps fully extended.

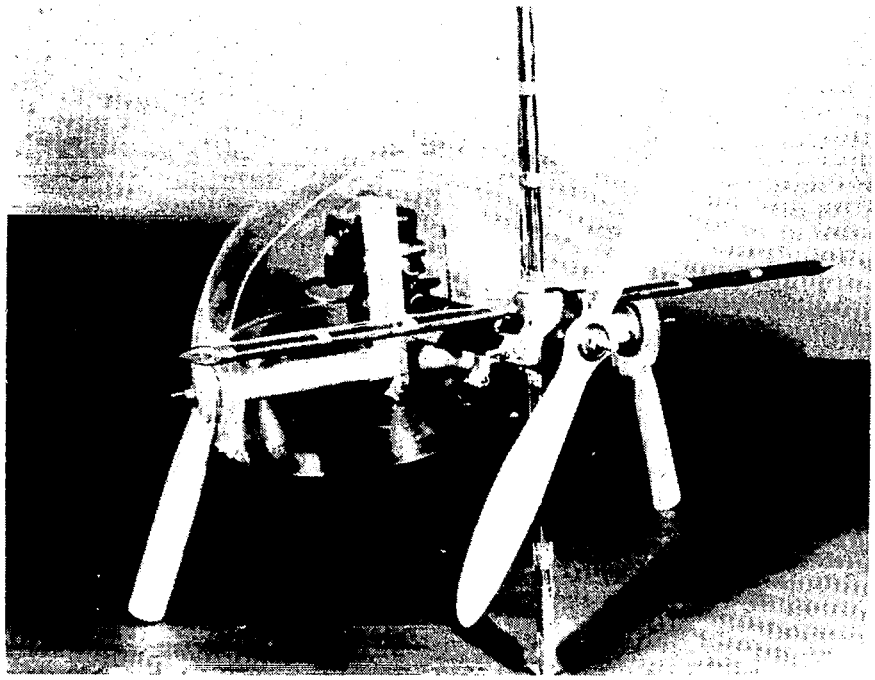

Figure 3.- Arcopter VTOL model, with canard control vanes.

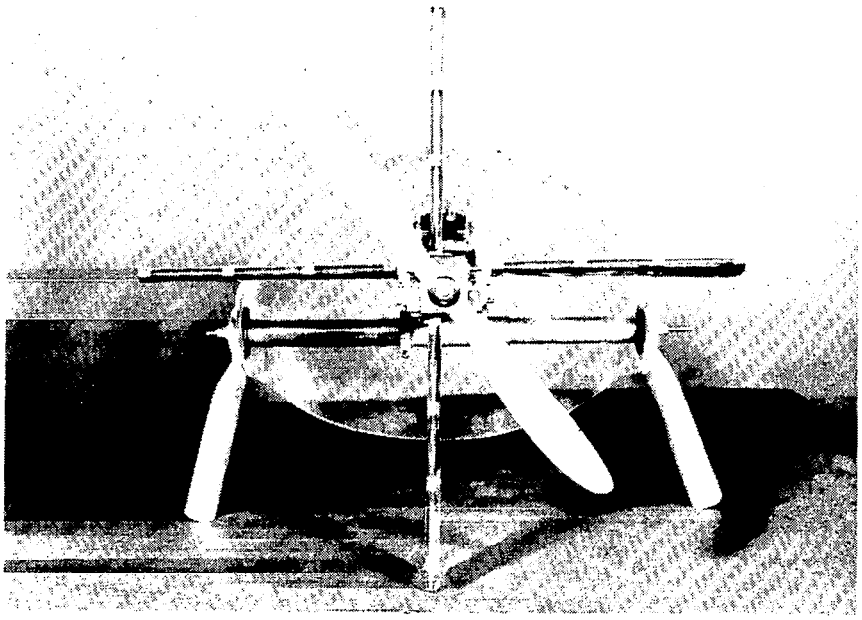

Figure 4.- Arcopter VTOL model (front view).

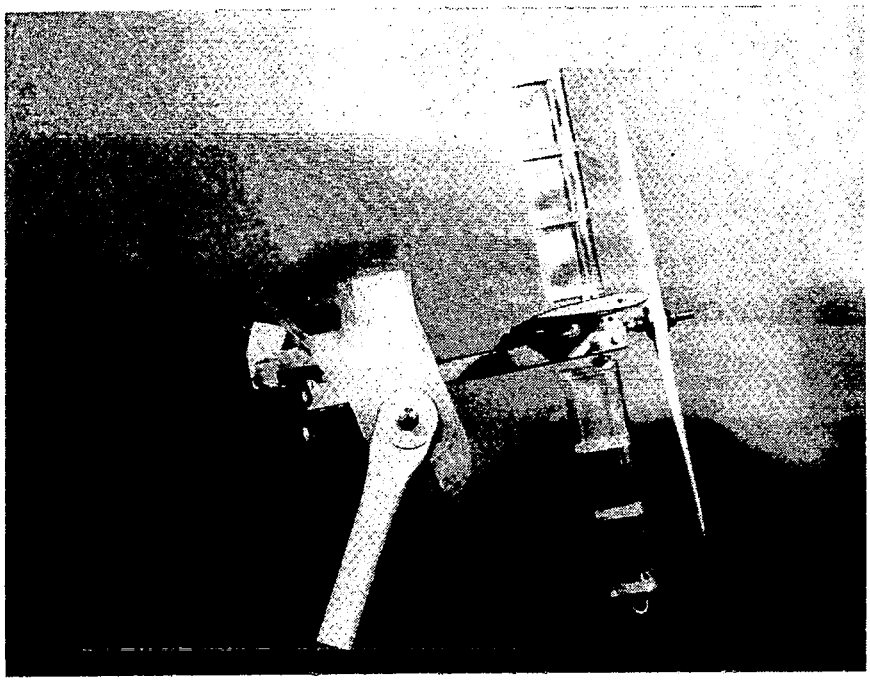

Figure 5.- Arcopter VTOL model, flaps retracted for cruise.

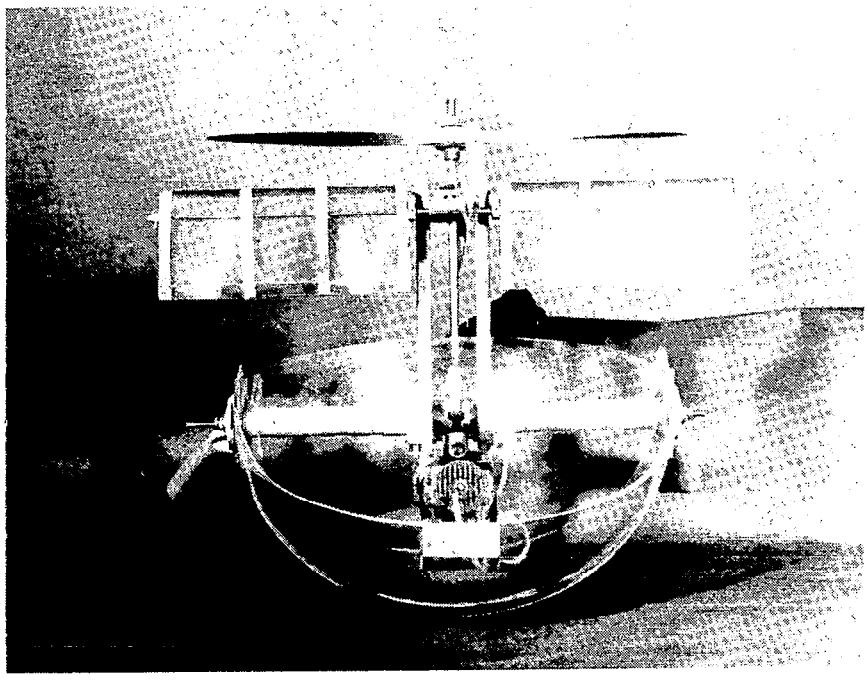

Figure 6.- Arcopter VTOL model, elliptical planform wing (top view).

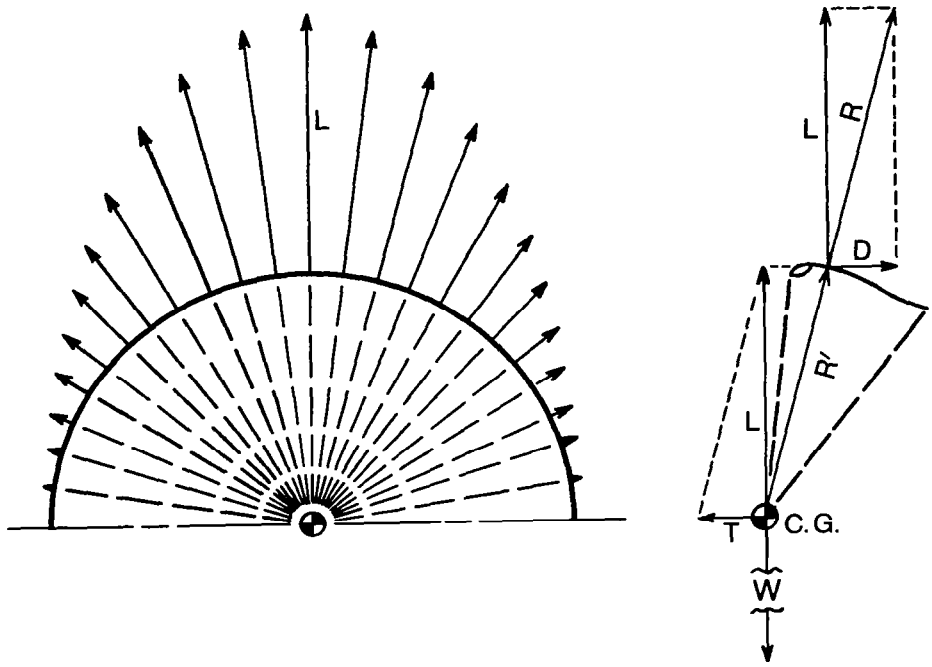

Figure 7.- Arc wing forces, single-element focus.

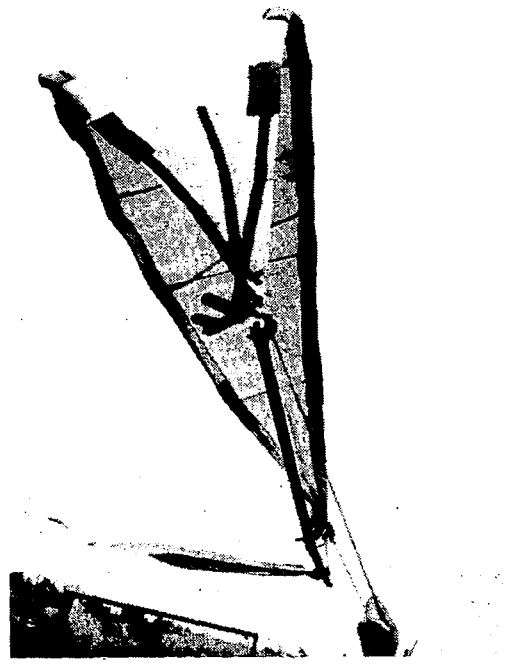

Figure 8.- Ultra-light arc wing,
3-m (10 ft.) wingspan.

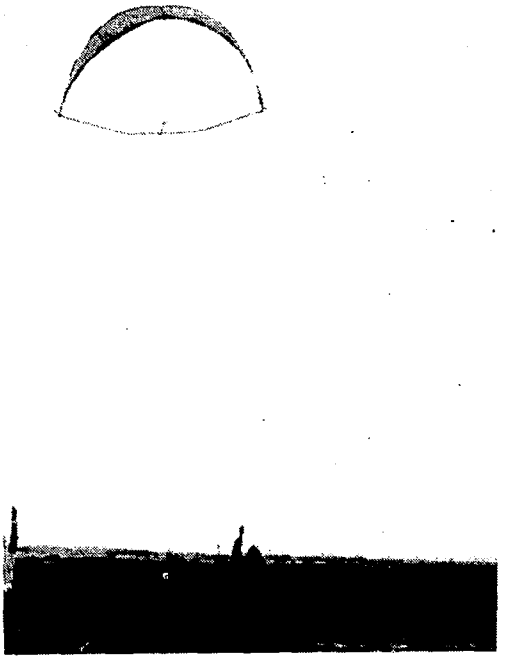

Figure 9.- 3-m arc wing, pitch-stable flight.

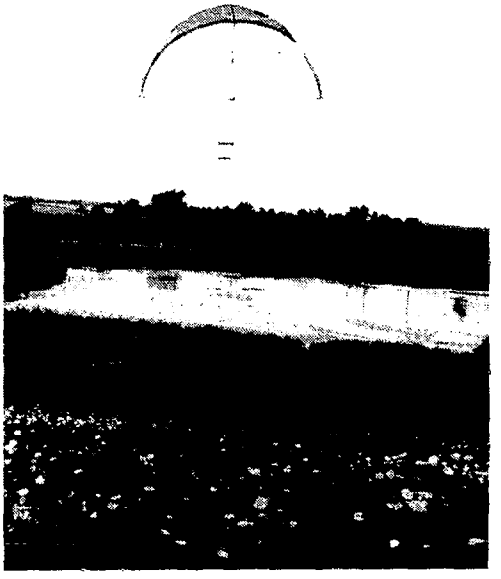

Figure 10.- 3-m arc wing, tethered flight with payload.

Figure 11.- 7.3-m (24 ft.) arc wing, pitch control detail.

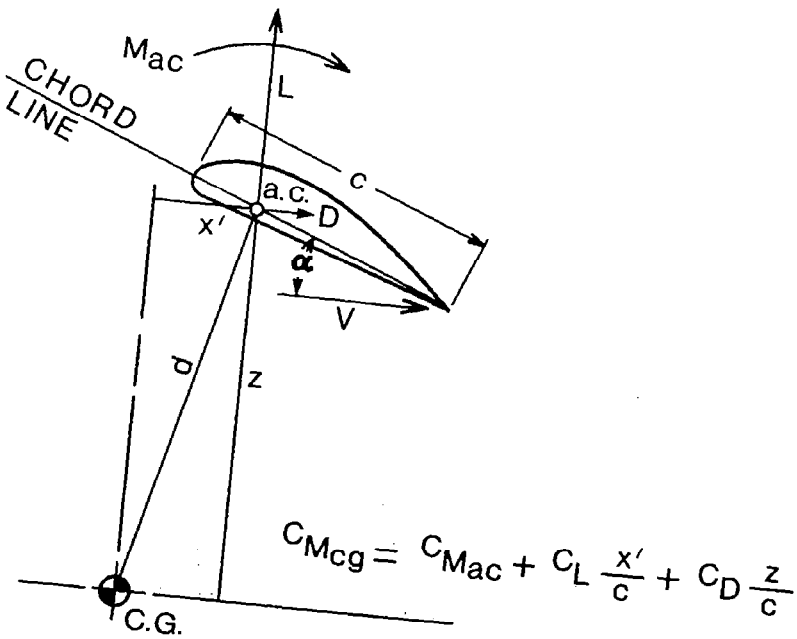

Figure 12.- Moment relation of wing and low C.G.

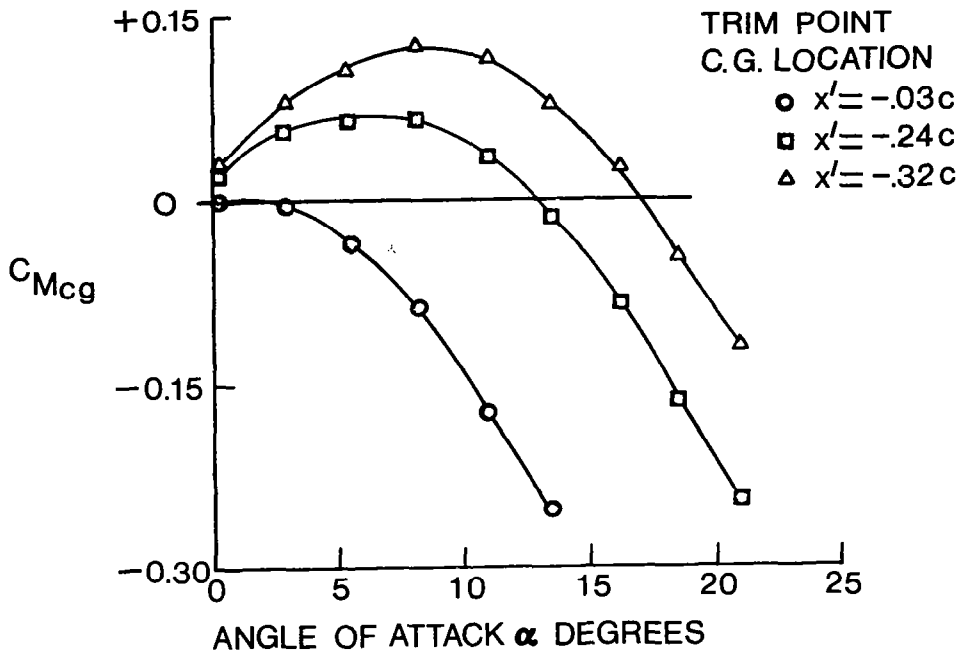

Figure 13.- Pitching moment of wing with low C.G.

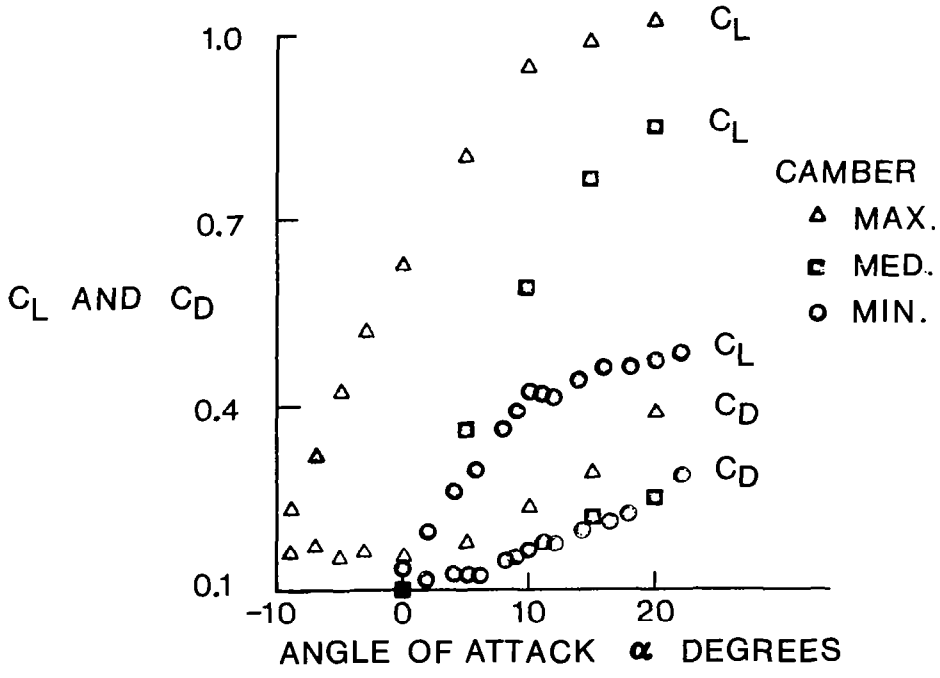

Figure 14.- Arc wing lift and drag (wind tunnel data).

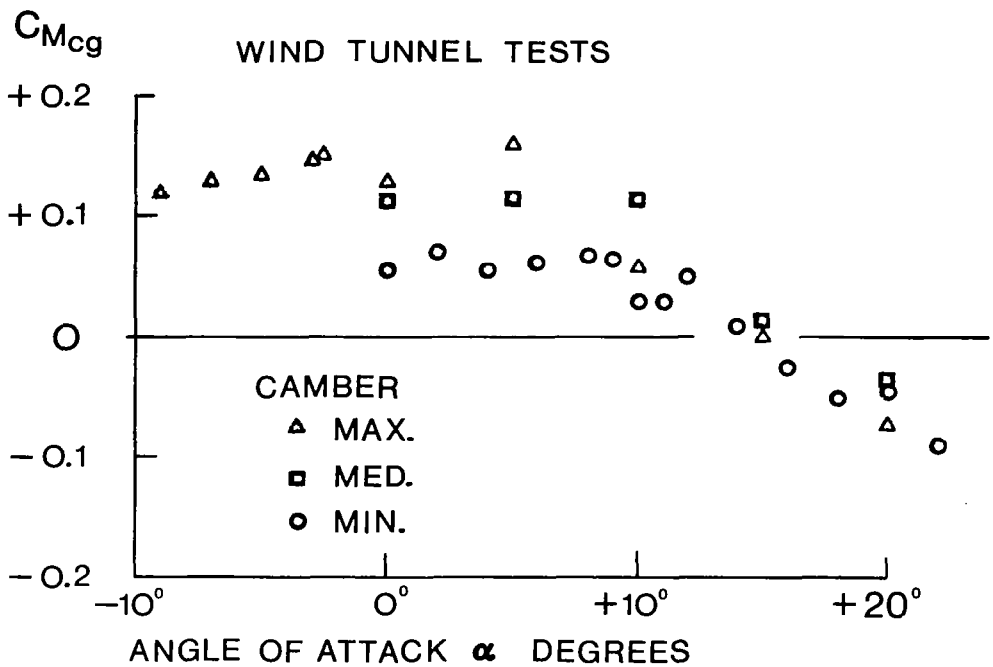

Figure 15.- Arc wing pitching moment (wind tunnel data).

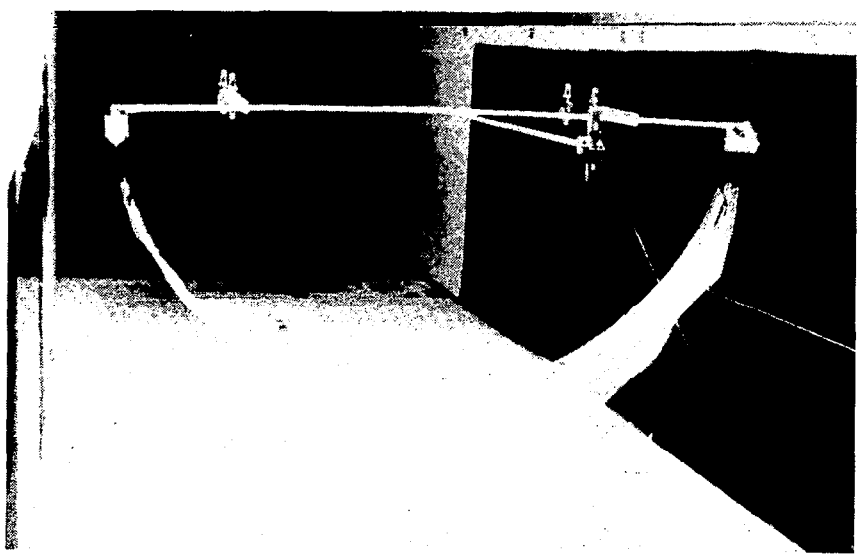

Figure 16.- 1.2-m (4 ft.) arc wing in wind tunnel.

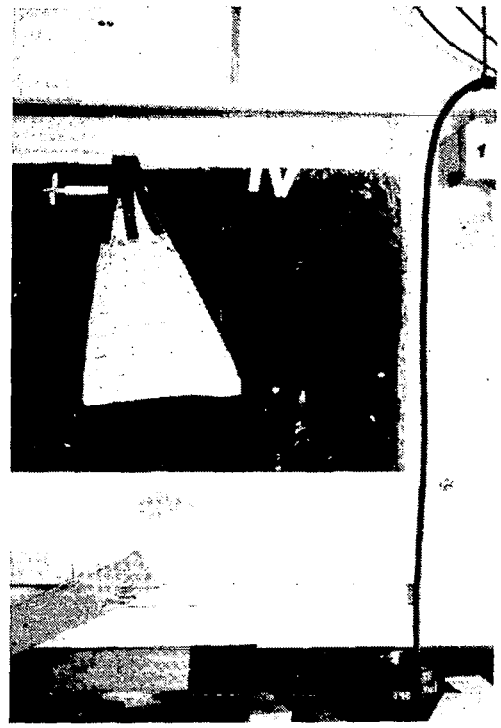

Figure 17.- Wind tunnel test, minimum camber.

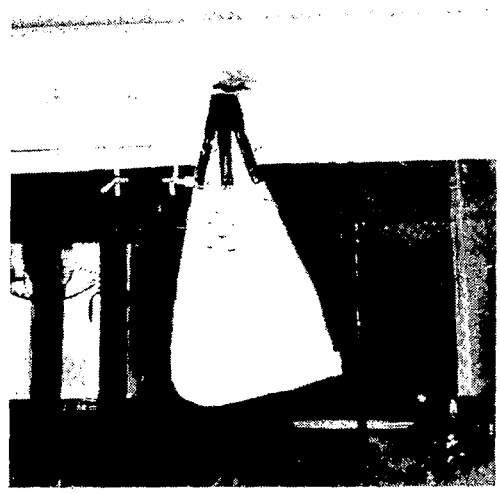

Figure 18.- Wind tunnel test, maximum camber.

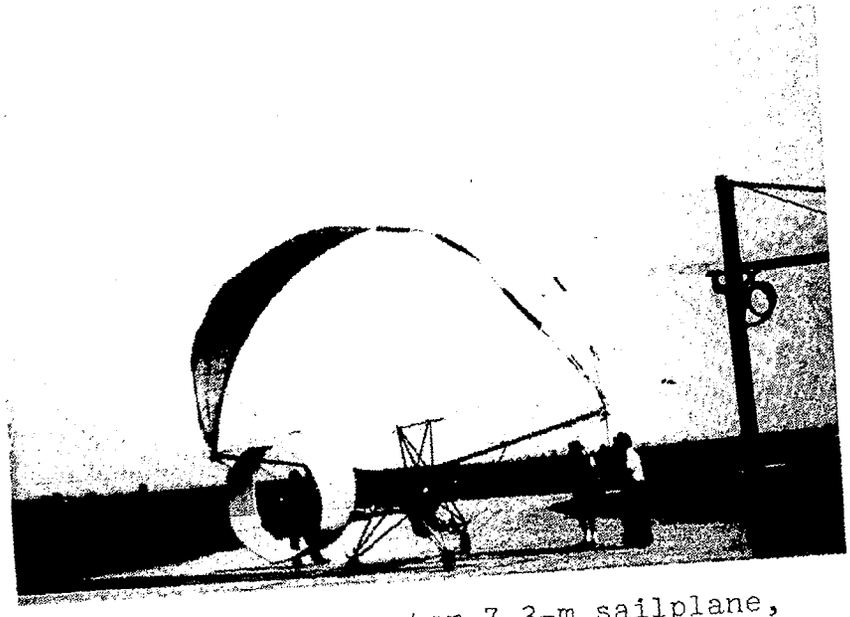

Figure 19.- Arcopter 7.3-m sailplane, ready for tow.

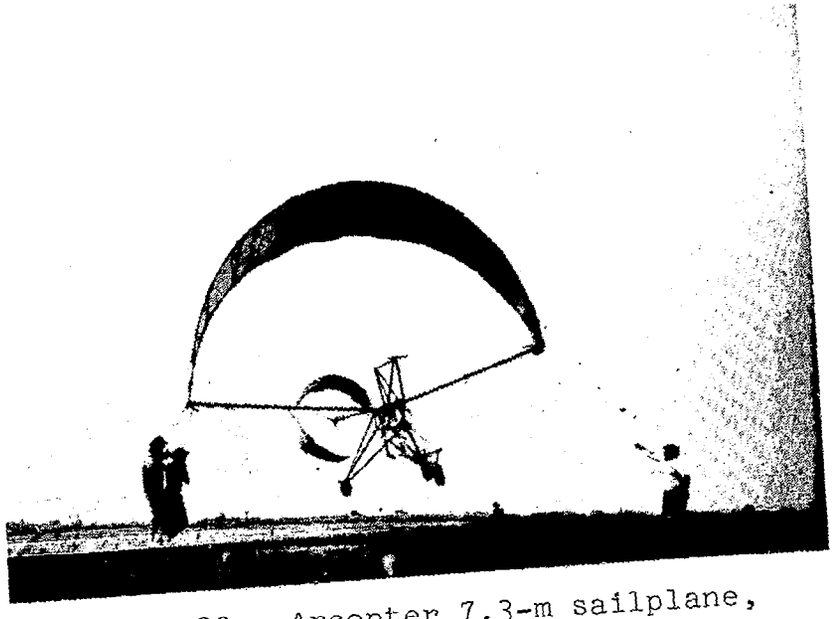

Figure 20.- Arcopter 7.3-m sailplane, tethered flight.

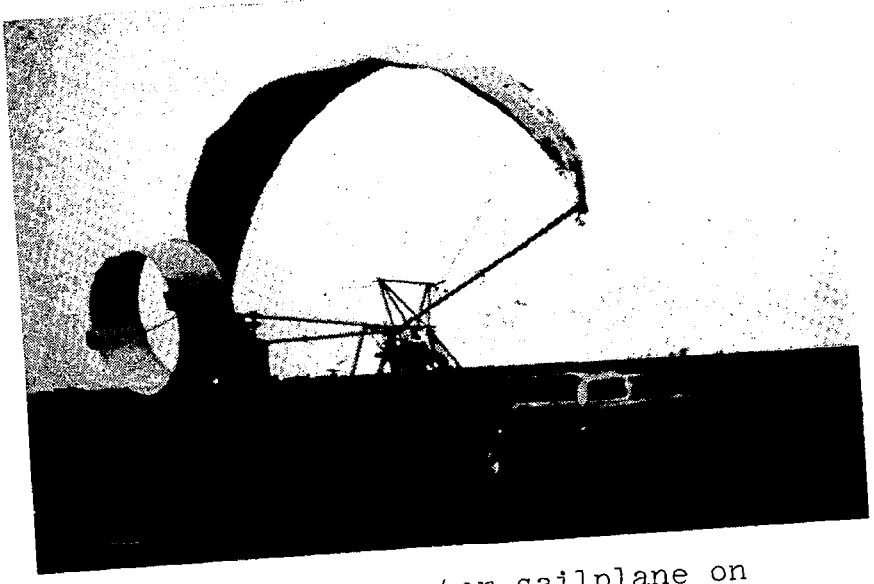

Figure 21.- Arcopter sailplane on mobile force balance.

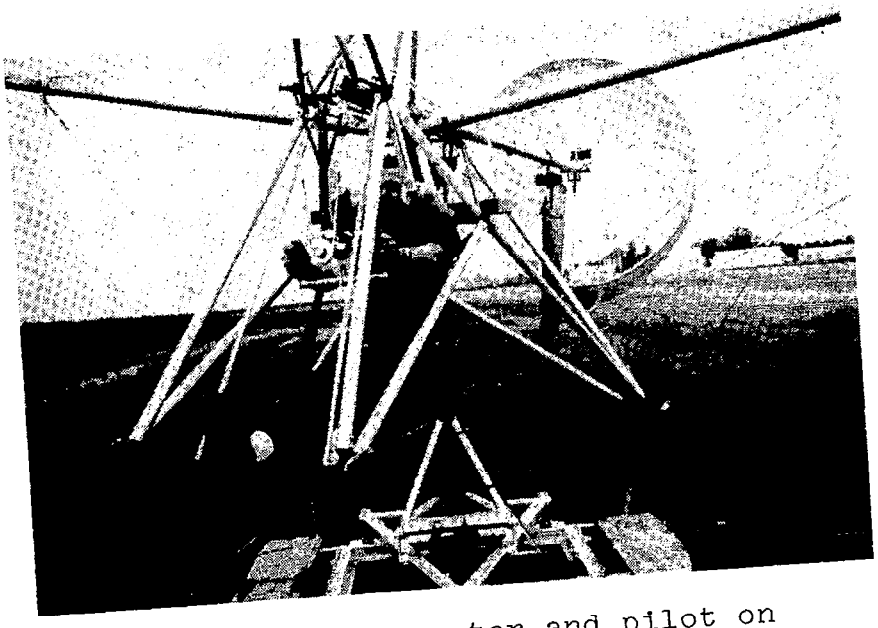

Figure 22.- Arcopter and pilot on mobile force balance, detail.

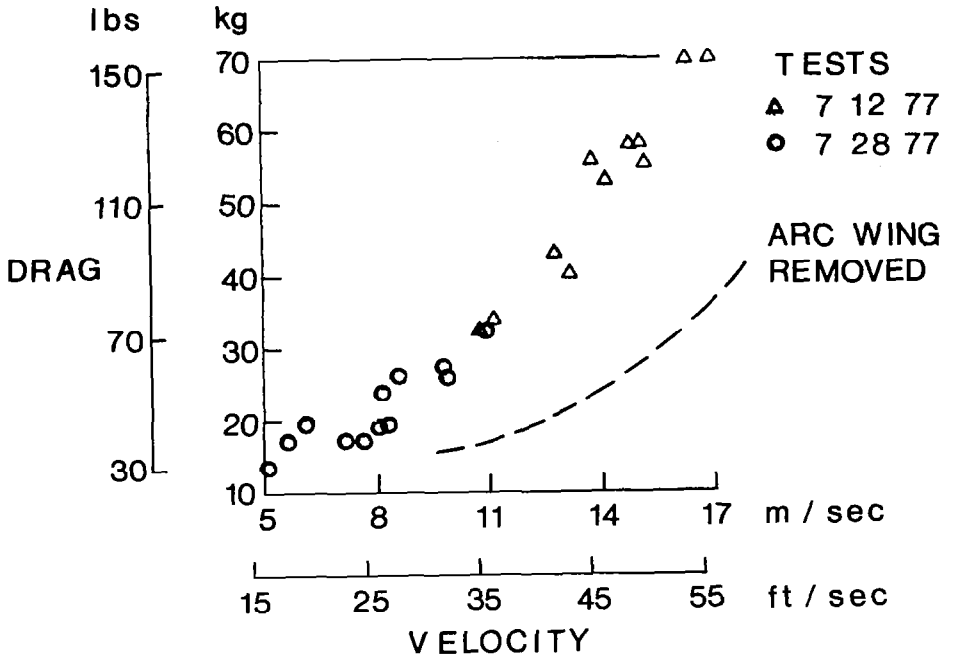

Figure 23.- Total drag of arcopter sailplane (mobile balance data).

Figure 24.- Arcopter foot-launched sailplane, tethered flight.

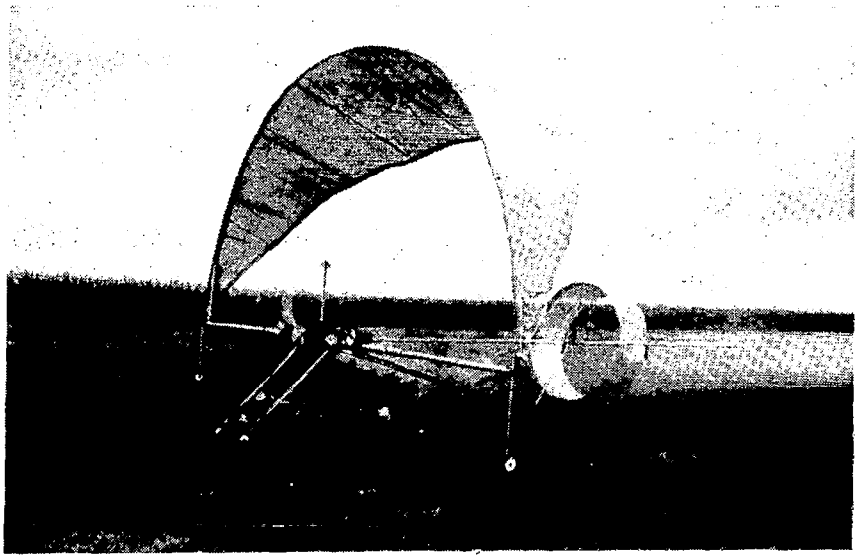

Figure 25.- Arcopter B-1A powered ultra-light aircraft.

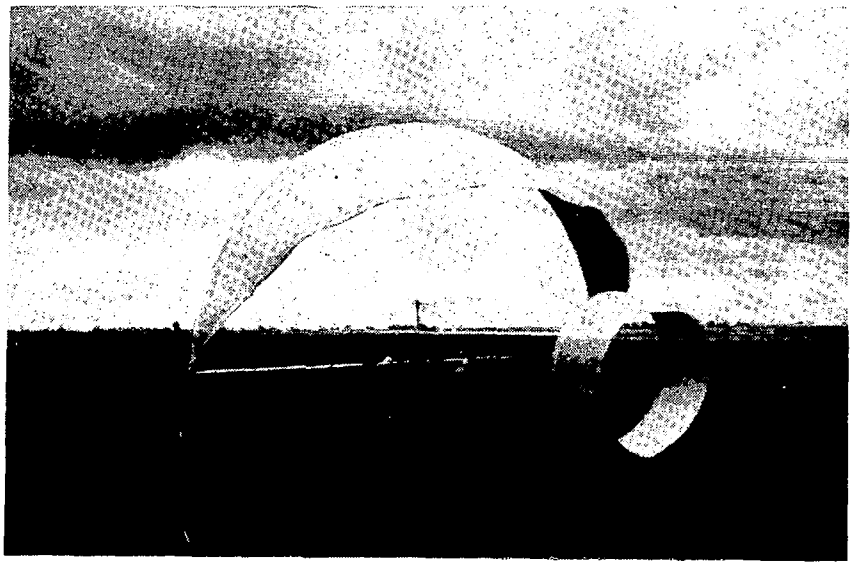

Figure 26.- Arcopter B-1A, empty weight 82.5 kg (181 lbs.).

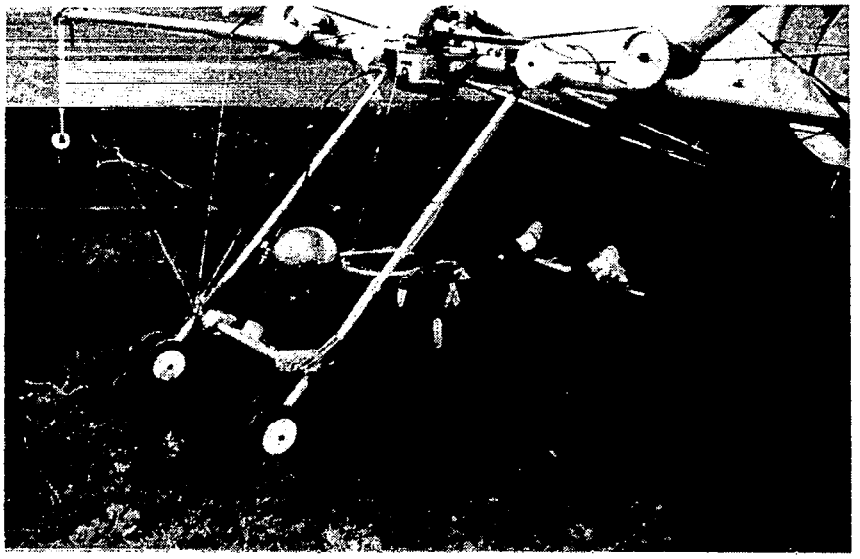

Figure 27.- Arcopter B-1A, power system detail.

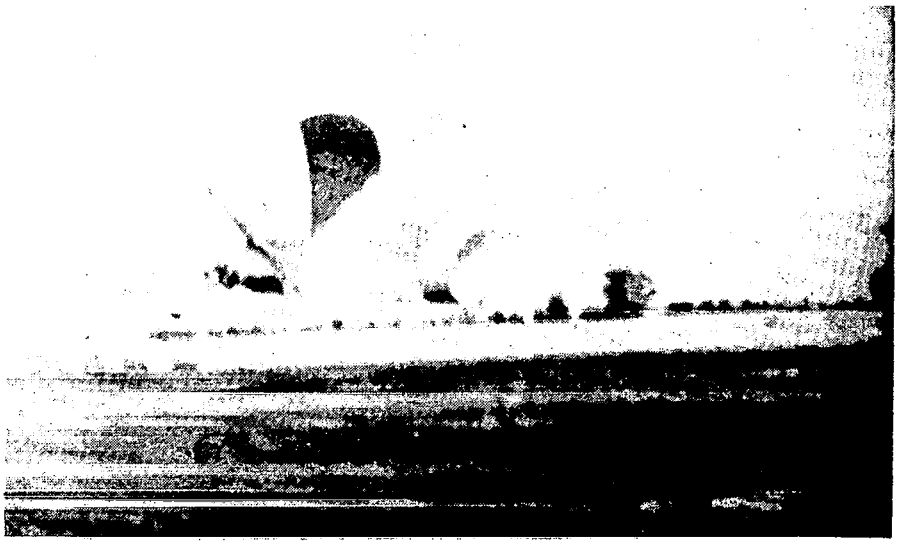

Figure 28.- Arcopter B-1A in powered flight.

SOME NEW AIRFOILS

Richard Eppler
Universität Stuttgart
Stuttgart, West Germany

SUMMARY

A computer approach to the design and analysis of airfoils and some common problems concerning laminar separation bubbles at different lift coefficients are discussed briefly. Examples of application to ultralight airplanes, canards, and sailplanes with flaps are given.

INTRODUCTION

In the 1940's, NACA demonstrated clearly that it is possible to design airfoils from pressure distributions in such a way that the boundary layer would behave in a desired manner (Refs. 1 and 2). At that time, it was discovered that the boundary layer would remain laminar longer if the pressure minimum occurred further aft on the airfoil. This realization led to the first laminar airfoils. Since that time, better methods for designing airfoils from pressure distributions have been developed (Ref. 3). Simple methods for computing the characteristics of laminar and turbulent boundary layers including a feasible transition criterion have also been developed (Ref. 4). The occurrence of laminar separation bubbles has been detected and studied experimentally (Ref. 5) and correlated with theory (Ref. 4). Good methods for the analysis of the potential flow around a given airfoil have been developed (Ref. 6). Thus, it was possible to write computer programs which combine all of these methods. These programs allow airfoils to be designed with prescribed pressure-distribution properties, the boundary-layer characteristics to be determined, and the effects of shape modifications such as plain or variable geometry flap deflections to be analyzed. A complete description of such a program system will soon be published as a NASA technical memorandum (Eppler and Somers). This system is somewhat equivalent to a wind tunnel. Three fundamental differences do exist, however. First, the computer analysis of an airfoil is much less expensive than the corresponding wind-tunnel test. Second, the total time required to obtain the final results is much shorter. Third, much more data, such as development of the boundary-layer shape factor and thickness, are available. Moreover, the modification of an airfoil through prescribing the pressure distribution, which must be done on the computer, is integrated into the program system. This allows a boundary-layer development with prescribed properties to be obtained directly.

Thus, the time has come to use the computer when a new airfoil is to be developed. Wind-tunnel and flight tests should be used to obtain a better

understanding of fundamental phenomena in support of the theory. Accordingly, an appropriate, or even an optimized, airfoil could be developed for each application rather than looking for an acceptable airfoil in an airfoil catalog. All such catalogs together could not cover all practical requirements. The Reynolds numbers, wing loadings, flaps, takeoff and landing requirements, structural constraints, moment restrictions, surface qualities, and many other specifications vary over wide ranges. It is not possible to develop catalogs for all such requirements. Only for a few applications, such as sailplanes with smooth surfaces and model airplanes, have catalogs been used successfully (Refs. 7 and 8). Even for these applications, new requirements arise which cannot be satisfied by existing airfoils. Other applications (e.g., general aviation, remotely piloted vehicles, and hydrofoil boats) are still far from having a list of standard requirements.

So, the tailoring of airfoils to specific applications becomes increasingly important. This paper presents some general considerations for tailoring airfoils and some examples of specific applications.

GENERAL CONSIDERATIONS

Airfoil design means to specify an airfoil from its pressure distribution in such a way that the boundary layer behaves in a desired manner. This approach usually leads to certain problems. Some of these problems are briefly discussed in this section.

The velocity distribution over an airfoil changes with angle of attack. An example is given in Figure 1 which shows the velocity distributions of an airfoil at seven angles of attack. (Note that all velocity distributions in this paper are presented in terms of the ratio (V) of the local potential-flow velocity to the free-stream potential-flow velocity.) The differences between the different curves are nearly independent of the particular airfoil and are approximately proportional to the differences between the corresponding flat-plate velocity distributions. Normally the design of an airfoil means the specification of the entire velocity distribution at one angle of attack only. This is called a one-point design. The design method mentioned previously (Ref. 3), however, permits a multipoint design in which the velocities are specified along different segments of the airfoil at different angles of attack.

For Reynolds numbers below about 4×10^6, one of the most important problems concerns laminar separation bubbles which usually occur if transition takes place in an adverse pressure gradient. It is well known that this phenomenon can cause a substantial increase in the total drag (Ref. 5). This increase depends primarily on the Reynolds number R and the degree of adverse pressure gradient near transition. At lower Reynolds numbers, less adverse pressure gradient is allowed. A so-called "transition ramp" must be introduced ahead of the pressure recovery in order to obtain a fully developed, turbulent boundary layer. At Reynolds numbers below about 10^5, a fully developed, turbulent boundary layer is not possible at all and, accordingly, the adverse pressure gradient can be only slightly steeper than the one which a laminar boundary

layer could overcome without separating. The theory (Ref. 4) as used in the program system provides a certain bubble analog. If this analog is prevented, the real flow does not normally show an additional bubble drag.

The problems associated with laminar separation bubbles become more difficult as angle of attack changes. As shown in Figure 1, the transition ramp introduced on the upper surface at high angles of attack α is reduced and even eliminated at lower α. For all multipoint designs, this problem is most difficult to solve. Fortunately, another effect helps the situation. For an airplane in flight, the Reynolds number changes with angle of attack or lift coefficient c_l. Thus, lower c_l means higher velocity and correspondingly higher Reynolds number. This fact can be exploited by requiring a less steep transition ramp at lower c_l. On the upper surface, it is even possible to eliminate the transition ramp required at higher c_l and, thereby, allow an extension of the laminar flow region at lower c_l and higher R. On the lower surface, a laminar separation bubble and even separation of the turbulent boundary layer can be permitted at low c_l and low R. As R increases to the free-flight value, the bubble and the turbulent separation should disappear. As c_l increases, the adverse pressure gradient should be reduced to an amount suitable for a transition ramp.

All of these features are illustrated in Figure 2 which contains the theoretical section characteristics for the airfoil shown in Figure 1. This airfoil was designed for a sailplane. The Reynolds number corresponding to low c_l is approximately $R = 3 \times 10^6$. The Reynolds number for high c_l is about $R = 10^6$. For $c_l < 0.5$ and $R = 10^6$, which is not achievable in flight by the sailplane, turbulent boundary-layer separation was permitted on the lower surface. As c_l is decreased from 1.2 to 0.6, the transition point on the upper surface moves aft approximately 10% of the chord because the transition ramp essentially "disappears."

Some unpublished wind-tunnel data (Althaus, Universität Stuttgart, 1975), and free-flight data (Ref. 9) are included in Figure 2. The latter data agree very well with the theory, while the wind-tunnel results show some discrepancies. The differences in transition point are inconsequential because a microphone was used in the wind tunnel to detect transition. This technique probably detects only a fully developed, turbulent boundary layer, and therefore, experimental points lay somewhat behind the theoretical ones. Of more importance are the differences among the drag polars. The wind-tunnel curve for $R = 10^6$ is characteristic of a polar for an airfoil with a small laminar separation bubble. That is to say that low drag is achieved at low and high, but not medium, lift coefficients. This problem was apparently not experienced in flight. Even more important are the drag differences for $c_l < 0.2$ and $R = 3 \times 10^6$. Here the free-flight tests indicate that the theoretical results are probably more reliable than those measured in the wind tunnel.

In summary, it is very likely that the "computer wind tunnel" can predict at least the differences between different airfoils so reliably that it should be used to design an airfoil for a specific application.

AIRFOILS FOR ULTRALIGHT AIRPLANES

Ultralight airplanes usually have only one side of the airfoil covered. This means that the airfoil has essentially zero thickness. The structure is concentrated primarily near the leading edge and to a lesser extent near the trailing edge. The problem, then, is the sharp suction peak which occurs near the leading edge at all off-design conditions. A high maximum lift coefficient $c_{l_{max}}$ and a soft stall are desirable for takeoff and landing, whereas because of the low aspect ratio, the lift coefficient for minimum sinking speed as well as for maximum glide ratio is usually somewhat less than $c_{l_{max}}$. Good penetration at even lower c_l is also sometimes desired. Thus, the problem is to design thin airfoils exhibiting a range of lift coefficient over which the flow is not entirely separated. Some thickness is, of course, required near the leading edge for structure. The following examples demonstrate what can be achieved by carefully shaping the leading-edge region. The first example, airfoil 379, is shown in Figure 3 along with its velocity distributions. At $\alpha = 7^{o}$ relative to the zero-lift direction, a very high suction peak has already occurred on the lower surface near the leading edge. On the upper surface, a suction peak forms as α increases but the $\Delta V_{max}/\Delta\alpha$ is much less than for the lower surface. The pressure recovery is slightly concave, but by no means as severe as the recovery typical of the Stratford distribution. This shallow, concave pressure recovery together with the rounded, upper-surface suction peak results in a soft stall which is most important for the application.

The section characteristics for this airfoil are shown in Figure 4. A high maximum lift and a soft stall are achieved, but below $c_l = 1.0$, the lower-surface flow is separated. The separation is predicted at about $x/c = 0.8$. This is a consequence of the assumption that the flow will reattach in a favorable gradient which, in this case, is probably not true. Thus, the flow on the lower surface must be considered separated from the leading edge aft.

An attempt to lower the lower-surface, leading-edge suction peak is shown in Figure 5. This airfoil, 378, is much thicker than the previous one (3.88% versus 2.10%). As shown in Figure 6, lower-surface separation is now predicted below $c_l = 0.6$, and thus, a much wider range of lift coefficient is available.

Figures 7 and 8 show airfoil 377, which is similar to 378 except that it is shifted to a higher lift coefficient. Using the design method mentioned above, this is easily accomplished.

The lower surface of this airfoil was then modified so that "zero" thickness was reached at a more forward x/c. The new shape and its velocity distribution are shown in Figure 9 and an overlay of Figures 7 and 9 is presented in Figure 10. Notice that the lower-surface flow exhibits much more adverse pressure gradient after the modification. As a consequence, the flow on the lower surface for this case is separated at all lift coefficients. This demonstrates the danger involved in arbitrarily modifying an airfoil to a shape which only looks appropriate.

Airfoil 376 was designed to have the same upper-surface behavior as airfoil 377 but to have less thickness and reach zero thickness at about $x/c = 0.25$ (Fig. 11). This airfoil has a maximum thickness of 2.21%. It has a certain c_l range over which the flow is not separated, and hence, is much better than airfoil 377 modified (Fig. 12). This range is still considerably less than that for the original airfoil 377.

These five examples illustrate the possibilities for thin airfoils. Many other constraints probably exist and, therefore, more tailoring would be required for this application.

Another category of ultralight airplanes is becoming more popular, the so-called foot-launched sailplane with an empty weight of around 45 kg, full controls, and an enclosed cockpit. This concept was demonstrated in the 1930's when the "Windspiel" was built. Today's materials allow much more efficient structures than were available at that time.

The airfoil requirements for this application include high maximum lift coefficient, soft stall, and low drag down to $c_l \approx 0$. Because of the low wing loadings involved, penetration always means low c_l. Airfoil 748 (Fig. 13) was tailored for this application which covers a Reynolds number range from 0.6×10^6 to 3×10^6 (Fig. 14). This airfoil requires a smooth surface for the forward 45% of the chord. If this can be accomplished, an aircraft with much lower wing loading than, say, a Ka-6 or Schweizer 1-26 can achieve the penetration of these heavier sailplanes and yet have a minimum speed which would permit simple takeoff procedures including foot-launch from a ridge with little wind.

AIRFOILS FOR CANARDS

Because of longitudinal-stability requirements, a canard (forward wing) must always operate at a higher c_l than the main (rear) wing. The maximum lift coefficient of the main wing is, therefore, constrained by the $c_{l_{max}}$ of the canard. Thus, it would be senseless to incorporate lift-increasing devices on the main wing if none were included on the canard. Fortunately, the canard usually includes an elevator which is deflected down to obtain higher c_l from the main wing. Thus, the elevator acts as a lift-increasing device for the canard. This effect, however, does depend on center-of-gravity position. The design objectives of airfoils for canards, therefore, include high $c_{l_{max}}$ with small downward flap deflection, low drag at low c_l with no flap deflection, and a certain thickness for structural reasons. The Reynolds numbers are relatively low because of the small chord lengths.

Two examples illustrate this application. The velocity distributions for the first example, airfoil 1230, are shown in Figure 15. The upper surface is designed only for high $c_{l_{max}}$. This is accomplished by preventing suction peaks and by including a certain transition ramp. Even at low c_l, only 20% of the upper surface can sustain laminar flow. The lower surface can have about

50% laminar flow. The theoretical section characteristics are shown in Figure 16. For positive flap deflection (down), some problems exist at low c_l. This combination, however, cannot occur in flight. The second example, airfoil 1233 (Fig. 17), achieves even higher $c_{l_{max}}$ (Fig 18). This airfoil is also thicker, and therefore, a drag penalty is paid at low c_l. The lower surface of this airfoil can sustain only 30% laminar flow. An airfoil between these two examples has been successfully applied on Burt Rutan's "Defiant" (Ref. 10).

AIRFOILS FOR SAILPLANES WITH FLAPS

Sailplanes with normally hinged flaps are a standard application of airfoils. The difficulties with this application come from two requirements. First, the flap-down case usually corresponds to a Reynolds number of 10^6 or below. For this case, laminar separation bubbles can be dangerous. This danger is increased by the steep adverse pressure gradient immediately downstream of the suction peak at the flap hinge. Second, the negative-flap-deflection (up) case corresponds to $R > 3 \times 10^6$. For this case, transition can occur earlier than desired. For a zero pressure gradient at these Reynolds numbers, the boundary layer is not stable enough to remain laminar for 60% to 70% of the surface and, therefore, a certain favorable pressure gradient is necessary to keep the boundary layer laminar.

Airfoil 662 was designed for this application. The velocity distributions for this airfoil with flap deflections (β) of 0°, 10° (down), and -7.5^o (up) are shown in Figure 19. The pressure recovery on the upper surface for the undeflected-flap case must be less than would be possible for the case where no flap deflections were intended. A flap deflection in either direction increases the amount of adverse pressure gradient. Severe separation would occur in these cases if the pressure recovery for the undeflected case were already approaching the separation limit. The flap deflection can, however, be exploited in a favorable sense as well. For the flap-down case, a distinct transition ramp forms between the original pressure recovery and the suction peak caused by the flap. On the lower surface, an additional favorable pressure gradient occurs with the flap up which stabilizes the laminar boundary layer at the higher Reynolds numbers. Attention to all of these details together with the careful designing of the leading-edge region results in the good performance illustrated in Figure 20. Notice that, at low c_l and low R, a lower-surface separation was again permitted.

Another application resulted from the practical achievement of the variable-geometry concept. A flap which extends the chord 20% while introducing essentially no disturbances in the flap-retracted configuration was developed by F. Mahrer and incorporated into his sailplane, "Delphin" (Ref. 11). This flap could only be applied over that portion of the span which required no aileron. It was, therefore, desirable to deflect the ailerons down for the high-lift case. A negative flap deflection was not allowed. Thus, an airfoil was required which would have a laminar bucket that would extend down to around $c_l = 0.05$ and which would achieve a high $c_{l_{max}}$ with a plain and a variable-geometry flap.

The velocity distributions for such an airfoil, 664, are shown in Figure 21. The transition ramp between the original pressure recovery and the flap hinge is again exploited for the flap-down case. The favorable pressure gradient aft of $x/c = 0.5$, however, had to be introduced for this airfoil because no flap-up deflection was possible. The section characteristics for this airfoil are shown in Figure 22.

CONCLUSIONS

Some new airfoils have been designed for specific applications through the use of a computer program. The applications included ultralight airplanes, canards, and sailplanes with flaps. The coordinates, moment coefficients, and zero-lift angles for all the airfoils presented are given as an appendix. The tailoring of airfoils should be encouraged because it is highly unlikely that airfoil catalogs will be produced for all possible applications. The reliability of this theoretical approach increases as more wind-tunnel and flight-test data are correlated with the theory. So far, many such theoretically developed airfoils have been successfully applied.

APPENDIX

COORDINATES, MOMENT COEFFICIENTS, AND ZERO-LIFT ANGLES FOR VARIOUS AIRFOILS

PROFIL 376 2.21%

N	X	Y
0	100.000	0.000
1	99.712	.036
2	98.849	.145
3	97.421	.333
4	95.449	.614
5	92.973	.991
6	90.032	1.458
7	86.668	2.006
8	82.930	2.627
9	78.865	3.308
10	74.528	4.036
11	69.976	4.794
12	65.266	5.566
13	60.459	6.330
14	55.616	7.067
15	50.796	7.746
16	46.060	8.335
17	41.448	8.787
18	36.977	9.073
19	32.667	9.180
20	28.535	9.106
21	24.597	8.851
22	20.866	8.433
23	17.362	7.879
24	14.119	7.217
25	11.168	6.463
26	8.532	5.640
27	6.235	4.767
28	4.289	3.865
29	2.708	2.960
30	1.493	2.078
31	.646	1.255
32	.154	.528
33	.001	-.032
34	.208	-.294
35	.853	-.209
36	2.019	.261
37	3.812	1.147
38	6.345	2.430
39	9.745	4.025
40	14.128	5.792
41	19.602	7.425
42	25.964	8.437
43	32.615	8.690
44	39.205	8.452
45	45.654	7.935
46	51.910	7.233
47	57.925	6.433
48	63.663	5.586
49	69.093	4.739
50	74.180	3.910
51	78.885	3.126
52	83.174	2.404
53	87.016	1.763
54	90.386	1.213
55	93.264	.767
56	95.632	.433
57	97.496	.219
58	98.864	.095
59	99.712	.026
60	100.000	-.000

CM= -.1197 β= 5.97°

PROFIL 377 3.63%

N	X	Y
0	100.000	0.000
1	99.709	.039
2	98.840	.157
3	97.407	.363
4	95.434	.664
5	92.957	1.060
6	90.015	1.545
7	86.650	2.112
8	82.909	2.751
9	78.841	3.449
10	74.501	4.193
11	69.944	4.966
12	65.229	5.751
13	60.416	6.527
14	55.567	7.272
15	50.741	7.959
16	45.998	8.553
17	41.379	9.006
18	36.901	9.292
19	32.584	9.397
20	28.446	9.316
21	24.503	9.054
22	20.766	8.625
23	17.259	8.059
24	14.014	7.381
25	11.062	6.611
26	8.428	5.767
27	6.134	4.871
28	4.196	3.945
29	2.625	3.013
30	1.428	2.102
31	.602	1.244
32	.136	.482
33	.010	-.102
34	.324	-.406
35	1.141	-.443
36	2.442	-.204
37	4.290	.363
38	6.755	1.263
39	9.928	2.461
40	13.876	3.866
41	18.637	5.342
42	24.199	6.713
43	30.484	7.754
44	37.233	8.211
45	44.016	8.077
46	50.591	7.580
47	56.901	6.879
48	62.899	6.056
49	68.544	5.179
50	73.800	4.292
51	78.634	3.436
52	83.016	2.639
53	86.923	1.926
54	90.333	1.316
55	93.231	.821
56	95.607	.456
57	97.474	.226
58	98.849	.100
59	99.707	.028
60	100.000	-.000

CM= -.1291 β= 6.08°

PROFIL 377
LOWER SURFACE CHANGED

N	X	Y
0	100.000	0.000
1	99.710	.040
2	98.841	.159
3	97.407	.363
4	95.434	.664
5	92.957	1.060
6	90.015	1.545
7	86.650	2.112
8	82.909	2.751
9	78.841	3.449
10	74.501	4.193
11	69.944	4.966
12	65.229	5.751
13	60.416	6.527
14	55.567	7.272
15	50.741	7.959
16	45.998	8.553
17	41.379	9.006
18	36.901	9.292
19	32.584	9.397
20	28.446	9.316
21	24.503	9.054
22	20.766	8.625
23	17.259	8.059
24	14.014	7.381
25	11.062	6.611
26	8.428	5.767
27	6.134	4.871
28	4.196	3.945
29	2.625	3.013
30	1.428	2.102
31	.602	1.244
32	.136	.482
33	.010	-.102
34	.324	-.406
35	1.141	-.443
36	2.442	-.204
37	4.290	.363
38	6.500	1.250
39	8.758	2.431
40	11.227	3.916
41	14.000	5.500
42	17.176	6.882
43	20.770	7.930
44	24.500	8.550
45	28.450	8.820
46	32.634	8.860
47	36.956	8.713
48	41.380	8.410
49	46.100	7.964
50	50.844	7.411
51	55.570	6.770
52	60.486	6.027
53	65.291	5.249
54	69.940	4.470
55	74.539	3.692
56	78.878	2.950
57	82.910	2.250
58	86.668	1.597
59	90.029	1.058
60	92.960	.660
61	95.452	.391
62	97.423	.212
63	98.849	.093
64	99.711	.023
65	100.000	0.000

CM= -.1080 β=6.20°

APPENDIX

PROFIL 378 3.88%

N	X	Y
0	100.000	0.000
1	99.707	.024
2	98.827	.100
3	97.362	.240
4	95.333	.469
5	92.783	.797
6	89.760	1.219
7	86.308	1.727
8	82.476	2.312
9	78.318	2.964
10	73.888	3.670
11	69.247	4.413
12	64.455	5.177
13	59.574	5.940
14	54.668	6.680
15	49.798	7.368
16	45.027	7.968
17	40.394	8.430
18	35.916	8.726
19	31.611	8.841
20	27.496	8.772
21	23.586	8.521
22	19.892	8.105
23	16.435	7.554
24	13.248	6.894
25	10.362	6.144
26	7.801	5.325
27	5.586	4.457
28	3.734	3.563
29	2.255	2.666
30	1.153	1.795
31	.426	.985
32	.064	.285
33	.055	-.201
34	.521	-.423
35	1.528	-.424
36	3.027	-.172
37	5.074	.378
38	7.733	1.224
39	11.076	2.329
40	15.155	3.606
41	19.995	4.932
42	25.572	6.148
43	31.813	7.052
44	38.466	7.414
45	45.133	7.232
46	51.587	6.724
47	57.777	6.038
48	63.657	5.253
49	69.190	4.428
50	74.339	3.607
51	79.073	2.825
52	83.363	2.110
53	87.186	1.481
54	90.522	.956
55	93.356	.545
56	95.678	.259
57	97.504	.105
58	98.856	.043
59	99.707	.013
60	100.000	-.000

CM= -.1012 β= 5.02°

PROFIL 379 2.10%

N	X	Y
0	100.000	0.000
1	99.707	.020
2	98.827	.085
3	97.364	.214
4	95.339	.428
5	92.795	.739
6	89.779	1.143
7	86.335	1.632
8	82.511	2.200
9	78.361	2.834
10	73.942	3.522
11	69.312	4.250
12	64.531	5.000
13	59.662	5.751
14	54.768	6.481
15	49.911	7.162
16	45.152	7.757
17	40.531	8.217
18	36.065	8.513
19	31.772	8.632
20	27.668	8.570
21	23.767	8.329
22	20.081	7.926
23	16.630	7.390
24	13.447	6.749
25	10.562	6.022
26	7.999	5.228
27	5.779	4.388
28	3.916	3.524
29	2.419	2.662
30	1.292	1.827
31	.529	1.060
32	.116	.400
33	.009	-.066
34	.282	-.106
35	1.162	.240
36	2.710	.884
37	4.946	1.820
38	7.946	2.997
39	11.768	4.325
40	16.471	5.630
41	21.948	6.646
42	27.930	7.227
43	34.165	7.412
44	40.492	7.251
45	46.771	6.826
46	52.900	6.209
47	58.806	5.488
48	64.446	4.714
49	69.778	3.935
50	74.764	3.176
51	79.368	2.468
52	83.559	1.825
53	87.308	1.269
54	90.592	.806
55	93.393	.449
56	95.695	.204
57	97.510	.079
58	98.857	.033
59	99.707	.012
60	100.000	-.000

CM= -.0822 β= 4.88°

PROFIL 748 19.73%

N	X	Y
0	100.000	0.000
1	99.641	.122
2	98.632	.505
3	97.102	1.131
4	95.133	1.899
5	92.723	2.711
6	89.835	3.545
7	86.485	4.425
8	82.726	5.357
9	78.615	6.330
10	74.212	7.330
11	69.581	8.340
12	64.785	9.335
13	59.887	10.290
14	54.948	11.177
15	50.028	11.967
16	45.180	12.630
17	40.456	13.136
18	35.901	13.453
19	31.541	13.546
20	27.392	13.402
21	23.468	13.018
22	19.779	12.401
23	16.337	11.577
24	13.164	10.572
25	10.282	9.417
26	7.714	8.142
27	5.482	6.781
28	3.606	5.368
29	2.104	3.939
30	.992	2.534
31	.284	1.201
32	.000	.006
33	.275	-.985
34	1.174	-1.865
35	2.614	-2.728
36	4.542	-3.540
37	6.925	-4.279
38	9.731	-4.932
39	12.923	-5.485
40	16.454	-5.923
41	20.278	-6.224
42	24.342	-6.362
43	28.592	-6.284
44	33.026	-5.899
45	37.743	-5.174
46	42.826	-4.217
47	48.237	-3.189
48	53.855	-2.189
49	59.567	-1.259
50	65.278	-.434
51	70.888	.248
52	76.292	.759
53	81.380	1.084
54	86.044	1.220
55	90.181	1.180
56	93.695	.984
57	96.483	.673
58	98.462	.338
59	99.621	.090
60	100.000	-.000

CM= -.1732 β= 6.65°

APPENDIX

PROFIL 1230 17.46%

N	X	Y
0	100.000	0.000
1	99.850	.039
2	99.418	.167
3	98.742	.396
4	97.859	.715
5	96.797	1.095
6	95.562	1.503
7	94.141	1.915
8	92.517	2.331
9	90.691	2.765
10	88.676	3.221
11	86.484	3.699
12	84.128	4.199
13	81.622	4.720
14	78.980	5.258
15	76.219	5.812
16	73.353	6.378
17	70.399	6.950
18	67.373	7.524
19	64.290	8.094
20	61.167	8.655
21	58.019	9.200
22	54.861	9.722
23	51.708	10.214
24	48.574	10.671
25	45.472	11.085
26	42.415	11.449
27	39.414	11.758
28	36.482	12.005
29	33.627	12.186
30	30.860	12.294
31	28.190	12.325
32	25.623	12.274
33	23.166	12.138
34	20.823	11.911
35	18.594	11.591
36	16.479	11.180
37	14.478	10.683
38	12.591	10.105
39	10.817	9.454
40	9.157	8.744
41	7.618	7.987
42	6.206	7.191
43	4.928	6.366
44	3.787	5.521
45	2.789	4.665
46	1.937	3.807
47	1.236	2.958
48	.688	2.129

PROFIL 1230 17.46%

N	X	Y
49	.560	2.054
50	.217	1.209
51	.035	.415
52	.021	-.302
53	.231	-.913
54	.702	-1.465
55	1.401	-2.010
56	2.299	-2.536
57	3.390	-3.029
58	4.672	-3.483
59	6.142	-3.900
60	7.792	-4.279
61	9.613	-4.621
62	11.595	-4.925
63	13.724	-5.187
64	15.990	-5.404
65	18.381	-5.572
66	20.883	-5.686
67	23.484	-5.735
68	26.178	-5.706
69	28.964	-5.592
70	31.844	-5.391
71	34.818	-5.103
72	37.887	-4.731
73	41.054	-4.285
74	44.315	-3.782
75	47.662	-3.238
76	51.083	-2.671
77	54.562	-2.098
78	58.079	-1.536
79	61.613	-.997
80	65.141	-.496
81	68.639	-.043
82	72.081	.352
83	75.441	.681
84	78.691	.939
85	81.804	1.122
86	84.754	1.229
87	87.513	1.261
88	90.056	1.223
89	92.358	1.118
90	94.390	.953
91	96.124	.746
92	97.538	.524
93	98.627	.317
94	99.394	.149
95	99.850	.039
96	100.000	-.000

CM= -.1769 β= 7.01°

PROFIL 1233 19.38%

N	X	Y
0	100.000	0.000
1	99.855	.051
2	99.438	.214
3	98.791	.497
4	97.954	.880
5	96.952	1.329
6	95.787	1.807
7	94.442	2.290
8	92.898	2.778
9	91.154	3.284
10	89.224	3.813
11	87.119	4.364
12	84.850	4.935
13	82.432	5.526
14	79.878	6.133
15	77.202	6.752
16	74.419	7.380
17	71.545	8.011
18	68.594	8.640
19	65.582	9.262
20	62.525	9.870
21	59.437	10.458
22	56.332	11.020
23	53.226	11.548
24	50.132	12.036
25	47.063	12.477
26	44.032	12.864
27	41.050	13.192
28	38.129	13.454
29	35.278	13.644
30	32.509	13.757
31	29.830	13.787
32	27.246	13.727
33	24.761	13.575
34	22.379	13.328
35	20.102	12.985
36	17.929	12.549
37	15.863	12.025
38	13.904	11.418
39	12.053	10.736
40	10.312	9.991
41	8.688	9.195
42	7.186	8.357
43	5.814	7.486
44	4.576	6.589
45	3.478	5.676
46	2.524	4.757
47	1.717	3.839
48	1.061	2.934

PROFIL 1233 19.38%

N	X	Y
49	.296	1.331
50	.066	.581
51	.002	-.103
52	.126	-.675
53	.507	-1.165
54	1.154	-1.641
55	2.015	-2.102
56	3.077	-2.538
57	4.334	-2.937
58	5.789	-3.294
59	7.441	-3.613
60	9.284	-3.898
61	11.309	-4.152
62	13.505	-4.378
63	15.860	-4.575
64	18.361	-4.745
65	20.997	-4.887
66	23.753	-5.000
67	26.617	-5.084
68	29.574	-5.139
69	32.610	-5.162
70	35.711	-5.153
71	38.861	-5.110
72	42.045	-5.031
73	45.249	-4.910
74	48.460	-4.739
75	51.674	-4.516
76	54.884	-4.239
77	58.083	-3.912
78	61.264	-3.537
79	64.419	-3.116
80	67.547	-2.648
81	70.660	-2.150
82	73.749	-1.654
83	76.791	-1.186
84	79.759	-.762
85	82.626	-.395
86	85.364	-.093
87	87.944	.137
88	90.340	.294
89	92.524	.380
90	94.468	.397
91	96.144	.357
92	97.530	.278
93	98.612	.183
94	99.384	.092
95	99.846	.025
96	100.000	-.000

CM= -.1079 β= 4.88°

APPENDIX

PROFIL 662 15.02%

N	X	Y
0	100.000	0.000
1	99.642	.118
2	98.640	.483
3	97.117	1.056
4	95.113	1.745
5	92.609	2.516
6	89.626	3.395
7	86.231	4.390
8	82.500	5.493
9	78.528	6.682
10	74.435	7.890
11	70.276	8.968
12	65.983	9.824
13	61.519	10.489
14	56.922	10.988
15	52.232	11.331
16	47.501	11.525
17	42.776	11.570
18	38.108	11.470
19	33.541	11.225
20	29.121	10.841
21	24.891	10.324
22	20.891	9.681
23	17.159	8.923
24	13.729	8.062
25	10.631	7.113
26	7.892	6.094
27	5.535	5.024
28	3.578	3.926
29	2.037	2.828
30	.921	1.761
31	.239	.770
32	.003	-.074
33	.351	-.733
34	1.336	-1.289
35	2.879	-1.785
36	4.966	-2.210
37	7.571	-2.567
38	10.668	-2.858
39	14.221	-3.088
40	18.189	-3.264
41	22.522	-3.392
42	27.165	-3.474
43	32.061	-3.512
44	37.148	-3.506
45	42.363	-3.456
46	47.642	-3.357
47	52.919	-3.206
48	58.130	-2.993
49	63.214	-2.702
50	68.116	-2.302
51	72.841	-1.742
52	77.449	-1.061
53	81.940	-.382
54	86.229	.169
55	90.177	.509
56	93.628	.611
57	96.423	.500
58	98.431	.276
59	99.613	.077
60	100.000	-.000

CM= -.1497 β= 5.92°

PROFIL 664 16.63%

N	X	Y
0	100.000	0.000
1	99.623	.092
2	98.557	.391
3	96.923	.881
4	94.774	1.491
5	92.110	2.193
6	88.964	3.005
7	85.407	3.927
8	81.512	4.942
9	77.353	6.020
10	73.008	7.122
11	68.549	8.197
12	64.043	9.167
13	59.497	9.937
14	54.869	10.482
15	50.167	10.840
16	45.437	11.029
17	40.727	11.060
18	36.087	10.938
19	31.564	10.670
20	27.205	10.262
21	23.051	9.720
22	19.145	9.055
23	15.521	8.277
24	12.216	7.401
25	9.258	6.441
26	6.674	5.416
27	4.487	4.348
28	2.714	3.261
29	1.371	2.183
30	.468	1.155
31	.023	.229
32	.146	-.521
33	.903	-1.173
34	2.234	-1.817
35	4.097	-2.423
36	6.471	-2.979
37	9.334	-3.482
38	12.651	-3.936
39	16.380	-4.341
40	20.474	-4.693
41	24.882	-4.990
42	29.552	-5.229
43	34.429	-5.406
44	39.452	-5.522
45	44.556	-5.572
46	49.678	-5.546
47	54.754	-5.433
48	59.719	-5.219
49	64.512	-4.867
50	69.117	-4.322
51	73.561	-3.567
52	77.909	-2.623
53	82.219	-1.637
54	86.399	-.808
55	90.260	-.224
56	93.641	.102
57	96.395	.198
58	98.400	.142
59	99.602	.045
60	100.000	-.000

CM= -.0908 β= 3.85°

PROFIL 664
VARIABLE GEOMETRY

N	X	Y
0	120.000	-9.000
1	119.373	-8.620
2	117.500	-7.496
3	114.391	-5.708
4	110.000	-3.500
5	107.054	-2.294
6	103.709	-1.132
7	100.000	0.000
8	96.923	.881
9	92.110	2.193
10	85.407	3.927
11	81.512	4.942
12	77.353	6.020
13	73.008	7.122
14	68.549	8.197
15	64.043	9.167
16	59.497	9.937
17	54.869	10.482
18	50.167	10.840
19	45.437	11.029
20	40.727	11.060
21	36.087	10.938
22	31.564	10.670
23	27.205	10.262
24	23.051	9.720
25	19.145	9.055
26	15.521	8.277
27	12.216	7.401
28	9.258	6.441
29	6.674	5.416
30	4.487	4.348
31	2.714	3.261
32	1.371	2.183
33	.468	1.155
34	.023	.229
35	.146	-.521
36	.903	-1.173
37	2.234	-1.817
38	4.097	-2.423
39	6.471	-2.979
40	9.334	-3.482
41	12.651	-3.936
42	16.380	-4.341
43	20.474	-4.693
44	24.882	-4.990
45	29.552	-5.229
46	34.429	-5.406
47	39.452	-5.522
48	44.556	-5.572
49	49.678	-5.546
50	54.754	-5.433
51	59.719	-5.219
52	64.512	-4.867
53	69.117	-4.322
54	74.184	-3.641
55	79.152	-3.041
56	84.000	-2.650
57	88.180	-2.542
58	92.188	-2.639
59	96.000	-2.900
60	100.411	-3.401
61	104.421	-4.078
62	108.000	-4.900
63	112.280	-6.177
64	115.631	-7.351
65	118.047	-8.254
66	119.510	-8.812
67	120.000	-9.000

REFERENCES

1. Abbott, Ira H.; Von Doenhoff, Albert E.; and Stivers, Louis S., Jr.: Summary of Airfoil Data. NACA Rep. 824, 1945.

2. Abbott, Ira H.; and Von Doenhoff, Albert E.: Theory of Wing Sections. Dover Publications, Inc., 1959.

3. Eppler, R.: Direct Calculation of Airfoils From Pressure Distribution. NASA TT F-15417, 1974.

4. Eppler, R.: Practical Calculation of Laminar and Turbulent Bled-Off Boundary Layers. NASA TM-75328, 1978.

5. Wortmann, F. X.: Über den Ablösewinkel laminarer Ablöseblasen. Beiträge zur Strömungsmechanik und Flugmechanik, DLR-FB 74-62, 1974, pp. 10-1 - 10-13.

6. Hess, John L.: The Use of Higher-Order Surface Singularity Distributions To Obtain Improved Potential Flow Solutions for Two-Dimensional Lifting Airfoils. Computer Methods in Applied Mechanics and Engineering, vol. 5, no. 1, Jan. 1975, pp. 11-35.

7. Althaus, D.: MeBergebnisse aus dem Laminarwindkanal des Instituts für Aerodynamik und Fasdynamik der Universität Stuttgart. Stuttgarter Profilkatalog I, Institut für Aerodynamik und Gasdynamik der Universität Stuttgart, 1972.

8. Eppler,Profile. Verlag für Technik und Handwerk (Baden-Baden, Germany), 1977.

9. McMasters, J. H.: Low-Speed Drag Estimation Procedure Applied to the Astir CS Sailplane. Boeing Document D6-46968TN, Boeing, Jan. 1979.

10. Garrison, Peter: Rutan's Defiant. Flying, vol. 103, no. 6, Dec. 1978, pp. 55-59 and 86.

11. Wyler, Ruedi: Spaltenlose Fowlerklappen bie Segelflugzeugen. Aero Revue, Feb. 1979, pp. 75-77.

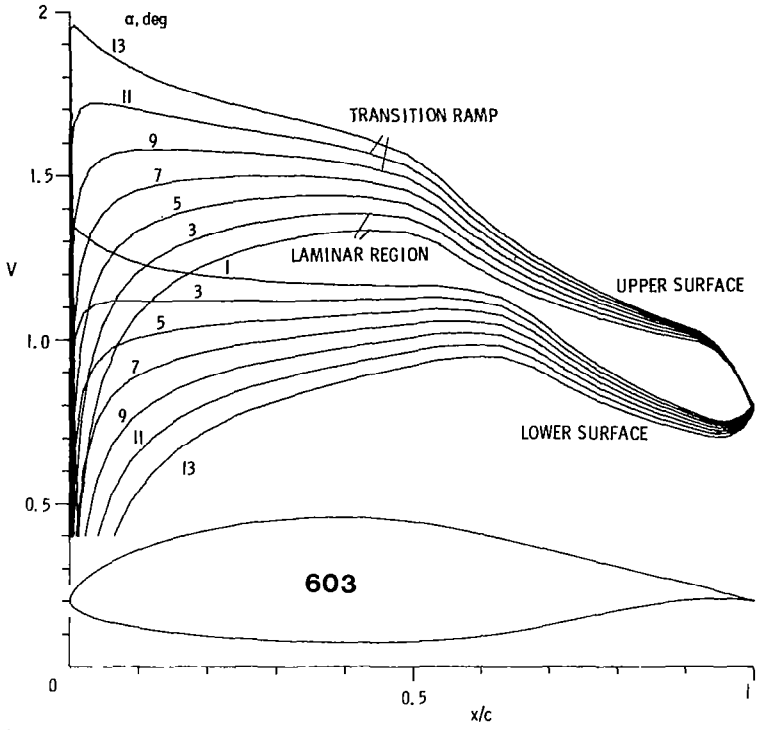

Figure 1.- Velocity distributions for airfoil 603.
α relative to zero-lift direction.

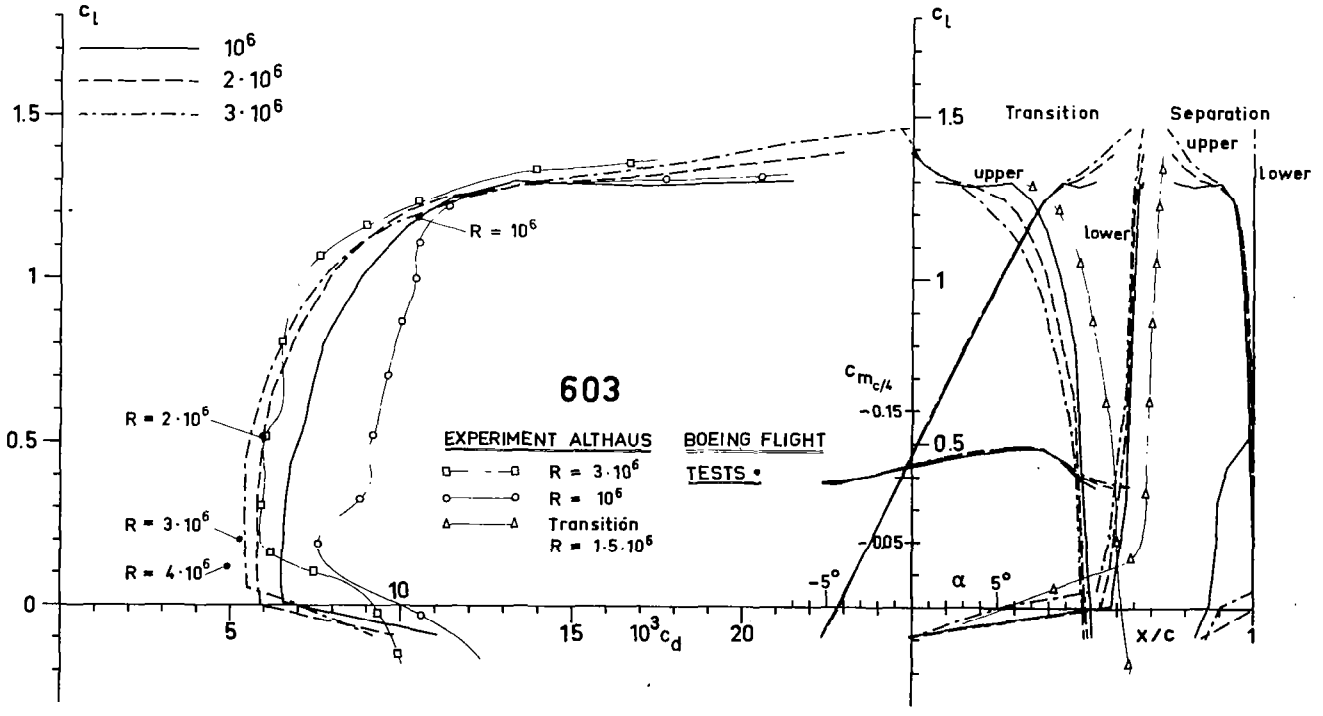

Figure 2.- Section characteristics for airfoil 603.

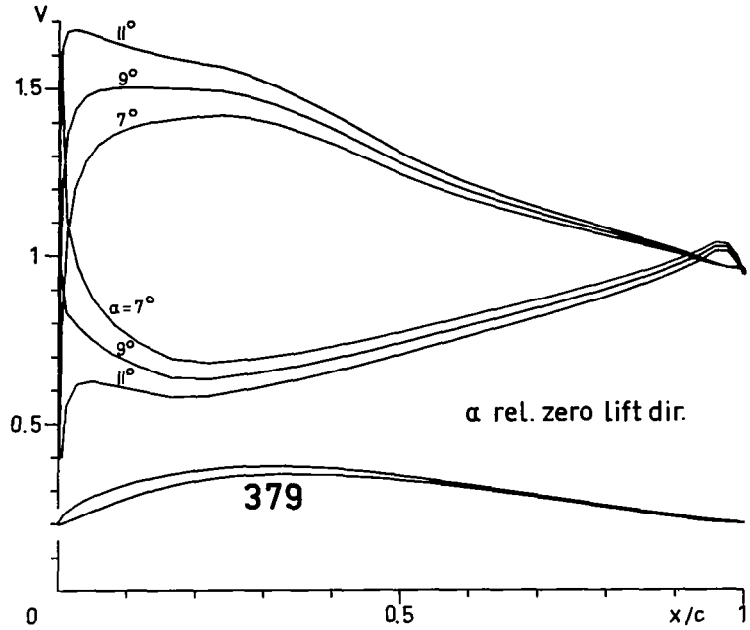

Figure 3.- Velocity distributions for airfoil 379.

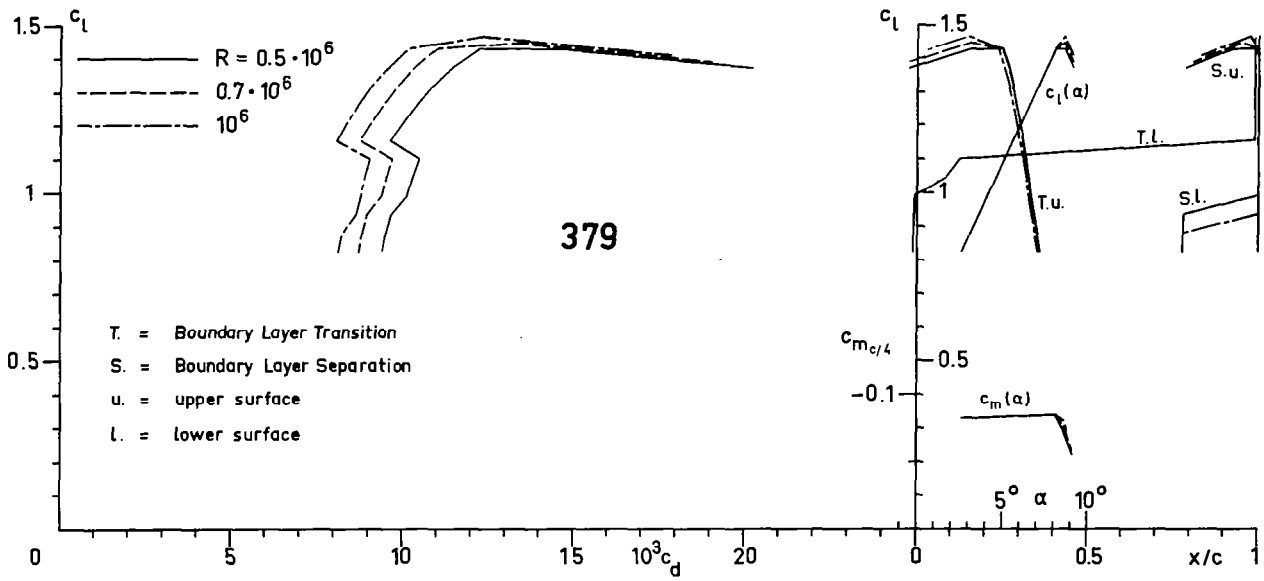

Figure 4.- Theoretical section characteristics for airfoil 379.

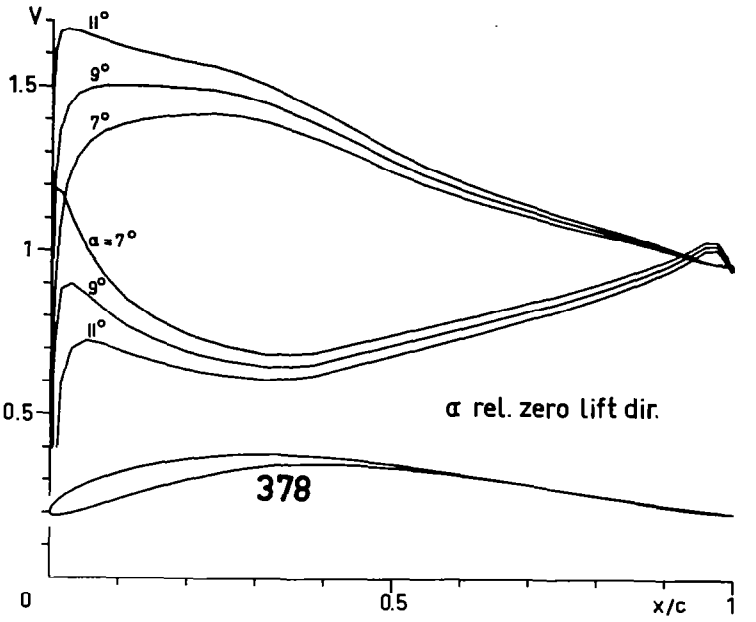

Figure 5.- Velocity distributions for airfoil 378.

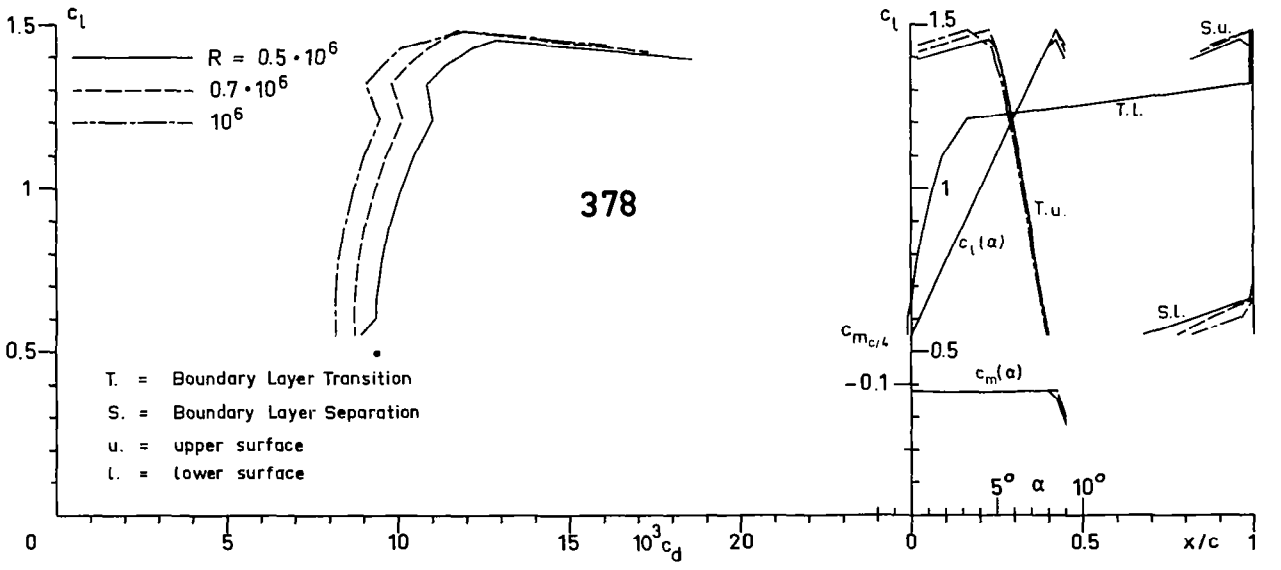

Figure 6.- Theoretical section characteristics for airfoil 378.

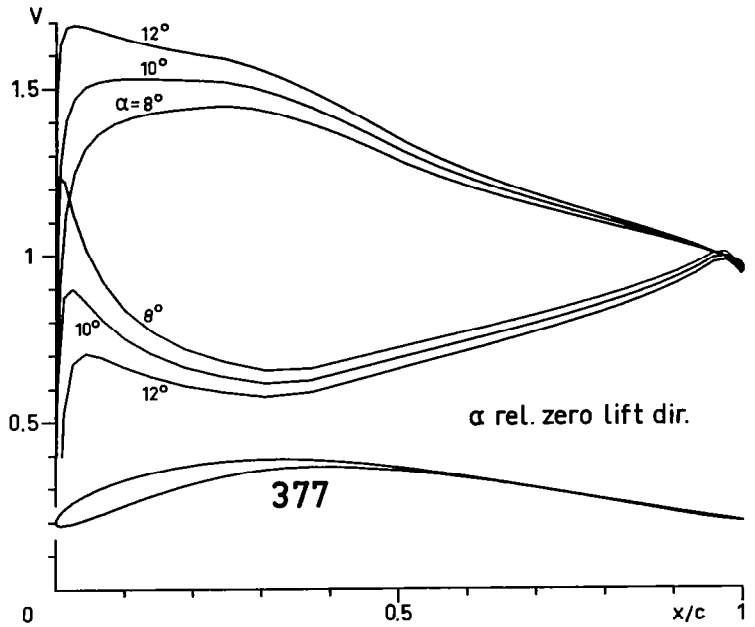

Figure 7.- Velocity distributions for airfoil 377.

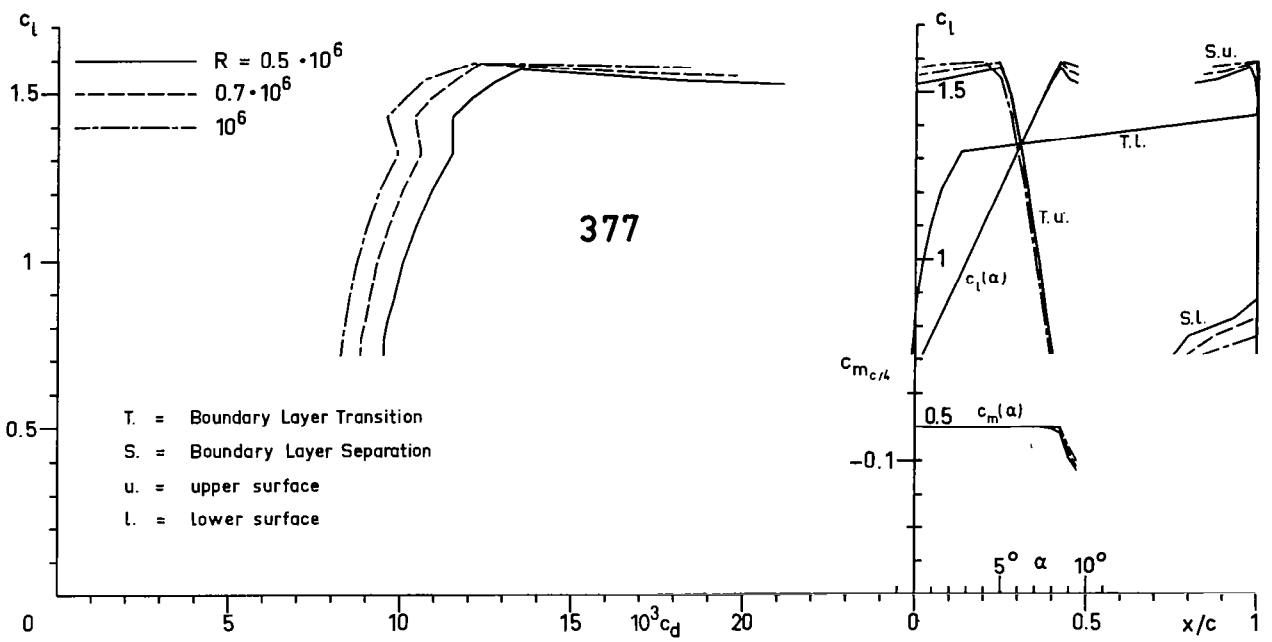

Figure 8.- Theoretical section characteristics for airfoil 377.

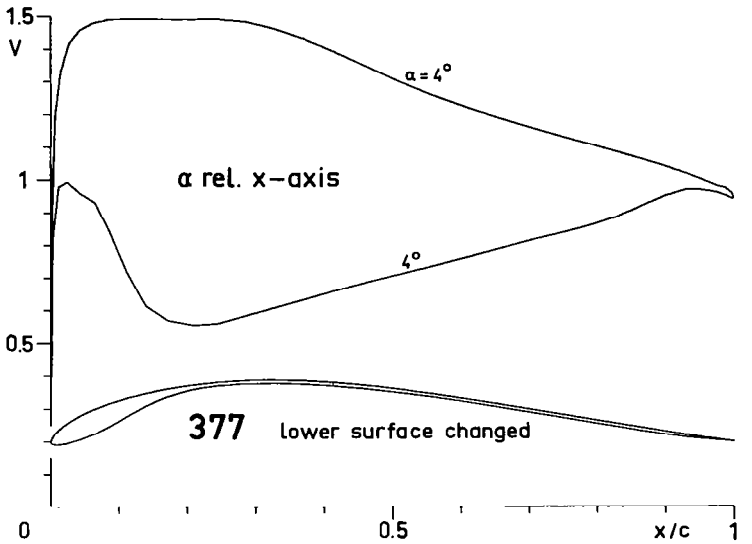

Figure 9.- Velocity distribution for airfoil 377 modified.

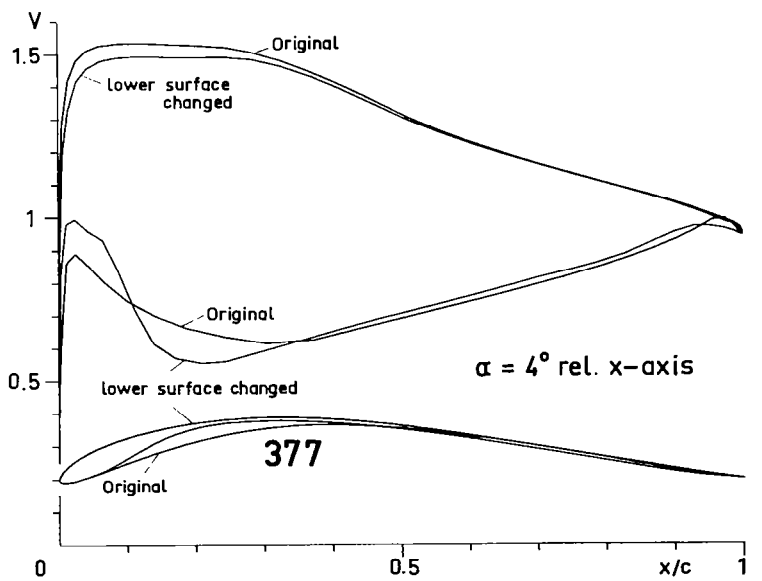

Figure 10.- Comparison of original and modified airfoil 377.

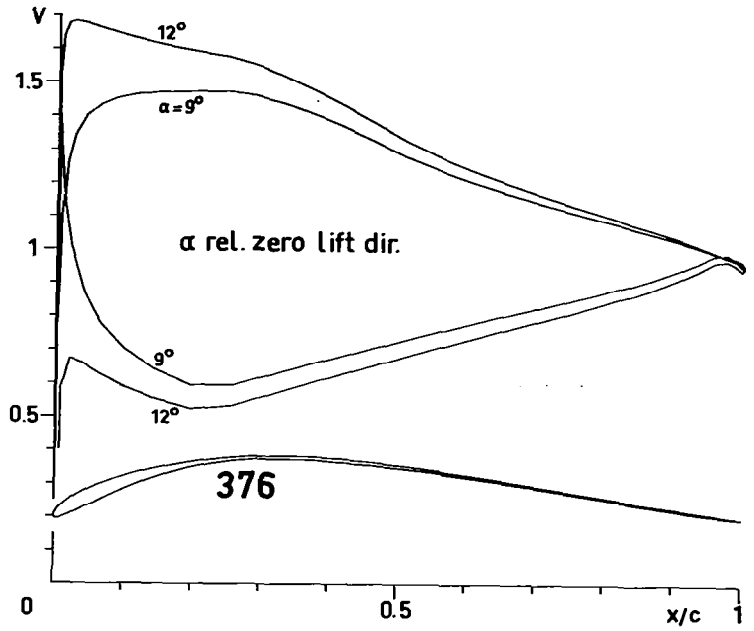

Figure 11.- Velocity distributions for airfoil 376.

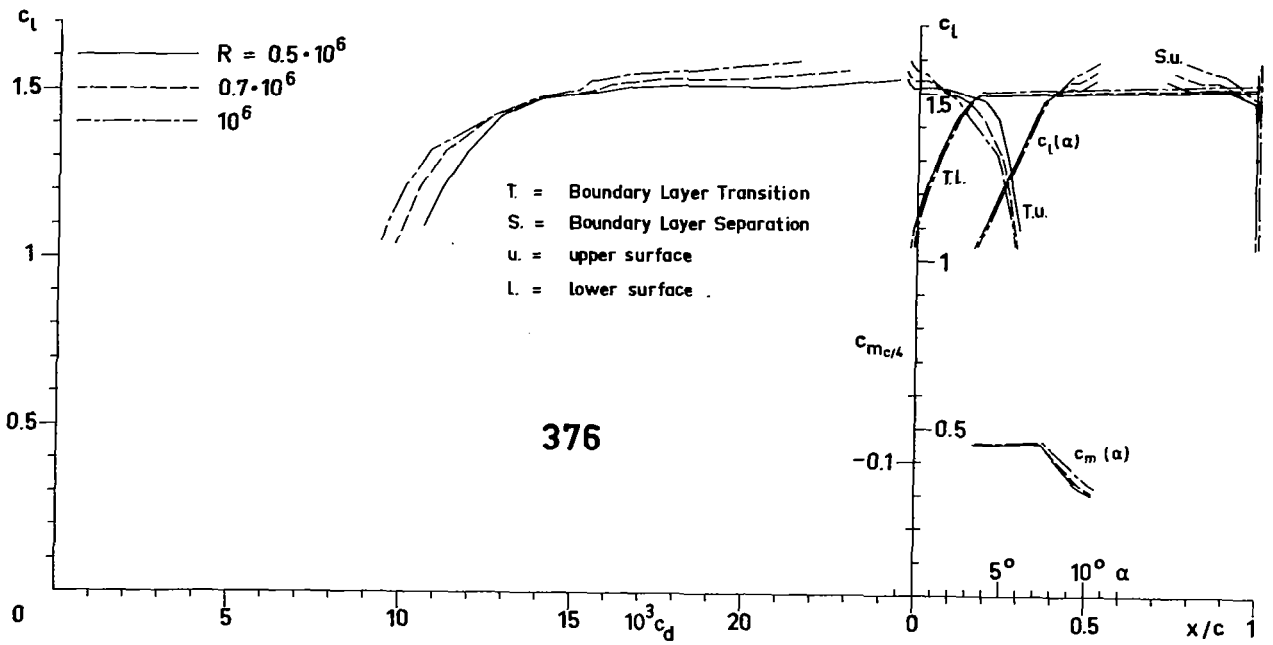

Figure 12.- Theoretical section characteristics for airfoil 376.

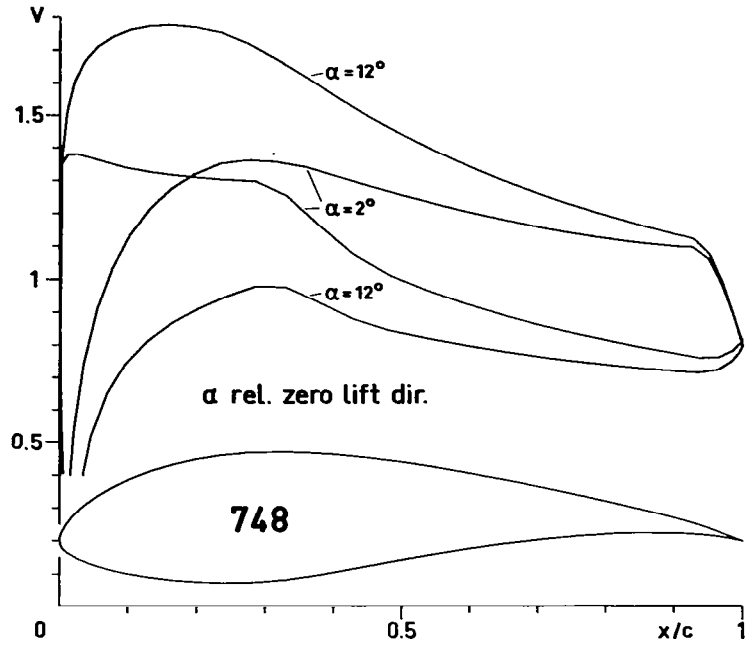

Figure 13.- Velocity distributions for airfoil 748.

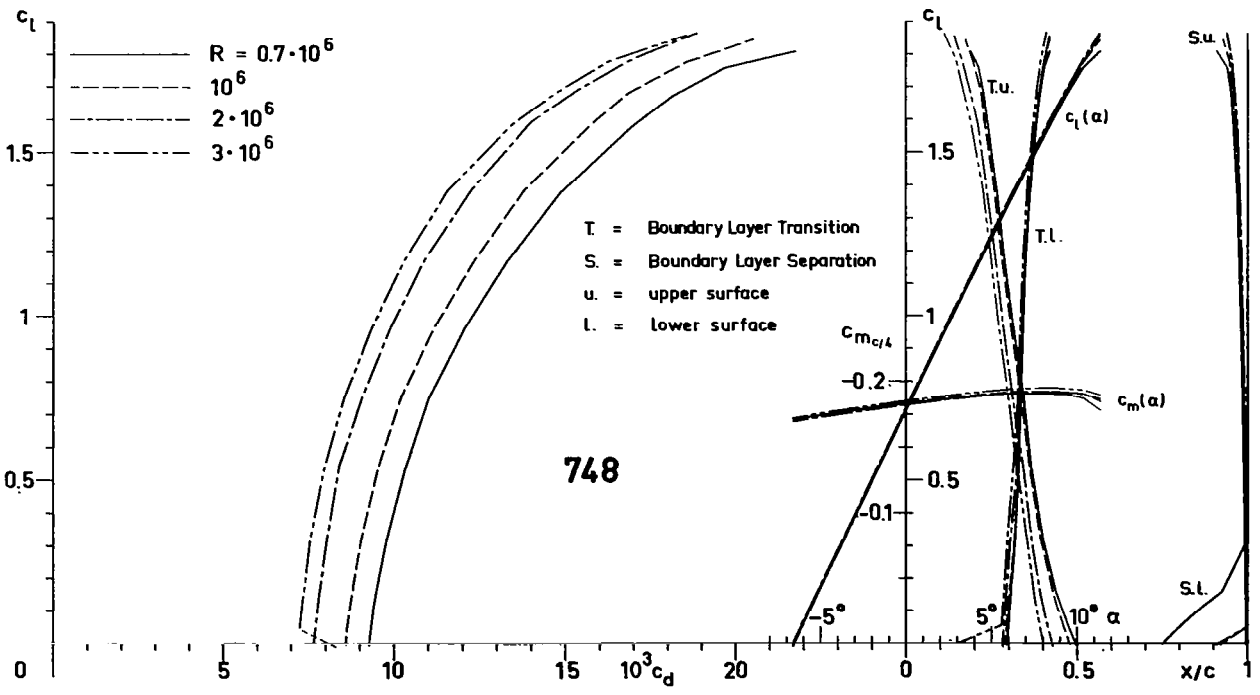

Figure 14.- Theoretical section characteristics for airfoil 748.

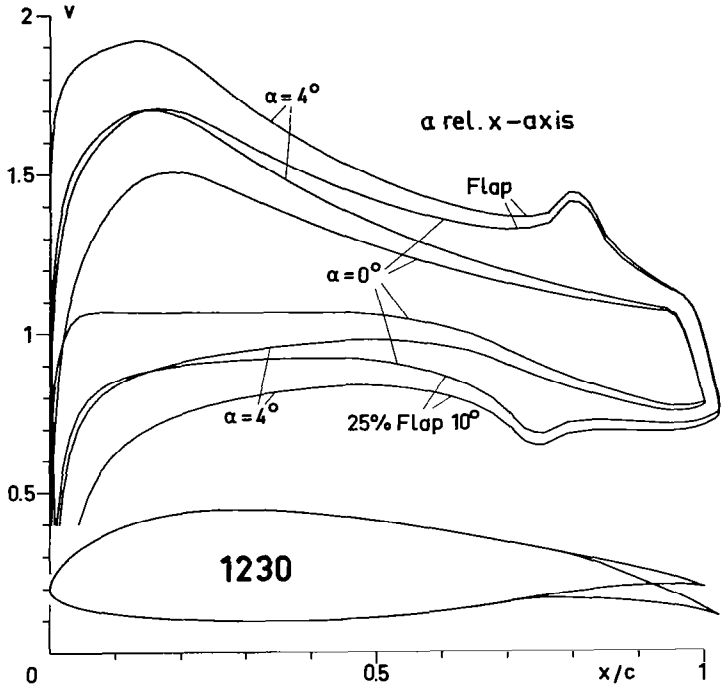

Figure 15.- Velocity distributions for airfoil 1230.

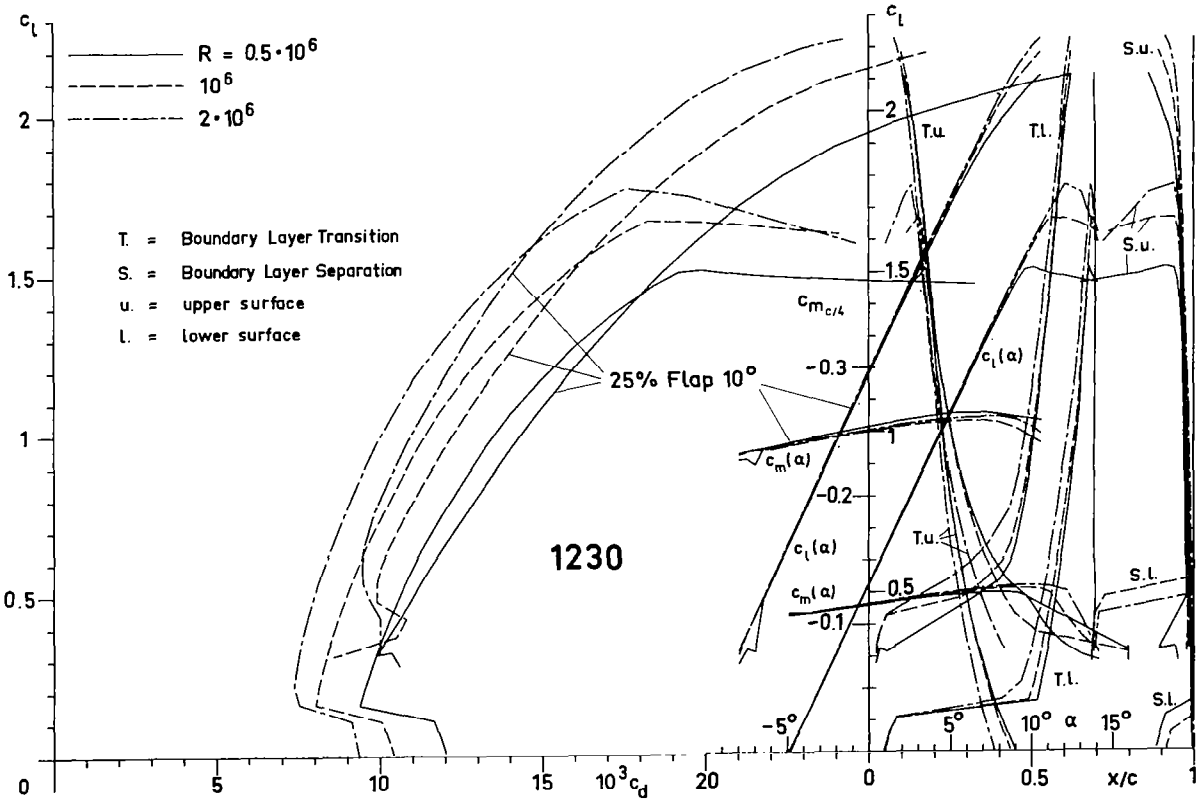

Figure 16.- Theoretical section characteristics for airfoil 1230.

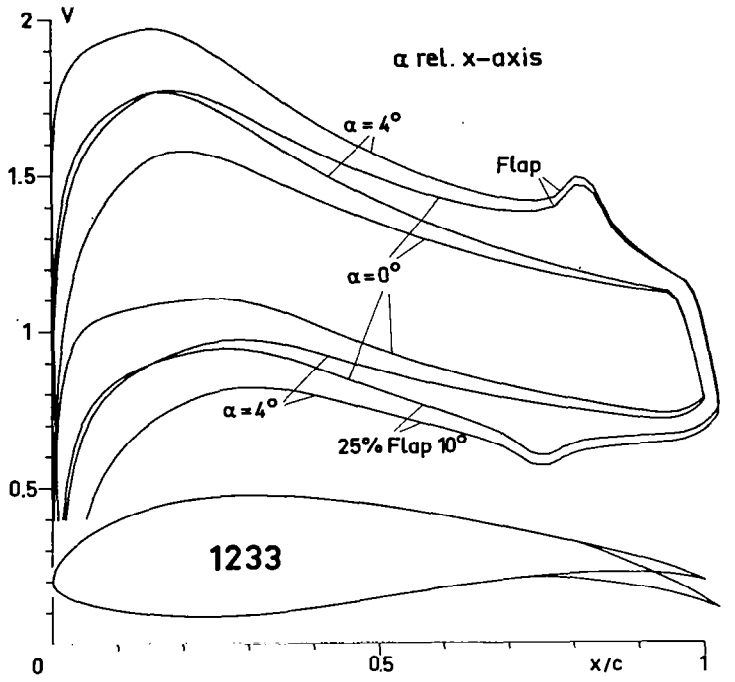

Figure 17.- Velocity distributions for airfoil 1233.

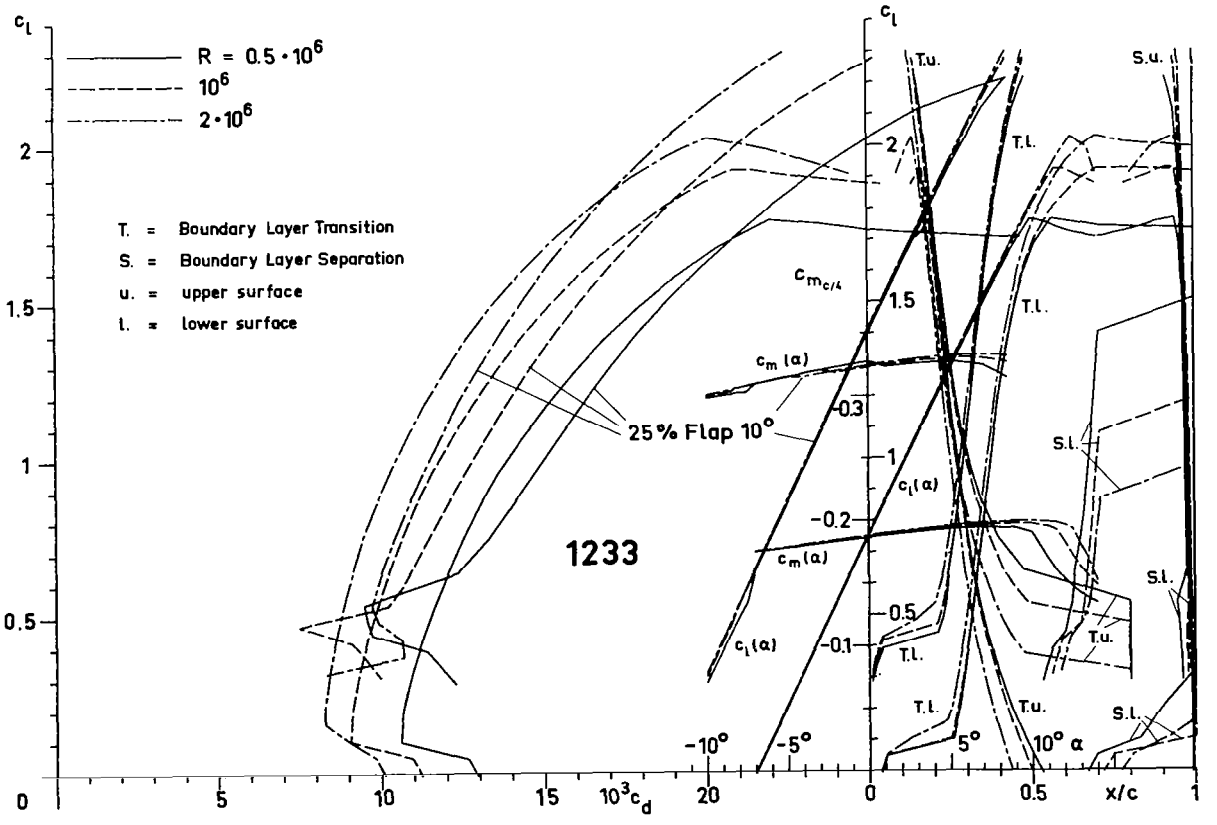

Figure 18.- Theoretical section characteristics for airfoil 1233.

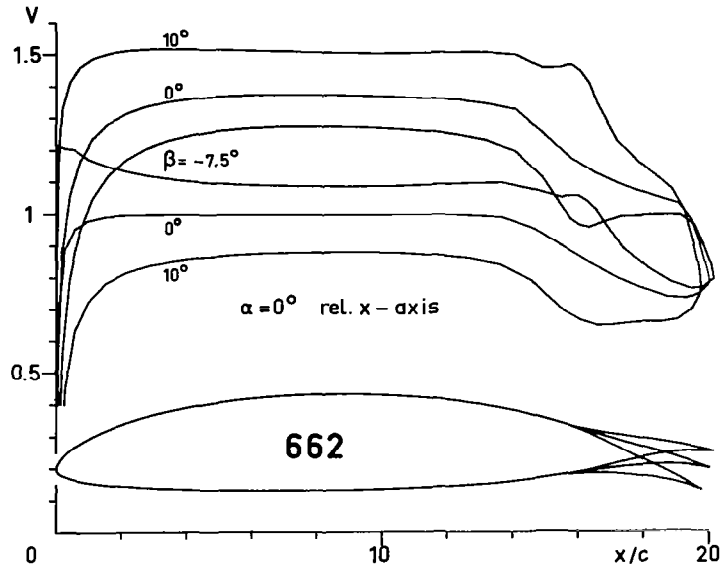

Figure 19.- Velocity distributions for airfoil 662.

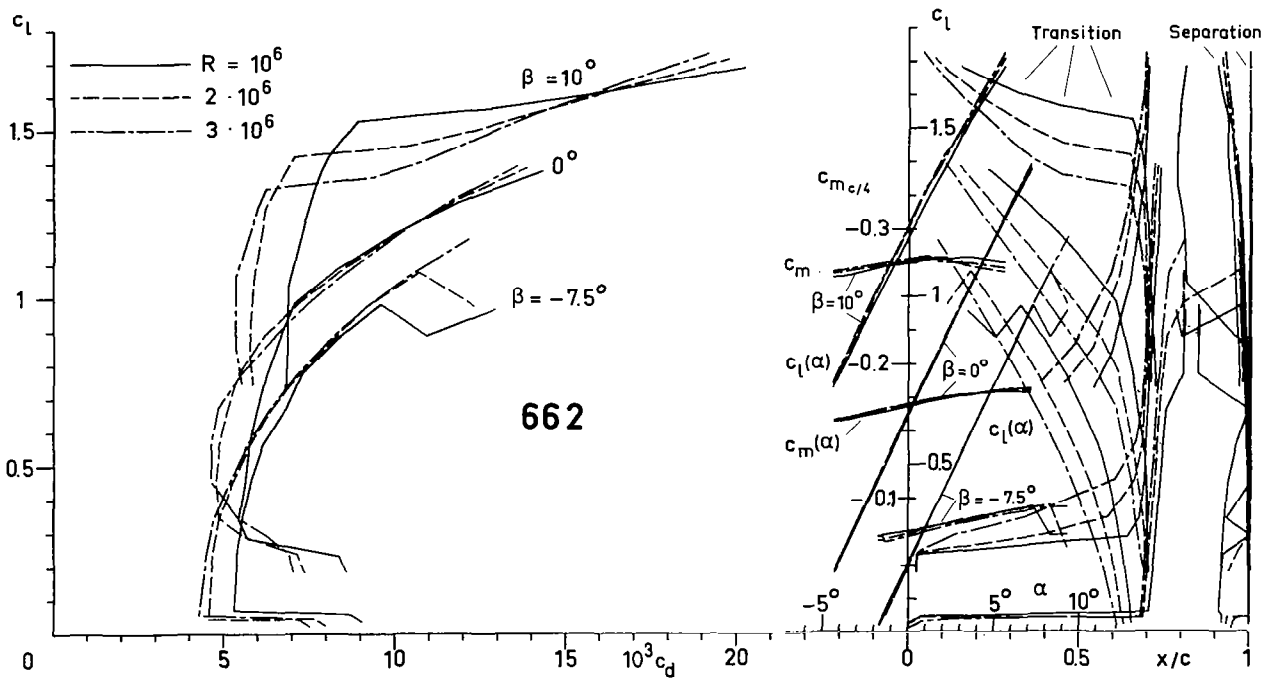

Figure 20.- Theoretical section characteristics for airfoil 662.

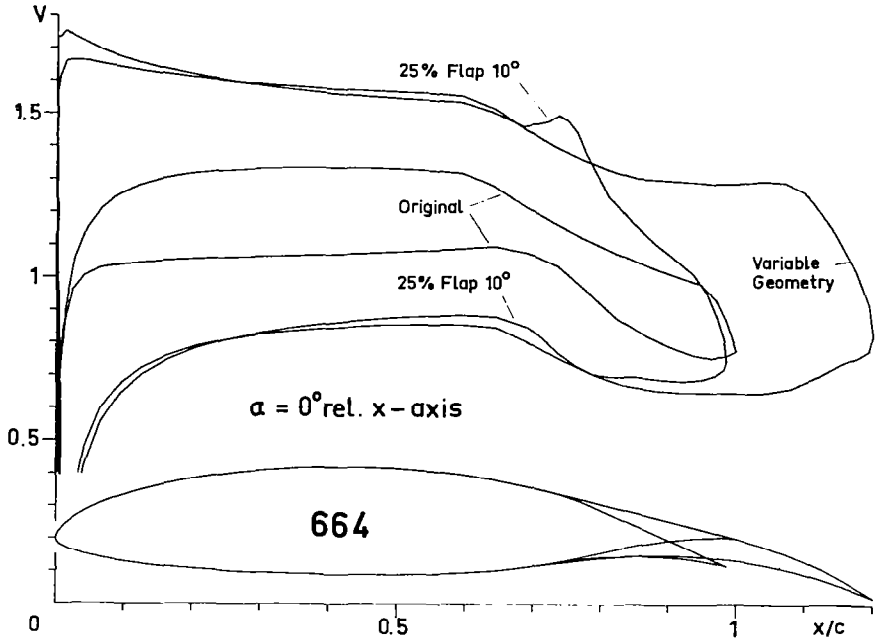

Figure 21.- Velocity distributions for variable geometry airfoil 664.

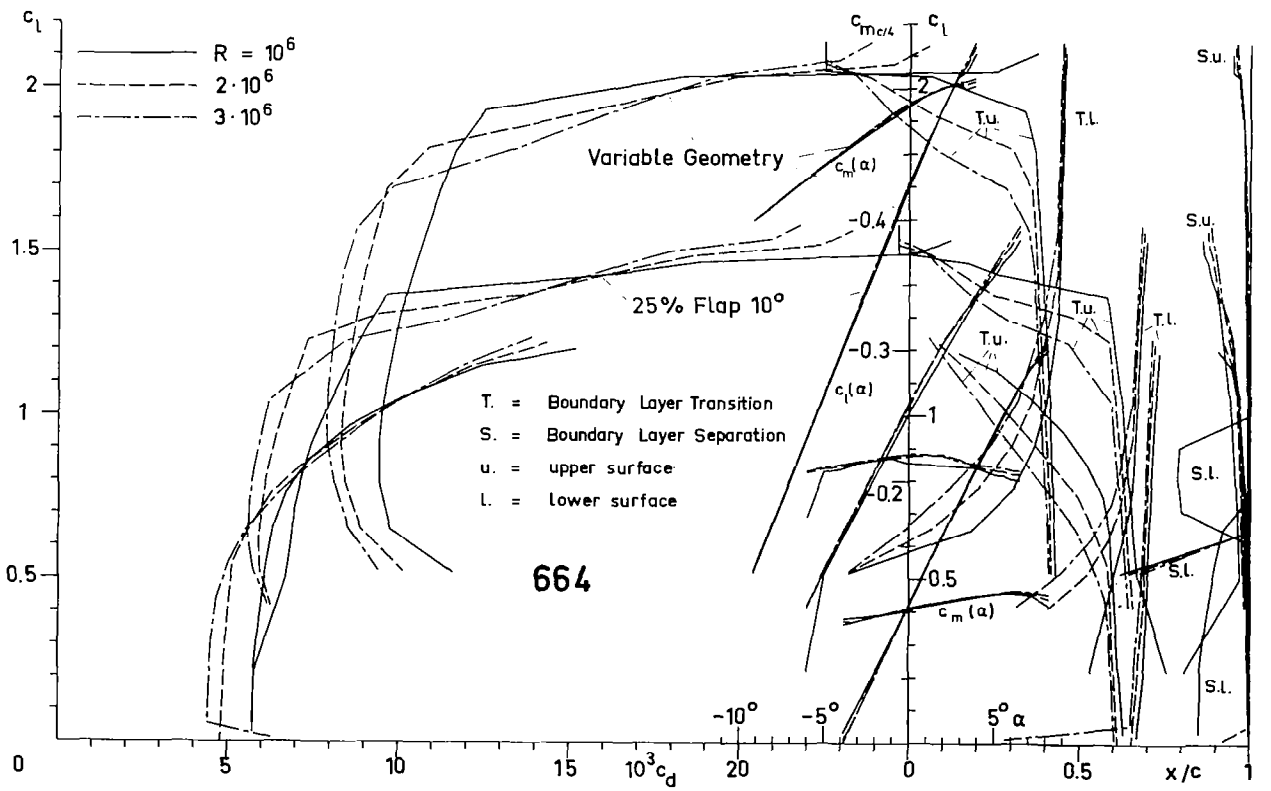

Figure 22.- Theoretical section characteristics for variable geometry airfoil 664.

A COMPARISON OF THE AERODYNAMIC CHARACTERISTICS OF EIGHT SAILWING AIRFOIL SECTIONS

Mark D. Maughmer*
Princeton University

SUMMARY

Because of its light weight, simple construction, and good aerodynamic performance, the Princeton sailwing may be a competitive alternative to conventional wings for many low-speed applications such as ultralight sailplanes, man-powered aircraft and high-performance hang gliders. The operational characteristics of the sailwing are discussed with some emphasis placed on the importance of the trailing-edge cable tension as it controls several aerodynamic properties. The three-dimensional aerodynamic characteristics of eight different sailwing profile sections have been obtained from wind tunnel tests and the results compared to determine the magnitude of the aerodynamic penalties paid for various structural simplifications. For the sectional thickness ratios considered in this research, it is concluded that, while the basic double-membraned sailwing has exceptional aerodynamic performance, even superior for some applications to the conventional hardwing, any notable deviation from this configuration results in an unacceptably large performance penalty.

INTRODUCTION

While there is currently a great deal of interest in the use of flexible wings for use on hang gliders, man-powered aircraft, and ultralight sailplanes, the design and evaluation of these vehicles is complicated a great deal by the fact that very little data is available to aid in analyzing the aerodynamic characteristics of such aircraft. Although the data presented herein was motivated by a National Science Foundation sponsored research program directed toward optimizing a windmill utilizing the Princeton sailwing, reference 1, it is hoped that these data will be of some value to designers of flexible-winged aircraft.

The Princeton sailwing, which has been under development since 1948, is a unique, semiflexible wing intended to provide the practical ultimate in a light-weight, low-cost lifting surface suitable for a number of low-speed applications. Basically, the structural configuration of the sailwing consists

*Currently with the Department of Aeronautical and Astronautical Engineering, University of Illinois, Urbana, Illinois.

of a leading-edge spar with attached ribs which ideally form a rigid framework supporting a trailing-edge cable in tension. A non-porous, non-stretchable cloth membrane, usually dacron, is then wrapped around the leading-edge and attached to the trailing-edge forming the upper and lower sail surfaces. The purpose of the pre-tensioned trailing-edge is to impart a chordwise tension in the membrane to minimize the deflections caused by the aerodynamic loads. Originally, it was not thought that the performance of such a device would compare favorably to that of a conventional wing; however, as a result of numerous experimental investigations, including those of reference 2, it has been found that the aerodynamic efficiency of the sailwing can indeed approach that of a hard wing.

Specifically, the data presented in this report were obtained as a result of a wind tunnel program which was undertaken and structured in such a manner as to ascertain the relative magnitude of the penalties associated with using a readily available circular cross-sectioned leading-edge as opposed to the D-section normally used in sailwing construction. In addition, the importance of the full double cloth membrane was explored by testing sailwing sections which did not utilize the lower membrane as well as several having only a partial lower membrane. In total, eight wings, identical in all respects except for the airfoil section utilized, were tested and compared.

In addition to the experimental development the sailwing has undergone, it should be noted that it has also received considerable analytical treatment such as that discussed in references 3-5.

SYMBOLS

b	Span
$\bar{c}$	Geometric mean chord
q	Dynamic pressure
t	Sectional thickness ratio
AR	Aspect ratio
C_D	Drag coefficient, Drag/qS
C_L	Lift coefficient, Lift/qS
C_M	Moment coefficient about the quarter-chord point of the geometric mean chord, $M/q\bar{c}S$
C_T	Trailing edge cable tension coefficient, Tension/qb^2
L/D	Lift-to-drag ratio
S	Wing area

MODEL DESCRIPTION

The tests of the eight different wing profiles, shown in figure 1, were performed in the Princeton University 1.2 m by 1.5 m force-balance wind tunnel. The wing planform utilized in this study is characterized by a span b of .96 m, a geometric mean chord $\bar{c}$ of .113 m, and a total area S of .108 square meters. The planform aspect ratio $AR = b^2/b\bar{c}$ is equal to 8.5. Relative to the length of the geometric mean chord, the sectional thickness ratio t is 11.5 percent. It was possible to adjust the tension of the trailing-edge cable in each of the models which, for the results discussed herein, was set at 42 N as well as 160 N. These settings yield a trailing-edge cable tension coefficient C_T of .07 and .28 respectively.

TEST CONDITIONS AND DATA REDUCTION

Most of the data collected in the series of experiments included in this report were obtained with the tunnel speed adjusted to yield a dynamic pressure q of 622.4 N/m^2. Although the corresponding Reynolds number based on the geometric mean chord is calculated to be approximately 230,000, because of the turbulence level in the tunnel, the aerodynamic data collected is considered to be qualitatively representative of a Reynolds number on the order of 750,000. In any case, the test results were obtained at a Reynolds number above the subcritical value for which laminar separation dominates and are therefore indicative of the operating conditions expected for somewhat higher Reynolds numbers.

The mounting of one of the test models in the wind tunnel is shown in figure 2. By means of an electrically driven tail-jack, it was possible to adjust the wing angle-of-attack to any value between -12 and +24 degrees while the tunnel was in operation. Thus, force balance data for lift, drag, and pitching moment were obtained at each two-degree angle increment between these limits. The test data were then reduced to the standard coefficient form and plotted as a function of the wing angle-of-attack as referenced to the unloaded (no-wind) orientation of the geometric mean chord, figures 5-8. In addition, the performance of each wing is summarized in a plot of lift-to-drag ratio as a function of lift coefficient, figures 9-10, and lift coefficient as a function of drag coefficient, figures 11-12.

CHARACTERISTICS OF THE SAILWING

Because many of the properties of the Princeton sailwing are uniquely different from those of a conventional hard wing, it is appropriate to discuss its operation to better understand the overall aerodynamic characteristics. For example, when the sailwing is at rest (no-wind), the cloth membrane is held taut by the trailing-edge cable and is essentially, except for the leading-edge, a symmetrical section as the upper and lower surfaces experience the same

pressure, figure 2. As the wing experiences airloads in a net lifting orientation (wind-on), the asymmetrical pressure distribution that is established between the upper and lower surfaces causes the membrane (or membranes) to displace away from the high pressure regions (underside) and move toward the low pressure regions (upperside). Thus, when a section is at an angle of attack greater than that of zero-lift, figure 3, it assumes a positive camber distribution that fairs the membrane in smoothly with the shape of the airfoil leading edge. It should be noted that the actual shape of the sailwing section is a function of the wind velocity, the angle-of-attack, the no-wind airfoil shape, and the amount of tension in the trailing-edge cable. Thus, as the angle-of-attack is increased, the resulting increased pressure differential between the upper and lower surfaces causes the amount of camber in the section to increase. This situation not only causes the maximum value of wing efficiency, the lift-to-drag ratio, to occur at relatively high lift coefficients, but also delays the impending stall. At this point, the importance of maintaining the desired trailing-edge cable tension should be noted. As might be expected, relaxing the cable tension allows a greater amount of camber to be established and therefore a higher maximum lift coefficient is obtainable; however, simultaneously, the maximum lift-to-drag ratio is decreased as well as the threshold of critical velocity at which detrimental sail luffing occurs. Thus, the amount of tension in the sailwing trailing-edge cable controls an important trade-off between the maximum lift coefficient and the maximum lift-to-drag ratio. It might be considered that as the cable tension becomes higher, the sailwing behavior is more like that of a rigid wing while as it becomes lower, the behavior approaches that of a high aspect ratio Rogallo wing.

Another interesting characteristic of the lifting sailwing is the upward deformation of the trailing-edge in the unsupported mid-span regions of each wing-panel, figure 4. The result of this action is a reduced angle of attack in these regions and one would expect a local reduction in lift; however, it is generally the case that this effect is more than offset by the increased amount of camber that occurs which results in a local increase in the generation to lift. In fact, because of this effect, the span lift distributions that occur over many of the sailwings that have been tested are often very close to that of the elliptical optimum.

The constant chordwise tension that is a result of the trailing-edge cable and the catenary-arc sail cut is responsible for many of the desirable features of the sailwing over other flexible designs. One such feature is that relatively low drags are present at low angles-of-attack and lift coefficients. Furthermore, unlike many flexible wing designs, the sailwing has the ability to pass smoothly through the zero-lift condition from that of a positive camber and lifting configuration to that of a negative camber and downward loading.

All in all, through many years of extensive research, the sailwing has been found to provide a simple, light-weight, and low-cost alternative to the conventional hard wing while not suffering any notable performance penalties throughout many low-speed applications.

PRESENTATION AND DISCUSSION OF TEST RESULTS

Representative three-dimensional lift, drag, and moment curves for four of the eight sailwing models tested are presented in the plots of figures 5-8. For each wing tested, the lift coefficient, drag coefficient, and pitching moment coefficient about the quarter-chord point, are plotted as a function of the angle-of-attack of the unloaded geometric mean chord. The lift-to-drag ratio as a function of lift coefficient for all of the sections tested are plotted in figures 9-10 while the drag polars, lift coefficient as a function of drag coefficient, are presented in figures 11-13. Finally, the typical effect of lowering the trailing-edge cable tension coefficient on the lift-to-drag ratio and the drag polar are shown in figures 14-15.

It is important to note that a direct comparison of these data to those of a conventional wing is complicated a great deal by the flexible nature of the sailwing. For example, the sailwing data can be likened to that of a rigid wing in which an automatic flap is deflected an additional amount for each incremental increase in angle-of-attack. This characteristic is responsible for the fact that it is generally impossible in the case of a sailwing to linearize the drag polar or obtain a meaningful value for the span-efficiency factor as is done from wind tunnel test data for a conventional wing. Similarly, it should further be noted that at lower angles-of-attack (up to approximately five degrees), it is not uncommon for a sailwing to have a lift-curve slope which significantly exceeds the theoretical thin airfoil maximum for rigid wings of 2π per radian. This occurs because the section is continually varying camber over the angle-of-attack range. At higher angles-of-attack, the section is unable to deform proportionally as much as it does when less loaded and, therefore, as the angle-of-attack is increased to higher values, the lift-curve becomes increasingly more like that of a rigid wing.

The most notable observation in comparing the compilation of data presented in figures 9-12 is the significant performance advantage held by the conventional, double-membraned version tested over the more simplified versions. This advantage is so great that it is inconceivable of a situation in which the potential benefit in weight saving, cost, or more-simplified construction for any of the modified versions could be justified in relation to the performance penalties.

Examination of these data further indicate an important feature in that the sailwing highest L/D values occur in a range of relatively large values of lift coefficient. Furthermore, the flexible nature of the sailwing affords it low drag coefficient values over a relatively wide range of lift coefficients, particularly in the case of the double-membraned sections.

In order to further emphasize the fact that unlike a conventional wing, the shape of the sailwing section is governed by the dynamic pressure (wind velocity), a polar for sailwing model 2 is shown in figure 13 for the case of a constant wing loading. This polar was obtained by adjusting the tunnel velocity such that the lift force remained constant throughout the angle-of-attack range and is representative of the aerodynamic characteristics over the

speed range of an aircraft in level flight where the load factor is equal to unity. Thus, the high-speed flight conditions correspond to the lower lift coefficients while the low-speeds correspond to lift coefficients approaching the maximum value at stall. For comparison, the constant velocity polar of sailwing model 2 is also shown in figure 13. The difference between these two plots, excepting for the small contribution due to the changing Reynolds number over the speed range for the constant wing loading case, can be attributed to the flexible nature of the sailwing. For an equivalent hard wing, one would expect these two plots to be nearly identical. From the figure, it should be noted that the sailwing maximum lift-to-drag ratio of twenty, corresponding to the tangent to the curve drawn from the origin, occurs at a fairly high lift coefficient and that the operating range of low drag values is fairly wide. It is important to note, however, that in order to maintain a suitably high test Reynolds number these data were collected at a wing loading of 598 N/m^2 which is relatively high for most motorless applications. More practical wing loadings would cause the maximum lift-to-drag ratio to correspond to slightly lower lift coefficient values.

In attempting to generalize the effect of the different leading edge shapes employed, it is apparent that those sections having the smaller radius version have a wider region of low drag although, for the most part, the actual minimum values of the drag coefficient are slightly lower for the more rounded leading edge shape. Furthermore, as expected, the more pointed cross-section is accompanied by more abrupt stalling characteristics. Lastly, particular attention should be paid to the comparatively poor performance delivered by the often employed circular leading edge.

The effects of lowering the trailing edge cable tension are as expected and summarized by the data plotted in figures 14 and 15. Briefly a reduction of the trailing edge cable tension leads to a higher value of the lift curve slope, gentler stalling characteristics, a higher value of the maximum lift coefficient, and a generally lower value of the maximum lift-to-drag ratio; however, it should be noted, as observed in figure 14, that the lower trailing edge cable tension results in larger lift-to-drag ratios occurring in the region near the maximum lift coefficient.

CONCLUSIONS

In reviewing the applicability of the data presented herein, it should be born in mind that the quantitative information becomes less valid as deviation occurs from the equivalent test Reynolds number; however, as the test condition is above that of the critical Reynolds number, the trends, relationships, and approximate values of the data should remain valid to somewhat higher values. In addition, note that the sectional thickness ratios employed for those tests are somewhat higher than those used on many current hang gliders and should be taken into account when contemplating the use of these test results. In particular, it is expected that the importance of the leading edge shape should diminish as the thickness ratio decreases and the circular leading edge shape should prove adequate, as it often has, for some applications.

In considering the findings of these tests in addition to many others, it has been demonstrated that the three-dimensional performance of the Princeton sailwing is quite competitive with many hard wings of the same aspect ratio. Thus, the use of the sailwing should allow the benefits of simpler construction and lower costs to be realized without paying any significant price in performance. In fact, some consideration should be given to the fact that, unlike many of its rigid counterparts, the cambering characteristics found in the sailwing cause its three-dimensional lift-to-drag ratio to maximize at a fairly high lift coefficient as is desirable for many of the low-speed applications for which the sailwing is suitable. Furthermore, relative to many conventional wing sections, the sailwing has the favorable characteristic of a fairly slow rise in the drag coefficient, and consequently a slow decrease in the lift-to-drag ratio, with increasing values of the lift coefficient.

If one's mind is allowed to freely extrapolate from current trends and the results of this test program, one can envision the reality of a ultralight sailwing sailplane in which a cockpit lever is used to vary the wing trailing edge cable tension. Thus, in operation similar to that of a modern flapped sailplane, the pilot would slacken the cable upon entering a thermal to permit a slow tight circle with a high value of lift coefficient and upon exiting the thermal, pushes the lever to tighten the cable such that a high lift-to-drag ratio for inter-thermal cruise is obtained. Perhaps in the not too distant future, an aircraft of this type might bridge the gap between the limitations of hang gliding and the excessive costs of high performance.

REFERENCES

1. Maughmer, M. D. "Optimization and Characteristics of a Sailwing Windmill Rotor." NSF/Rann/GI-41891/PR/75/4, Princeton University AMS Report No. 1297, July 1976.

2. Fink, M. P. "Full-Scale Investigation of the Aerodynamic Characteristics of a Model Employing a Sail-Wing Concept." NASA Technical Note TN D-4062, July 1967.

3. Ormiston, R. A. "Theoretical and Experimental Aerodynamics of an Elastic Sailwing." Department of Aerospace and Mechanical Sciences, Princeton University, Ph.D. Dissertation, October 1969.

4. Ormiston, R. A. "Theoretical and Experimental Aerodynamics of the Sailwing." Journal of Aircraft, Vol. 8, No. 2, February 1971, pp. 77-84.

5. Mercer, J. E. "Steady and Unsteady Aerodynamics of an Elastic Sailwing: Theory for Design." Department of Aerospace and Mechanical Sciences, Princeton University, Ph.D. Dissertation, April 1970.

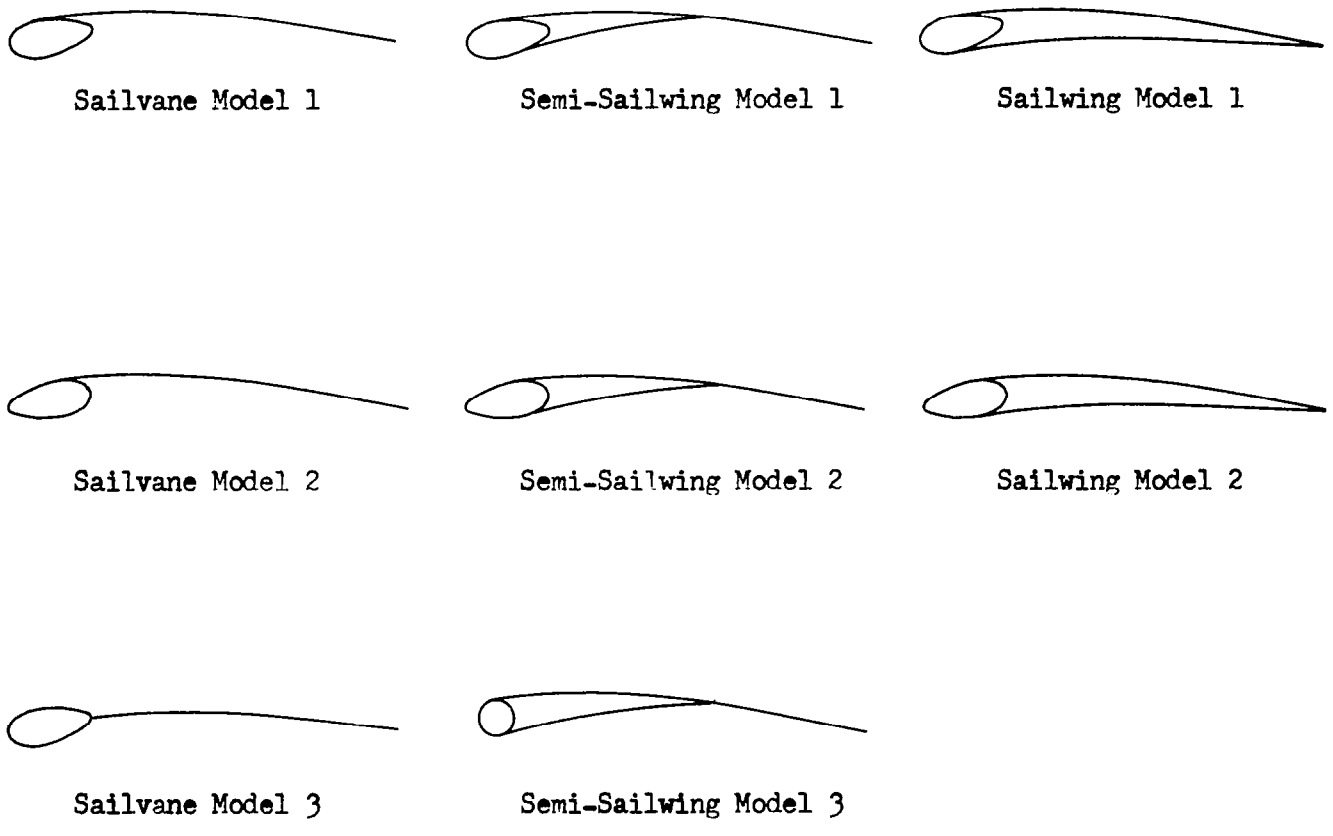

Figure 1.- Sailvane and sailwing sections tested.

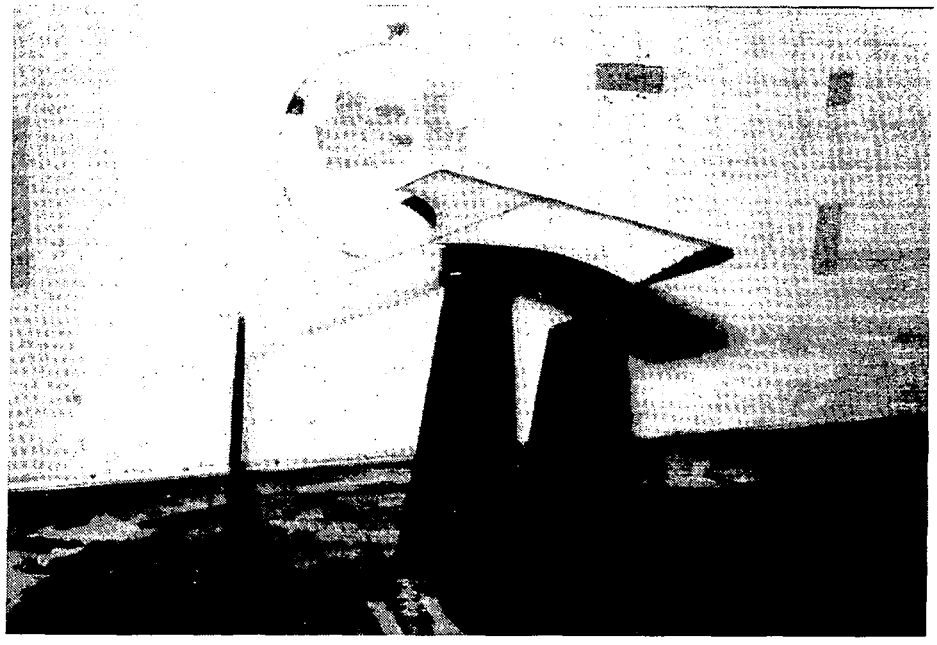

Figure 2.- Typical sailwing model mounted in wind tunnel with wind off.

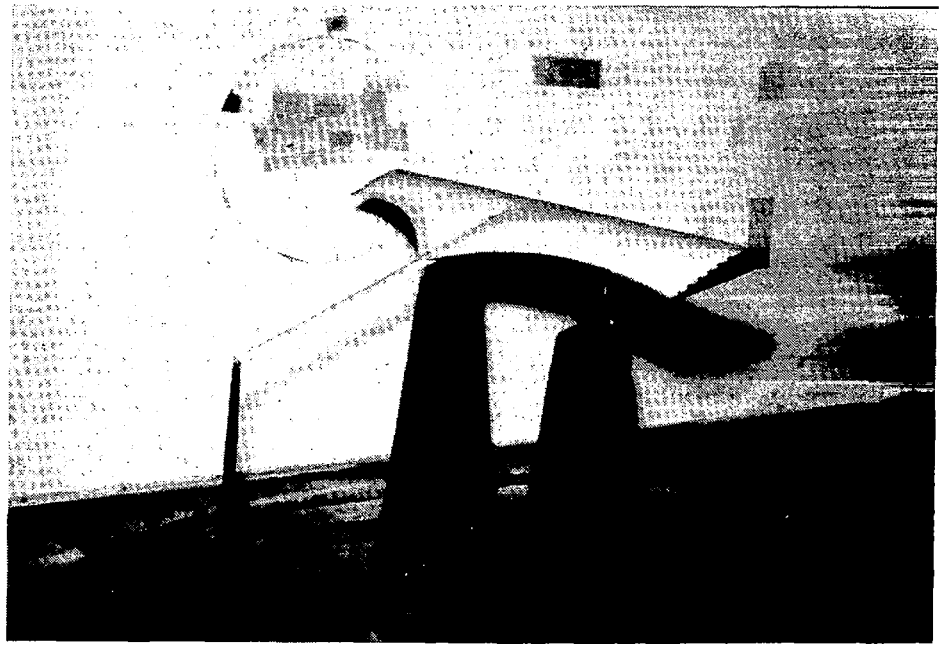

Figure 3.- Sailwing mounted in wind tunnel with wind on.

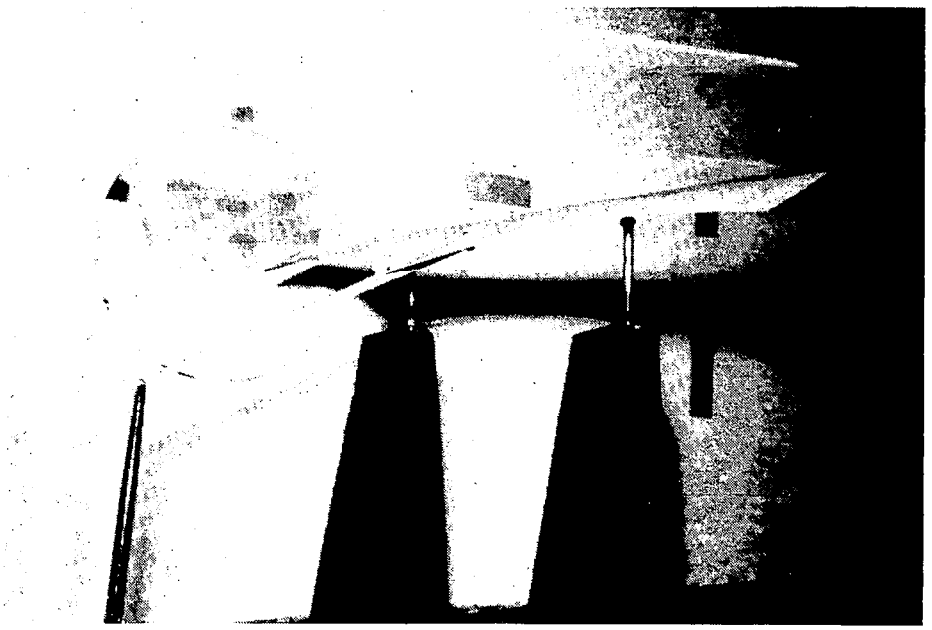

Figure 4.- Detail of sailwing trailing edge deformations.

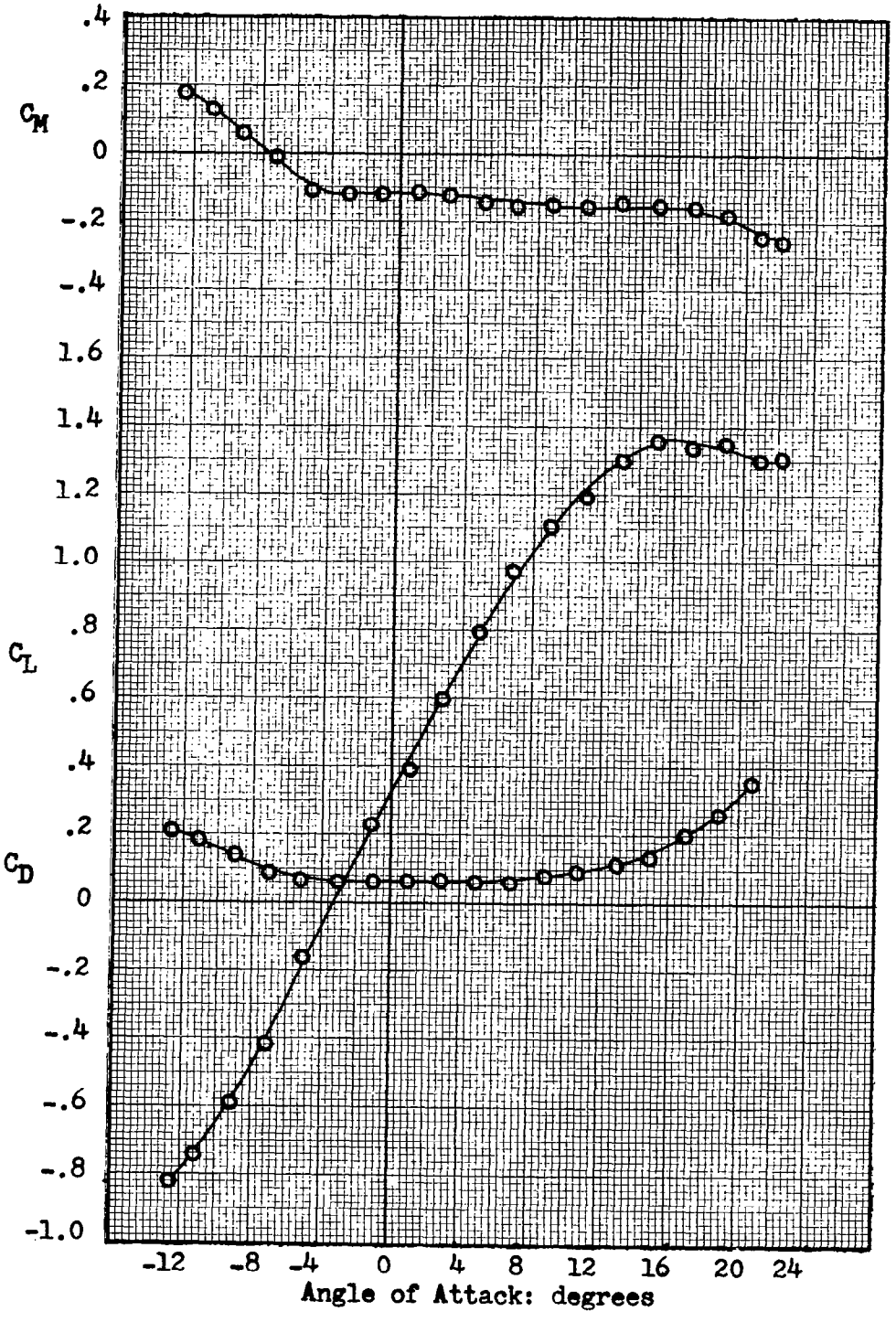

Figure 5.- Aerodynamic characteristics of the sailvane model 2.

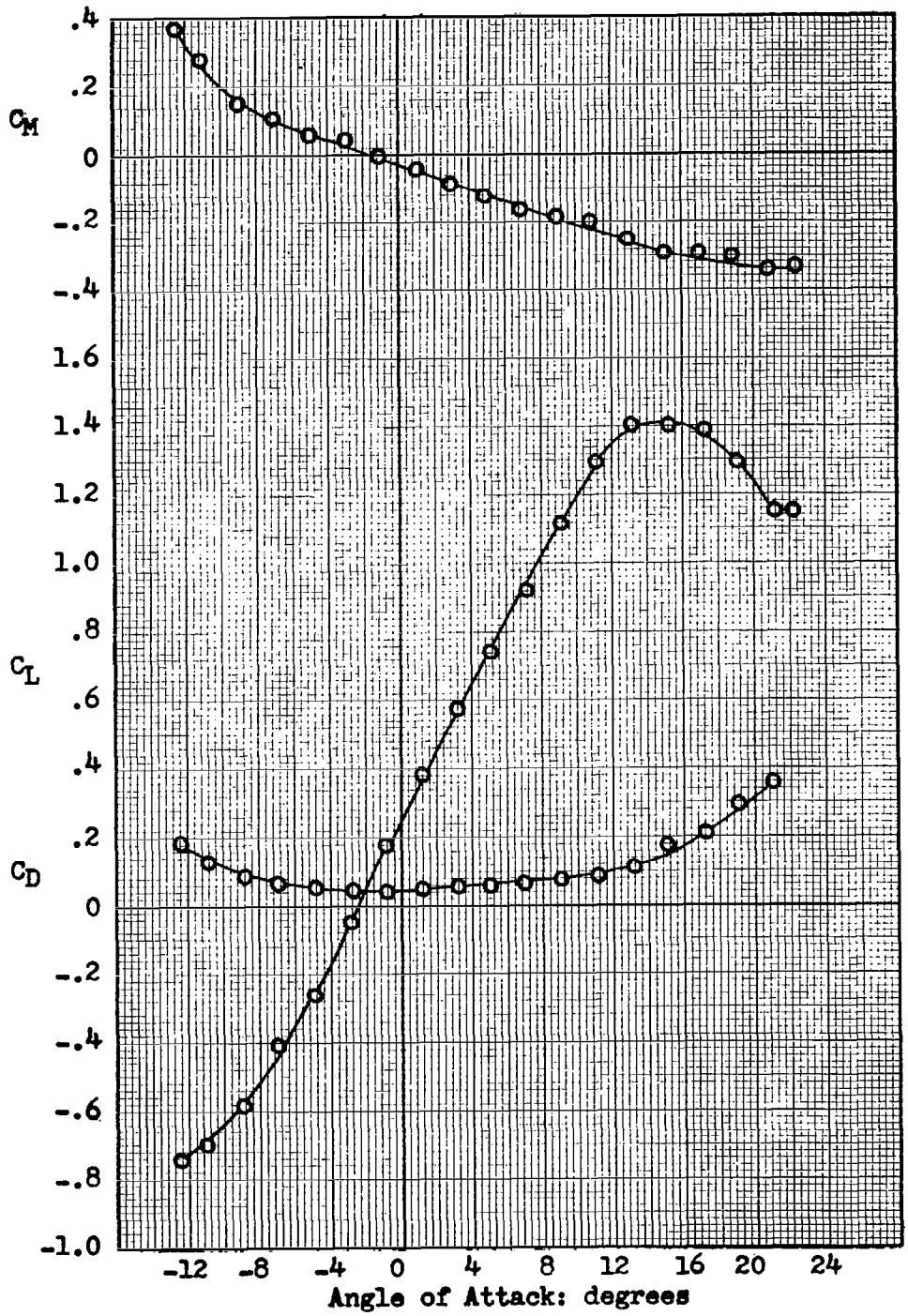

Figure 6.- Aerodynamic characteristics of the semi-sailwing model 2.

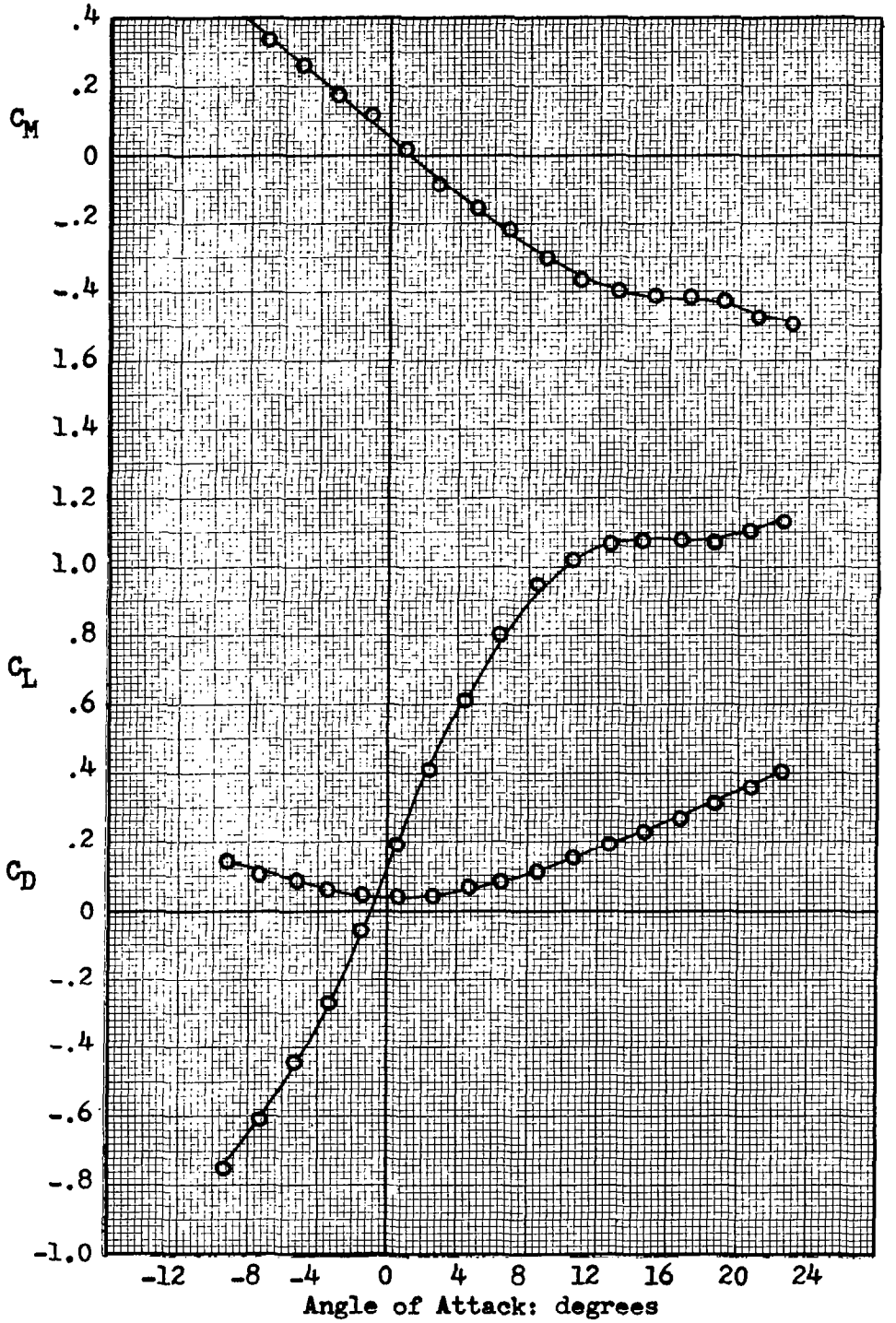

Figure 7.- Aerodynamic characteristics of the semi-sailwing model 3.

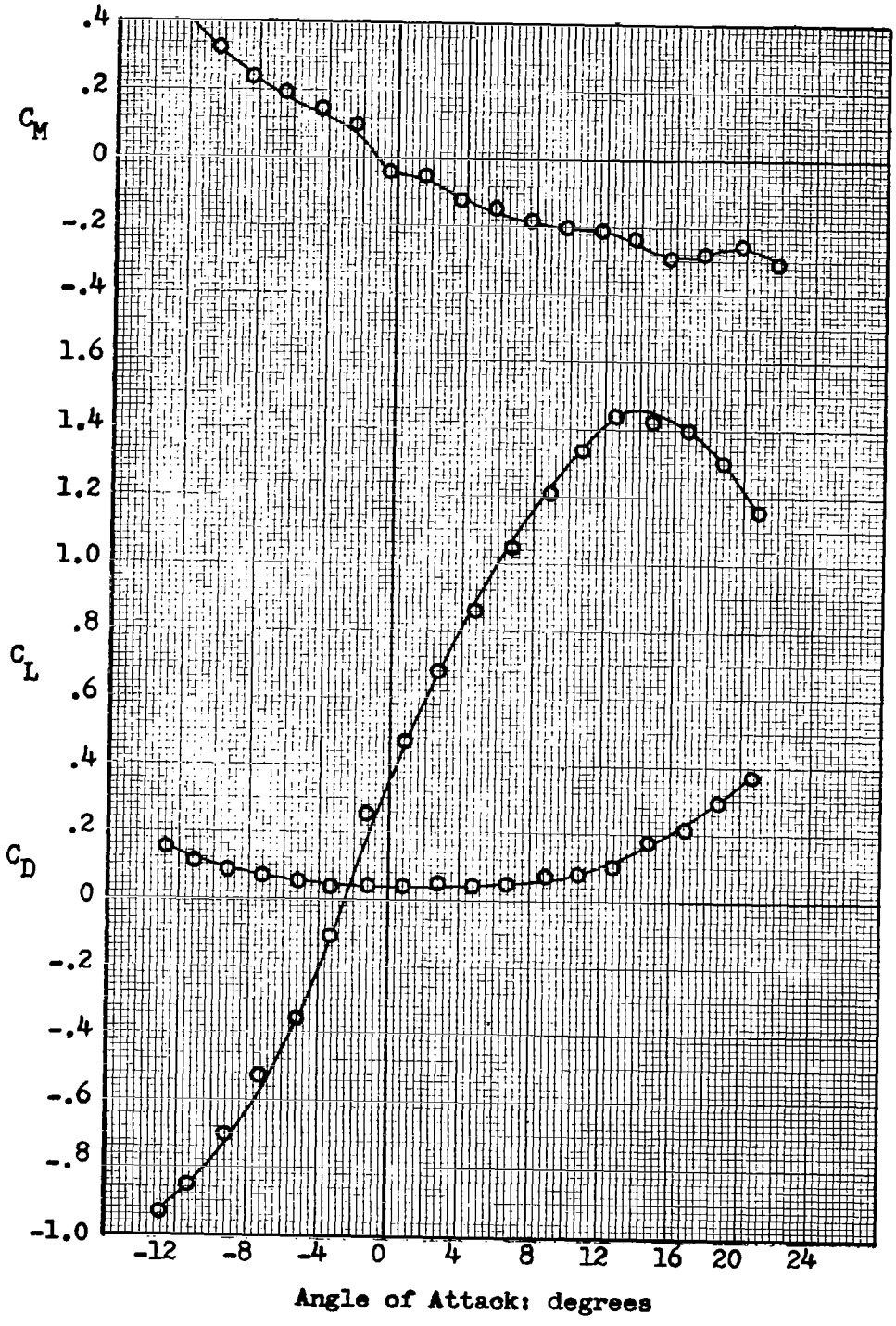

Figure 8.- Aerodynamic characteristics of the sailwing model 2.

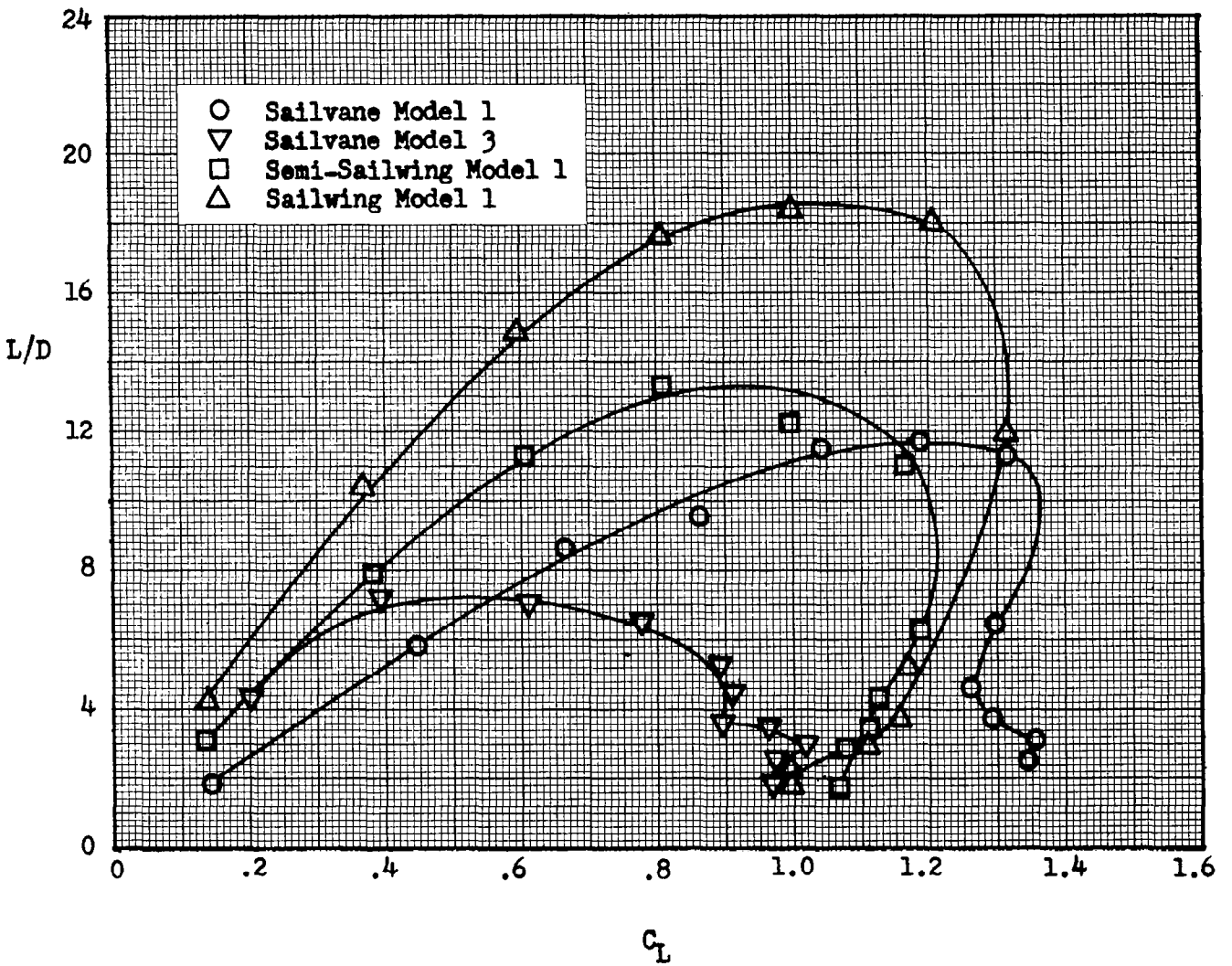

Figure 9.- Composite L/D vs. C_L plot of sailwings with the larger radius leading-edge.

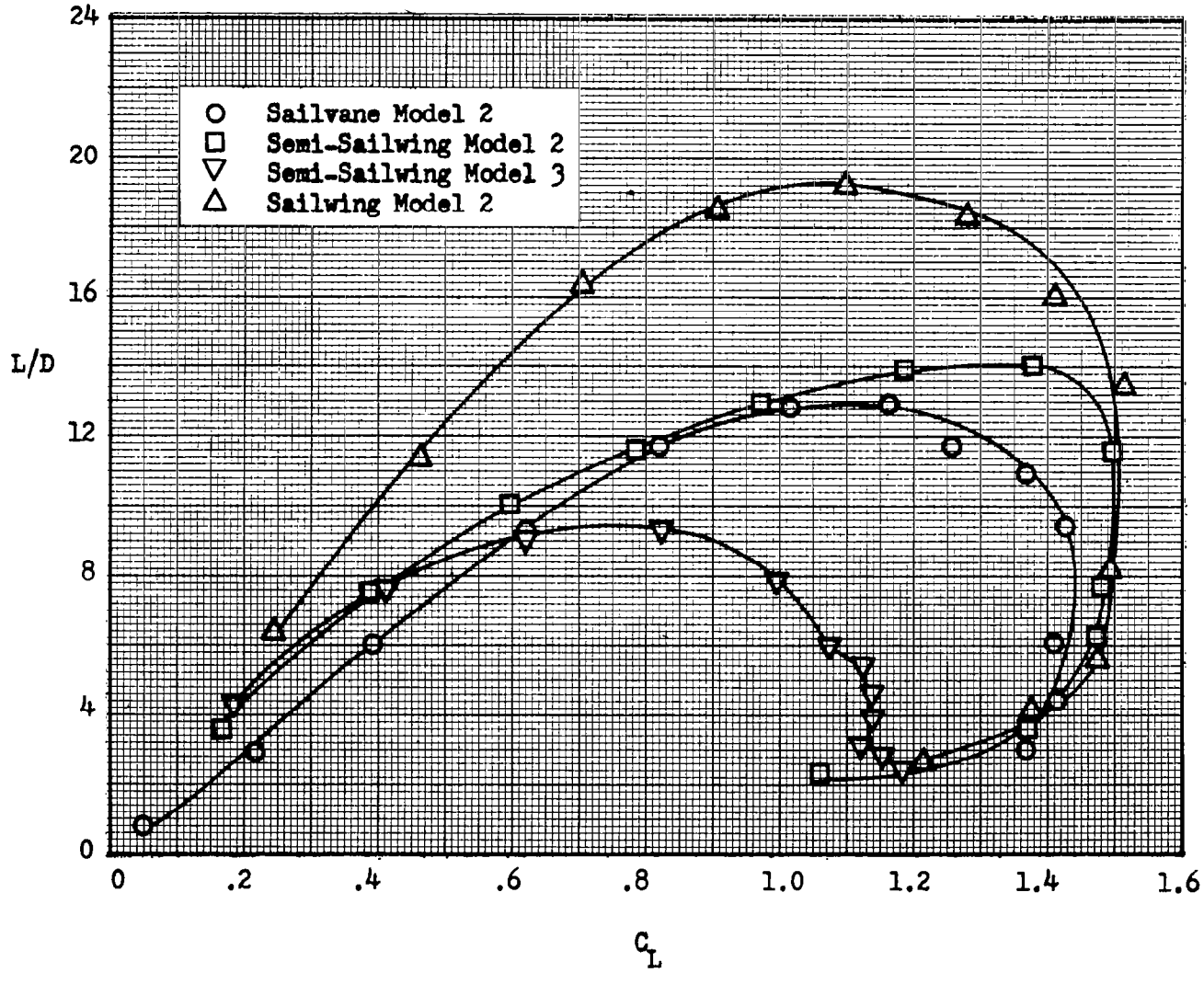

Figure 10.- Composite L/D vs. C_L plot of sailwings with the smaller radius leading-edge.

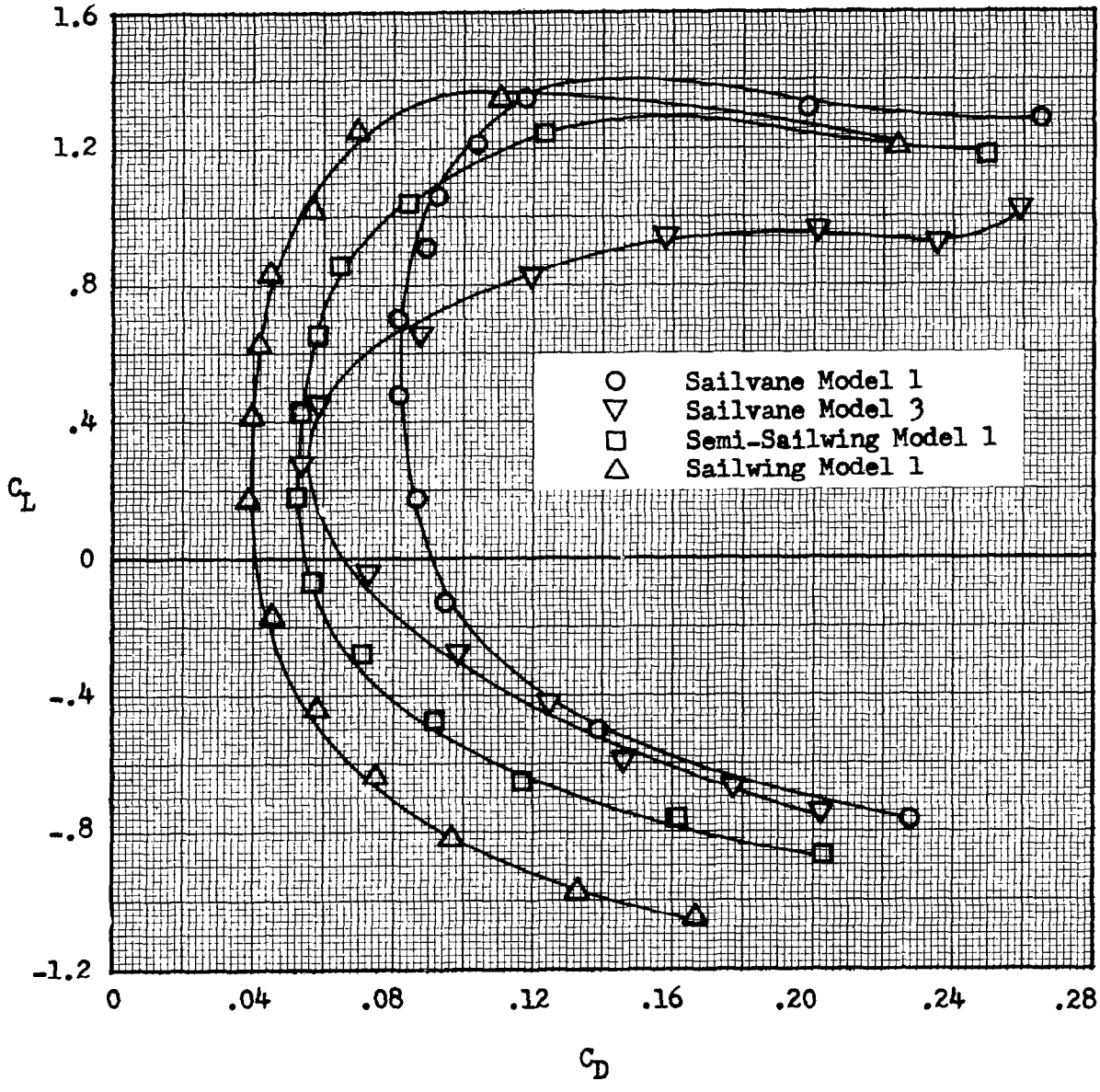

Figure 11.- Composite polar plot of sailwings with the larger radius leading-edge.

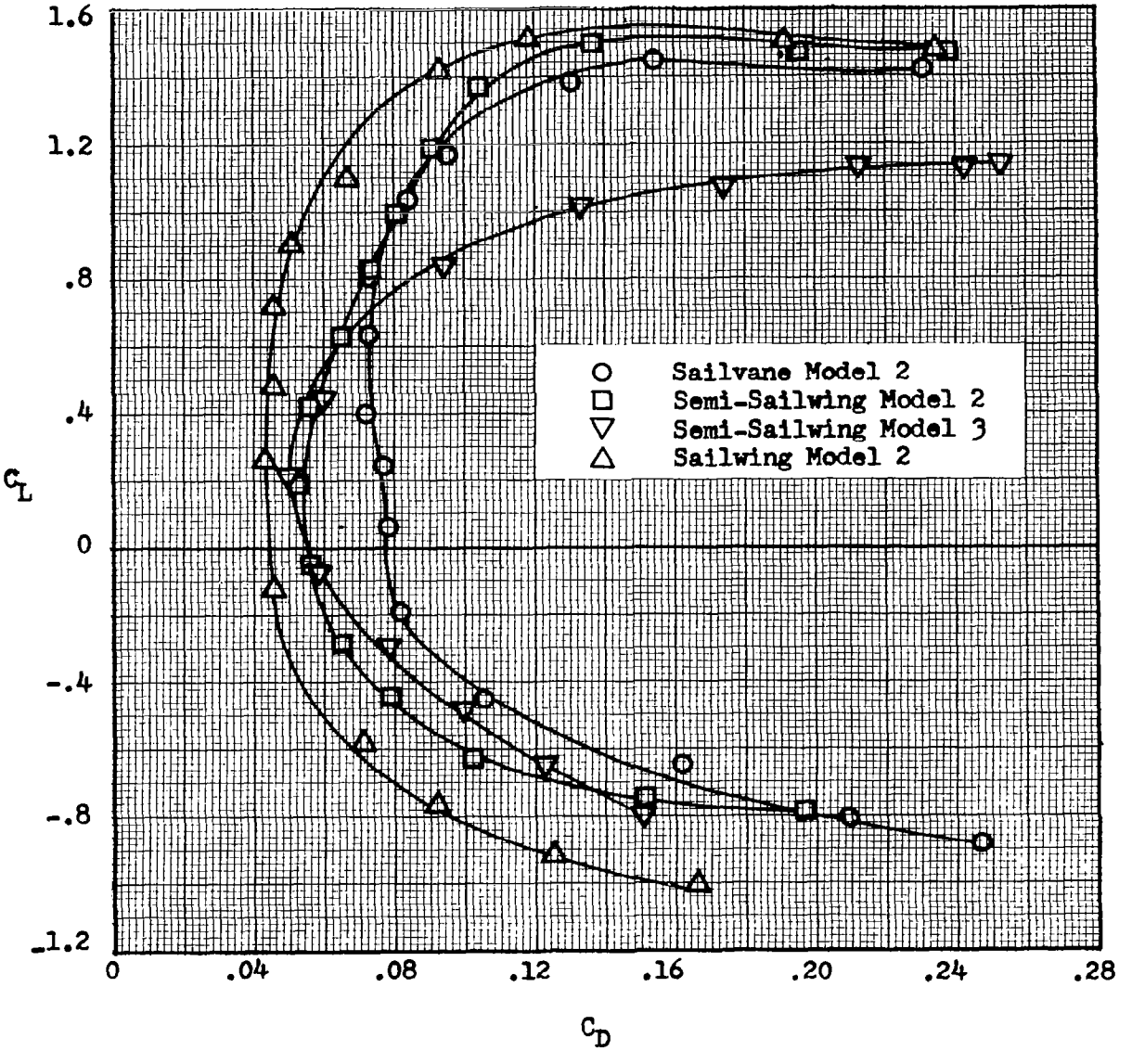

Figure 12.- Composite polar plot of sailwings with the smaller radius leading-edge.

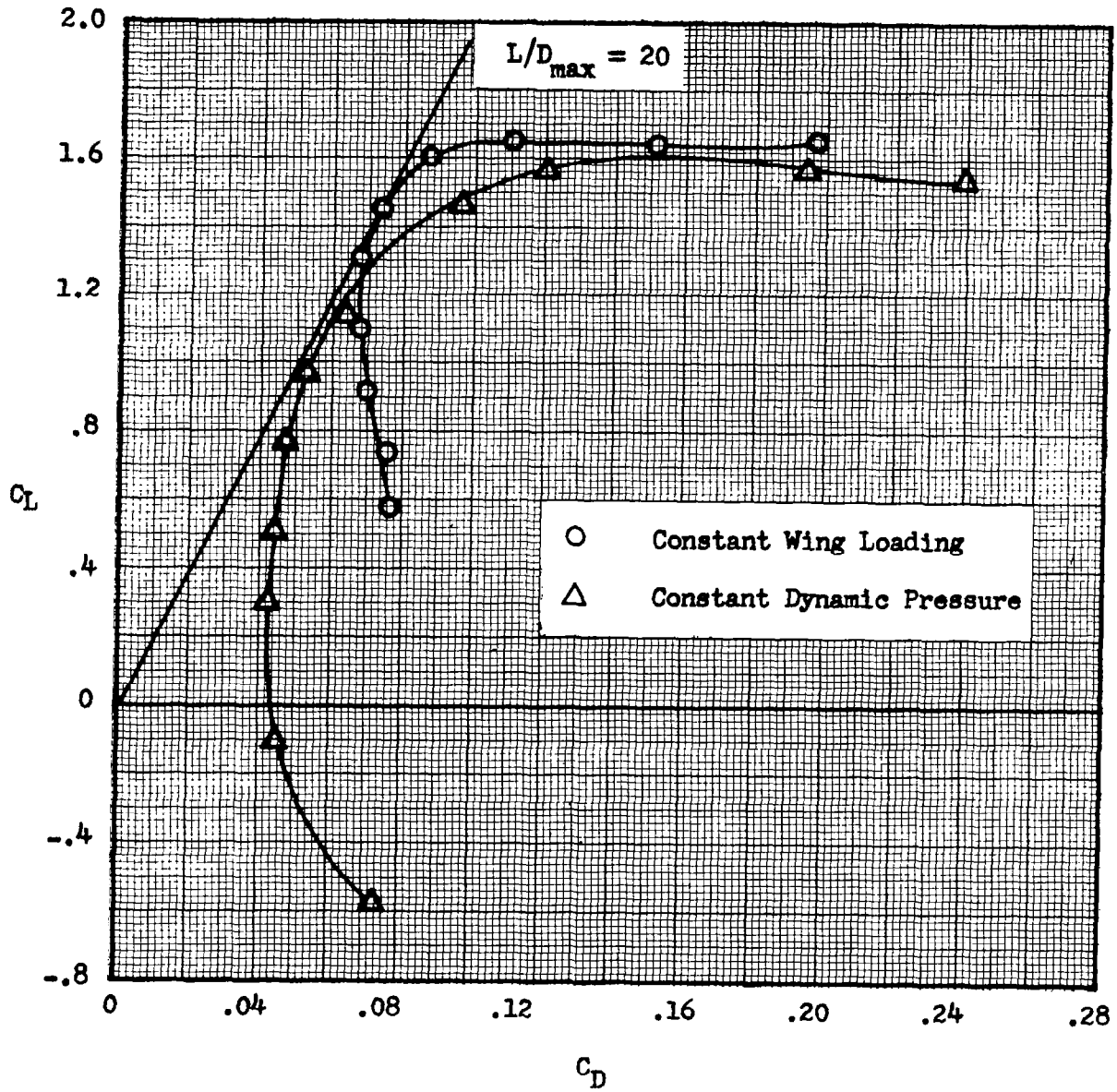

Figure 13.- Sailwing model 2 constant wing loading drag polar compared to the constant dynamic pressure drag polar.

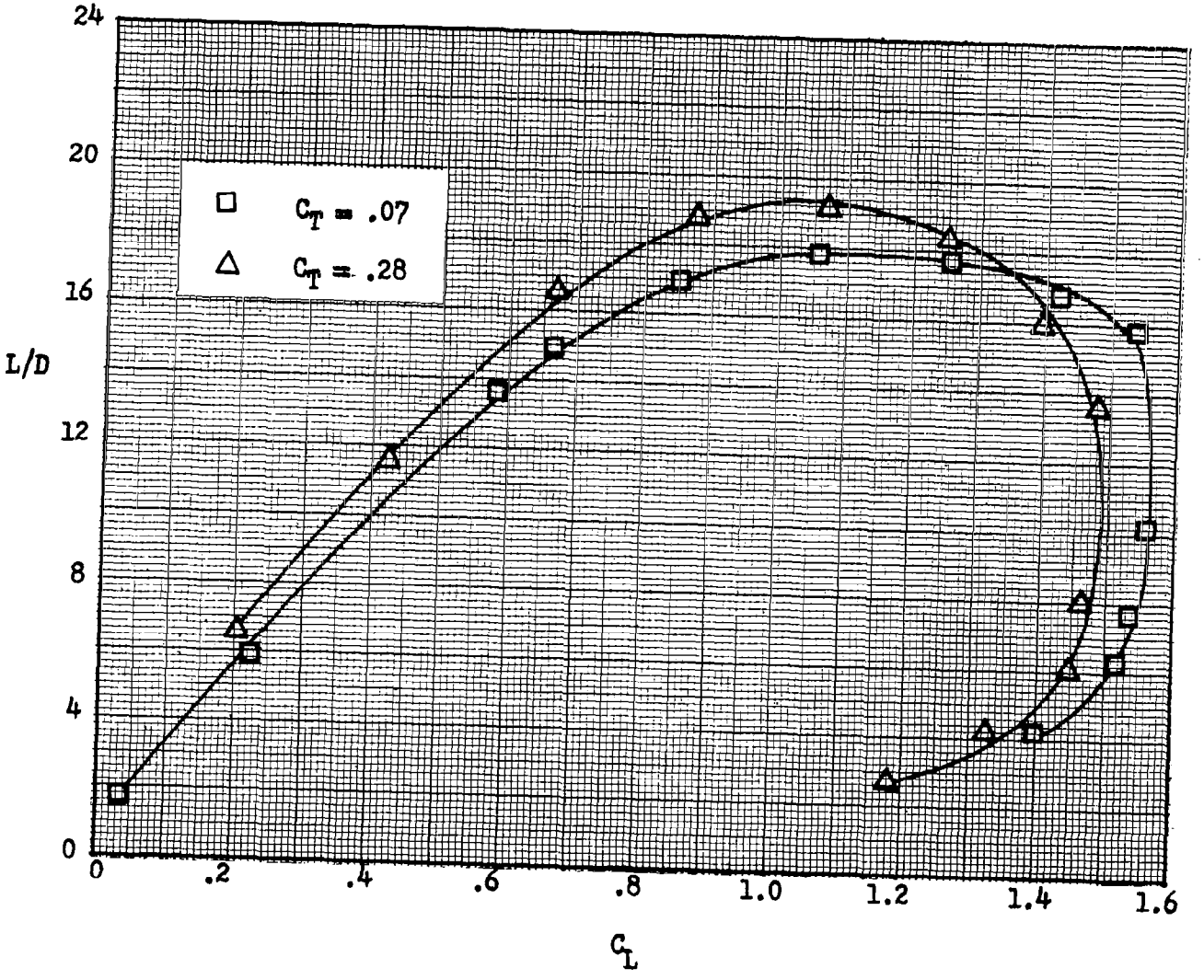

Figure 14.- Effect of sailwing trailing-edge cable tension on lift-to-drag ratio: sailwing model 2.

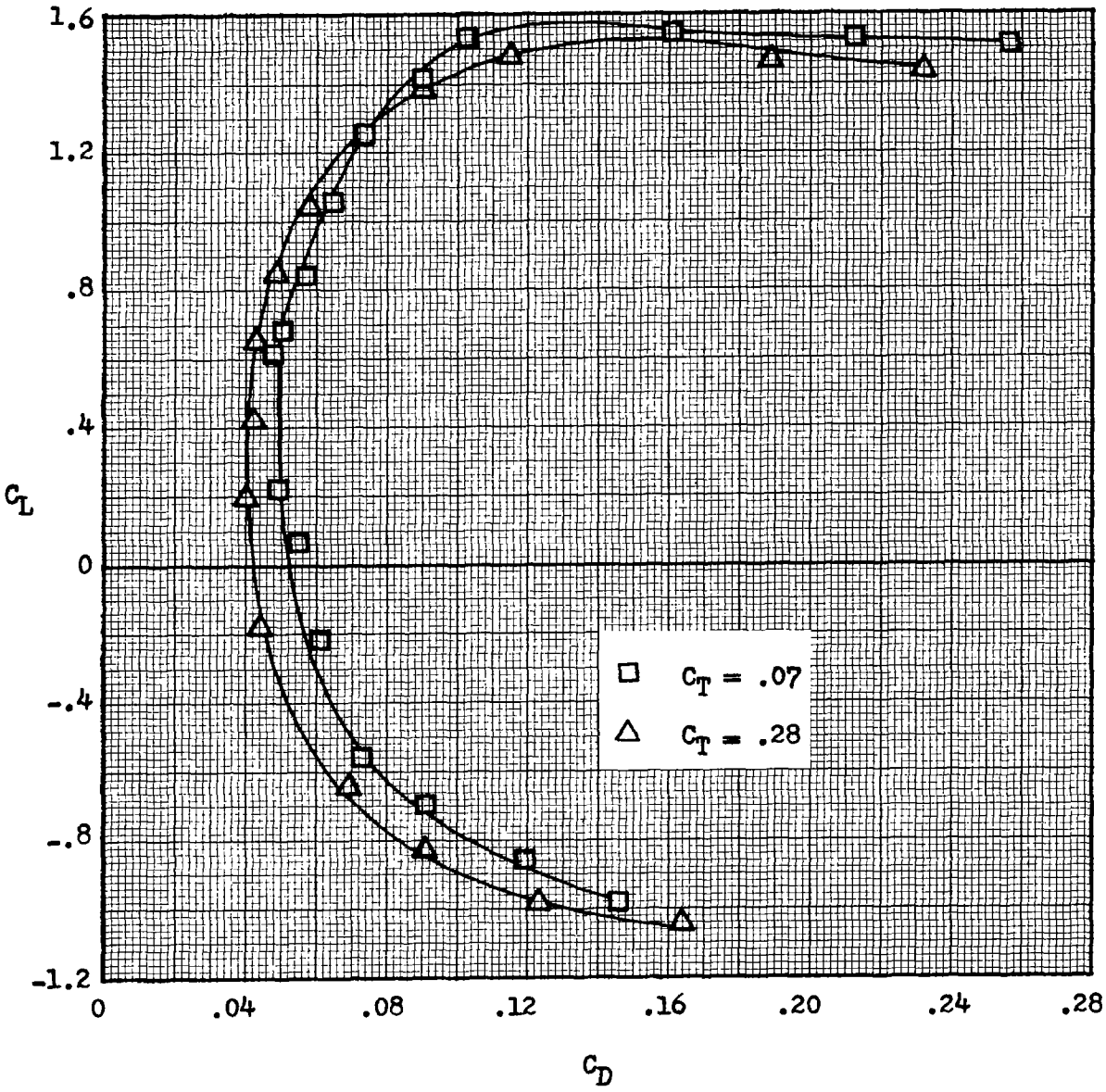

Figure 15.- Effect of sailwing trailing-edge cable tension on the drag polar: sailwing model 2.

LENGTH AND BURSTING OF SEPARATION BUBBLES: A PHYSICAL INTERPRETATION*

John M. Russell
Department of Aeronautics and Astronautics
Massachusetts Institute of Technology

SUMMARY

A physical interpretation of the observed form of the pressure distribution beneath a two-dimensional "short" separation bubble (which modifies the external inviscid pressure distribution only locally) is given in terms of boundary layer concepts (i.e., constancy of static pressure across the layer as long as the layer is "thin"). At the mean separation and reattachment points (which lie on the same mean streamline), the local static pressure equals the local stagnation pressure, since the velocity is zero at these points. The boundary layer hypothesis then implies that reattachment can only occur at a point $x - x_s$ downstream of the separation point x_s if the jump in external inviscid static pressure $\frac{\rho}{2}\left[U^2(x) - U^2(x_s)\right]$ is less than or equal to the rise in stagnation pressure $H(x) - H(x_s)$ along the separation streamline after separation. A simple method for estimating the growth of $H(x)$ along a mean streamline entrained into the underside of a growing shear layer through the transition region is discussed, and predictions of bubble bursting conditions and a lower bound on the bubble length are compared with experiment.

INTRODUCTION

Since the early work of Melvill Jones (ref. 1), it has been known experimentally that a laminar boundary layer on an airfoil, after entry into a region of adverse pressure gradient strong enough to cause laminar separation, will separate in the laminar state, sometimes achieve transition to turbulent flow in the separated shear layer, and (if the adverse pressure gradient is not too severe) reattach to the surface to form a closed recirculating flow eddy known as a separation bubble. In a typical case (fig. 1), the turbulent boundary layer downstream of the reattachment point R either does not separate at all over the remaining portion of the upper surface or separates only a short distance upstream of the trailing edge. In such a flow, the form of the external static pressure distribution outside of the region of separation is approximated

---

*This work was supported by the German Academic Exchange Service (DAAD) in the form of a fellowship (Stipendium 430-402-015-7), and was carried out at the Institut A fuer Mechanik, Universitaet Stuttgart. I am indebted to my supervisor Prof. Richard Eppler and to Dr. Herman Fasel for many useful discussions during the course of the research.

reasonably well by the potential flow pressure distribution, though the magnitude of the actual pressure is somewhat smaller. It follows that the lift of an airfoil with this type of bubble separation is approximately equal to the value predicted by inviscid theory. Following Tani (ref. 2), we will refer to this flow phenomenon as a separation bubble of the "short" type, to distinguish it from another type of closed recirculating flow in which the entire pressure distribution differs radically from the potential flow form. The latter is referred to as a "long" bubble.

Separation bubbles are of great importance in engineering because of the role they play in the phenomenon of airfoil stalling, which may sometimes be identified with a transition of the flow from a short type of bubble separation to the long type. This abrupt transition, known as "bursting" of the short bubble, is in some cases responsible for producing the well-known "critical" Reynolds number region in the plot of drag coefficient versus Reynolds number for circular cylinders and spheres (ref. 2) and for moderately thick airfoils at Reynolds numbers lower than about 10^5 (refs. 3 and 4).

Reference 2 contains a thorough background discussion of the phenomenon of separation bubbles and a review of the experimental work prior to 1964. Reference 5 reviews most of the more recent experimental work up to 1976. The reader is referred to these sources for general information about the subjects treated in this paper.

In recent years, there have been several attempts to develop semi-empirical calculation methods for predicting the length and bursting conditions for separation bubbles of the short type. These range in sophistication from solution of the full time-dependent two-dimensional Navier-Stokes equations (with modeling of the turbulence), as in reference 7, to simpler modifications of existing boundary layer calculation methods incorporating iterative methods to account for viscous-inviscid interaction between the external stream and the flow within the bubble (refs. 6 and 8). All of these methods use experimental data on separation bubbles to fix the values of certain numerical coefficients appearing in the theory. In each case, the shape of the separation streamline and the external pressure distribution between separation and reattachment are unknowns in the problem and are not determined until the calculation is finished. Since the distributions of these quantities play a crucial role in determining the length and bursting of the bubble, there is some difficulty in using the numerical prediction methods (or the theories on which they are based) to deepen one's understanding of the fundamental physical processes controlling the flow.

The objectives of the present study are to explain why reattachment occurs at all, to explain why the observed pressure distribution has its characteristic form, and to develop a shortcut method for calculating the length of a short separation bubble, if one exists, or to determine the conditions under which a short bubble cannot exist.

PHYSICAL MODEL

The Cause of Reattachment

The principal cause of turbulent reattachment following laminar separation has been discussed by Cebici and Bradshaw (ref. 9). Consider the separation of a laminar boundary layer from a smooth surface as shown in figure 2. The edge of the shear layer has been drawn to show the spreading of the shear layer in the downstream direction due initially to laminar and later to turbulent mixing of momentum. This spreading results in a greater mass flux across the segment BB' in figure 2 than across the segment AA'. In two-dimensional flow, mass conservation requires that there be a net inflow across the segment AB. This entrainment of fluid into the underside of a growing shear layer will be greatly increased by the transition from laminar to turbulent flow. If this entrainment rate is greater than any reversed flow coming from far downstream, then the shear layer simply sucks itself back onto the surface from which it separated (ref. 9, p. 366) to form the short separation bubble shown in figure 3, in which the entrainment flow is supplied by the splitting of the shear layer at reattachment.

The Form of the Pressure Distribution

In trying to identify the most important factors controlling the dynamics of separation bubbles, it is useful to see how many of the qualitative features of the flow can be accounted for adequately by simple boundary layer concepts. If, for example, simple boundary layer theory is found to account adequately for the observed length and pressure distribution of a bubble, then one can infer that the direct effects of streamline curvature and nonzero pressure gradients in the cross-stream direction (which are neglected in boundary layer theory) are indeed unimportant, at least in determining the gross qualitative features of the flow. This process of testing hypotheses that certain terms in the equations of motion are negligible will serve to increase our understanding of what a separation bubble is if it allows us to identify the few important from among the many unimportant effects operating at once in the flow.

In this spirit, we attempt to explain the characteristic pressure distribution beneath a short separation bubble (cf. fig. 1) by supposing that the assumptions of classical boundary layer theory hold. In particular, the static pressure across the separation bubble in figure 3 is assumed to be constant, and the velocity component in the direction normal to the wall is assumed to be an order of magnitude smaller than the component parallel to the wall. With these assumptions, the pressure distribution along the wall between points S and R in figure 3 can be inferred. The pressure gradient between points S and K must be small since the velocities and shear stresses in the slowly moving interior of the bubble are driven only by entrainment and are, therefore, small. In the region downstream of the point K, the streamwise velocity along each closed recirculating flow streamline will be zero at the downstream extremity of that streamline. Since the vertical velocity at such a downstream extremity is small, the static pressure is very nearly equal to the local stagnation pressure at that point. It follows that the distribution of pressure along the line connecting all such downstream extremities of streamlines (represented as the

dotted line in fig. 3) will approximately equal the distribution of stagnation pressure between the lower edge of the shear layer (at point K) and the separation streamline (at point R). This difference in stagnation pressures may be substantial because the velocity on the separation streamline (which lies close to the center of the shear layer at the streamwise station K) will typically be much larger than the velocity on the lower edge of the shear layer at any given streamwise station.

In general, we expect the pressure distribution beneath the separation bubble in figure 3 to be as shown in figure 4, which is in good qualitative agreement with the examples of short separation bubbles in reference 2. The rather sharp corner in the pressure distribution in figure 4 is interpreted here as the point where the lower edge of the shear layer impinges on the wall. According to our model, this point also coincides with the center of the innermost closed streamline in figure 3. Note that the point K is not identified with the transition from laminar to turbulent flow (which we assume takes place somewhere upstream of the point K).

It has been assumed in all experimental studies on separation bubbles known to the author that the sharp corner in the pressure distribution coincides with the transition point. Gault (ref. 10) proposes this as a means of experimentally determining transition, while Van Ingen (ref. 11) uses the same assumption to fix the numerical values of the adjustable constants in a form of his "e to the ninth" method for transition prediction, developed especially for use in separation bubbles. In view of the fact that transition from laminar to turbulent flow occurs quite readily in a free shear layer in zero pressure gradient without modifying the static pressure, one is at a loss to see why transition as such should have any effect on the pressure distribution at all, much less account for the abrupt, nearly discontinuous pressure rise that occurs at the rear of a short separation bubble. The rather arbitrary and ad hoc character of the conventional interpretation of the pressure distribution renders it less favorable from a fundamental viewpoint than the interpretation in terms of stagnation pressures given above.

Length and Bursting of Short Bubbles

We have included among the defining features of short separation bubbles the condition that the bubble modify only locally the static pressure distribution about the body on which the bubble occurs; that is, the pressure distribution everywhere ahead of and behind the bubble is approximately equal to the value predicted by potential theory. In particular, the pressures at the separation and reattachment points (which are the inner limits of the portion of the pressure distribution lying outside the bubble) must both be points lying very near the inviscid pressure distribution curve. These endpoint conditions, together with our model of the pressure distribution within the bubble in terms of stagnation pressures on the recirculating flow streamlines, provide a clue as to what determines the length of a short separation bubble, when it is possible for one to exist, and why it is sometimes impossible for a short bubble to exist.

Now the difference in static pressure between the points S and R in figure 3 equals the net rise in stagnation pressure along the separation streamline, since the velocity is zero at both endpoints. It follows that if a plot of the rise in stagnation pressure along the separation streamline downstream of separation is drawn on the same graph as the rise in inviscid static pressure downstream of the same point, then an estimate of the bubble length is the streamwise distance from separation to the first point where the curves cross.

One difficulty with such a graphical procedure for the calculation of the bubble length is that the curves may cross at more than one point, giving a choice of several possible bubble lengths rather than a single one. Another difficulty is that the stagnation pressure along the whole length of the separation streamline is not known under general conditions. It can, however, be estimated by assuming that the growth of the shear layer downstream of separation is nearly equal to that of a free shear layer in zero pressure gradient, for which the mean velocity and, hence, stagnation pressure and stream function profiles are known from experiments on transition in a laminar mixing layer (ref. 12).

A calculation based on similar physical concepts was made by Tani (ref. 2) to estimate the maximum attainable value of the coefficient of pressure recovery within a bubble σ defined by the relation

$$\sigma = \frac{p_R - p_S}{\frac{\rho}{2} U_S^2} \tag{1}$$

Owen and Klanfer (ref. 13) had proposed the value $\sigma_{max} = 0.35$ from experimental evidence. By noting that the velocity along any streamline entrained into the low velocity side of a growing shear layer cannot exceed the velocity on the dividing streamline $(u/U)_{D.S.} = 0.5873 \ldots$, Tani argued that a lower bound on the nondimensional stagnation pressure rise existed and was given by

$$\left(\frac{\Delta H}{\frac{\rho}{2} U_S^2}\right)_{max} = \left[(u/U)_{D.S.}\right]^2 = 0.3449 \ldots \tag{2}$$

which is in excellent agreement with the figure 0.35 given by Owen and Klanfer. Tani did not suggest the extension of the stagnation pressure idea to the calculation of the bubble length, however.

The method of estimating the reattachment position as the streamwise coordinate of the point of intersection of the curves of inviscid pressure rise and stagnation pressure rise on the separation streamline after separation provides a necessary condition for the existence of a short bubble, namely, that the two curves indeed intersect. A possible condition for the impossibility of a short separation bubble (i.e., a "bursting" condition) might then be that the inviscid

pressure gradient downstream of separation be so steep that the two curves never intersect. The borderline case in which a short bubble is just barely possible, but would become impossible with an infinitesimal increase in the inviscid pressure gradient, is when the two curves are tangent to each other at a single point. Later in this paper we will use this tangency condition to derive a close approximation to Gaster's "bursting line" (ref. 14), which has been found by several experimentalists (see ref. 5) to be a reliable empirical formula for predicting the boundary between the short and long type of bubble separations.

DEVELOPMENT OF THE SHEAR LAYER

For reasons indicated in the last section, it is desirable to have an explicit formula for the development of the stagnation pressure $H(s)$ along the separation streamline in a short bubble.

For simplicity, we will assume that the actual distribution of stagnation pressure along the separation streamline can be approximated by the stagnation pressure distribution along a particular streamline entrained into the underside of a self-similar shear layer in zero pressure gradient, for which the velocity profile has been calculated from the Blasius equation in the laminar case (ref. 15), and has been measured experimentally in the transitional and fully turbulent cases (refs. 12 and 16, respectively). It has been found experimentally (cf. ref. 12, fig. 12) that the functional form of the mean velocity profile is experimentally indistinguishable for these three cases, the effect of transition being a large and abrupt increase of the rate of spreading of the shear layer measured by, say, the growth of the momentum thickness $\theta(s)$.

Before treating the problems of the location of the transition region, the growth of the resulting turbulent layer, and the determination of the value of the stream function (relative to the reference streamline in a self-similar shear layer) appropriate for representing the separation streamline in a separation bubble, it is necessary to recall certain properties of self-similar shear layers, and, in particular, to obtain explicit approximate formulas for the velocity and stream function profiles.

The Laminar Shear Layer

The nomenclature for self-similar shear layers is as shown in figure 5, which illustrates the flow downstream of a hypothetical splitter plate, the upper surface of which moves with the velocity U_1 (precluding the formation of a boundary layer there), while the lower surface is stationary. The fluid above the plate ($x < 0$, $y > 0$) moves with the uniform velocity U_1 while the fluid below the plate ($x < 0$, $y < 0$) is at rest. The effect of these boundary conditions is the elimination of any length scale other than the streamwise coordinate x, so that self-similarity in laminar flow is to be expected.

The steady two-dimensional Prandtl boundary layer equations for zero pressure gradient,

$$u \frac{\partial u}{\partial x} + v \frac{\partial u}{\partial y} = \frac{\partial^2 u}{\partial y^2} \tag{3}$$

$$\frac{\partial u}{\partial x} + \frac{\partial v}{\partial y} = 0 \tag{4}$$

thus reduce to the Blasius equation,

$$2 f'''(\eta) + ff''(\eta) = 0 \tag{5}$$

in the usual way (e.g., ref. 17, p. 126), where

$$\eta = y\left(\frac{U_1}{\nu x}\right)^{1/2} = \frac{y}{\ell(x)} \tag{6}$$

$$f(\eta) = \frac{\psi(x,y)}{(\nu U_1 x)^{1/2}} = \frac{\psi(x,y)}{U_1 \ \ell(x)} \tag{7}$$

$$u = \frac{\partial \psi}{\partial y} = U_1 \ f'(\eta) \qquad v = -\frac{\partial \psi}{\partial x} = \frac{1}{2}\left(\frac{U_1 \nu}{x}\right)\left[\eta \ f'(\eta) - f(\eta)\right] \tag{8}$$

The boundary conditions appropriate for a free shear layer are

$$u \to U_1 \Rightarrow f' \to 1 \quad \text{as} \quad \eta \to +\infty \tag{9}$$

$$u \to 0 \Rightarrow f' \to 0 \quad \text{as} \quad \eta \to -\infty \tag{10}$$

$$\psi = f = v = 0 \quad \text{when} \quad \eta = 0 \tag{11}$$

The exact solution of equation (5) satisfying the boundary conditions (9), (10), and (11) has been tabulated by Lock (ref. 15) to four significant figures. The tabulated solution provides a useful check on the accuracy of approximate representations of the velocity profile in terms of elementary functions.

Approximation of the Velocity Profile

For the present purpose, it is sufficient to obtain an approximate solution to equation (5) in terms of elementary functions whose forms are chosen to reproduce as many of the properties of the exact solution as is convenient. For example, the condition $f(0) = 0$ implies that $f'''(0) = 0$ (from equation (5)), so that the velocity f' has an inflection point at the origin, or, equivalently, the shear stress is maximum there. In addition, the conditions $f(\eta) \approx \eta$ as $\eta \to +\infty$ and $f(\eta) \approx$ Constant as $\eta \to -\infty$ imply that f' behaves like a complementary error function for large positive η and like a simple exponential for large negative η. These conditions, together with the requirement that the velocity profile be a smooth monotonic function of η, suggest the approximate forms

$$\eta > 0: \quad f'(\eta) = 1 - \left[1 - f'(0)\right] \frac{2}{\sqrt{\pi}} \int_{a\eta/2}^{\infty} e^{-x^2}\, dx \tag{12}$$

$$\eta < 0: \quad f'(\eta) = f'(0)\, \frac{3}{2}\, \mathrm{sech}^2 \left[b\eta + \tanh^{-1}\left(\frac{1}{\sqrt{3}}\right)\right] \tag{13}$$

each of which has an inflection point at $\eta = 0$ and the correct asymptotic behavior as $|\eta| \to \infty$. Equations (12) and (13) are constructed so that the velocity $f'(\eta)$ is continuous at the juncture $\eta = 0$. The requirement that the slope of the velocity be continuous at $\eta = 0$ provides one equation relating the constants a and b:

$$-\left[1 - f'(0)\right] a\left(\frac{-1}{\sqrt{\pi}}\right) = f'(0)\left(\frac{-2}{\sqrt{3}}\right) b \tag{14}$$

Equation (14) provides an expression for the ratio a/b in terms of $f'(0)$, where either a or b remains free to be determined by a suitable normalization.

The only important unknown that remains is now $f'(0)$, which we will determine by a momentum integral method. Integrating equation (5) from $-\infty$ to 0, we obtain

$$2\, f''\Big]_{-\infty}^{0} + ff'\Big]_{-\infty}^{0} - \int_{-\infty}^{0} (f')^2\, d\eta = 0$$

while the integral from 0 to ∞ gives

$$2\, f''\Big]_0^{\infty} + f(f' - 1)\Big]_0^{\infty} - \int_0^{\infty} f'(-1 + f')\, d\eta = 0$$

Applying the boundary conditions for a shear layer, these equations become

$$2\, f''(0) = \int_{-\infty}^{0} (f')^2\, d\eta = \int_0^{\infty} f'(1 - f')\, d\eta \tag{15}$$

which are forms of the Von Kármán momentum integral equation (e.g., ref. 17, p. 146) for each half of the flow, and which have direct counterparts when the flow is turbulent (e.g., ref. 18, p. 227).

If equations (12), (13), and (14) are substituted into equation (15), then a cubic equation for the quantity $1 - f'(0)$ is obtained (see appendix), the relevant solution of which gives $f'(0) = 0.58923$, which agrees well with the tabulated value $f'(0) = 0.5873$ in reference 15.

For our normalization condition (needed to determine either a or b from equation (14)), we note that equation (15) implies

$$\frac{\theta}{\ell} \equiv \theta^* = \int_{-\infty}^{0} f'(1 - f')\, d\eta + \int_0^{\infty} f'(1 - f')\, d\eta$$

$$= f\Big]_{-\infty}^{0} - f''(0) + f''(0) = -f(-\infty) \tag{16}$$

which according to reference 16, has the numerical value $-f(-\infty) = 1.2386$.

It follows from equations (12), (13), (14), and (16) (see appendix) that $a = 0.88544$ and $b = -0.30160$, which completely determines all of the constants in our approximate velocity profile. For $\eta < 0$ (which is the region of interest in the separation bubble problem), the approximate velocity profile given by equation (13) is uniformly accurate to within 1 percent of the tabulated values in reference 16.

Development of the Momentum Thickness

The nondimensional velocity profile $f'(\eta)$, together with the definition of the transverse length scale $\ell(x)$ in equation (6) and the free stream velocity U_1 completely determine the flow in a laminar shear layer. It is convenient to express $\ell(x)$ in terms of information available at a station $x = x_1$, rather than in terms of the distance x downstream of the splitter plate in figure 5. From equation (6),

$$\ell(x) = \left(\frac{\nu x}{U_1}\right)^{1/2} = \left[\frac{\nu(x - x_1)}{U_1} + \ell(x_1)^2\right]^{1/2}$$

$$= \ell_1\left[\frac{1}{\left(\frac{U_1\ell_1}{\nu}\right)}\frac{x - x_1}{\ell_1} + 1\right]^{1/2}$$

where ℓ_1 is defined to be $\ell(x_1)$. Rewriting in terms of the momentum thickness $\theta(x_1)$ and using the fact that $\theta(x)/\ell(x) = \theta^* = 1.2386$, we have

$$\frac{\theta(x)}{\theta(x_1)} = \left\{\frac{(\theta/\ell)^2}{\left[\frac{U_1\ \theta(x_1)}{\nu}\right]}\frac{x - x_1}{\theta(x_1)} + 1\right\}^{1/2} \qquad \text{(Laminar flow)} \qquad (17)$$

As mentioned before, we will assume that the functional form of the mean velocity profile in a self-similar turbulent shear layer is the same as in laminar flow. Thus, we continue to use equations (12) and (13) for the velocity profile, though the definition of the transverse length scale $\ell(x)$ (which equals $(\nu x/U_1)^{1/2}$ in laminar flow) must be altered. Since the equation $\theta = \theta^*\ \ell(x)$ holds in general, this may serve as the definition of $\ell(x)$ in turbulent flow, provided that an adequate empirical formula for the development of $\theta(x)$ can be found.

From the data of Sato (ref. 12), such a formula is not hard to develop. We may take, for example, in the transitional and fully turbulent regions of the flow

$$\frac{\theta(x)}{\theta_s} = \left[\frac{\theta(x)}{\theta_s}\right]_{lam} + \left[\frac{\theta}{\theta_s}\right]_{extra} \qquad (18)$$

where, for $(x - x_s)/\theta_s \geqq N_t$,

$$\left[\frac{\theta}{\theta_s}\right]_{extra} = 0.046\left[\left(\frac{x - x_s}{\theta_s} - N_t\right) + \frac{\lambda_1}{\theta_s}\tanh\left(\frac{\frac{x - x_s}{\theta_s} - N_t}{\frac{\lambda_2}{\theta_s}}\right)\right] \qquad (19)$$

and where $\left[\theta(x)/\theta_s\right]_{lam}$ is given by equation (17) with $x_1 = x_s$. A plot of equation (19) with the numerical values $\lambda_1/\theta_s = 34$, $\lambda_2/\theta_s = 135$, and $N_t = 56$ is shown in figure 6. Also shown are the measured values of $\theta(x)/\theta_s - \left[\theta(x)/\theta_s\right]_{lam}$ for three different flows in reference 12. The agreement is seen to be quite reasonable.

The condition $(s - x_s)/\theta_s = N_t$ represented a transition criterion and appears to hold quite generally for two-dimensional laminar separated flows of the type under discussion. For example, figure 12 of Freymuth (ref. 19), which shows the growth of the streamwise fluctuation velocity component $|u'|_{max}$ in a free shear layer downstream of separation for a variety of separation Reynolds numbers, indicates that the range of $(x - x_s)\theta_s$ in which the disturbances grow exponentially is almost completely independent of Reynolds number for $61 \leqq R_{\theta_s} \leqq 334$. This range was found to be $0 \leqq (x - x_s)/\theta_s \leqq 60$. Strong nonlinearity (indicating the onset of transition) appears for $(x - x_s)/\theta_s \geqq 60$, which agrees well with the value $N_t = 56$ used here. A similar independence of the onset of transition with Reynolds number can be found in separation bubbles. For example, Gaster's results (ref. 14, fig. 11) of intermittency measurements in seven short separation bubbles in the range $136 \leqq R_{\theta_s} \leqq 394$ show that the onset of transition occurs for $50 \leqq (x - x_s)/\theta_s \leqq 80$ for all but one of the bubbles. Unlike the case of fully attached flow, it therefore appears that transition in fully separated flow is relatively easy to predict in terms of the critical value of a single parameter, at least in the case of nominally two-dimensional incompressible flow in the Reynolds number range under discussion under conditions of small background turbulence and acoustic noise.

VELOCITY DISTRIBUTION ALONG A STREAMLINE

The stream function ψ can be obtained from our approximate velocity profile (13) by integration. Applying the boundary condition $\psi = 0$ on $\eta = 0$, we have, from equations (7) and (13),

$$\psi = U_1\,\ell(x)\,f(\eta) = \frac{U_1\,\ell(x)}{b}\,\frac{3}{2}\,f'(0)\left\{\tanh\left[b\eta + \tanh^{-1}\left(\frac{1}{\sqrt{3}}\right)\right] - \frac{1}{\sqrt{3}}\right\} \tag{20}$$

Now the value of the stream function at $\eta = -\infty$, which represents the mass flow across the entire lower half of the shear layer in figure 5, is a function of x and may be used to define the (constant) stream function along the streamline that just enters the underside of the shear layer at any station x. In our model of the separation bubble, we will suppose that the separation point $x = x_s$ corresponds to the point where the separation streamline enters the underside of the separated shear layer in a bubble in just this way. That is, we will take

$$\psi_s = U_s\,\ell(x_s)\,f(-\infty) = -U_s\theta_s \tag{21}$$

as the value of the stream function (relative to the shear layer) that represents the separation streamline in a bubble.

The distribution of velocity along the streamline $\psi = \psi_s$ can now be found easily. From equations (20) and (21) (with $U_1 = U_s$), we have

$$\tanh\left[b\eta + \tanh^{-1}\left(\frac{1}{\sqrt{3}}\right)\right] = -\frac{\theta_s}{\theta}\,\frac{2b}{3\,f'(0)}\left(\frac{\theta}{\ell}\right) + \frac{1}{\sqrt{3}} \tag{22}$$

It follows from equation (13) and the identity $\operatorname{sech}^2(x) = 1 - \tanh^2(x)$ that

$$\left(\frac{u}{U}\right)^2_{\psi=\psi_s} = \left[f'(\eta)\right]^2_{\psi=\psi_s} = \left(f'(0)\frac{3}{2}\left\{1 - \left[\frac{-2b\theta^*}{3\,f'(0)}\,\frac{\theta_s}{\theta} + \frac{1}{\sqrt{3}}\right]^2\right\}\right)^2 \tag{23}$$

Figure 7 is a plot of equation (23) for various separation Reynolds numbers. Equations (17) through (19) have been used to evaluate the quantity θ/θ_s.

STAGNATION PRESSURE ALONG $\psi = \psi_s$

Equation (23), which was calculated from the known behavior of a free shear layer in zero pressure gradient, provides a measure of the stagnation pressure distribution along the streamline $\psi = \psi_s$, since in zero pressure gradient, the stagnation pressure $H(x,\psi)$, defined by

$$H(x,\psi) = p + \frac{\rho}{2}u^2 \tag{24}$$

is simply equal to the dynamic pressure $(\rho/2)u^2$.

We recall that in a general shear flow, the stagnation pressure varies along a mean streamline according to the approximate equation

$$\frac{\partial H}{\partial s} = \frac{\partial \tau}{\partial n} \tag{25}$$

where τ is the combined viscous and turbulent shear stress

$$\tau = \mu\frac{\partial u}{\partial n} - \rho\overline{u'v'} \tag{26}$$

and where s and n are orthogonal curvilinear coordinates in the plane of the flow oriented in the streamwise and cross-stream directions, respectively. Equation (23) thus represents the cumulative effect of such cross-stream stress gradients in the downstream direction.

The use of equation (23) to model the actual stagnation pressure distribution along $\psi = \psi_s$ in a separation bubble involves the assumption that the modification of the shear stress distribution due to the abrupt rise in static pressure at the rear of the bubble is small, or, equivalently, that the turbulent shear stresses are dominated by "memory" effects. Such an approximation of memory-dominated shear stresses is familiar in many analyses of turbulent flows following entry into a region of severe adverse pressure gradient (see especially refs. 20 and 18). The validity of this approximation when applied to the bubble problem has yet to be established, however.

With due regard for this uncertainty, we may take the nondimensional form of equation (24) as our working equation for the distribution of stagnation pressure along the streamline $\psi = \psi_s$:

$$\frac{H}{\frac{\rho}{2} U_s^2} = \frac{p}{\frac{\rho}{2} U_s^2} + \left(\frac{u}{U_s}\right)^2 \sim \frac{p_s}{\frac{\rho}{2} U_s^2} + \left(\frac{u}{U_s}\right)^2_{\substack{\text{plane}\\ \text{layer}}} \tag{27}$$

where the last term on the right-hand side is given by equation (23).

GASTER'S BURSTING CRITERION

M. Gaster (ref. 14) has obtained an empirical correlation in terms of the parameters R_{θ_s} and the pressure gradient parameter $\bar{P}$, defined by

$$\bar{P} = \frac{U_r - U_s}{x_r - x_s} \frac{\theta_s^2}{\nu} = \frac{(U_r - U_s)/U_s}{(x_r - x_s)/\theta_s} \frac{U_s \theta_s}{\nu} \tag{28}$$

that distinguishes between flow conditions permitting a short separation bubble and the conditions when a short bubble is not possible (i.e., a "bursting" condition). Figure 8 shows Gaster's so-called "bursting line," which we will attempt to derive from equation (27).

If we define a pressure coefficient c_p^* relative to the free stream conditions at the separation point in a bubble, then

$$\frac{p - p_s}{\frac{\rho}{2} U_s^2} = c_p^* = 1 - \left(\frac{U}{U_s}\right)^2 = \frac{c_p - c_{p_s}}{1 - c_{p_s}} \tag{29}$$

where $c_p = 1 - (U/U_\infty)^2$ is the conventional pressure coefficient. In terms of c_p^*, equation (27) becomes, on $\psi = \psi_s$,

$$c_p^* + \left(\frac{u}{U_s}\right)^2 = \left(\frac{u}{U_s}\right)^2_{\substack{\text{plane}\\ \text{layer}}} \tag{30}$$

At the reattachment point, the streamwise velocity u on $\psi = \psi_s$ equals zero, so that

$$\begin{pmatrix}\text{Reattachment}\\ \text{condition}\end{pmatrix} \qquad \sigma = c_{p_r}^* = \left(\frac{u}{U_s}\right)^2_{\substack{\text{plane}\\ \text{layer}}} \tag{31}$$

where the pressure recovery coefficient σ is the same as in equation (1).

Equation (31) together with equation (28), which at reattachment can be written as

$$\bar{P} = \frac{\sqrt{1 - c_{pr}^*} - 1}{(x - x_s)/\theta_s} R\theta_s \tag{32}$$

define the largest possible $\bar{P}$ that can be achieved by a short bubble at a given $R\theta_s$. That is, if c_{pr}^* from equation (31) is substituted into equation (32) and the resulting $\bar{P}$ tabulated as a function of $(x - x_s)/\theta_s$ for a particular $R\theta_s$, then an extremum of $\bar{P}$ is found. For the Reynolds numbers $R\theta_s$ = 100, 200, 300, and 400, we find that the extreme values of $\bar{P}$ are -0.0996, -0.1868, -0.2732, and -0.3593, occurring at $(x - x_s)/\theta_s$ = 103, 111, 115, and 117, respectively. A faired curve through these points is shown in figure 8 and exhibits suprisingly good qualitative agreement with Gaster's empirical curve.

The agreement between theory and experiment is particularly pleasing in view of the fact that all of the empirical input to the present calculation method was obtained from measurements of transition in free shear layers in zero pressure gradient at a remote distance from any wall. Our calculations therefore lend support to the view that the processes of bubble bursting and shear layer reattachment are linked to the processes of laminar-turbulent transition and shear layer growth in a fundamental way.

COMPARISON WITH EXPERIMENTAL BUBBLE LENGTHS

As a caution against overly optimistic conclusions drawn from the present analysis, we present in figure 9 the results of an attempt to verify the reattachment condition (31) directly. In the figure, we have plotted the measured pressure recovery coefficient σ and length $(x_r - x_s)/\theta_s$ for a number of separation bubbles from various sources. On the same scale, we have drawn a copy of figure 7, which represents the nondimensional stagnation pressure along the separation streamline for a plane layer. If equation (31) held exactly, then all of the experimental points would lie on the dashed curves.

In fact, the experimental points are scattered quite widely about the analytic curves. More serious than the scatter in σ, however, is the discrepancy between the measured length of the bubbles, which are typically in the range $150 \leq (x_r - x_s)/\theta_s \leq 300$, and the values calculated from our analytic derivation of Gaster's bursting line. We have indicated the latter points in figure 9 by "plus" symbols, which lie, to within graphical accuracy, on the family of straight lines drawn through the origin and the points of tangency with the various curves of $(u/U)^2_{\psi=\psi_s}$ for the plane layer. As can be seen, the calculated bubble lengths are typically a factor two or three too small. This error is significant, and indicates that the present theory is not sufficiently refined for practical use in the quantitative prediction of bubble lengths.

It is not clear which of the many effects neglected in the theory are responsible for this discrepancy. We may speculate, however, that the neglect of changes in the shear stress gradient $\partial\tau/\partial n$ on the separation streamline during reattachment is important. Some such change must occur, since in the real flow the shear stress on $\psi = \psi_s$ vanishes at reattachment, which places the reattachment point below the point of maximum τ in the layer. The crude theory developed above assumes that as the separation streamline gets swallowed up into the underside of the shear layer, the shear stresses on the streamline tend asymptotically toward the value of the center of the layer (which is the maximum value). It follows that $\partial\tau/\partial n$ is underestimated by the crude theory. This implies (from equation (25)) an unrealistically low prediction of the stagnation pressure H. It is not obvious how the present theory could be refined to take such effects into account.

CONCLUSIONS

From our investigation of the physics of separation bubbles, we may state the following tentative conclusions:

1. The form of the static pressure distribution about a short separation bubble can be explained qualitatively in terms of boundary layer concepts. In particular, the sharp corner in the pressure distribution at the rear of a short bubble is more properly interpreted as the point where the lower edge of the reattaching shear layer grazes the surface than as the point of transition from laminar to turbulent flow, as has traditionally been assumed.

2. The observation that the static pressure distribution about the body on which a short separation bubble occurs very nearly coincides with the inviscid pressure distribution at all points other than those between separation and reattachment leads to a plausible hypothesis regarding the factors controlling bubble bursting and a simple but crude calculation method for estimating the length of a short bubble when it is possible for one to exist. Specifically, the reattachment point x_r coincides with the earliest downstream station x at which the stagnation pressure on the separation streamline is large enough to support an abrupt rise to the local inviscid static pressure at x.

3. The attempt to approximate the rise in stagnation pressure on the separation streamline in a bubble by the corresponding rise along a streamline entrained into the underside of a laminar mixing layer undergoing transition leads to a reasonably accurate prediction of Gaster's bursting line, but significantly underestimates the length of short bubbles in general. This inaccuracy is probably due to the failure of the calculation method to take account of changes in the viscous and turbulent shear stress profiles occurring prior to reattachment that produce (according to equation (25)) an increase in the actual stagnation pressure along the separation streamline beyond what exists in a free shear layer.

4. The present results are in every way consistent with and support the view of Cebeci and Bradshaw and others that reattachment is a direct consequence of the increased entrainment of fluid into the underside of the growing separated shear layer downstream of transition, the entrainment causing the shear layer to suck itself back down onto the surface.

APPENDIX

We rewrite equation (15) in the equivalent form

$$\int_0^{\infty} \left[(1 - f') - (1 - f')^2\right] d\eta = \int_{-\infty}^{0} (f')^2 \, d\eta \tag{A1}$$

Substituting equations (12) and (13) into equation (A1) gives

$$\left\{\left[1 - f'(0)\right] I_1 - \left[1 - f'(0)\right]^2 I_2\right\} \frac{1}{a} = I_3 \frac{f'(0)^2}{b} \tag{A2}$$

where

$$I_1 = \int_0^{\infty} \left(\frac{2}{\sqrt{\pi}} \int_{a\eta/2}^{\infty} e^{-x^2} \, dx\right) a \, d\eta = \frac{2}{\sqrt{\pi}} \tag{A3}$$

$$I_2 = \int_0^{\infty} \left(\frac{2}{\sqrt{\pi}} \int_{a\eta/2}^{\infty} e^{-x^2} \, dx\right)^2 a \, d\eta = \frac{2}{\sqrt{\pi}}\left(2 - \sqrt{2}\right) \tag{A4}$$

and

$$I_3 = \int_{-\infty}^{0} \left\{\frac{3}{2} \operatorname{sech}^2 \left[b\eta + \tanh^{-1}\left(\frac{1}{\sqrt{3}}\right)\right]\right\}^2 b \, d\eta = \frac{4\sqrt{3} - 9}{6} \tag{A5}$$

(assume $b < 0$ throughout)

The right-hand side of equation (A2) can be rewritten by means of equation (14) as

$$\frac{I_3 \, f'(0)^2}{b} = I_3 \frac{-f'(0)^3}{1 - f'(0)} \frac{2\sqrt{\pi}}{\sqrt{3}} \frac{1}{a} \tag{A6}$$

Substituting the identity

$$-f'(0)^3 = \left[1 - f'(0)\right]^3 - 3\left[1 - f'(0)\right]^2 + 3\left[1 - f'(0)\right] - 1$$

into equation (A6) and combining with equation (A2) gives the cubic equation

$$\left[1 - f'(0)\right]^3\left(-I_2 - I_3 \frac{2\sqrt{\pi}}{\sqrt{3}}\right) + \left[1 - f'(0)\right]^2\left(I_1 + 3I_3 \frac{2\sqrt{\pi}}{\sqrt{3}}\right)$$

$$+ \left[1 - f'(0)\right]\left(-3I_3 \frac{2\sqrt{\pi}}{\sqrt{3}}\right) + I_3 \frac{2\sqrt{\pi}}{\sqrt{3}} = 0 \tag{A7}$$

which may be solved numerically by Newton's method to give the solution $1 - f'(0) = 0.41077$, or $f'(0) = 0.58923$.

The constants a and b may be calculated from the normalization condition (16) in the following way. The first integral on the right-hand side of equation (16) may be written

$$\int_{-\infty}^{0} \left[f' - (f')^2\right] d\eta = \frac{f'(0)}{b} I_4 - \frac{f'(0)^2}{b} I_3$$

$$= \left[\frac{-f'(0)}{1 - f'(0)} \frac{2\sqrt{\pi}}{\sqrt{3}}\right]\frac{1}{a}\left\{f'(0)\ I_4 - \left[f'(0)\right]^2 I_3\right\} \tag{A8}$$

where we have used equation (14), and where

$$I_4 = \int_{-\infty}^{0} \frac{3}{2} \operatorname{sech}^2\left[b\eta + \tanh^{-1}\left(\frac{1}{\sqrt{3}}\right)\right] b\, d\eta = \frac{\sqrt{3} - 3}{2} \tag{A9}$$

The second integral on the right-hand side of equation (16) is just the left-hand side of equation (A2). According to equation (16), the sum of these two integrals equals $-f(-\infty) = 1.2386$, which immediately gives $a = 0.88544$. Equation (14) then gives $b = -0.30160$.

REFERENCES

1. Jones, B. Melvill: An Experimental Study of the Stalling of Wings. R. & M. No. 1588, British A.R.C., 1934.

2. Tani, Itiro: Low Speed Flows Involving Bubble Separations. Progress in the Aeronautical Sciences, D. Kuechemann, ed., vol. 5, 1964.

3. Schmitz, F. W.: Zur Aerodynamik der Kleinen Reynoldszahlen. Jb. 1953 Wiss. Ges. Luftfahrt. Brauschweig 1954, S. 149/166.

4. Kraemer, K.: Fluegelprofile im Kritischen Reynolds-zahl-Bereich. Forschung auf dem Gebiete des Ingenieurwesens, Band 27, S. 33/46.

5. Young, A. D.: Some Special Boundary Layer Problems. 20th Ludwig Prandtl Lecture. Zeit. Flugwiss. u. Weltraumforschung, Band 1, S. 401/414, 1977.

6. Crimi, P.; and Reeves, B. L.: Analysis of Leading Edge Separation Bubbles on Airfoils. AIAA J., vol. 14, pp. 1548-1554, 1976.

7. Briley, W. R.; and McDonald, H.: Numerical Prediction of Incompressible Separation Bubbles. J. Fluid Mech., vol. 69, pp. 631-656, 1976.

8. Geropp, D.; und Grashof, J.: Berechnumg von Stroemungsfeldern mit Abloeseblasen bei Grossen Reynoldszahlen. DLR-FB 76-52, Institut fuer Stroemungslehre und Stroemungsmachinen, Universitaet Karlsruhe, 1976.

9. Cebeci, T.; and Bradshaw, P.: Momentum Transfer in Boundary Layers. New York: McGraw-Hill, 1977.

10. Gault, Donald E.: An Experimental Investigation of Regions of Separated Laminar Flow. NACA TN 3505, 1955.

11. Ingen, J. L. van: On the Calculation of Laminar Separation Bubbles in Two-Dimensional Incompressible Flow. In AGARD CP-168: "Flow Separation," Goettingen, 1975.

12. Sato, Hiroshi: Experimental Investigation of the Transition of Laminar Separated Layer. J. Phys. Soc. Japan, vol. 11, pp. 702-709, 1956.

13. Owen, P. R.; and Klanfer, L.: On the Laminar Boundary-Layer Separation From the Leading Edge of a Thin Aerofoil. British A.R.C. C.P. 220, 1953.

14. Gaster, M.: The Structure and Behavior of Laminar Separation Bubbles. British A.R.C. R. & M. 3575, 1969.

15. Lock, R. C.: The Velocity Distribution in the Laminar Boundary Layer Between Parallel Streams. Quart. J. Mech. and Appl. Math., vol. 4, pp. 42-63, 1951.

16. Liepmann, H. W.; and Laufer, J.: Investigations of Free Turbulent Mixing. NACA TN 1257, 1947.

17. Schlichting, H.: Boundary Layer Theory, 6th edition, J. Kestin, trans., New York: McGraw-Hill, 1968.

18. Townsend, A. A.: The Structure of Turbulent Shear Flow. Cambridge: Cambridge University Press, 1976.

19. Freymuth, Peter: On Transition in a Separated Laminar Boundary Layer. J. Fluid Mech., vol. 25, pp. 683-704, 1966.

20. Stratford, B. S.: The Prediction of Separation of the Turbulent Boundary Layer. J. Fluid Mech., vol. 5, pp. 1-16, 1959.

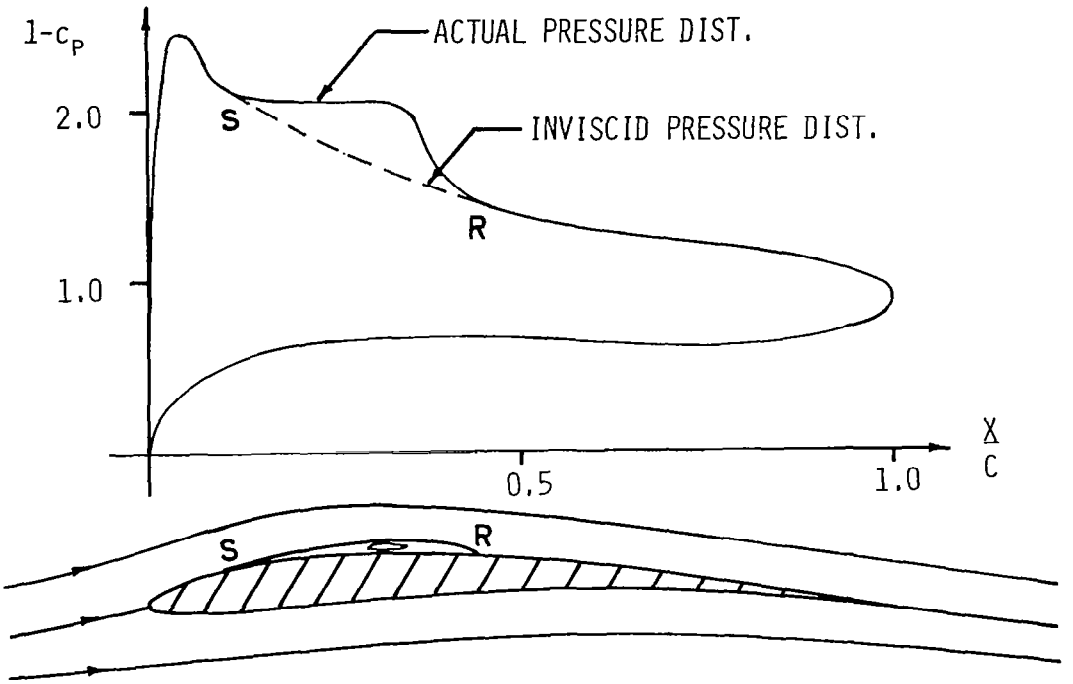

Figure 1.- Characteristic pressure distribution beneath a separation bubble of the "short" type.

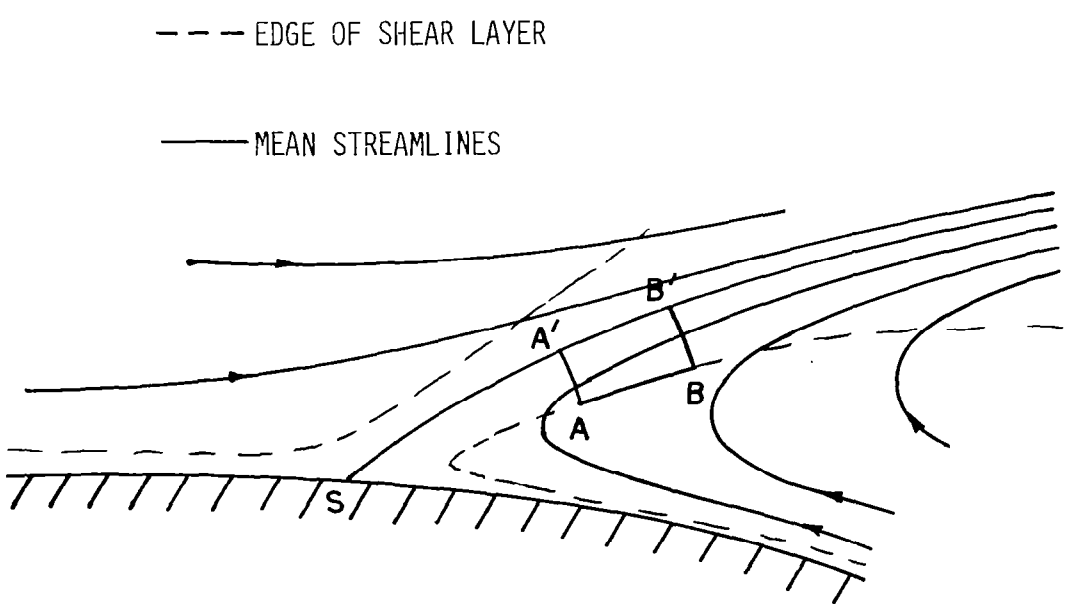

Figure 2.- Two-dimensional steady separation from a solid wall showing entrainment of fluid into the underside of the shear layer due to spreading in the downstream direction.

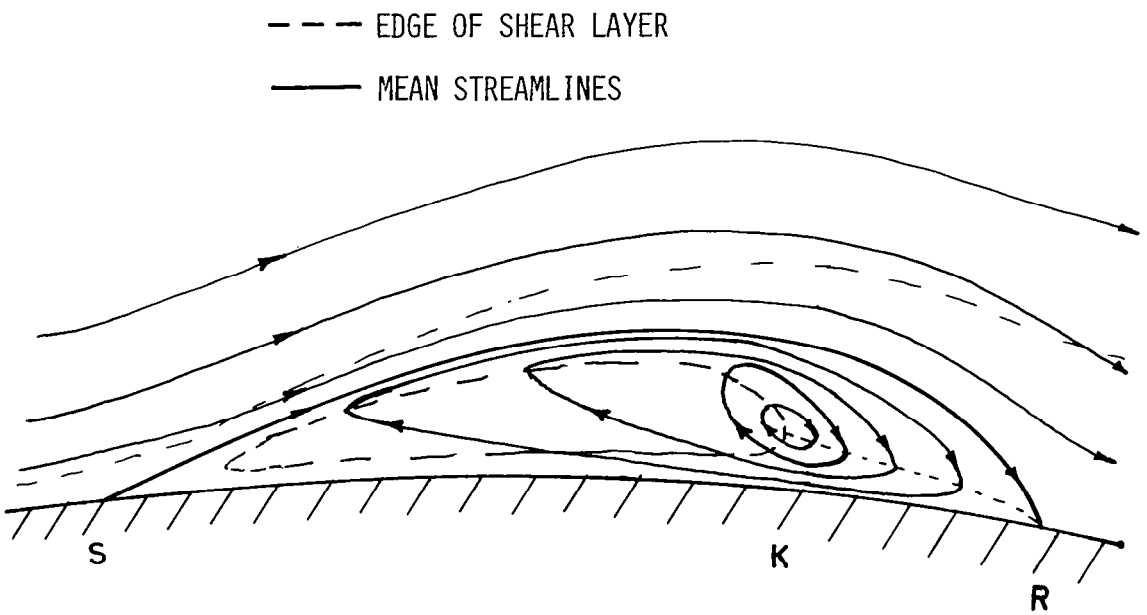

Figure 3.- Recirculating flow pattern within a bubble showing splitting of the shear layer at reattachment to supply the entrainment (vertical scale greatly exaggerated).

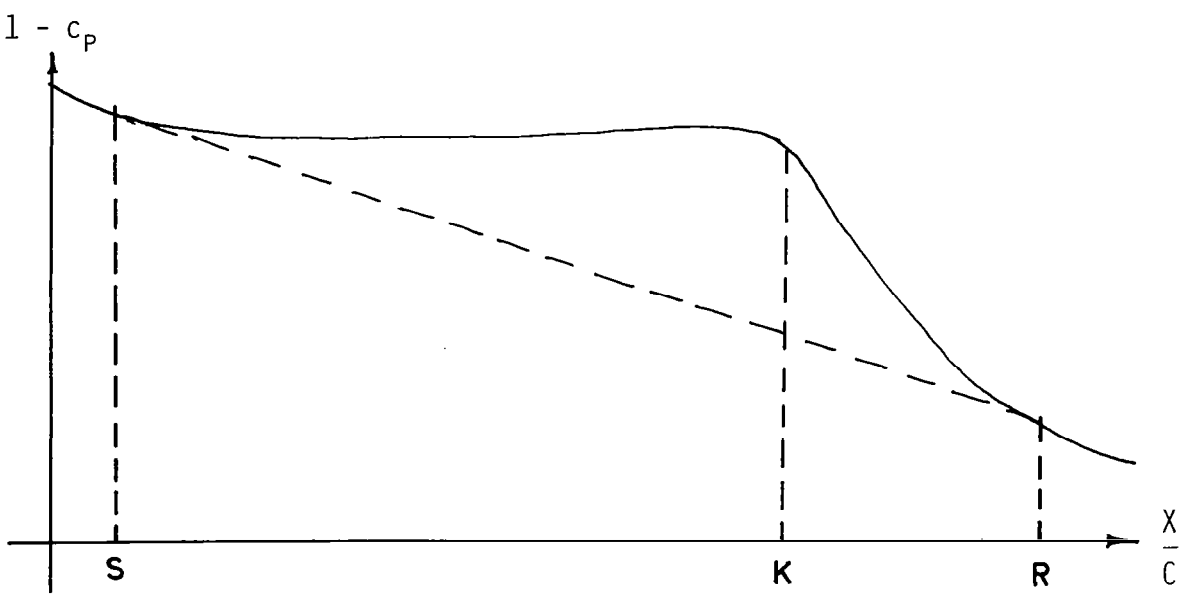

Figure 4.- Pressure distribution inferred from figure 3. Small entrainment velocities beneath shear layer imply small pressure gradients between S and K. Steep gradient between K and R due to splitting of shear layer at reattachment and gradient of stagnation pressure across lower half of shear layer.

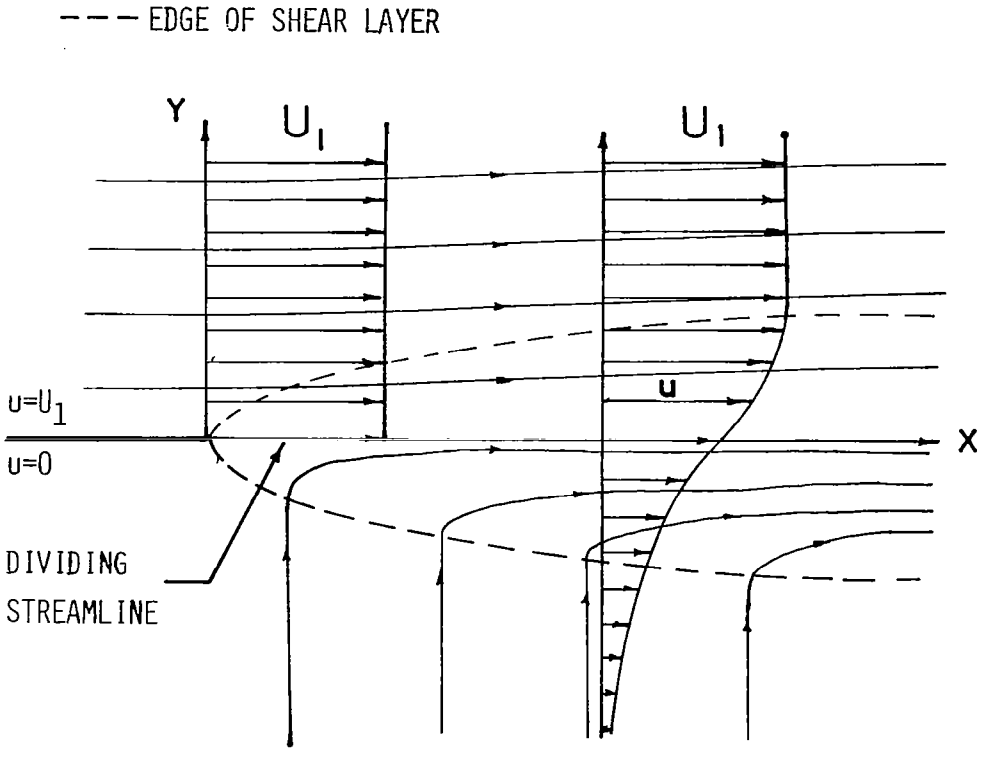

Figure 5.- Nomenclature for free shear layers in zero pressure gradient.

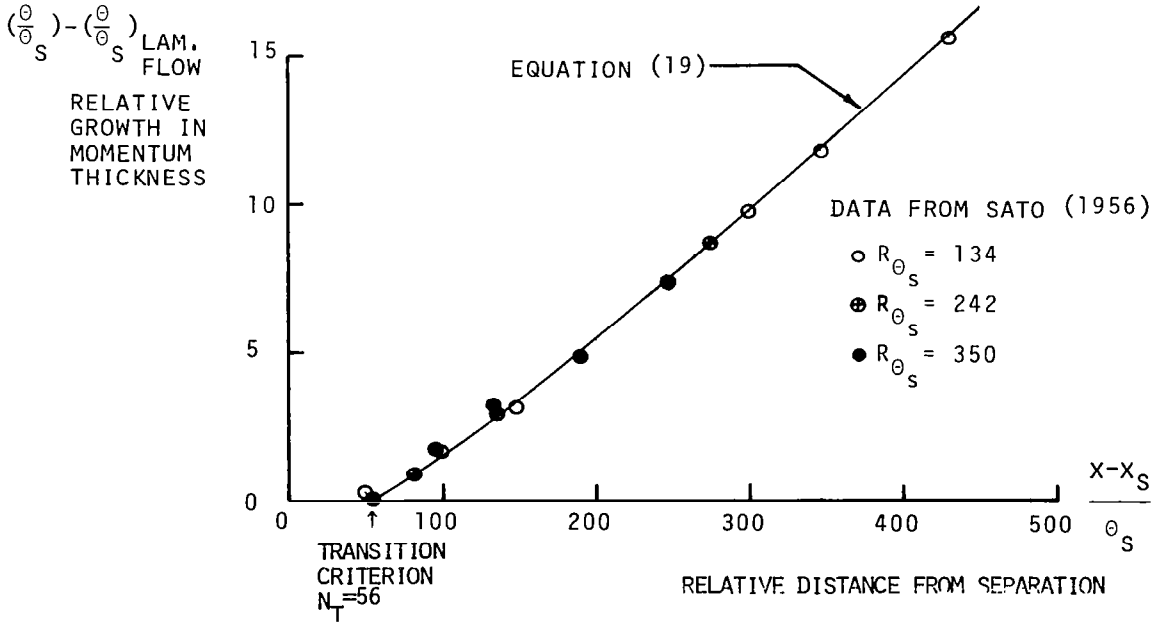

Figure 6.- Verification of empirical formula for growth of momentum thickness downstream of transition. Data from reference 12.

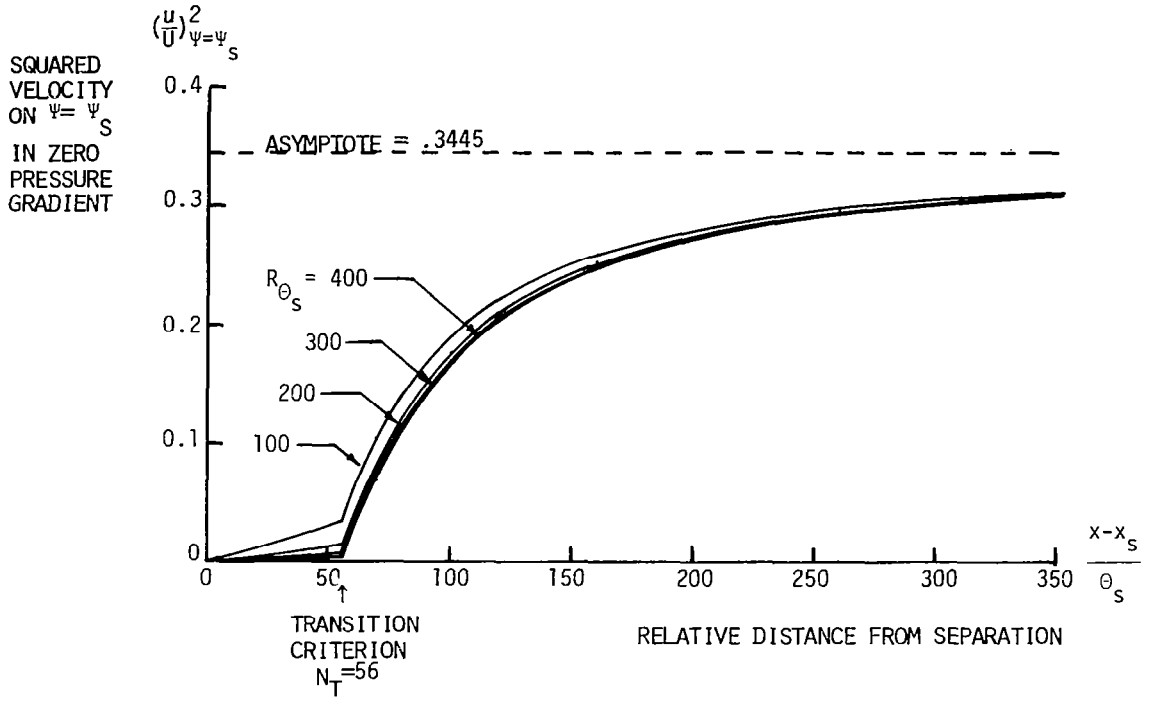

Figure 7.- Plot of equation (23) using equations (17), (18), and (19).

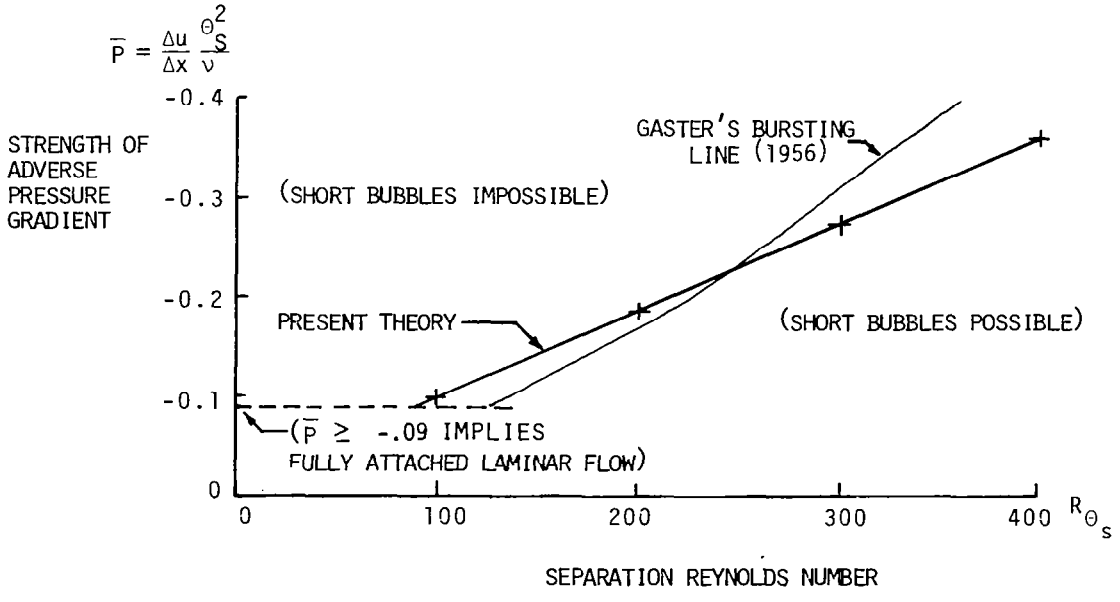

Figure 8.- Gaster's bursting line derived from present theory, which is based entirely on data from free shear layers.

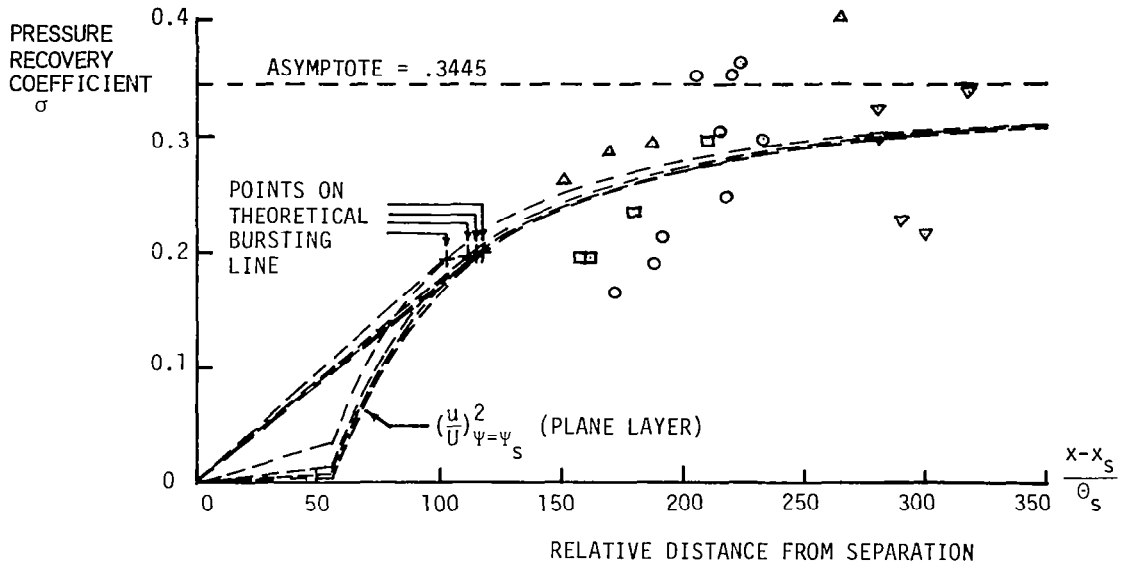

Figure 9.- Attempt to verify reattachment condition (31). Measured lengths and pressure recovery coefficients from various sources: □, Gaster (ref. 14) "series I"; △, Gaster "series II"; ○, Van Ingen (ref. 11); ▽, Tani (ref. 2, fig. 17, based on data from Gault, ref. 10). If equation (31) held exactly, then all measured points should lie on dashed curves. Note: each set of data represents a series of runs at various tunnel speeds, which, to avoid cluttering the figure, have not been shown.

WING SHAPE OPTIMIZATION FOR MAXIMUM CROSS-COUNTRY SPEED, WITH MATHEMATICAL PROGRAMMING

Gunter Helwig
Rensselaer Polytechnic Institute

SUMMARY

A computer program was developed to calculate numerically the speed and circling polars of an aircraft when the lift and drag characteristics of the wing airfoils are known. The planform of the wing is described by variables which are optimized so that the cross-country speed of the glider is maximum for the particular type of thermal model. Two thermal models will be compared and it can be shown that with a greater wing area than now normally used the performance can be increased.

SYMBOLS

b	half span
c_d	section drag coefficient
c_l	section lift coefficient
C_D	total drag coefficient of the aircraft
C_L	total lift coefficient of the aircraft
C_{D_i}	induced drag coefficient
C_{Do}	parasite drag coefficient
g	acceleration of gravity
H	height
r	radius of thermal
S	area
t	time
v_c	net climb rate of the glider
v_s	sink rate for the speed polar

v_{sc}	sink rate for the circling polar
$v_{thermal}$	vertical velocity of thermal
V	airspeed
V_R	average cross-country speed
V_{R_i}	cross-country speed for the i-th thermal
W	total weight
Z	object function
x_i	variables
α_i	weighting factors
ρ	air density
ϕ	sweep angle
λ	aspect ratio
ψ	bank angle

INTRODUCTION

The most important part of an airplane is a well designed wing. Only a few variables are necessary to describe the planform (fig. 1). The halfspan b and the sweep-angle ϕ are fixed. The airfoils with their lift and drag characteristics must be prescribed. The total lift of the airplane is

$$C_L = C_{L_{wing}} + C_{L_{tail}} \frac{S_{tail}}{S} \tag{1}$$

The C_L is calculated either by Multhopp's method (ref. 1) or, for swept wings, by Truckenbrodt's method (ref. 2). The tail lift is in general so small that it can be neglected. From the lift calculation the induced drag C_{D_i} (ref. 1) is obtained, too. The total drag is

$$C_D = C_{D_{profile}} + C_{D_i} + C_{Do} \tag{2}$$

$$C_{Do} = \frac{1}{S} \sum_{p} C_{Do_p} S_p \quad (p = 1,2..P) \tag{3}$$

C_{Do_p} is the drag coefficient of the p-th part, with surface area S_p. The profile drag coefficient $C_{D_{profile}}$ can be calculated from the measured Reynolds-number-dependent c_d-versus-c_l plots (fig. 2).

$$C_{D_{profile}} = \frac{1}{S} \sum_{n} c_{d_n} S_n \quad (n = 1,2..N) \tag{4}$$

From fig. 2 (measured data), fig. 3 can be determined, and by linear interpolation, the local c_{d_n} at the strip n with surface S_n is obtained. The aircraft equivalent parasite area $\sum_{p} C_{Do_p} S_p$ is assumed to be constant for a given aircraft.

SPEED AND CIRCLING POLARS

With the weight as the fifth variable (x_5 = weight), the principal performance characteristic of the glider, which is its cross-country speed, can be calculated. The speed polar is given by the equations

$$V = \sqrt{\frac{2}{\rho} \cdot \frac{W}{S} \cdot \frac{1}{C_L}} \; ; \quad v_s = \frac{C_D}{C_L^{3/2}} \sqrt{\frac{2}{\rho} \cdot \frac{W}{S}} \tag{5,6}$$

The circling polar is obtained from

$$v_{sc} = \frac{C_D}{C_L^{3/2} \cdot \cos^{3/2}\psi} \sqrt{\frac{2}{\rho} \cdot \frac{W}{S}} \tag{7}$$

$$\cos^{3/2}\psi = \left[1 - \left(\frac{2\ W/S}{\rho C_L\ r\ g}\right)^2\right]^{3/4} \tag{8}$$

CROSS-COUNTRY SPEED

The net rate of climb of the glider in the thermal (fig. 4) is

$$v_c(r) = v_{thermal}(r) - v_{sc}(r) \tag{9}$$

The maximum climb rate must be calculated as a function of the diameter of the thermal. With these two polars (speed and circling) the cross-country speed can easily be determined (fig. 5),

$$V_R = \frac{D}{t} \tag{10}$$

(D = distance; t = time from point A to C). The loss in height is

$$H = t_1 v_s \tag{11}$$

The gain in height is

$$H = t_2 \cdot v_c \tag{12}$$

Therefore,

$$t_2 = t_1 \frac{v_s}{v_c} \tag{13}$$

and with the time t_1 to go from point B to C, and the total time t, respectively,

$$t_1 = \frac{D}{V} ; \tag{14}$$

$$t = t_1 + t_2 \tag{15}$$

the cross-country speed by using the equations (13) to (15) and (10) is finally

$$V_R = \frac{V \cdot v_c}{v_c + v_s} \tag{16}$$

THE OBJECT FUNCTION

The program can be used with different types of thermal models. Two examples are given in fig. 6 and fig. 7 (ref. 3,4). As object function for the optimization, an average cross-country speed is defined for each thermal model

$$Z = \sum_i \alpha_i V_{R_i} \qquad \begin{array}{l}(i = 1,2,3 \text{ for Carmichael}) \\ (i = 1,2,..4 \text{ for Horstmann})\end{array} \tag{17}$$

$$\sum_i \alpha_i = 1 \text{ and } \quad 1 \geq \alpha_i \geq 0 \tag{18}$$

The V_{R_i}'s are the cross-country speeds from the i-th thermal and α_i is its weighting function. The α_i's must be chosen by the designer and then the optimization is achieved for the particular distribution of thermals assumed.

THE OPTIMIZATION PROCEDURE

The maximum cross-country speed is calculated by a penalty optimization program (ref. 5,6), so that constraints like $x_i \geq a_i$ $(i = 1,2,..5)$ (a_i = lower bound) or others can be observed. Using the performance polars from equations (1) and (2), two sub-optimization problems are solved: (a) determination of max v_c by using C_L and r as variables in equations (7) to (9), and (b) determination of max V_R (eq. 16) by using C_L as a variable through equations (5) and (6), with max v_c fixed. V_{R_i} has to be calculated for each thermal (index i). Then Z (eq. 17) can be calculated and optimized.

RESULTS

Only gliders with a span of 15m = 2b and $\phi = 0°$ were optimized. In diagrams 1 and 2 an optimization is shown with the profile FX-61-184 (ref. 7) for two thermal models with different sets of α_i's. For a convenient representation (this is only one possibility), $\alpha_1 = \alpha_2$ was used for the Carmichael thermals and $\alpha_1 = \alpha_2$ and $\alpha_3 = \alpha_4$ for the Horstmann thermals. For comparison, the performance of the D-38, an <u>almost</u> optimized competition glider in the 15m class from the Akaflieg Darmstadt (ref. 8), is shown in both diagrams. The curves were calculated by changing only the weight of the glider. The difference between the two curves gives the gain in performance over the D-38. On the average, the gain in performance is more than 2% for both thermal models. The Carmichael thermals deliver a higher cross-country speed because it is narrow and strong. This leads to a higher optimal wing area for Carmichael thermals compared to the Horstmann thermals (see table 1 and 2). In general, the optimized wing area is significantly larger than the normally used $11m^2$ area for rigid 15m wings.

In diagram 3 the wing loading and the aspect ratio are plotted versus the variable sets of α_i's for both thermal models, using the numbers from tables 1 and 2. The difference in the aspect ratio, $\Delta\lambda$, is about 1 and therefore the wing area difference, ΔS, is about $1m^2$. The average wing area is $14.4m^2$ for the Carmichael and $13.5m^2$ for the Horstmann thermals. Clearly the influence of the shape of the wing planform is small. The aspect ratio is almost constant from weak to strong thermals. This is true for both thermal models. The wing loading is the dominant factor influencing the cross-country speed. The dotted line (diagram 2) which was obtained by changing the weight, using optimal design for all α_i's equal, shows the importance of the weight (wing loading) but a relatively small influence of the wing shape. The proper wing loading, again, is more important for the Horstmann model (greater gradient) than for the Carmichael model for maximum cross-country speed.

Because of the dominating rule of the weight for the gliders, the curves in diagram 4 were calculated for various masses by using the optimal design with all α_i's equal. The optimal variables are given in table 3. The comparison between the 7 profiles shows that the best rigid profile is the FX-61-184, and the best profile with flaps is the FX-K-170

CONCLUSION

An increase of performance of more than 2% is possible with an increase in wing area. It is not necessary to design a glider for extreme (strong and weak) thermal conditions. The use of average weather (all α_i's equal) for the optimization of a glider results in an almost optimal design for all weather conditions. But the glider must be built as light as possible and should be able to carry up to 150 kg water ballast. The thermal model (Carmichael, Horstmann, or perhaps others) plays a minor part in the design but is extremely important for the proper choice of the water ballast to maintain maximum performance. Here it matters whether to believe in the Carmichael, Horstmann, or other thermal models. The program can then be used for a single variable optimization (the weight) to calculate the optimal water ballast curves for any type of weather condition.

REFERENCES

1. Multhopp, H., "Die Berechnung der Auftriebsverteilung von Tragflüegeln," Luftfahrtforschung 15, 1938.

2. Truckenbrodt, E., "Beitraege zur erweiterten Traglinientheorie," Zeitschrift fuer Flugwissenschaft, Vol. 2, 1953.

3. Carmichael, B.H., "What Price Performance," Soaring, May-June, 1954.

4. Horstmann, K.H., "Neue Modellaufwindverteilung und ihr Einfluss auf die Auslegung von Segelflugzeugen," 15 OSTIV-Kongress, Raengskaela, Finland, 1976.

5. Baier, H., Helwig, G., "Optimizationprogram PENOPT," Fachgebiet Leichtbau, TH-Darmstadt, 1976.

6. Kowalik, J., Osborne, M.R., Methods for Unconstrained Optimization Problems, Elsevier, New York, 1968.

7. Althaus, D., Stuttgarter Profilkatalog I, University of Stuttgart, 1962-1972.

8. Akaflieg Darmstadt, Jahresbericht 1968-70.

Table 1: Optimal Variables for 15m Gliders with the Profile FX-61-184 (Carmichael thermals, $C_{Do}S = 0.04m^2$)

OPTIMAL VARIABLES	OPTIMAL 15m GLIDERS					D-38
	$\alpha_1=\alpha_2=0$ $\alpha_3=1$	$\alpha_1=\alpha_2=0.2$ $\alpha_3=0.6$	$\alpha_1=\alpha_2=\alpha_3$	$\alpha_1=\alpha_2=0.45$ $\alpha_3=0.1$	$\alpha_1=\alpha_2=0.5$ $\alpha_3=0$	
x_1 (m)	1.31	1.19	1.23	1.14	1.19	0.94
x_2 (m)	1.11	1.07	1.09	1.04	1.02	0.753
x_3 (m)	0.49	0.47	0.51	0.45	0.45	0.376
x_4 (m)	3.78	4.17	3.87	3.62	4.25	4.5
x_5 (kg)	249	289	327	360	381	300
DERIVED VALUES						
S (m^2)	14.89	14.6	14.76	13.65	14.2	11
λ	15.11	15.4	15.22	16.48	15.85	20.45
max C_L/C_D	34.3	34.8	34.8	35.7	35.5	37

Table 2: Optimal Variables for 15m Gliders with the Profile FX-61-184 (Horstmann thermals, $C_{Do}S = 0.04m^2$)

OPTIMAL VARIABLES	OPTIMAL 15m GLIDERS				D-38
	$\alpha_1=\alpha_2=0$ $\alpha_3=\alpha_4=0.5$	$\alpha_1=\alpha_2=0.25$ $\alpha_3=\alpha_4=0.25$	$\alpha_1=\alpha_2=0.4$ $\alpha_3=\alpha_4=0.1$	$\alpha_1=\alpha_2=0.5$ $\alpha_3=\alpha_4=0$	
x_1 (m)	1.32	1.19	1.149	0.999	0.94
x_2 (m)	0.99	0.884	1.012	0.995	0.753
x_3 (m)	0.507	0.384	0.394	0.389	0.376
x_4 (m)	4.05	4.48	4.28	3.679	4.5
X_5 (kg)	254	328	390	432	
DERIVED VALUES					
S (m^2)	14.53	13.2	13.5	12.64	11
λ	15.48	17.04	16.67	17.8	20.45
max C_L/C_D	34.6	35.9	36.0	36.7	37

Table 3: Optimal 15m Gliders with Different Profiles
(Horstmann thermals, $C_{Do}S = 0.04m^2$)

	$\alpha_1 = \alpha_2 = \alpha_3 = \alpha_4$ Profile						
OPTIMAL VARIABLES	FX-60-126	FX-61-163	FX-66-S-196V1	FX-61-184	FX-K-131	FX-K-150	FX-K-170
x_1 (m)	0.94	1.07	0.98	1.19	1.18	1.03	1.077
x_2 (m)	0.76	0.927	0.919	0.884	0.99	0.866	0.911
x_3 (m)	0.379	0.395	0.37	0.384	0.38	0.39	0.37
x_4 (m)	4.37	4.08	3.37	4.48	4.9	4.26	4.14
x_5 (kg)	290	311	316	328	348	344	367
DERIVED VALUES							
S (m^2)	10.76	12.8	11.52	13.2	14.08	12.1	12.74
λ	20.9	17.58	19.53	17.04	15.98	18.6	17.66
max C_L/C_D	36.4	35.7	34.3	35.9	38.5	37.6	37.1

x_1 = chord at the root
x_2 = chord at the break
x_3 = chord at the tip
x_4 = span to the break

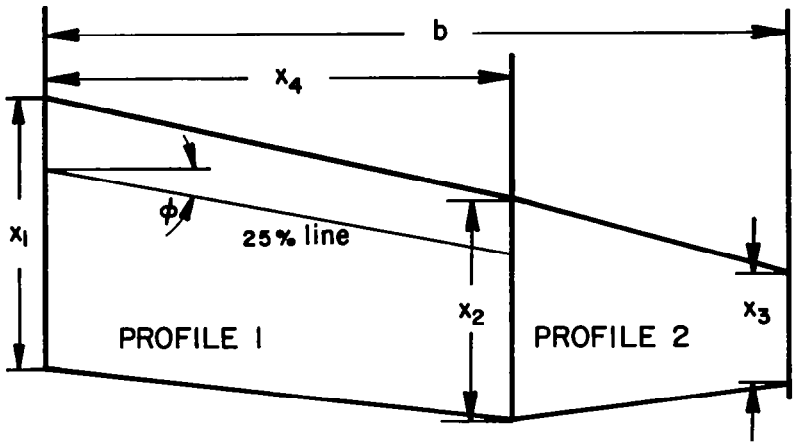

Fig. 1: Wing planform

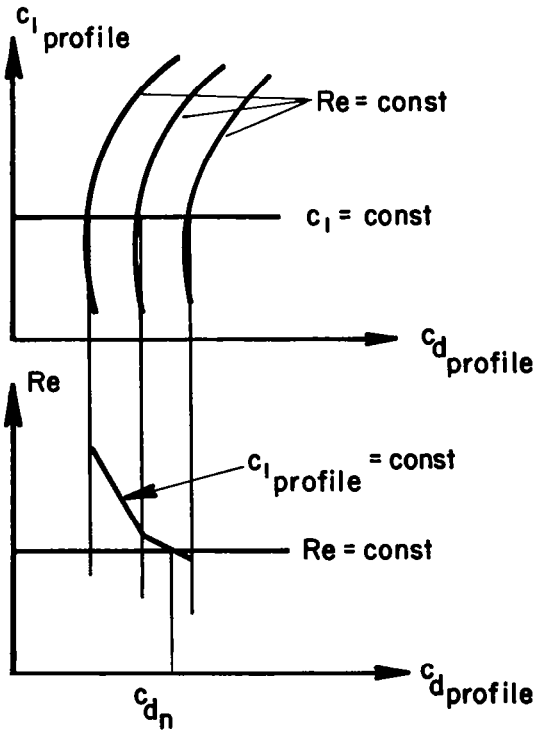

Fig. 2: Reynolds-number-dependent lift and drag characteristics

Fig. 3: Reynolds-number-dependent $c_{d_{profile}}$ for c_l=constant

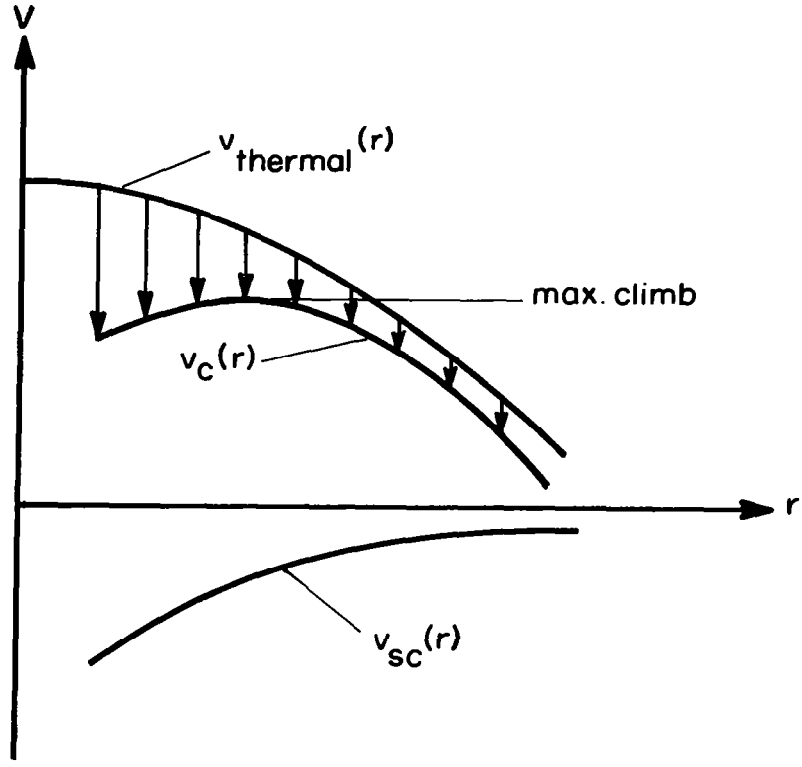

Fig. 4: Circling Climb Rate

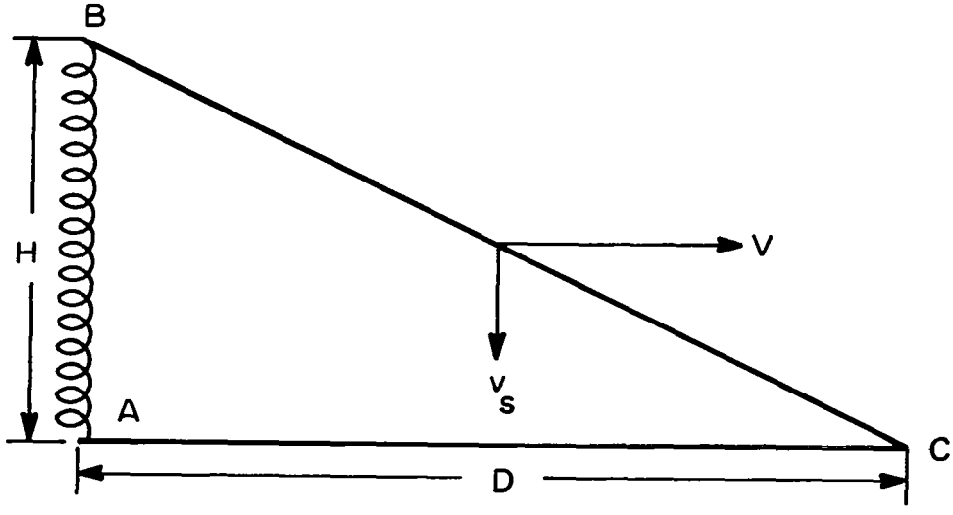

Fig. 5: Typical Flight Section

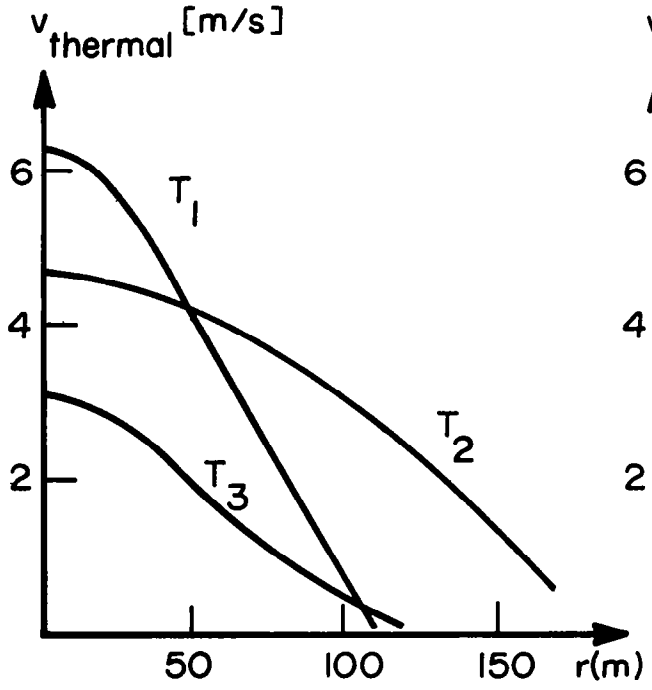

Fig. 6: Carmichael Thermals

T_1 = strong

T_2 = wide

T_3 = weak

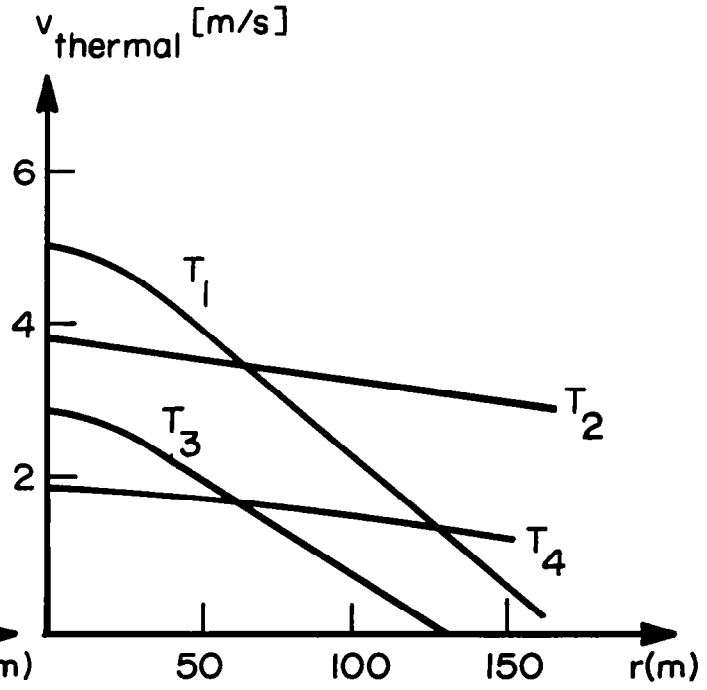

Fig. 7: Horstmann Thermals

T_1 = narrow, strong

T_2 = wide, strong

T_3 = narrow, weak

T_4 = wide, weak

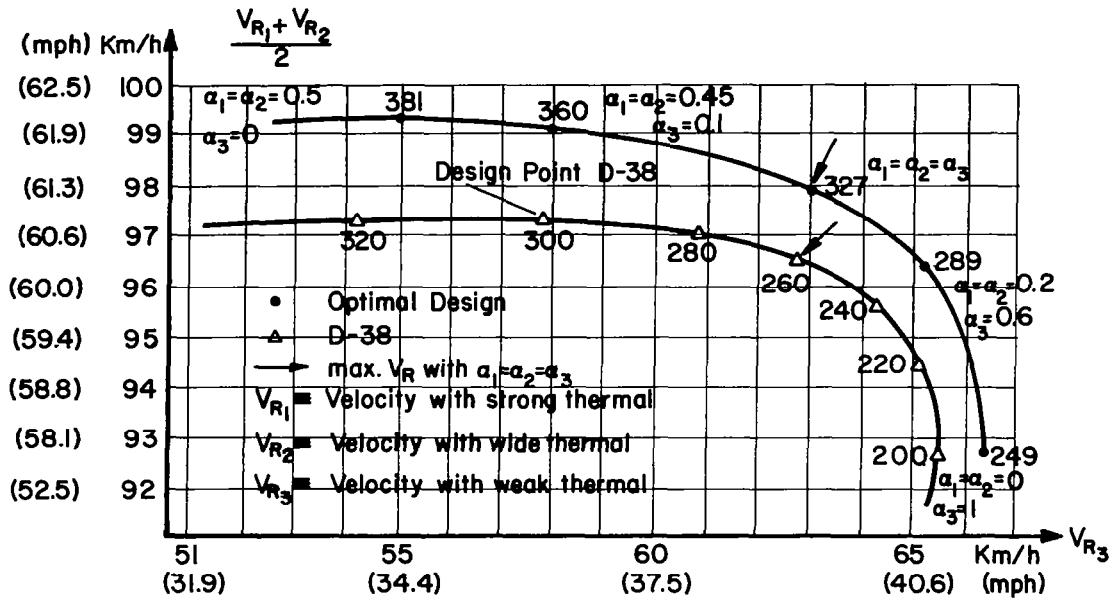

Diagram 1: Optimal performance of a 15m glider with the profile FX-61-184 for the Carmichael thermals. The numbers on the curves are total weights of the gliders in kg. ($C_{Do}S = 0.04m^2$ = const.)

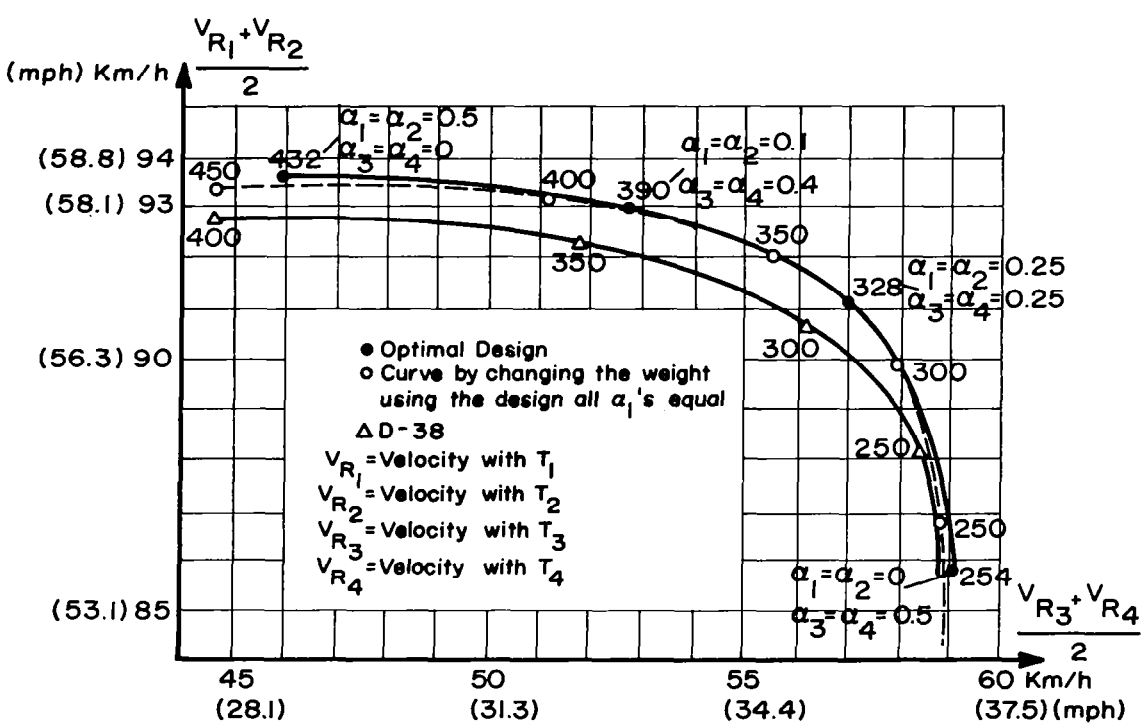

Diagram 2: Optimal performance of a 15m glider with the profile FX-61-184 for the Horstmann thermals. The numbers on the curves are total weights for the gliders in kg. ($C_{Do}S = 0.04m^2$ = const.)

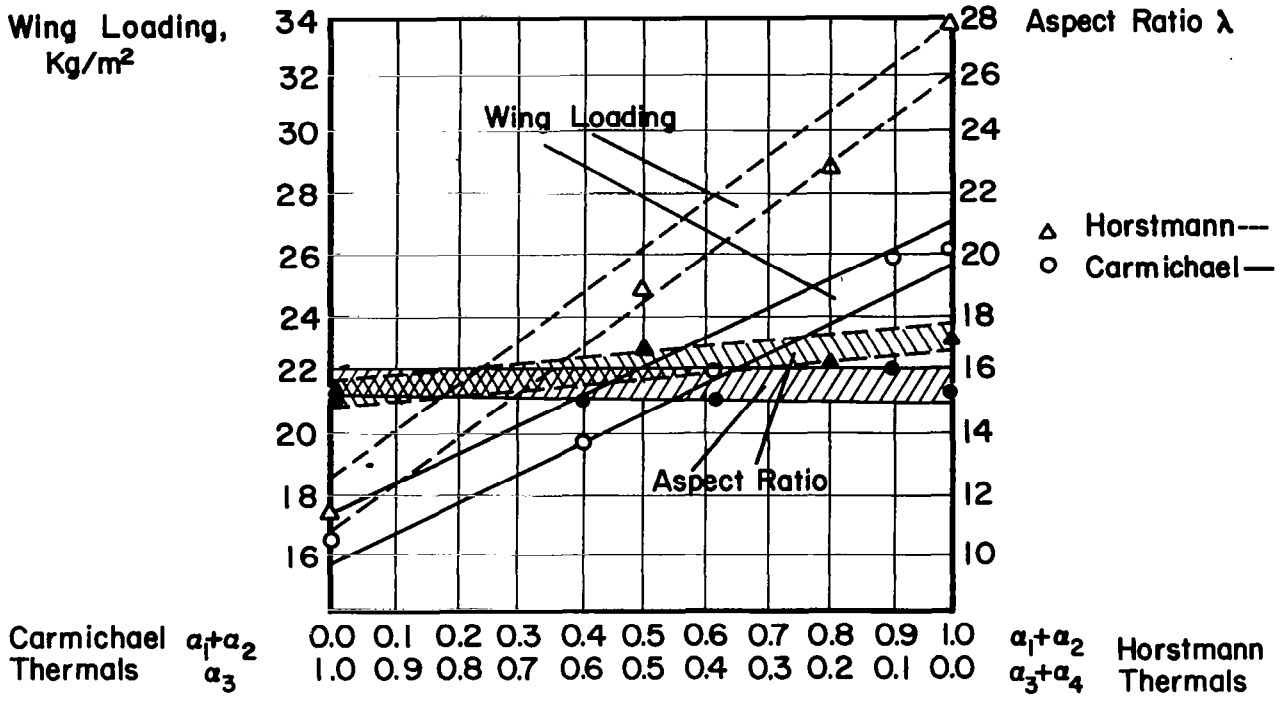

Diagram 3: Comparison Between Carmichael and Horstmann Thermals.

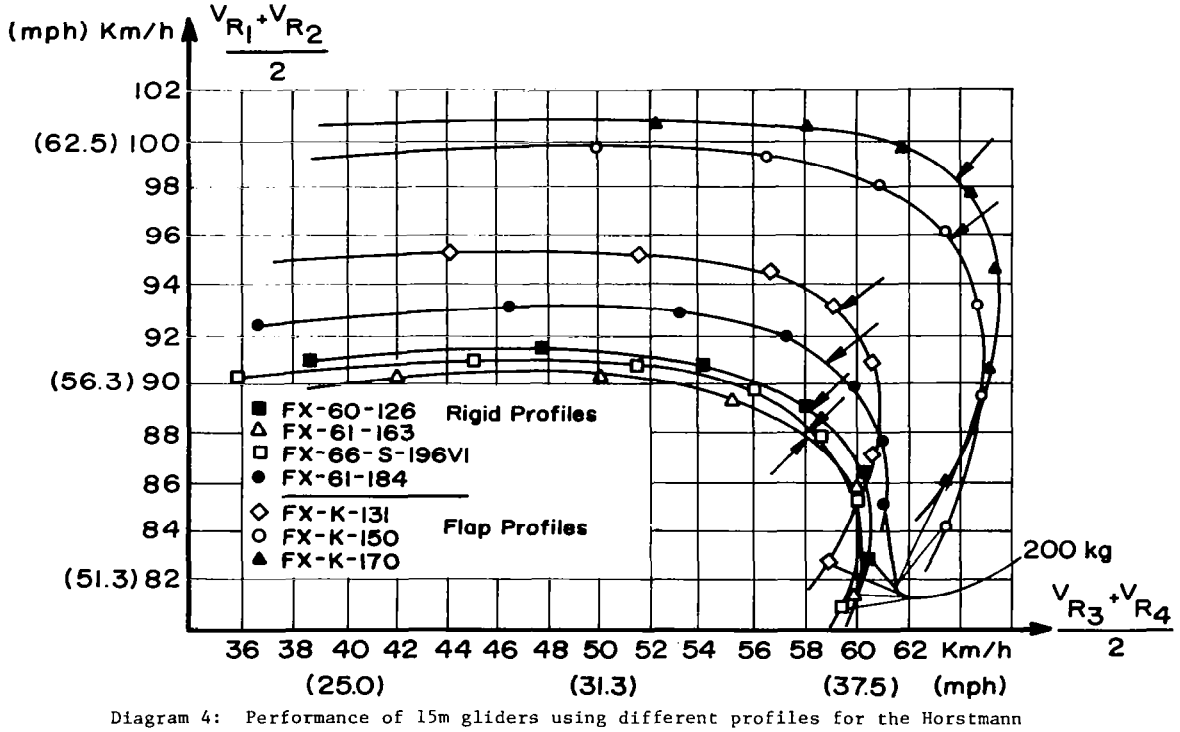

Diagram 4: Performance of 15m gliders using different profiles for the Horstmann thermals. Curves are calculated by using the optimal design (→ design point) with all α_i's equal. The change of the total mass from point to point is 50 Kg ($C_{Do}S = 0.04m^2$)

FURTHER DEVELOPMENTS IN SIMPLE TOTAL ENERGY SENSORS

Oran W. Nicks
Langley Research Center

SUMMARY

In 1976, research results were published on a simple total energy probe concept using principles of laminar flow around a cylinder. A number of probes employing these principles have been built. Additional tests have been conducted to further support earlier findings and options for probes made of a single bent-up tube.

Total energy pressure relationships are reviewed and flow fields around cylinders normal to and inclined to the flow are described. A variety of bent-up probe configurations were tested to explore variations in geometry. Test results are presented on the effects of sensor length, hole location, and angle of sweep. Comparisons are made with other probe tests reported in the literature.

A brief summary of damping restrictors and their use in filtering gusts is presented. Flow field effects, indicating the variables involved for different mounting locations on aircraft, are discussed.

INTRODUCTION

Since the 1976 publication of research results on a simple total energy sensor using principles of laminar flow around a cylinder, reference 1, a number of developments in their application have occurred. One objective of the research was to help sailplane owners improve their soaring instrumentation with a simple "do it yourself" design for a total energy sensor, references 2 and 3; the principles and broader applications are outlined in the Patent description, reference 4.

Many sensor probes have been made embodying the principles advanced; some are in use and reported to be performing quite satisfactorily, a number of modifications have been reported to suit the individual application, and some difficulties have been encountered with home-built sensors and applications for various reasons. In order to expand the general reference knowledge of the principles and sensitivities involved, this report provides information and data on further analyses and tests of simple total energy sensors using principles of laminar flow around a cylinder.

TOTAL ENERGY - PRESSURE RELATIONSHIPS

First, it is appropriate to briefly review the physical relationships of gliding flight which make a total energy sensor useful. Figure 1 shows how the useful total energy of a sailplane can be visualized in terms of altitude and velocity. The potential energy is directly proportional to altitude, the kinetic energy is directly proportional to the square of the velocity, and the sum of potential and kinetic energies is the total energy. At a particular instant, the best indications of the total energy state are provided to the pilot by the altimeter and airspeed indicator. For real-time energy management, however, the rate of change in this total energy state is most important. The basic requirement for a total energy sensor is to help provide the pilot such an indication.

When a sailplane dives, it gains kinetic energy at the expense of potential energy; the opposite occurs in a zoom; however, the only change in total energy during such maneuvers is caused by the drag of the sailplane and atmospheric energy variations, if any. The steady state drag effects are proportional to the drag times the velocity squared as indicated by a sailplane "polar" (where "polar" is defined as sink rate vs. airspeed), and the most significant atmospheric effects are rising and sinking air currents. Secondary effects on changes in total energy are caused by drag increases during rapid accelerations such as sharp pullups and tight turns, and horizontal wind gradients or shears can be significant near the ground. However, these are generally ignored as secondary during non-aerobatic flight at soaring altitudes. Thus, in simple terms, the rate of change in useful total energy may be indicated by a simple variometer instrument, if the total energy sensor connected to it provides proper compensation for exchanges in velocity and altitude.

We have said that the total energy TE of a sailplane of mass M gliding at a velocity V and at altitude H is:

$$TE = MgH + 1/2\ MV^2$$

The energy per unit mass of the sailplane can be written:

$$\overline{TE} = gH + 1/2\ V^2 \qquad (1)$$

Differentiating to obtain the rate of change gives:

$$d(\overline{TE}) = gdH + 1/2\ d(V^2) \qquad (2)$$

Assuming constant altitude, making use of the relation $dP_o = -\rho gdH$, where P_o is the ambient static pressure, and $dq = 1/2\ \rho d(V^2)$, where $q = 1/2\ \rho V^2$ we have:

$$d(\overline{TE}) = \frac{-dP_o}{\rho} + \frac{1/2\ d(V^2)}{\rho} \qquad (3)$$

Assuming the total energy of the sailplane remains constant, $d(\overline{TE}) = 0$ and equation (3) becomes:

$$dP_o - dq = 0 \tag{4}$$

Integration of equation (4) yields the following:

$$P_o - q = P_s \tag{5}$$

where P_s is the constant of integration.

P_s obviously is a pressure and must be positive, since for $q = 0$, $P_s = P_o$. Changes in the pressure P_s therefore provide an indication of changes in total energy of the sailplane. Putting equation (5) in coefficient form:

$$C_p \equiv \frac{P_s - P_o}{q} = -1 \tag{6}$$

THE FLOW OF AIR AROUND A RIGHT CIRCULAR CYLINDER

As indicated in reference 1, a number of sources pointed to the nearly correct pressure relationship on the downstream side of a right circular two-dimensional cylinder aligned normal to the flow, when the size of the cylinder and flow characteristics produce Reynolds numbers based on diameter from about 5,000 to perhaps 350,000. Within this Reynolds number range, the flows are described as subcritical, well established laminar flows before separation occurs.

Figure 2 shows the nature of the streamlines calculated for the flow around a cylinder in this regime, reference 5. The separated flow region results in relatively constant base pressures over the aft 110° to 160° of the cylinder. This large, relatively constant pressure region is the reason that a sensor made from a cylinder is insensitive to angles of yaw or circumferential hole position accuracy within this region. The separated flow does tend to fluctuate, however, and a high frequency vorticity can be sensed with dynamic instrumentation. Fortunately, these rapid pressure fluctuations can be damped and need not compromise a total energy sensor output for practical application.

A sample plot of a typical pressure distribution, figure 3, is shown to illustrate the nature of the pressure distribution in the Reynolds number range of greatest interest. This plot shows the relative sameness of the pressures on the aft side of the cylinder, corresponding with the separation region downstream in the streamline diagram. Such data provided the inspirations to use a small cylinder as a means of achieving the desired pressure relationships for a total energy sensor.

THE INCLINED THREE-DIMENSIONAL CYLINDER AS A TOTAL ENERGY SENSOR

Reference 1 described experimental studies which included the discovery that pressures on the aft side of a cylinder could be modified near the flat end of a three-dimensional cylinder to the value desired for total energy relationships. Further testing showed that sweeping the cylinder forward into the airstream about 20°, combined with a specific hole location relative to the end of the cylinder, produced the proper pressure relationship with an insensitivity to flow inclinations of at least $\pm 10^{\circ}$. This is more than adequate for use during soaring flight, as pitch variations for sailplanes of less than 6° to 8° are normal.

The combination of insensitivities to sideslip and angle of attack is especially desirable features of the simple probe. In addition, data were provided which indicated that the sensor holes could be of various diameters, saw slots, or multiple orifices as long as the average dimensions with respect to the cylinder end were maintained. Two specific total energy probe configurations were described which had been based on laboratory results and flight tests.

The most scientifically significant findings of reference 1 are summarized below for reference during the discussions to follow:

1. Flow normal to a right circular cylinder at subcritical Reynolds numbers produces pressure coefficients very close to the value needed for useful total energy rate of change indications.

2. For the velocity and altitude operating range of sailplanes, practical cylinder diameters of about 4.76 mm (3/16-inch) to 6.35 mm (1/4-inch) provide Reynolds numbers within a range from about 8,000 to 30,000, where sensor pressure coefficient and drag coefficient remain practically constant.

3. Orifices on the downstream side of a cylinder provide pressures that are relatively insensitive to sideslip angles.

4. Whereas pressures on the downstream side of a two-dimensional cylinder produce coefficients that tend to be too negative, it is possible to obtain predictably biased pressures with three-dimensional flow effects on a practical sensor by locating rearward facing orifices a given distance from the end of the cylinder; furthermore, the variation in pressure coefficient with hole distance from the end of the cylinder tends to be linear in the region of interest for coefficients near $C_p = -1.0$.

5. Pressure coefficients on the aft side of such a cylinder remain relatively constant over a range of forward sweep angles from about 10° to 30°; thus, a nominal cylinder orientation of 20° forward sweep provides a sensor with $\pm 10^{\circ}$ insensitivity to pitch changes.

BENT-UP PROBES - PURPOSE OF TESTS

The fin mounted probe configuration described in references 1, 2, 3, and 4 was made by joining two straight sections of tubing. Many homebuilders have made total energy probes from a single piece of tubing bent to provide the 20° forward swept portion, thus eliminating the two-piece manufacturing difficulties and the chance for leaks at the intersection of the two tubes. It is understood that many of the probes made in this way have been made of 6.35 mm (1/4-inch) steel tubing commonly used for hydraulic brakelines or fuel lines. This size tubing offers the strength and stiffness to support an extension of about 40 cm (15 inches) ahead of the fin leading edge.

Homebuilders who had difficulties with such probes report that pressure coefficients too low in absolute value were achieved, thus causing undercompensation in flight. One of the suspected causes of the low pressure coefficients was the likelihood that the bent-up sections of tubing were not long enough to sustain the two-dimensional flow field below the orifice. Further wind tunnel testing has been conducted on simple bent-up probes to determine the effects of various probe lengths on pressure coefficients and to better define the geometry of suitable probes made in this manner.

WIND TUNNEL TEST SETUP AND PROBE CONFIGURATIONS

The small wind tunnel used for the tests outlined in reference 1 was used for these tests. An atmospheric tunnel with velocities on the order of 20 meters (60 feet) per second, it provided Reynolds numbers based on diameter with the 6.35 mm (1/4-inch) tubing of 8,000 to 10,000.

The probe test setup was made to allow a common set of sensors to be used. This insured that no differences in results were caused by manufacturing differences on the sensors or hole location geometry.

A simple mounting arrangement allowed changes in the probe angle of attack so that sensitivity to sweep angle or angle of incidence could be determined. The angle of attack could be varied over a range of 35°. Since the probe had been designed with a forward sweep angle of 20° as the nominal mounting position, this meant that the probes were tested with forward sweep into the airstream over a range of +5° to +40°; for simplicity, all data are presented on that basis. The mounting and angle of attack changing system allowed the sensor to remain in the core of the wind tunnel flow where flow was uniform and velocities constant. As each probe configuration change was made, leak tests were performed to insure sealed joints.

Three types of configurations were tested with a combination of four sensors and two extenders, giving a total series of 13 configurations. These allowed a range of geometric parameters to be tested including sensor length, hole position from the probe end, hole position circumferentially, and two holes at a fixed orientation. These are shown in figure 4.

WIND TUNNEL RESULTS

As indicated in figure 5, variations in the length of the straight section of the sensor above the bend did have an effect on the pressure coefficient for sensors with the end geometry described in reference 1. Sensor lengths of 7 and 9 diameters produced pressure coefficients lower than the desired $C_p = -1.0$, whereas Y/D's of 11 and 13 both produced $C_p = -1.0$. These data support the findings from earlier tests where Y/D's of 12 or greater gave satisfactory results. Since the drop-off in coefficient apparently began to occur for lengths between 9 and 11 diameters, sensor lengths of 11 diameters or greater from the bend appear necessary to insure the proper flow effects at an orifice located two diameters from the probe end.

These data also confirm that a nominal forward sweep angle of 20° is a good choice to allow variations in flow direction which may result from downwash, slight mounting misalignments, or attitude changes during flight, without effects on the sensor pressure.

After it was determined that lengths shorter than 11 diameters did not produce the desired pressure coefficient with the hole at $X/D = 2.0$, an experiment was performed to determine whether locating the sensor hole nearer the end of the probe might counteract this effect by capitalizing on the varying effects of hole position discovered earlier. Using bent-up probe configurations having a fixed length/diameter ratio of $Y/D = 7$, results were obtained with three hole positions as indicated in figure 6. These data show that a $C_p = -1.0$ should be achievable for a hole position between 1.5 and 1.75 diameters from the sensor end; however, it is also seen that the range of insensitivity to sweep has lessened somewhat when compared to probes with a hole location 2.0 diameters from the end.

In a personal communication, Frank Irving of Imperial College referred to data on pressure distributions around cylinders normal to the flow showing less variation in pressure coefficient at circumferential hole locations other than 180°. He reported that he had tested probes with two holes located at $\theta = \pm 130^{\circ}$ which gave good results.

His comments led to a review of earlier data from references 1, 6 and 7 for cylinders normal to the flow. A slight trend toward greater dispersion of coefficient at $\theta = 180^{\circ}$ as a function of Reynolds number was evident, but perhaps more interesting are trends from reference 8 shown in figure 7 for two-dimensional cylinders swept at various angles to the flow. The trend toward more negative pressure coefficients at higher θ values is seen, along with the interesting fact that differences in coefficient for various sweep angles are less at lower θ values. This led to the conclusion that a broader range of insensitivity to incidence changes might be achieved if circumferential hole positions less than $\theta = 180^{\circ}$ were used.

Figure 7 shows the variations in pressure coefficient with sweep to be very slight at $\theta = 140^{o}$; for symmetry in a probe, it would be desirable to have two holes at a $\pm\theta$ value. Since it is much easier to position two holes 90° apart at $\theta = \pm 135^{o}$, this was chosen as a practical compromise to keep the two-hole probe as simple as possible to construct.

Tests with the 135° azimuth hole position were conducted using the same probe sensor sections tested earlier with the holes reoriented to $\theta = 135^{o}$, thus insuring consistent and comparable results with the same sensor sections that had been tested at $\theta = 180^{o}$. The tests were conducted at various X/D's for only two Y/D values of 7 and 11. These two probe sensor lengths were used because the results from earlier tests, shown in figures 5 and 6, indicated that coefficients of the desired values could be achieved for these lengths.

The data from tests of the shortest bent-up probe, Y/D = 7 configuration, are shown in figure 8. As indicated, the holes at the $\theta = 135^{o}$ position do increase the range of insensitivity to forward sweep over the range of interest. These data show the best X/D to be 1.75, producing a coefficient $C_p = -1.0$ over a 20° range of sweep angles. However, the mid-range appears biased such that 25° of forward sweep might be better than 20° as a nominal.

In figure 9, similar data are shown for the sensor length, Y/D = 11, found earlier to give consistent results with previous tests of probes employing the same and greater lengths. By comparing these data with figure 5, it is seen that the configuration with the $\theta = 135^{o}$ hole position gave results very comparable to the $\theta = 180^{o}$ hole position, except for the slightly lesser sensitivity to forward sweep.

Finally, as a confirmation check of an actual two-hole configuration, a new two-hole probe was made for Y/D = 7.0, X/D = 1.5, $\theta = \pm 135^{o}$. The results of this test showed consistent results with the single hole tests for $\theta = 135^{o}$ as shown in figure 10. This was expected since no variation in yaw occurred during tests of the single hole probe, but it provided positive assurance. The insensitivity to sweep was significantly extended for the short probe having two holes, although the particular hole location, X/D = 1.50, resulted in slightly over-compensating coefficients. However, as indicated in figure 8, the desired coefficient should be obtainable by locating two holes at X/D = 1.75. Thus, it has been shown that for a short sensor section with a straight length of 7 diameters, a two-hole configuration will produce good compensation. In general, it has been found that the closer the hole is to the end of the probe, the more sensitive the end effects and more rapid changes in coefficients are likely to occur for small variations in the bevel or chamfer. This tends to make tolerances more important; for this reason, it appears that more consistent results can be expected if bent-up probes are made with sensor lengths of 11 diameters or greater with hole positions 2 diameters from the end.

Perhaps a further word should be said about the shape of the end of the sensor and its effects. References 1, 2, 3, and 4 pointed out that the three-dimensional effects of the probe end were affected by the amount of rounding or chamfer of the end. To obtain consistent results, a squared-off end with a very slight chamfer to "break" the sharp edge was recommended. In reference 9, Wells discussed the matter of beveling edges and described a method of making a chamfering tool for this purpose. He indicated values of about 0.066-0.018 mm (0.004-0.007 inch) are typical. Such precision in chamfering has not been found essential, but experience has shown that rounding off the edges too much tends to produce over-compensation, and care is recommended in beveling the edge. While it is difficult to specify and measure dimensions for the beveled edge, it is believed that chamfered surfaces of about 0.013 mm (0.005-inch) are suitable.

COMPARISON OF VARIOUS CONFIGURATIONS

In addition to a number of informal reports of experiences with total energy probes based on the principles outlined in reference 1, several results have been presented in periodicals which are worthy of mention. In reference 9, Wells discussed a method used for calibrating total energy probes and some results of tests. Performance data were not shown; however, the article indicated satisfactory results with a bent tube approach, although the benefits of forward sweep were questioned. The importance of care in beveling the edge was specifically discussed.

Diplom-Physiker Westerboer (ref. 10) described probes made and tested in West Germany of both fin and fuselage mounted types. He indicated that good compensation was achieved and also mentioned other results obtained in Europe. He specifically mentioned that an experimenter from the Braunschweig Akaflieg had also found 60° to 80° forward sweep (equivalent of 10° to 30° measured from vertical) to be optimum. Dimensions given for a bent-up tube version included a straight section for the sensor portion of about 10 diameters. The test results reported in figure 5 show that greater than 9 diameters are required to achieve the desired sensor pressure coefficient; thus, it would seem that Diplom-Physiker Westerboer also confirmed the suitability of this geometry for a bent-up probe configuration.

An article (ref. 11) by Charles W. Shaw described a probe made for a nose mounting installation. The report stated that excellent compensation was achieved, along with improved response rate, and no effects due to sideslip. The probe was mounted on the nose cap of the fuselage and projected eleven inches above the surface at about the 20° forward sweep angle.

A probe using these principles was discussed in reference 12 by Frank Irving. Although a complete description did not accompany the data presented in the article, a photograph of a probe mounted on a sailplane fin indicated it to be a bent tube design. In the description, it was

stated that the design incorporated the 70° bend inclination to the airstream (20° forward sweep), the same as suggested in reference 1. The data show the probe as being relatively insensitive to incidence or angle of attack changes, although variations of 4 percent were indicated at about $\pm 10^{\circ}$ of incidence.

In the same article, data were presented for a so-called "Modified Nicks" probe which undercompensated; however, no details of the modification were given, so it is not possible to assess the reasons for the undercompensating pressure coefficients. Data from this report on the best probe tested by Irving are shown in figure 11 for comparison with the configurations reported in reference 1 and the bent-up probes reported here. In a personal communication, Irving described his probe as a bent probe configuration having two holes at $\theta = \pm 130^{\circ}$ at an X/D value of 1.5, with a Y/D of about 7. Based on these data, it appears that the probe tested by Irving has a greater variation during pitch changes than the bent probe versions having sensor lengths of 11 diameters or more as tested and discussed in this report.

As a matter of general interest, it should be mentioned that probes made like configuration A of reference 1 have been tested in the NASA 8-foot Transonic Pressure Tunnel over a Mach number range from $M = 0.15$ to $M = 0.75$. Although test results have not been published, a variety of X/D values were tested confirming the $X/D = 2$ as most suitable for obtaining C_p values of -1.0. The preliminary data show coefficients within 5 percent of the desired value up to $M = 0.3$, with only slightly more variation to $M = 0.75$. The probes are being installed on a transport aircraft for experiments in wind shear detection and total energy management.

DAMPING RESTRICTORS

The separated flow region behind a cylinder operating at subcritical Reynolds numbers produces a fluctuating pressure which may couple with the dynamic characteristics of a sensitive variometer and cause needle oscillations or "vibrata" effects on an audio signal. Enlarging the orifice diameter or changing the tubing volume connecting the sensor to the variometer can affect these natural frequencies without modifying the average signal pressure, but a recommended solution to this effect involves the use of a damping restrictor-volume combination. Even if the natural frequencies of the sensor-variometer system do not cause oscillations, gustiness will produce fluctuations which tend to compromise the usefulness of total energy readings.

The simplest form of damping or gust filter can be made with a simple capillary restrictor and volume placed in the line between the total energy sensor and the variometer. Most mechanical variometers have time constants of about 2-7 seconds, although some electric variometers and a few mechanical models are capable of response times of less than a second (ref. 13). It is doubtful that response times of much less than two seconds are useful when gusty conditions exist; however, a gust filter will become the limiting factor if it has a slower response than the instrument, and the selection of a filter response rate must take this into account (ref. 14).

A good discussion of gust filters and ways to make them appeared in reference 15. The time constant for a restrictor-capacitor pneumatic gust filter is given by the equation:

$$T = (1.06 \times 10^{-7}) \frac{CL}{PD^4} \tag{7}$$

where:

T = gust filter time constant, sec

C = capacity of the gust filter flask, cubic inches

L = length of capillary tube restrictor, inches

P = absolute pressure of the atmosphere at expected flight levels, pounds per square inch

D = internal diameter of capillary restrictor, inches

Theoretically, it is desirable that the filter capacity volume be larger than the variometer flask when the variometer system uses such; however, a capacity equal that of the vario capacity seems to suffice. For electric varios having a built-in volume, a small capacitor may be suitable. For example, good results have been achieved with a fin mounted sensor having a built-in restrictor made of 0.508 mm (0.020 inch) inside diameter capillary 25.4 mm (1 inch) long, when used with an electric vario having a small internal volume. In this case, the length of tubing from the fin to the vario served as a capacitor.

Using the equation above, restrictor lengths have been calculated and presented in figure 12 for two restrictor inside diameters as a function of capacitor volume, for time constants of 1.0 and 2.0 seconds, at an altitude of 1524 meters (5000 feet). From these relationships, it can be seen that restrictors made of 0.508 mm (0.020 in.) or 0.794 mm (1/32-in.) inside diameter tubing are of practical lengths for a total energy system. Gust filtering is very important, and every total energy probe of the types described herein should have a restrictor added into the probe or installed in the line nearby. For fast response varios,

about 2.5 cm (1 inch) of 0.508 mm (0.020 inch), or about 8 cm (3 inch) of 0.794 mm (1/32-inch) tubing should be helpful for gust filtering without introducing undesirable delays, even if the capacitor volume is small.

FLOW FIELD EFFECTS ON TOTAL ENERGY SENSORS

Obtaining the pressure coefficient for good compensation is best achieved if the sensor can be located in the freestream, unaffected by attitude changes of the aircraft. It is not necessary that the local pressure be the same absolute value as the freestream; it is only necessary that the static pressure, relative to freestream, not vary as the aircraft attitude changes. Because of this, a desirable sensor location must take into consideration local flow field changes during maneuvers. There are several aspects of flow fields which may be important:

1. Boundary layer growth along the body
2. Flow angularities caused by the windshield and the wing body intersection
3. Downwash caused by lifting surfaces deflecting the flow
4. Movable control surfaces which may propagate pressure influences upstream
5. Induced velocities above wing or fuselage

The boundary layer consideration is largely relevant if probes are located on the aft portion of the fuselage. Flows tend to parallel fuselage surfaces aft of the wing, so that a location roughly mid-way between the wing trailing edge and the tail offers relatively constant flow conditions for total energy sensors, provided that the sensor is located far enough from the body to avoid the boundary layer at all angles of attack or yaw. For aft fuselage mounting on the upper side, the sensor element should be located about 7 inches above the surface to insure avoidance of boundary layer fluctuations as attitude changes.

Sensors have been located successfully on the noses of sailplanes; however, for this location there often are significant flow angularities as the flow streamlines are diverted around the body. Canopy bumps may cause local effects which would be undesirable, for example, and when positioning at the proper sweep angle, it should be recognized that streamlines parallel the surface at the surface.

High performance sailplanes usually achieve some laminar flow on the nose portion of the fuselage; a performance penalty may result with a probe in the laminar region which triggers an early transition from laminar to turbulent flow. This is not a problem for training sailplanes or others which do not depend on laminar flow for performance. Judgement must be

used in determining the proper sensor sweep angle on a curving surface, and experimenting with flight tests may be necessary.

The vertical fin location usually offers near freestream conditions, provided the probe is positioned so that the fin, rudder, stabilizer and elevator (especially for Tee Tail configurations) are taken into account.

The principal downwash in the flow field at the fin location is caused by the wing deflecting the air to produce lift. A series of calculations have been made to cover the range of effects for typical sailplanes during cruise and climb conditions. The downwash flow angle is a function of the lift coefficient being achieved at a given time. Reference 16 provides a thorough discussion of the mechanisms affecting the downwash as well as analytical methods for use in calculations. Based on these techniques, and the dimensions for short coupled sailplanes like the 1-26, the downwash angle at the fin tip in degrees is about three times the lift coefficient, C_L . In the cruise condition, the lift coefficient for the 1-26 is about 0.5, making the downwash angle only 1.5 degrees. In the climb condition, the lift coefficient is about 1, making the downwash about 3°. For high performance sailplanes having longer wings and fuselages, the downwash values decrease to about half those for a 1-26; that is, the range of downwash angles at the fin may be about 1.2 to 1.8 times C_L degrees. The range of lift coefficients may be somewhat greater due to flaps; however, the total downwash variation for high performance sailplanes may still be less than 3°.

For a fin installation, the sensor should be positioned at least 5 to 10 times the maximum fin thickness ahead of the leading edge (ref. 17). Severe rudder deflections may cause significant lateral flow inclinations; however, the insensitivities of the simple probes described herein are a real advantage. Horizontal tail movements affect the downwash flow field to some extent. When attitude changes are being made, transients may be noticed; however, the effects can be minimized by smooth movements of the control surfaces. Sailplanes that are well balanced will not have very large tail lift coefficients, and therefore small downwash effects.

In summary, a sensor location insensitive to changes in attitude is necessary for operation over a broad range of locations. Aft fuselage and vertical fin locations can be suitable for the probes discussed. Nose installations may be acceptable for low performance sailplanes; however, they must be positioned carefully.

CONCLUDING REMARKS

Experimental pressure coefficients suitable for total energy compensation have been obtained using principles of laminar flow around a small inclined cylinder. To obtain the correct flow relationships, the sensor orifice should be located carefully with respect to the end of a 3-dimensional cylinder; several options for providing the proper relationships have been extended by the current study of probes made of bent-up tubing. Total energy-pressure relationships have been reviewed to explain the principles involved and further explanations of 3-dimensional effects have been presented.

In general, it has been shown that probe sensors with lengths as short as 7 times the outside diameter of the tubing used can be made to work with certain orifice locations. On the other hand, data have shown that sensitivities to manufacturing tolerance and flow incidence angles are reduced when sensor lengths of 11 diameters or greater are used.

Comparative results from a number of experimenters have verified the principles and findings previously presented. The most significant of these probe dimensions are the sensor hole location geometry and the best angle of sweep for compensation that is insensitive to range of angles of incidence.

Damping restrictors are useful to filter gusts and may be simply made by installing a small section of capillary tubing in or near the total energy probe, in series with an appropriate capacitor volume.

Flow field effects around aircraft can affect the compensation of total energy sensors and must be considered. Among the effects are the boundary layer growth, flow angularities, downwash caused by lifting surfaces and movable control surfaces which may propagate pressure influences. The significance of these effects and ways of accounting for them are discussed.

REFERENCES

1. Nicks, Oran W.: A Simple Total Energy Sensor. NASA TMX-73928, March 1976. (Also presented at XV Congress of OSTIV, Rayskala, Finland, June 1976.)

2. Nicks, Oran W.: A Simple Total Energy Sensor. Soaring, Volume 40, No. 9, Sept. 1976.

3. Nicks, Oran W.: How to Make a Total Energy Sensor. Soaring, Vol. 41, No. 3, March 1977.

4. U. S. Patent Office, U. S. Patent No. 4,061,028. Aircraft Total Energy Sensor - Oran W. Nicks, Dec. 6, 1977.

5. Thom, A.: The Flow Past Circular Cylinders at Low Speeds. Proceedings of the Royal Society of London, Series A., Vol. CXLI. Printed for the Royal Society and sold by Harrison and Sons, Ltd., St. Martins Lane, Sept. 1933.

6. Thom, A.: An Investigation of Fluid Flow in Two Dimensions. Reports and Memoranda No. 1194 (AE356). Printed and Published by His Majesty's Stationary Office, London, Nov. 1928.

7. Goldstein, S.: Modern Developments in Fluid Dynamics. Vol. I, Oxford at the Clarendon Press, 1938.

8. Bursnall, William J., and Loftin, Laurence K., Jr.: Experimental Investigation of the Pressure Distribution About a Yawed Circular Cylinder in the Critical Reynolds Number Range. NACA TN 2463, Sept. 1951.

9. Wells, Bill: Calibrating Total Energy Tubes. Soaring, Vol. 41, No. 11, Nov. 1977.

10. Westerboer, Ingo: Die Neue Nicks-Duse: Ein ganz heiber Tip von der OSTIV-Tagung in Finnland. aerokurier, Vol. 9, Sept. 1976.

11. Shaw, Charles: T. E. Sensor, 1-26 Association Newsletter, Jan. 1977.

12. Irving, Frank: A New Total Energy Head. Sailplane and Gliding, Feb.-March 1978.

13. Johnson, Dick: Variometer Time Constants - Soaring Mail - Soaring Vol. 41, No. 6, June 1977.

14. Foster, K., and Parker, G. A.: Fluidics Components and Circuits. Wiley Interscience, A Division of John Wiley and Sons, Ltd., London, New York, Sydney, Toronto.

15. Newgard, Peter M.: Gusts and Gust Filters. Soaring, Vol. 43, No. 1, Jan. 1979.

16. Glauert, H.: The Elements of Aerofoil and Airscience Theory. Second Edition, Cambridge University Press, 1948.

17. Gracey, William: Measurement of Static Pressure on Aircraft. NACA Report 1364, 1958.

PHYSICAL RELATIONSHIPS
GLIDING FLIGHT

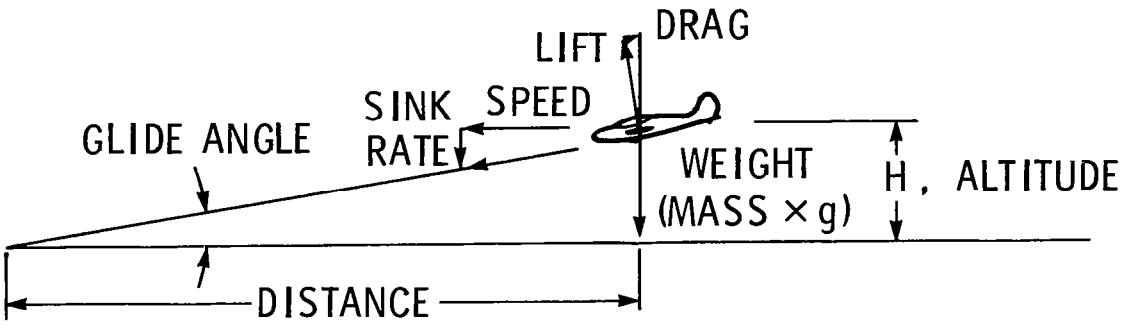

$$\frac{\text{LIFT}}{\text{DRAG}} = \frac{\text{DISTANCE}}{\text{ALTITUDE LOSS}} = \frac{\text{SPEED}}{\text{SINK RATE}}$$

POTENTIAL ENERGY,

$$PE = HMg \; ; \; \text{ALTITUDE} \times \text{MASS} \times g$$

KINETIC ENERGY,

$$KE = \frac{MV^2}{2} \; ; \; \text{MASS} \times \frac{(\text{VELOCITY})^2}{2}$$

TOTAL ENERGY,

$$TE = PE + KE = HMg + \frac{MV^2}{2}$$

FIGURE 1

CALCULATED STREAMLINES PAST A CIRCULAR CYLINDER

(REF. 5)

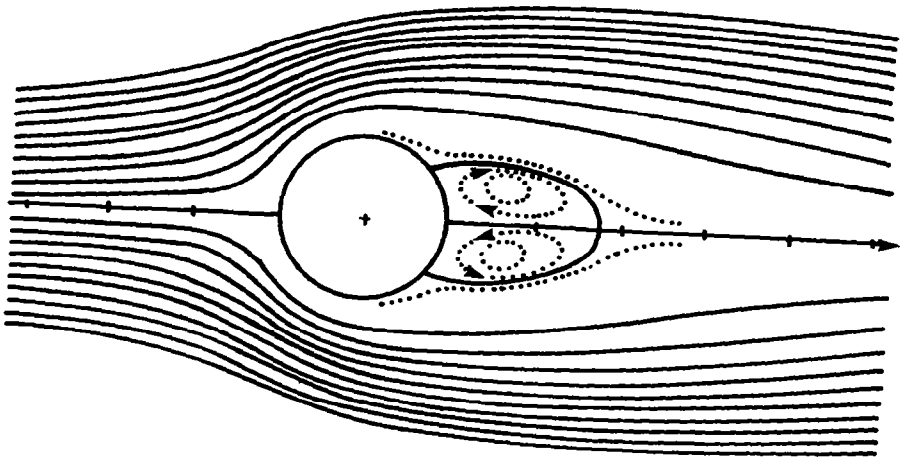

FIGURE 2

TYPICAL PRESSURE DISTRIBUTIONS

TWO-DIMENSIONAL CYLINDERS
(REFS. 6 AND 7)

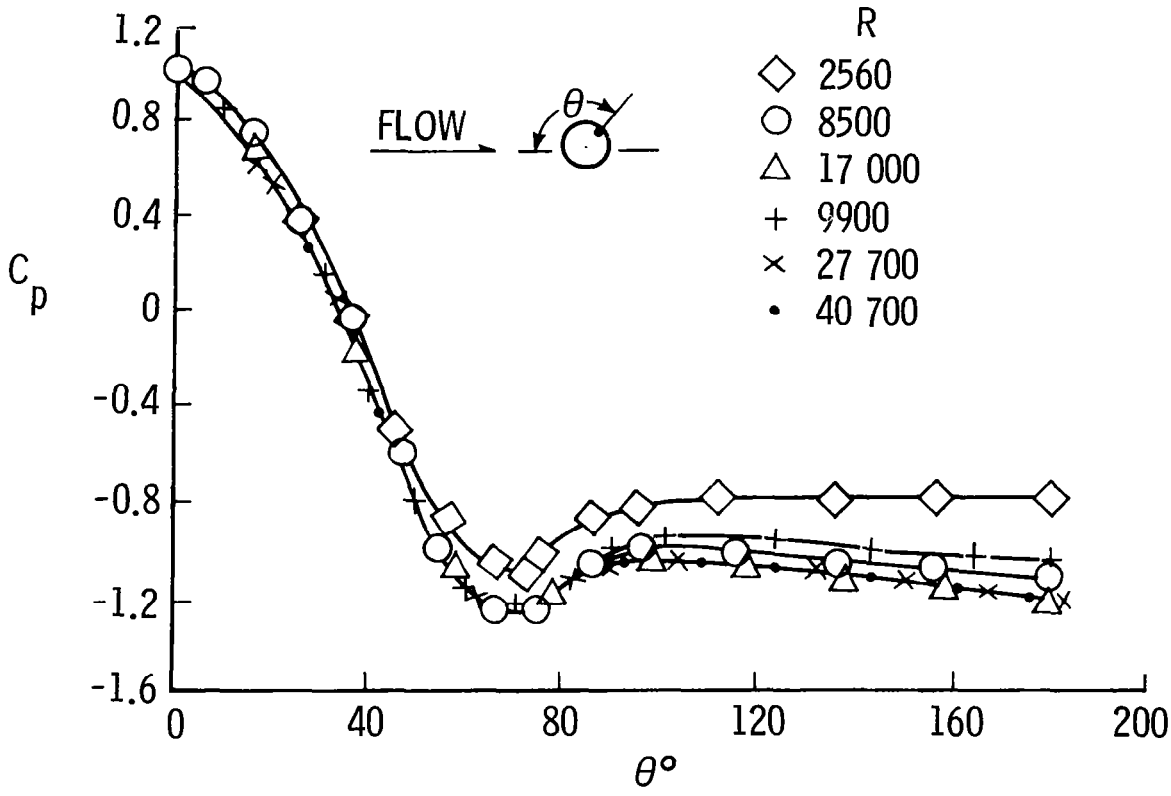

FIGURE 3

BENT-UP PROBE CONFIGURATIONS

CONFIG. NO.	1	2	3	4	5	6	7	8	9	10	11	12	13
Y/D	7	9	11	13	7	7	7	7	7	11	11	11	7
X/D	2.0	2.0	2.0	2.0	1.5	1.75	1.5	1.75	2.0	1.5	1.75	2.0	1.5
HOLE POSITION	$\theta = 180^0$						$\theta = 135^0$						$\theta = \pm 135^0$

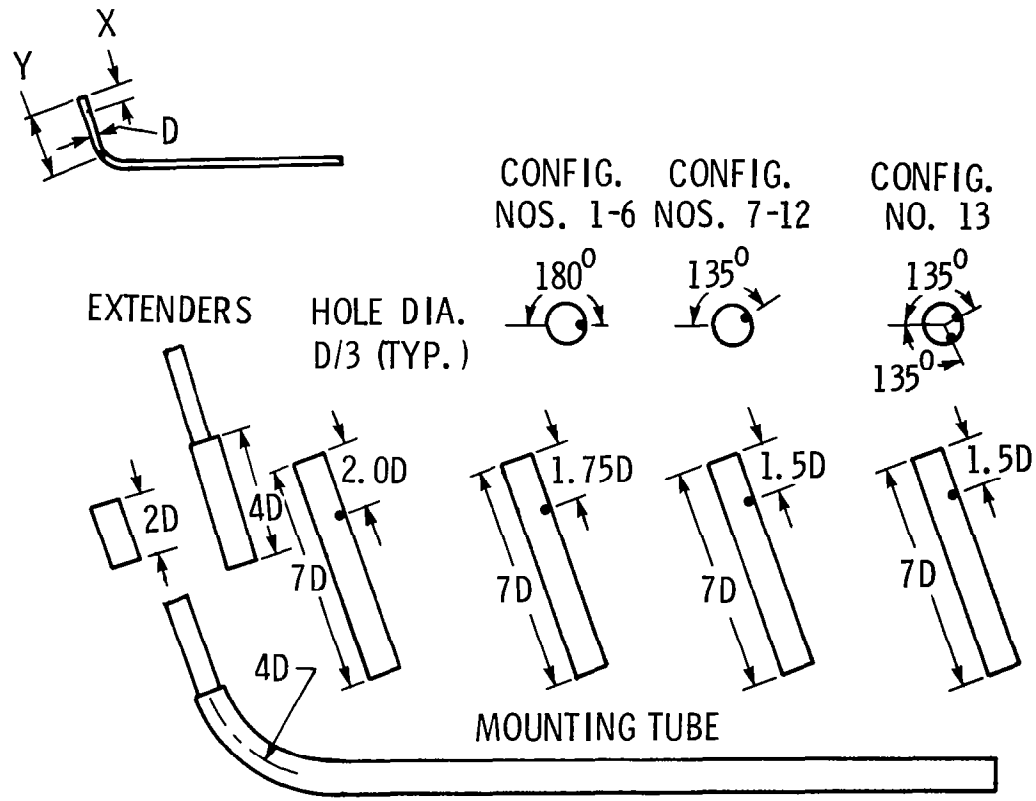

FIGURE 4

EFFECT OF PROBE LENGTH
BENT-UP PROBE, X/D = 2.0

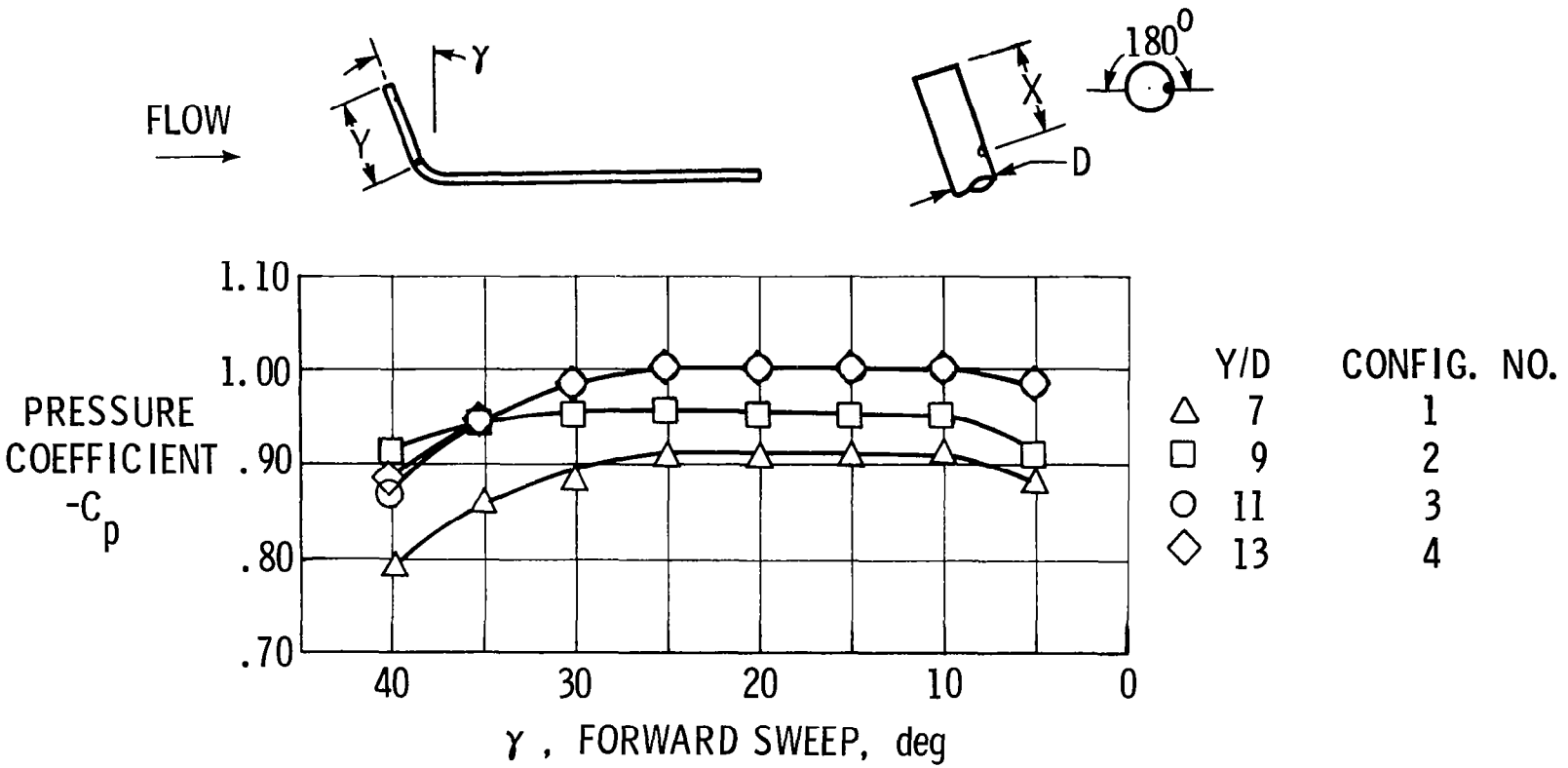

FIGURE 5

EFFECT OF HOLE POSITION
SHORT BENT PROBE, Y/D = 7

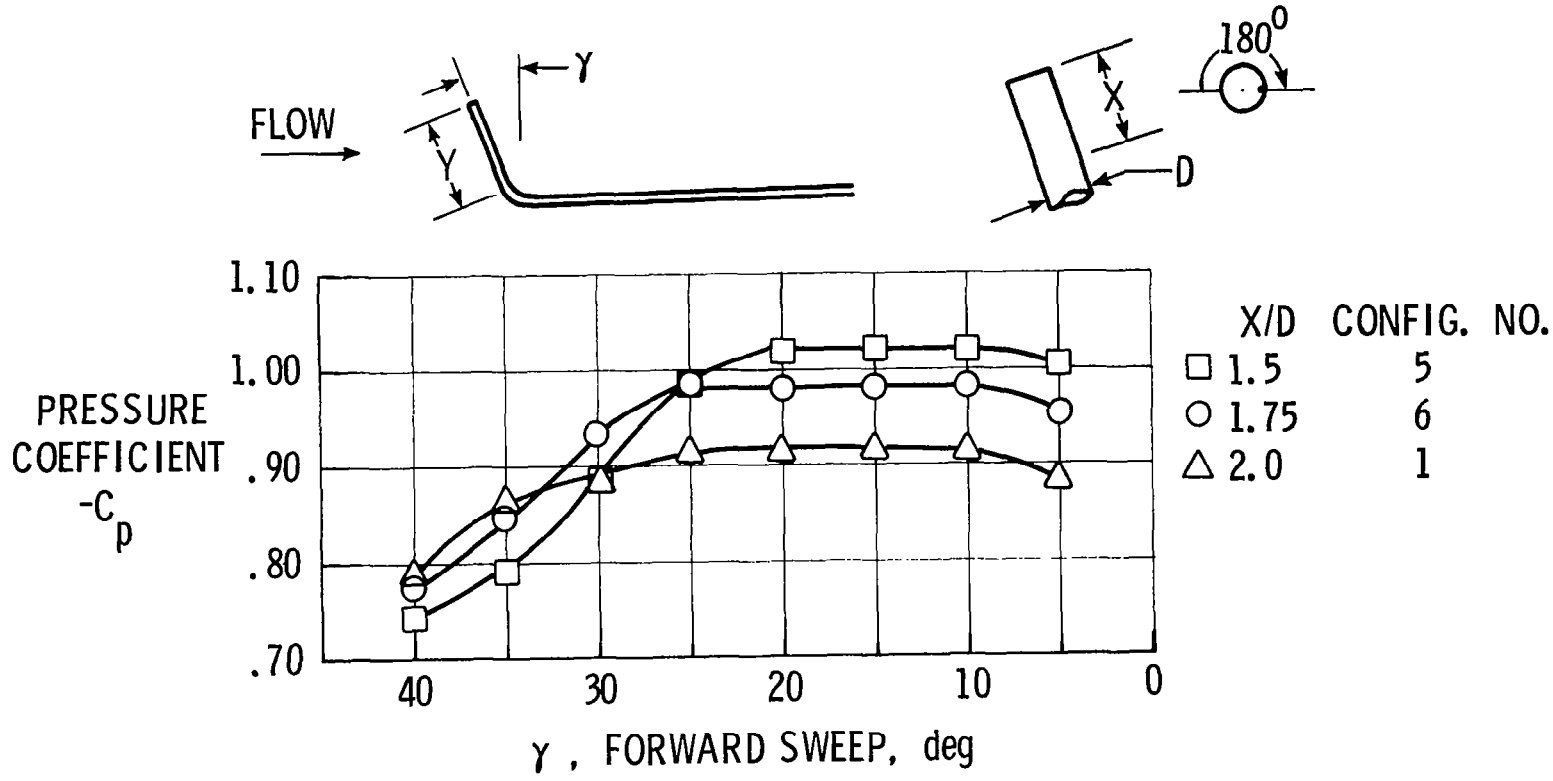

FIGURE 6

PRESSURE DISTRIBUTIONS AROUND A TWO-DIMENSIONAL CYLINDER AT VARIOUS SWEEP ANGLES

(REF. 8)

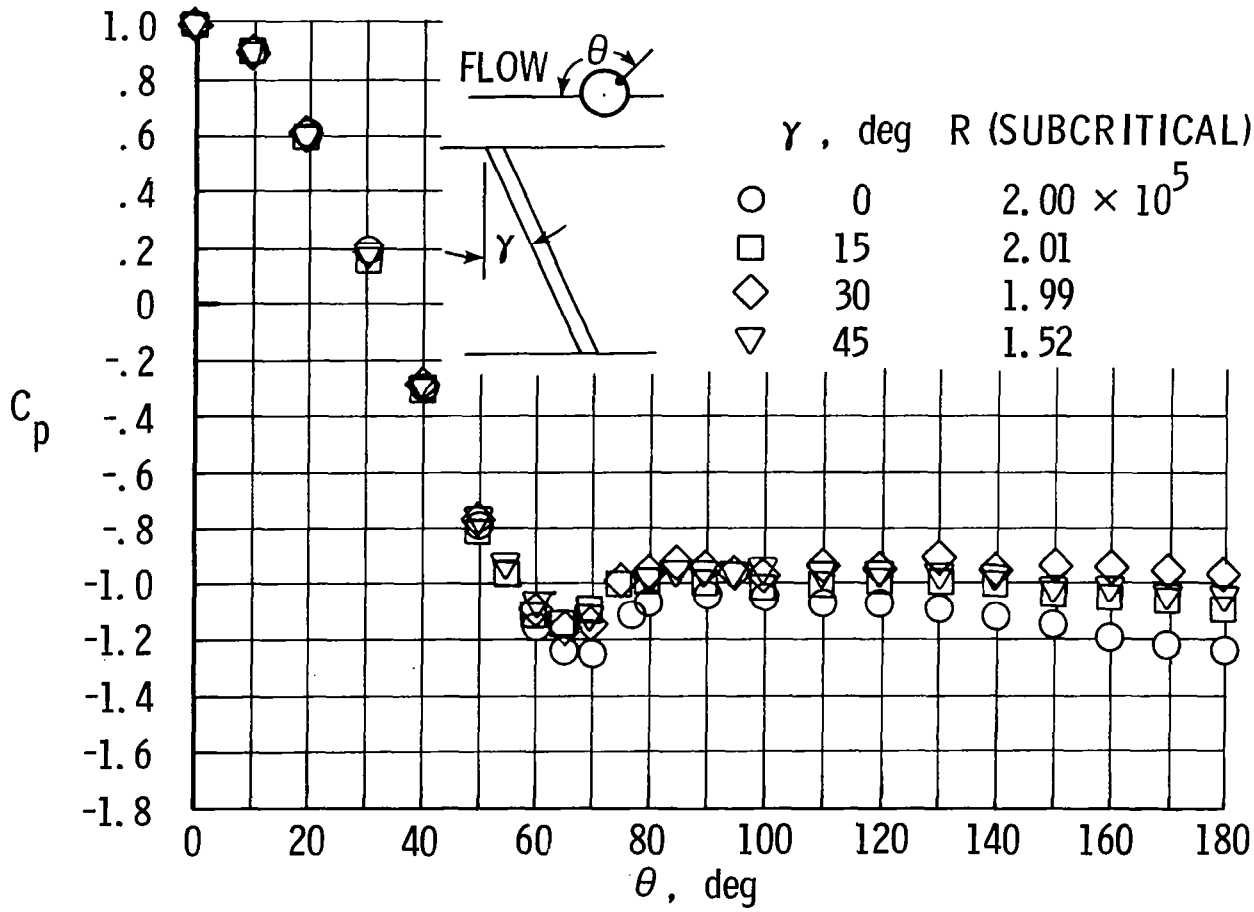

FIGURE 7

POSITION EFFECT OF ONE HOLE LOCATED AT θ = 135°; Y/D = 7 BENT-UP PROBE

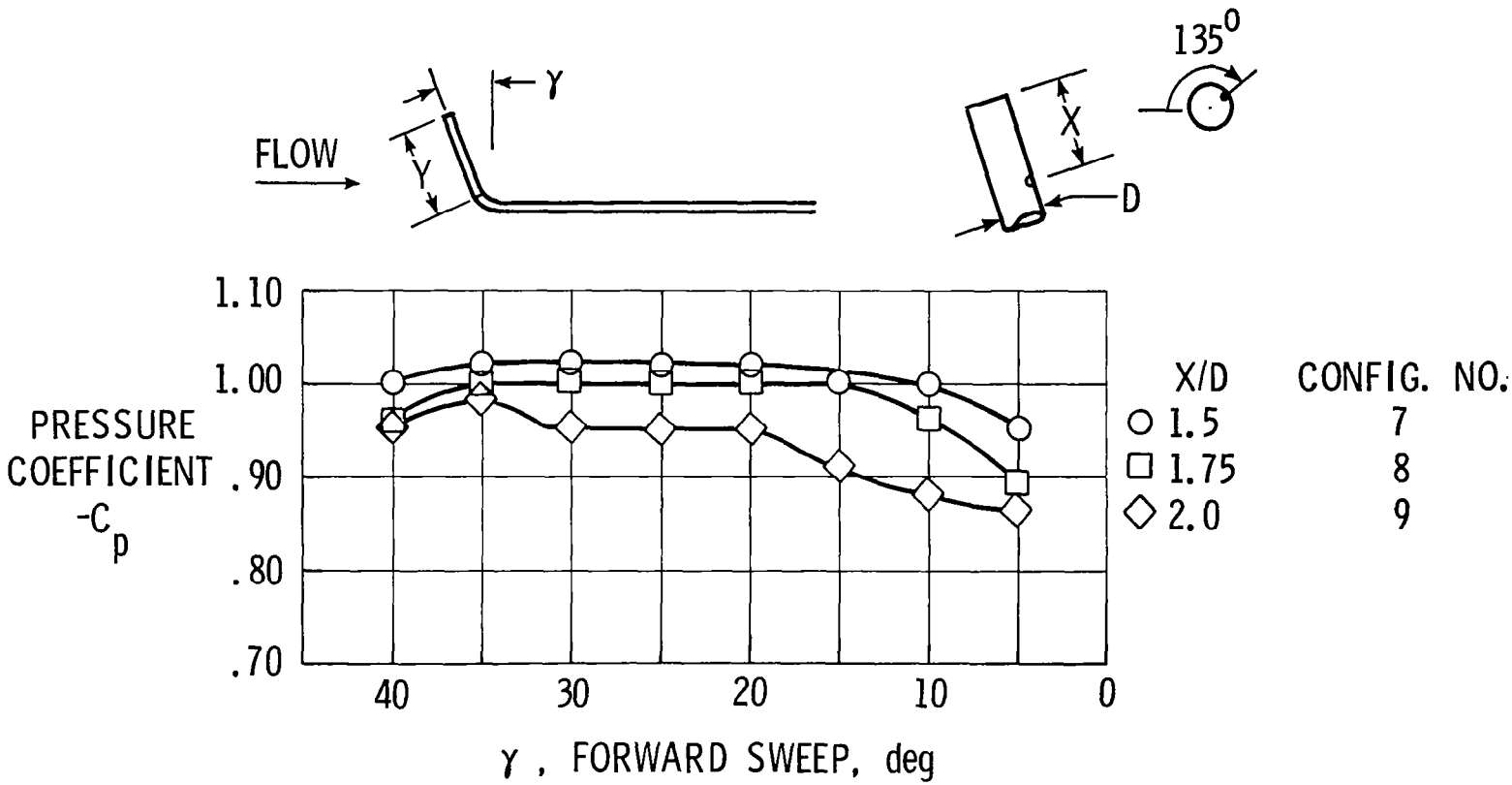

FIGURE 8

POSITION EFFECT OF ONE HOLE LOCATED AT θ = 135°, Y/D = 11

BENT-UP PROBE

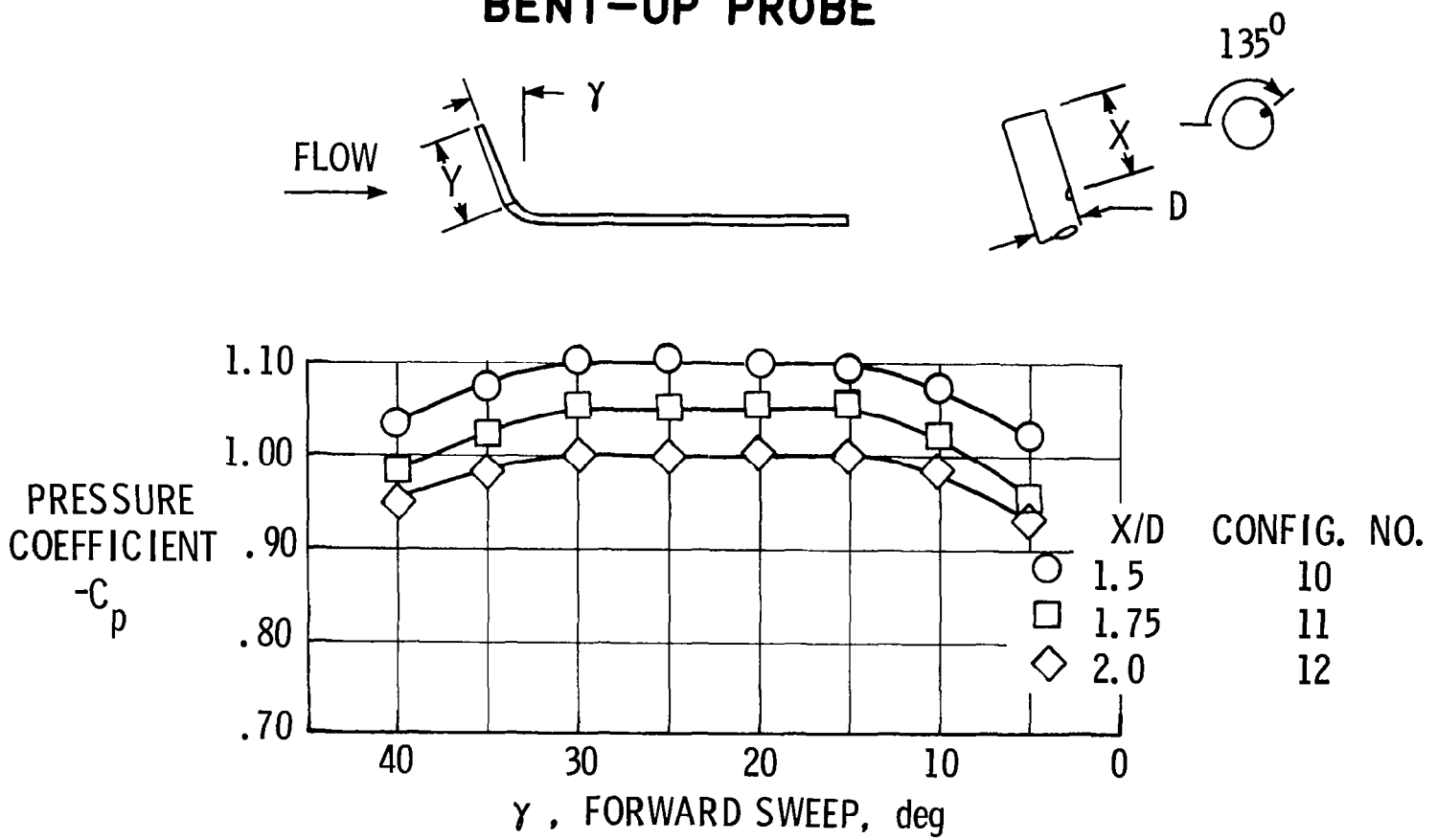

FIGURE 9

COMPARISON OF ONE HOLE VERSUS TWO HOLES, $\theta = 135°$ Y/D = 7, X/D = 1.5

BENT-UP PROBE

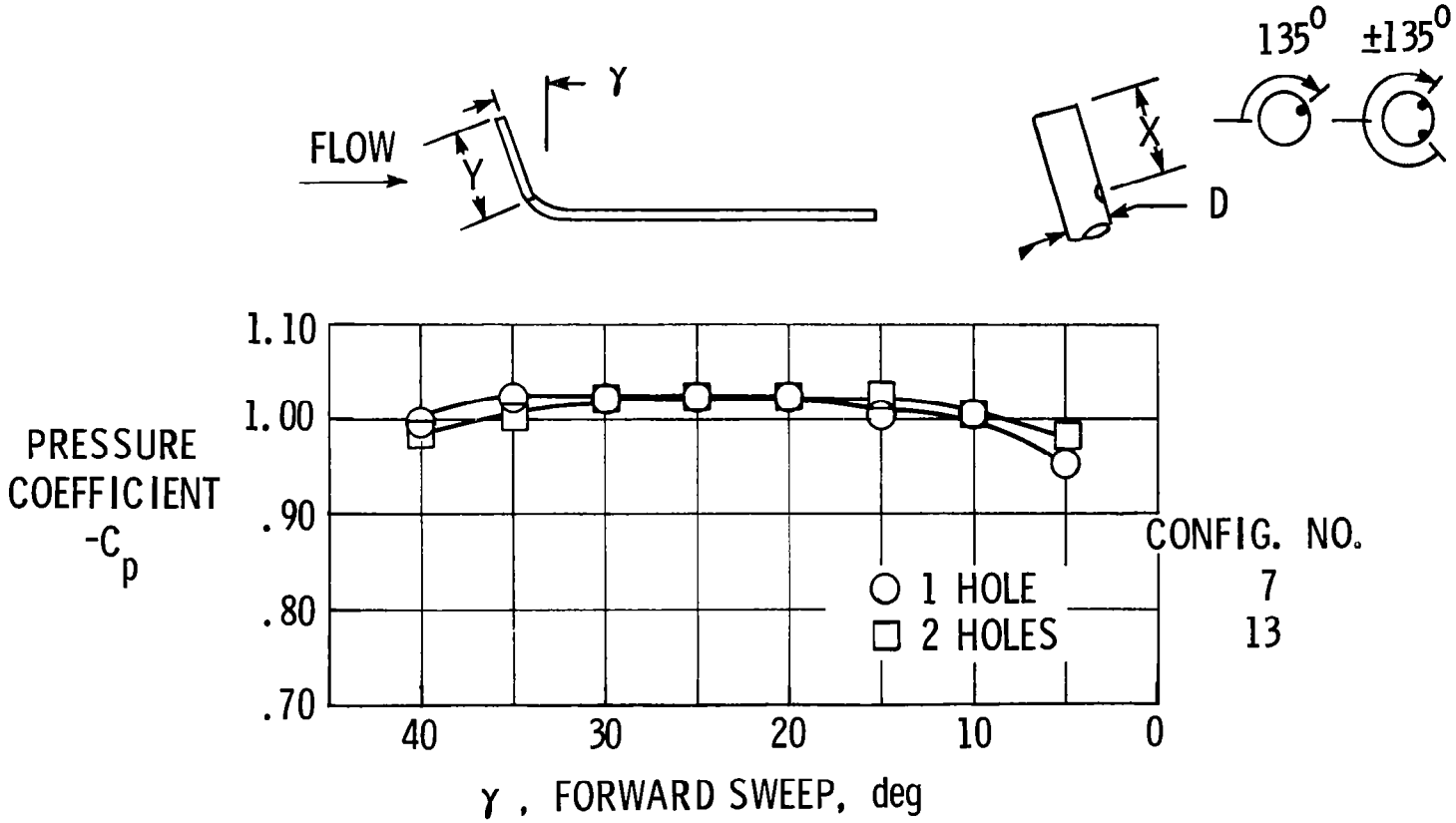

FIGURE 10

COMPARISON OF CONFIGURATIONS

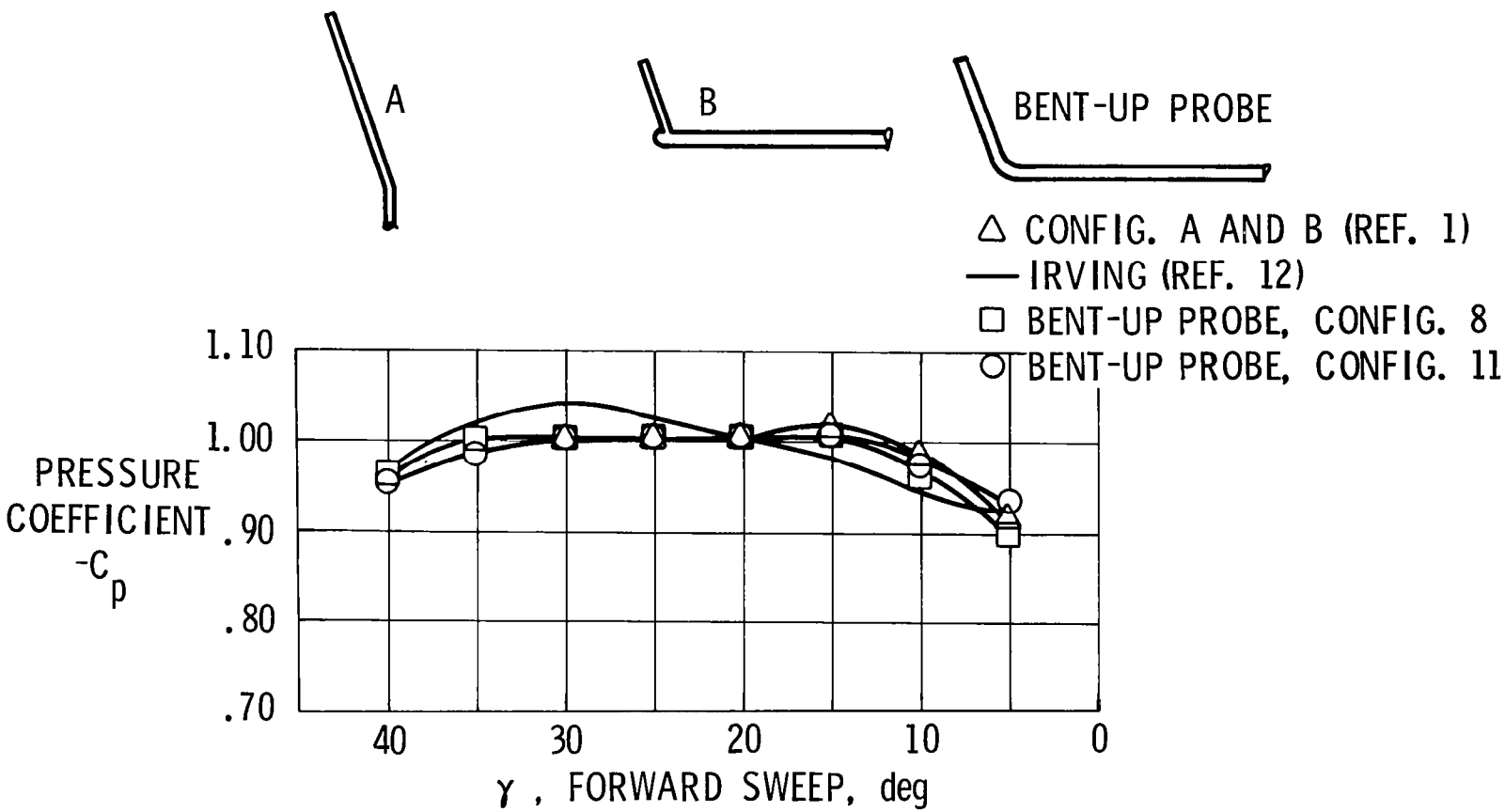

FIGURE 11

RESTRICTOR–CAPACITOR RELATIONSHIPS FOR TWO TIME CONSTANTS

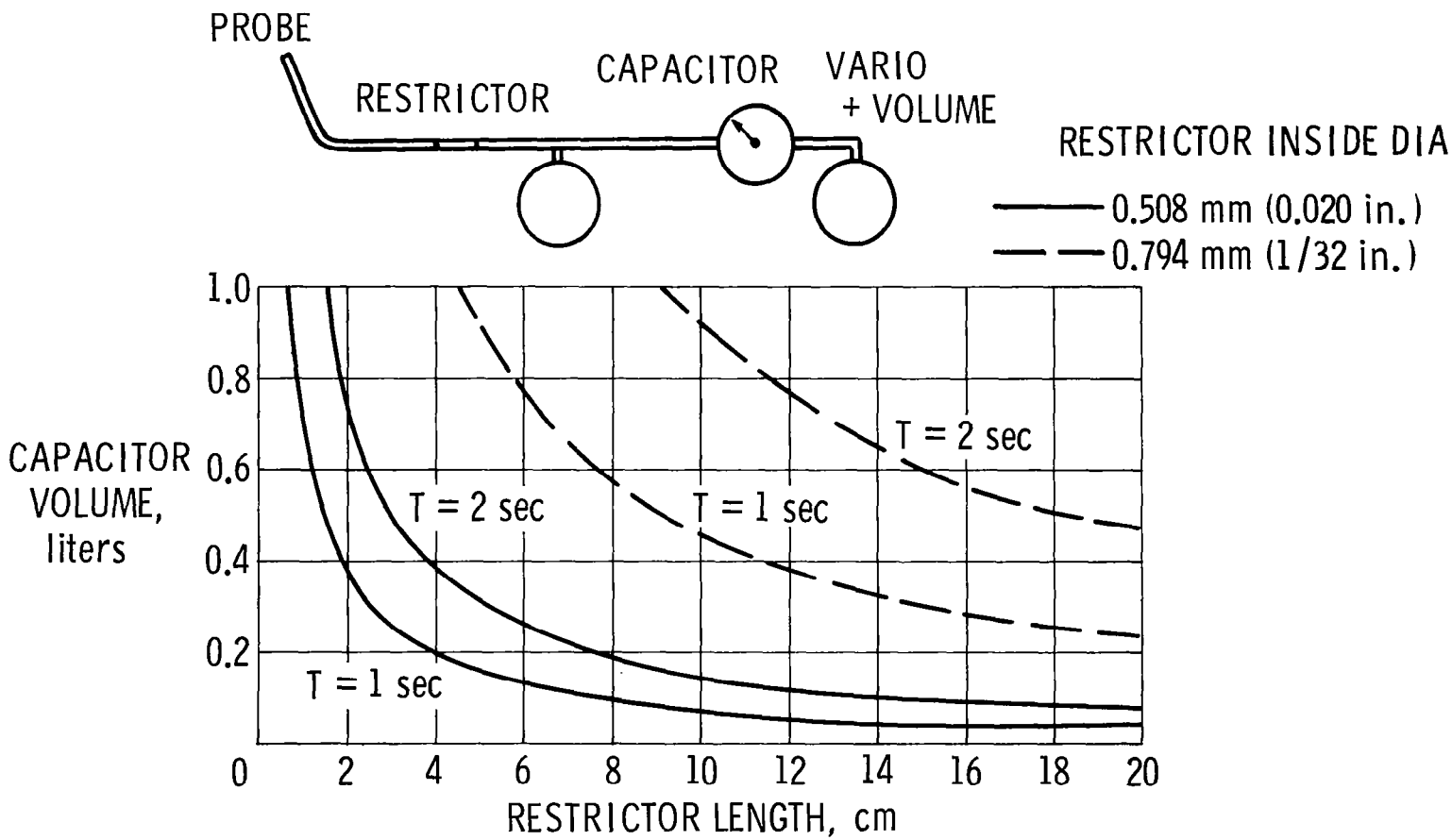

FIGURE 12

HOW ACCURATE IS NETTO?

Stephen du Pont
Soaring Society of America

SUMMARY

The historical origin and general history of the MacCready vertical current total energy variometer (now termed "netto"), including its optimum airspeed selector ring are reviewed, and some later developments of it are discussed. Polars of three sailplanes of different spans are charted for straight and circling flight, then plotted to reveal their parabolic anomaly and the effect of circling flight sink rate. These effects are further analyzed for their influence on the transient compensation of netto variometers as well as the speed ring. Some other disturbances due to the quality of sailplane preparation and flight dynamics are listed. Conclusions are drawn about the problems to pilots from imperfect netto variometer compensation and its effect on the maximization of ground speed from the speed ring. A modification for improvements to the speed ring and computer is suggested.

DISCUSSION

Ideally a variometer would be "compensated" to eliminate needle deflection resulting from speed changes so as to show only the vertical motion due to vertical air currents surrounding the glider. But the sailplane is an isolated energy system in which changing speed requires an exchange of its

potential energy for kinetic energy, causing changes of altitude. Its drag forces also increase generally with airspeed squared, producing a parabolic variation of sink rate with airspeed (ref. 1).

The pure total energy variometers are compensated through the change of dynamic pressure with airspeed which is converted by either a venturi (ref. 2), Braunschweig tube, etc., or an elastic bellows (ref. 3) to cancel the unwanted "stick thermal" coming from the zoom and dive maneuvers necessary to change speed in a glider. But they do not produce a fixed variometer needle with airspeed variations because of the drag force variation. Thus they leave something to be desired.

In 1949, Paul MacCready Jr. had disclosed his invention of the "speed ring" in a paper (ref. 4) read at the IAS-SSA meeting at Elmira while its author was busy winning the National Soaring Championship there. In 1954 MacCready first disclosed at the IAS-SSA meeting in New York his new "vertical current" variometer (ref. 1) today known as "netto" which more effectively than anything else known even today improved the "compensation" of sailplane variometers. At the same time it greatly simplified the use of the speed ring. The theory of the device was to leak a small calibrated flow of air proportional to V^2 outwards through the variometer, causing it to add the sink rate for still air to the variometer indication. The result was to indicate the vertical air current rather than the climb or sink rate of the sailplane. MacCready pointed out that with this arrangement the speed ring now indicated directly the speed to fly, dispensing with "iteration", that is the need to chase the needle while bringing the sailplane speed to a number never quite stabilized on the ring by the variometer needle. Today it seems incomprehensible that the soaring world took twenty years to appreciate

the device which twenty five years later remains the best. It is perhaps natural that a meteorologist would be preoccupied with the measurements of vertical currents, but only one who was also a sailplane expert would have combined the need with the tool and come up with such an ultimate solution.

There are several ways of plumbing the laminar leak (refs. 1, 3, and 5) used for the vertical current compensator to various total energy systems so as to produce the specified flow proportional to V^2. MacCready had placed the leak between the pitot and the variometer capacity line since he had used a venturi type total energy compensator (ref. 2) which is connected outboard of the variometer static vent. This produces a pressure differential across the leak of twice the dynamic pressure, which we call 2q, where $q = 1/2\ \rho V^2$, ρ being density. Thus, $P_s + q - (q + P_s) = 2q$, where P_s is the static pressure of the altitude of the sailplane. Because q contains V^2 the pressure across the leak is proportional to V^2 and the flow through a laminar leak is proportional to the pressure across it.

In "Soaring" for 1975 (ref. 5) Don Ott's arrangement of the leak with a total energy venturi was described. He ran the netto leak from the capacity line to static pressure, and showed that cockpit pressure was close enough, so he left the leak simply open to the cockpit. Here the pressure across the leak is:

$$P_s - (-q + P_s) = q$$

still giving the specified V^2 pressure variation of MacCready.

Where a bellows or diaphragm total energy compensator (ref. 3) is used which is driven by the difference of pitot pressure and the capacity (Burton, PZL, Schuemann etc.), the leak parallels the bellows and the pressure

differential is:

$P_s + q - P_s = q$

and again we have MacCready's V^2 pressure variation.

With the arrangement shown by MacCready, the capillary must be twice as long as with the other systems mentioned here. Reference to the 1975 Soaring article (ref. 5) will yield the formula for calculating the capillary.

In 1954 the Ka-6 sailplane was three years in the future. But many modern sailplanes today incorporate camber changing flaps, broad drag bucket airfoils, and very rigid and smooth wing skins, and realize broad areas of laminar flow in the boundary layer. Still the shape of the polar is much as MacCready had described it: "approximately" and "fairly exactly" and "within a few inches per second" of parabolic, which means of course that the sink rate is nearly proportional to airspeed squared. It is nearly proportional, but not quite, as figures 4 to 6 herein show. Those are generally sharper curved at the low end than the parabola, that is the sink rate in that area is greater. The PIK does not show any droop at the fast end while 1-26 and the AS-W 17 do show it.

SCOPE AND LIMITS OF STUDY

We investigate here specifically a) those netto errors, transient and steady, that come from the parabolic anomalies of some typical real world polars, b) those netto errors that are due to the variations from these straight flight polars that occur in banked circling flight, and c) errors from the netto speed ring. We do not go into some other errors due to

1) Flight off design altitude of variometers.

2) Transient variations in L/D from maneuvers causing accelerations that change the wing loading and from L/D changes caused by uncoordinated skidding or slipping.

3) Changes in L/D from wing loading variations due to weight of crew, equipment, ballast, center-of-gravity effect, etc.

4) L/D variations from flap position, aileron rig, aileron flap couplers, etc.

5) L/D variations coming from air leaks, ventilators, loose fairings and gear doors, etc.

6) Pitot static position and airspeed calibration errors.

7) Total energy probe and vent position errors from wing pressure field and wake, probe yaw and angle of attack errors, and uncoordinated skidding and slipping probe errors.

8) Plumbing hose length and capacity resistance in fittings, and hose pinch, restrictors, filters, electric damping, etc. as they affect variometer indication.

9) Dirty wings and skins, skin stress wrinkles, assymetrical ballast, etc.

Such errors may or may not be transient, will be difficult to predict, detect, and measure, may be cumulative, and may have comparative values that are significant compared to the errors analyzed.

In the light of the foregoing a knowledgeable pilot has a right to wonder about the reliability of his netto for finding better air as well as for the maximization of ground speed from the speed ring or computer. He may ask

1) How important is the effect of the parabolic anomaly of polars versus the true parabolic characteristics of the V^2 driven leak?

2) If the variometer that is read in circling flight, and the speed ring set to it, is compensated according to a polar derived in straight flight (since this indicates too low a climb and sets the ring too low (slow), will this significantly affect the maximization of ground speed?

3) If the speed ring that is derived for circling climb (no progress being made along course while climbing) is set during straightaway climb along course, this sets the ring too low (slow) (refs. 6 and 7). Does this affect the maximization of ground speed?

4) What are the effects of a mismatched leak to accomodate parabolic anomaly (it would be too short, too much flow) or one for the wrong sailplane or incorrect polar? (Capillary somewhat too short or too long.)

5) Is netto well enough compensated both for climb circling or straightaway so that it can be relied upon during small speed changes?

To obtain answers to these questions we have considered polars of the 12-meter 1-26 sailplane, the 15-meter PIK-20 and the 20-meter AS-W 17 (ref. 7). The polars have then been reworked by recalculating the slow ends for 40 and 50 degrees of banked turning (30 degrees has an insignificant effect) by the method of the Appendix (taken from ref. 8). (See figs. 1 to 3.)

The results, including the noncircling polar, have been replotted with the sink rate against airspeed squared. When any parabola is so plotted, it is a straight line passing through the origin. This makes it easy to inspect the parabolic anomalies of the curves. True parabolic characteristics of netto leaks can be compared to polars. If the polar were parabolic and the leak matched it they would plot the same, as one straight line. If the leak

is enlarged to compensate for some droop from the parabolism of the polar, the leak plot will be lower, cutting across the tighter curve of the polar (figs. 4 to 6). The leak sink rate in the midspeeds will then be lower and higher at the end portions. The difference, or the extent of the anomaly, can thus be directly measured on the plot along the sink direction under the square of the airspeed of interest, from any straight line that passes through the origin.

The effects on netto speed rings of the parabolic anomalies and of circling sink rates, as well as climbing along course with a ring designed for circling climb, have been computed for climb rates of 200 and 800 ft/min. The classic graphic analysis is used before and after modifying the polar values to reflect the above mentioned deviations. The work was done directly on the preplotted polar analysis sheets from reference 7 and is not reproduced here. Instead, the results are shown in table 1. There they can be seen to have an insignificant effect on the maximization of ground speed by the speed ring.

TRANSIENT ERRORS OF NETTO COMPENSATORS

Even small parabolic anomalies of the polars cause annoying transient netto compensation errors whose trends and speed ranges can be seen in figures 4 to 6, and are discussed below and further detailed in table 2.

The time lags of variometers (they vary widely between models and installations) (ref. 9) will modify these transient errors. In the slow portion of the polars (see figs. 4 to 6), slowing down causes an erroneous indication of worsening air (decreasing rise, increasing sink). Variometer time lag tends

to reduce this error. The effect begins as slight at about 55 knots and becomes larger with decreasing speed. This is an important regime of soaring flight where after the pilot has had a signal of better air he may be slowing down in an effort to locate the lift and use it, and possibly to circle and center it. If circling has begun during the slowing, the compensation errors are increased. Here the pilot should stay alert to his sense of vertical acceleration, heed the roll motion of his wing tips, and pay less attention to the netto variometer. As the charts show, the effects become significant with the 1-26 below 50 knots, the PIK -20 below 55 knots, and the AS-W 17 below 55 knots.

In the slow zones of the polars, speeding up will indicate erroneously better air than actual and the errors are increased by variometer time lag. But in this flight regime, the netto and its compensation become less important in the search for lift, because a pilot will probably be accellerating into his speed ring glide towards the next gaggle or cloud.

At the fast zones of the polar, slowing down will erroneously indicate improving air and variometer time lag will worsen the error. This is an important regime of soaring. The effect lessens as the speeds are lowered, vanishing with the 1-26 above 75 knots and with the AS-W 17 at above 85 knots. The PIK-20 is not affected.

In the fast portion of the polars, speeding up shows better air than actual and variometer lag will decrease the error. Searching for lift is less important in this regime, making the error less disruptive. The error increases with speed above the speeds noted in the previous example. Table 2 shows some values for smaller speed changes and steepened banks.

Pilots may check the calibration of their netto by flying in still air at three or preferably five speeds in the slow, medium, and fast portions of the polar. At the steady speed in still air the netto should indicate zero. The non netto total energy variometer should indicate the sink rate for each speed tested taken from reliable polars such as those derived by Bikle and Johnson in various issues of Soaring and those found in reference 7. Individual airspeed calibration errors may be troublesome here. It is convenient to tabulate the speeds and sink rates of interest for use in the cockpit. Indicated airspeeds are used.

Errors of transient compensation of netto can be noted in the slow and faster ends of polars by slowing down and speeding up while noting the behavior of the needle as it deviates from zero. Again the air must be still for this. What the pilot observes here in still air, he can apply to his actual soaring.

ERRORS OF THE NETTO SPEED RING

Calculations of speed rings and related computers (as well as of netto leak size) have usually been based upon the straight flight polars (refs. 1, 4, 9, and 10), but the ring is often set during banked circling climb where the actual vertical sink rate is greater than the netto variometer is indicating. This causes the ring or computer to be set too low (slow). Rings based on the pure MacCready mode (fig. 7) consider that no progress is being made along course while in circling climb (ref. 4). The so called street speed ring (refs. 6 and 7) of figure 8 acknowledges that some course distance is used up during straightaway climb, thus shortening the distance to go to

the next lift and so allowing a steeper glide at faster speed. The pure MacCready mode ring would be set too low (slow) while in climb along course. A street speed ring would seem better when set for both circling and along-course climb netto.

CONCLUSIONS

1) A Pilot who flys glued to his variometer may well be confused by the compensation errors of netto in slow straightaway climb and in steeply banked climb if his speed is not steady.

2) In slow speed climbing by netto, holding speed steady or use of a standby non netto total energy variometer may be helpful.

3) While shortening (increasing the flow of) the netto leak may give better steady speed matching to the anomalies of the polar, this will not help transient compensation errors.

4) The time lag of variometers has an effect on the transient compensation of netto. Where this is favorable speeding up, it will be unfavorable slowing down, and vice versa.

5) The netto errors studied have a negligible effect on the maximization of ground speed from the speed ring.

6) The match of the netto speed ring or computer might be very slightly better through use of the street ring construction.

7) The study hints that proponents of steady speeds instead of a miriad of little speed changes may have a point, due, if for no other reason, to the fact that even the best variometer system is plagued with compensation errors. A slow response variometer is favored by some to delude themselves to

thinking the variometer is compensated correctly, while fast repsonse is the goal of certain variometer makers who see better compensation giving more accurate information.

8) One total energy variometer with netto and a total energy variometer without netto might be the best solution for most of us, using the one that fits the soaring situation of the moment.

APPENDIX

Determination of sink rate due to circling flight for figures 4 to 6 is done by the method treated in "The New Soaring Pilot" by Welch and Irving. There it is assumed that the sailplane has the same L/D so long as the circling flight angle of attack is the same as in straight flight. The formulas are

$$V_{\phi} = V_o \frac{1}{\sqrt{\cos_{\phi}}} \tag{1}$$

and

$$S_{\phi} = S_o \frac{1}{\cos_{\phi} \sqrt{\cos_{\phi}}} \tag{2}$$

where the subscripts

ϕ and o are bank angles, V is airspeed and S is sink rate.

REFERENCES

1. MacCready, Paul B., Jr.: Measurements of Vertical Currents. Soaring, vol. 18, no. 3, May-June 1954, pp. 11, 14, 16, 17, and 25.
2. Dawydoff, Alexis: Total Energy Variometer. Soaring, vol. 7, nos. 1/2, pp. 7, 12.
3. Wolf, Mix: Total Energy Variometer Operated by Pitot Pressure. Soaring, vol. 25, no. 8, Aug. 1961, pp. 16-17.
4. MacCready, Paul B., Jr.: Optimum Airspeed Selector. Soaring, vol. 18, no. 2, Mar.-Apr. 1954, pp. 8-9.
5. Brandes, Tom: Competition Workshop. Soaring, vol. 39, no. 3, Mar. 1975, pp. 37-39.
6. Abzug, Malcolm J.: A Speed Ring for Cloud Street Flying. Technical Soaring, vol. IV, no. 1, [1975], pp. 9-14.
7. Du Pont, S.: New Soaring by the Number. Published by author, 1974, 1977.
8. Welch, Ann; Welch, Lorne; and Irving, Frank: The New Soaring Pilot. John Murray (London), 1960.
9. Schuemann, Wil: Advertisement - Second Annual Report to Soaring From Sage Instruments. Soaring, vol. 40, no. 6, June 1976, pp. 12-13.
10. Ball, Richard: Description of Netto Cruise Control Option. Ball Engineering Co., Boulder, Colorado, undated circa 1977.

TABLE 1

MAXIMIZATION OF GROUND SPEED AS AFFECTED BY PARABOLIC ANOMALY AND CIRCLING SINK RATES WITH NETTO SPEED RING AS COMPARED TO SOLUTION FROM CLASSIC MacCREADY GRAPH.

Glider types	(1) Actual glider climb, fpm	(2) Still air sink best sink speed, bank 40°	(3) Polar sink deviation from parabolic, fpm bank 40°	(4) Actual airmass rise, fpm (1)+(2)	(5) MacCready speed to fly, knots	(6) Netto indicated airmass rise at zero bank (1)+(2)+(3)	(7) Netto ring indicated speed to fly, knots	(8) MacCready ground speed, knots	(9) Netto ring ground speed knots
1-26		40° at 40 knots	40° at 40 knots						
	200	275	-80	475	53	555	55	22.5	22.5
	800	275	-80	1075	71	1440	73.5	43.5	44
PIK-20		40° at 51.5	40° at 51.5						
	200	195	-20	495	70	415	70	32	32
	800	195	-20	995	92	1015	87	59	59
AS-W 17		40° at 52	40° at 52						
	200	160	-50	360	64	410	75	38.5	36
	800	160	-50	960	105	1010	97	66	65

TABLE 2

SOME TRANSIENT COMPENSATION ERRORS OF NETTO VARIOMETER FOR THREE SAILPLANES, NOT CONSIDERING VARIOMETER LAG

	Slowing 5 knots, bank angle 50°	Slowing 5 knots, bank angle zero	Slowing 5 knots, bank angle zero
1-26			
ΔIAS	40 to 35	40 to 35	43 to 33
Δsink	- 15 fpm	- 30 fpm	- 50 fpm
at sink	- 350 fpm	- 180 fpm	- 210 fpm
PIK-20			
ΔIAS	60 to 55	40 to 35	55 to 45
Δsink	-30	-10	-20
at sink	-250	-130	-130
AS-W 17			
ΔIAS	60 to 55	50 to 45	55 to 45
Δsink	-25	-20	-20
at sink	-200	-120	-110

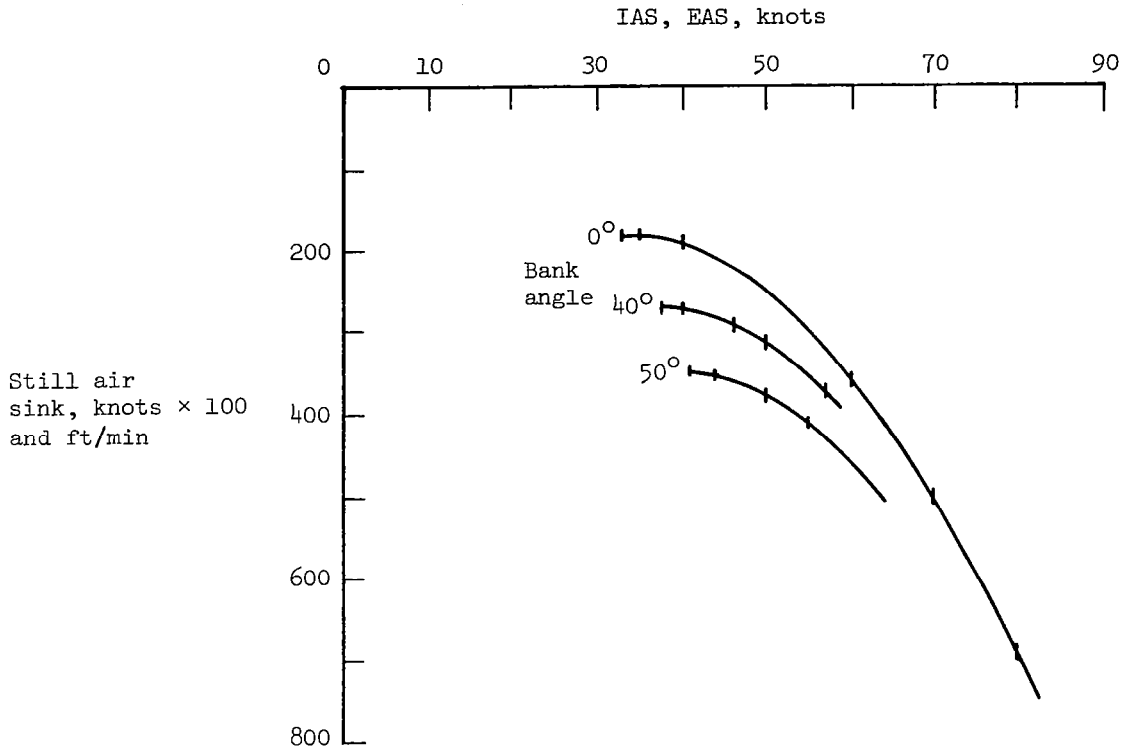

Figure 1. - Performance polars: I-26, 12 meter.

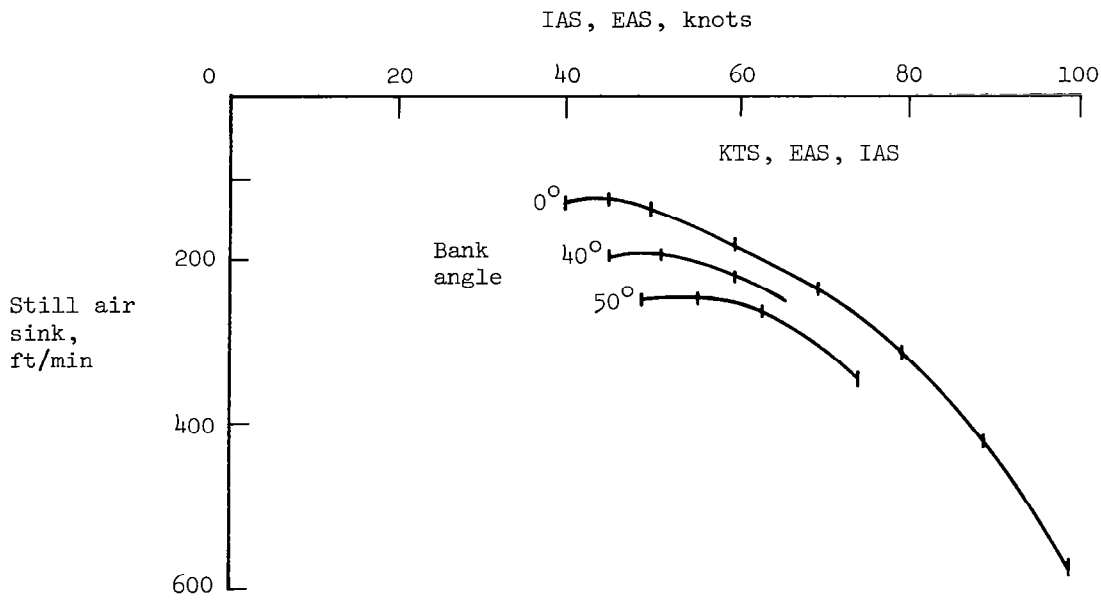

Figure 2. - Performance polars: PIK-20, 15 meter.

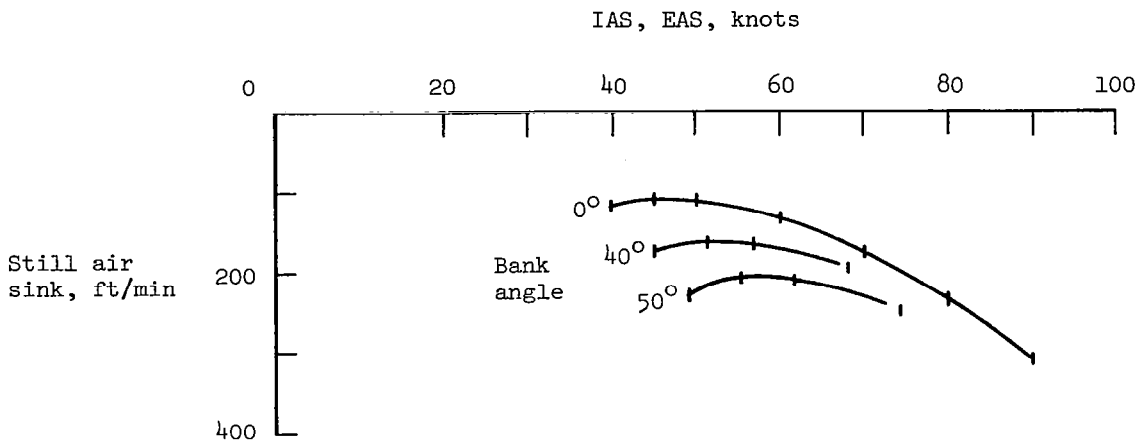

Figure 3. - Performance polars: AS-W 17, 20 meter.

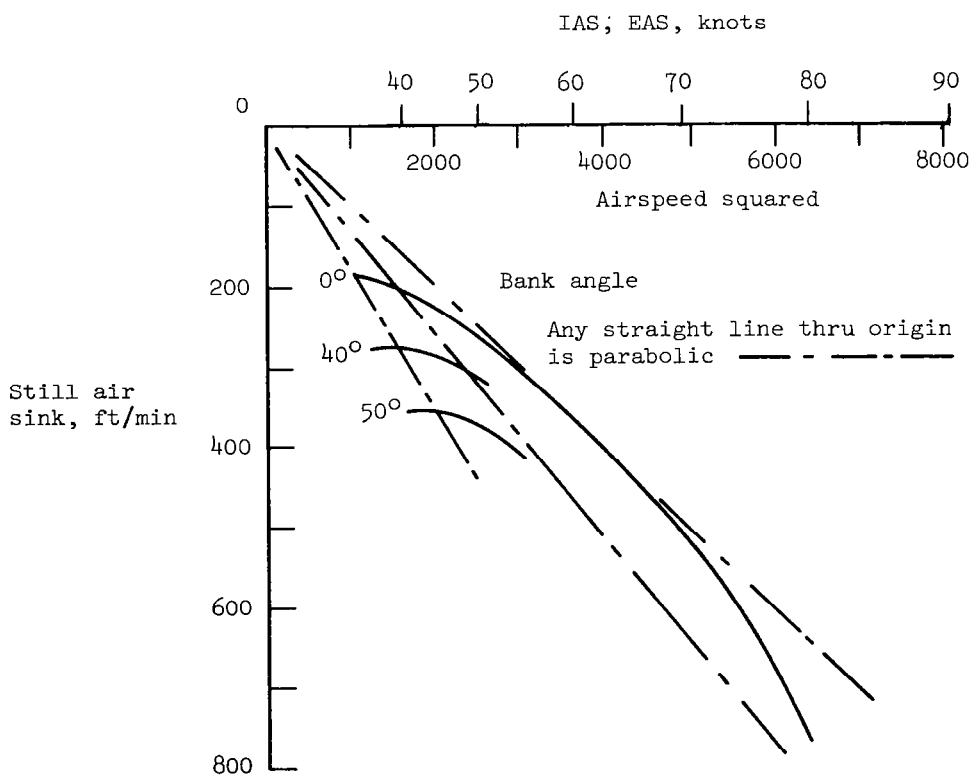

Figure 4. - Sink versus V^2 : I-26, 12 meter.

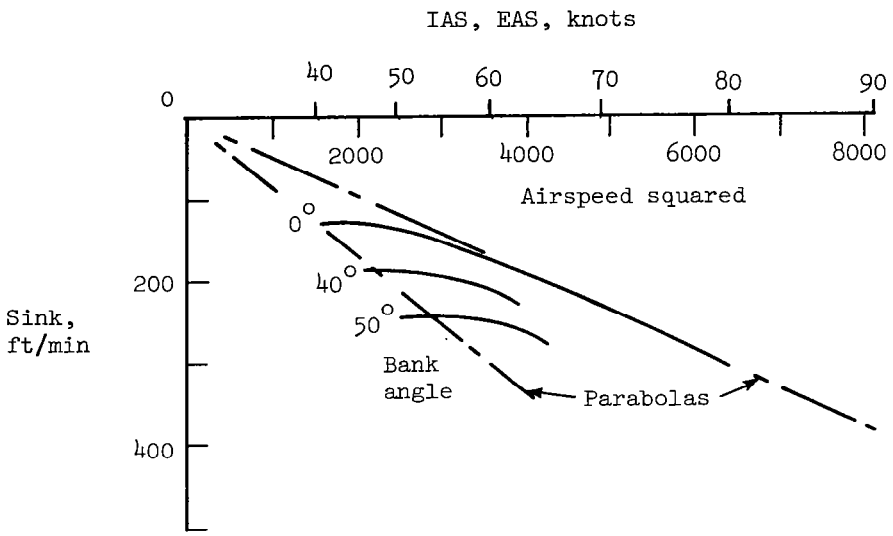

Figure 5. - Sink versus V^2 (see fig. 4): PIK-20, 15 meter.

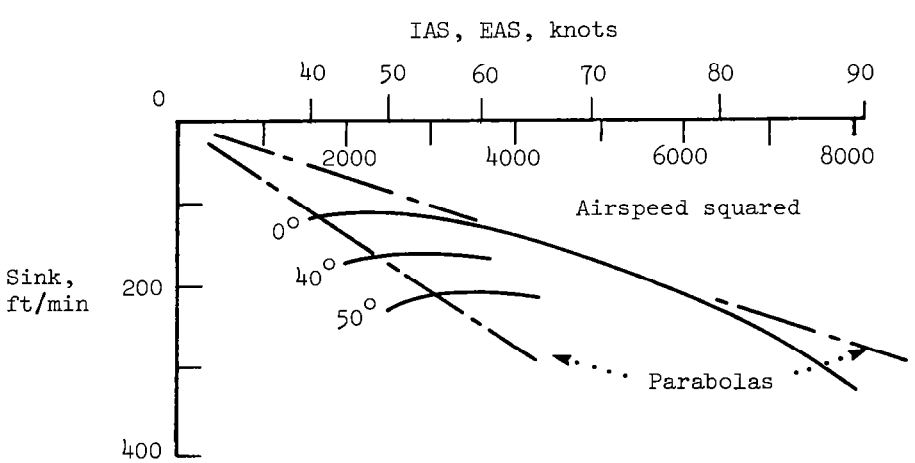

Figure 6. - Sink versus V^2 (see fig. 4): AS-W 17, 20 meter.

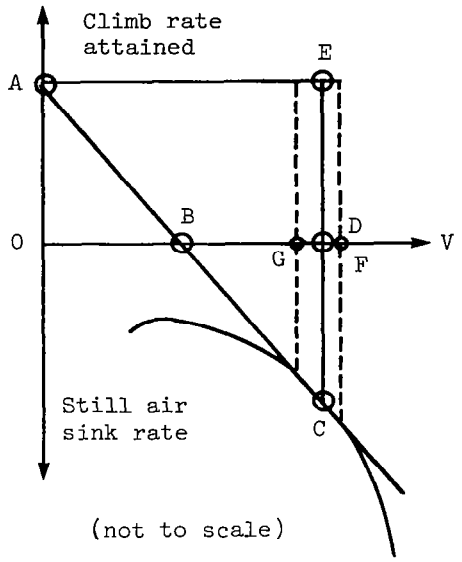

A Circling climb at zero speed along course.
B Average groundspeed, for one climb glide cycle, begin and end at same altitude.
C Tangent at polar.
D MacCready optimum airspeed between climb zones.
EC Ring layout arc, ft/min between index and speed to fly.
FG Tolerance of speed to fly for insignificant effect to average ground speed.

Figure 7. - Pure MacCready speed ring derivation, all climbs circling.

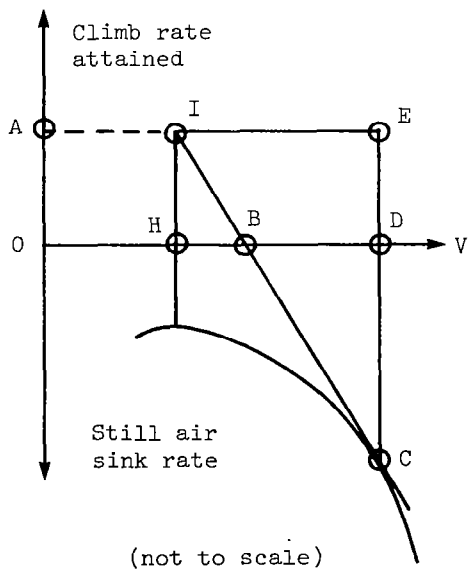

A Rate of climb along course at speed H
B Average ground speed for one climb glide cycle, begin and end at same altitude.
C Tangent at polar (see above FG)
D Ring optimum airspeed between climb zones.
EC Ring layout arc, ft/min between index and speed to fly.
H (I) flight speed during climb along course.
I Climb speed

Figure 8. - Street speed ring derivation, climbs are along course.

THE APPLICATION OF MICROPROCESSOR TECHNOLOGY TO IN-FLIGHT COMPUTATIONS

Patricia L. Sawyer and Dan M. Somers
Hampton, Virginia

INTRODUCTION

During the past decade, electronic microcomponent technology has developed to the point where microprocessors are appearing in an expanding number of diverse applications. Improved manufacturing techniques have allowed the computing power of the microprocessor to increase at the same time its physical size has decreased. The mass production of these tiny high-powered components has made them readily available for nominal costs to industry, research, government, and private individuals.

The application of this new technology proposed by the authors is a microprocessor-based system to essentially replace current panel instrumentation in sailplanes. A microprocessor-based system is particularly attractive for in-flight computations because of its accuracy and dependability, but more importantly because of its potential for flexibility of output. Given the two basic input values of dynamic and static pressures, the system could perform the functions of a conventional panel by providing the pilot with airspeed, altitude, and variometer readings, but could also be programmed to provide him with additional data at his request. Since all microprocessor-based systems contain an internal clock, time history data and moving averages could be computed. The microprocessor could easily handle computations involving integrations or requiring the manipulation of many data points or solutions of complex equations.

This paper will present a modular design of a general purpose microprocessor-based computer to perform in-flight computations for cross-country soaring pilots. The basic requirements for the system will be discussed. Several specialized applications of the computer will be presented, including real-time pilot feedback and flight-test data acquisition and reduction.

CURRENT INSTRUMENTATION

A brief examination of the instrumentation in current, competition sailplanes will reveal part of the motivation behind the microprocessor-based panel. An excellent overview of present-day instrumentation is contained in reference 1.

Today's airspeed indicators and altimeters, although simple and reliable, suffer from position errors caused by incorrect static-pressure sources. In

the case of the airspeed indicator, the relocation of static ports in the fuselage between the wing and the tail has eliminated the major portion of this error. The remaining correction can still be significant, however, especially when performing flight tests. The static-pressure source for the altimeter is usually cockpit pressure, for reasons which will be discussed later. In addition to this position error, altimeters have added problems caused by high relative friction forces within the instrument. This friction results in the sticking problems known to all sailplane pilots.

Present-day variometers are of two types — those which measure pressure differences and those which measure mass-flows. The pressure variometers have no altitude errors, whereas the mass-flow variometers exhibit a rather large altitude error, approximately 10%/3000 ft.

Of the four available pressure variometers, two are mechanical and two are electrical. The first, and presently most common, mechanical type is the classic vane variometer such as the PZL or Winter. This type is quite reliable, but has several disadvantages which include relatively slow response due to friction, close-tolerance construction, delicate mechanisms, and susceptibility to dirt. The second mechanical type, the taut-band variometer produced by Schuemann or Bohli, has a fast response. It also has some inherent problems, however, associated with tuning the required capillary and producing the delicate metal-band assembly.

The two electric types have the common virtues of fast response and audio capability. They also share the disadvantages of possible unreliability because of the required power source and wiring, and a response which is "too fast" and thus requires damping. The most common of this type, the capillary-leak variometer made by Ball, has further difficulties arising from the capillary which must be tuned and the close tolerances on the linear variable differential transformer (LVDT). The second type is the altitude derivative variometer (ref. 2). This variometer is expensive to produce because it requires a pressure transducer.

Mass-flow variometers, such as those made by Cambridge or Moore, incorporate thermistors which require some degree of matching.

All of the variometers mentioned above require total-energy and/or netto compensation. Total-energy compensation is usually provided by either an Althaus-type venturi or a diaphragm. The venturi, as well as similar devices such as Braunschwieg, Nicks, and Irving tubes, provides accurate compensation independent of altitude. They are, however, relatively sensitive to horizontal gusts, require careful positioning on the sailplane, and add drag. They also do not work well, if at all, in rain. A diaphragm compensator, such as the PZL, Winter, or Burton, does not increase the drag of the sailplane. It does, on the other hand, compensate exactly at only one altitude. Although less sensitive to gusts than a venturi, it is difficult, if not impossible, to correctly adjust. Recently, electronic compensation has been introduced, which incorporates thermistors like those in the electric mass-flow variometer. These thermistors require some matching.

In addition to total-energy compensation, netto compensation is also desirable. This compensation requires a capillary which can be tuned to approximate, but not necessarily exactly "fit," the given sailplane's polar. With this system, it is difficult to account for weight changes such as the addition of water ballast.

Regardless of type, all current instrumentation suffers from several problems. None of today's instruments are truly temperature-compensated. Because the entire system is pneumatic, the various pressure sources and instruments must be connected by tubing. This tubing adds volume to the system and introduces the possibility of leaks. Refinements to the variometer subsystem require additional restrictors and/or gust filters. While solving some problems, these devices have problems of their own, such as time-constant matching (ref. 3). Also, the interaction between the various instruments can cause difficult problems. These problems arise from the interaction of several diaphragms (airspeed, total-energy, and altimeter) through the variometer on the common static-pressure line. Disconnecting the altimeter from the static-pressure line alleviates part of this problem.

In summary, the instruments currently available are certainly adequate for safety, but are somewhat inadequate for efficient cross-country flight for the following reasons:

(1) The information they provide is not accurate for all altitudes, attitudes, and environments.

(2) To correct some of the errors inherent in the instrumentation, the devices for measurement and display have become inordinately delicate and complicated.

(3) The current equipment offers no facility for flexibility or expansion of the type of information provided.

EARLY ATTEMPTS AT IN-FLIGHT COMPUTERS

During the past few years, several attempts have been made to expand the amount and vary the type of information provided to the pilot by his instruments. In 1972, A. Raouf Ismail, of Cambridge Instruments, suggested that an analog air-data-computer (ADC) could provide the pilot with average rate-of-climb and speed-to-fly information during flight, but cautioned that this approach could be bulky, power consuming, complicated, and expensive (ref. 4). That same year, John Firth, of Ottawa, Canada, reported on his work, begun in 1969, involving the coupling of an electric variometer to a simple analog computer (ref. 5). The system performed normal variometer functions with fully electronic total-energy compensation. In addition, the system computed an average rate-of-climb over variable time periods and displayed the correct speed-to-fly using a nose-up/nose-down pitch indicator. Variable damping and sensitivity, variable time constants, and a dry/wet switch allowed

more variables to be adjusted during the computations, and hence provided the input necessary for a more accurate output.

During an average cross-country flight, the analog system was found to be quite reliable, and its flexibility enhanced the usefulness of the information provided. During the World Championships in Yugoslavia in 1972, however, the instrument was used very little because the soaring conditions did not match those for which the instrument was developed, the battery power on board had to be conserved for the radio and gyros, and the pilot's constant attention was required for navigation.

The analog air-data-computer was a definite improvement over standard instrumentation, but was still greatly limited in its flexibility, and, therefore, in its accuracy. In 1974, William Foley presented results of a study involving the use of mini-calculators in soaring flight (ref. 6). Foley's use of a programmable digital calculator partially solved the problem of inadequate flexibility encountered earlier, but introduced other problems which seemed insurmountable given the current technology.

The calculator was not connected to the instruments; thus, all data necessary for program execution had to be entered manually by the pilot. This visual-manual interface was not only slow, but held potential for error. The calculator itself was an obstacle in the cockpit. In order to enter data, a cumbersome kneeboard was required, and to read the LED output, the calculator had to be carefully shaded from sunlight. Depletion of battery power was a concern, and limited memory within the calculator demanded that the pilot load programs from magnetic cards during flight.

Because of these inconveniences, Foley described his mini-calculator as interesting, but impractical. He recognized that the first requirement of any instrument system must be that it provide better or more timely information than the pilot can obtain using his own resources.

REQUIREMENTS FOR AN IN-FLIGHT COMPUTER

The following requirements can be used to define an in-flight computer with sufficient capability to insure that this important condition of faster and better information is met.

Output Capability

1. The in-flight computer must display its output during flight in a format easily readable by the pilot. For example, if the pilot is accustomed to a needle-and-scale altitude instrument, then the in-flight computer must not force the pilot to read a digital display.

2. The system must provide, as a minimum, all information currently provided by standard panel instrumentation. For example, altimeter, airspeed

indicator, and variometer functions must be performed with all types of compensation, filtering, and signal conditioning.

3. The system must provide audio capability.

4. The system must be capable of digital, alphanumeric, and graphic display via an easily readable, glare-free output device.

5. The system must be compatible with other input/output devices, such as flexible disks or printers, for pre-flight system development or post-flight data reduction.

Computational Capability

1. The in-flight computer must be driven by a system clock of sufficient speed to provide real-time information to the pilot. Real-time, in this context, means that the pilot must detect no hesitancy or flicker in the output displays.

2. The system must be more accurate in its computations than standard current panel instrumentation.

3. The system must provide hardware and software signal conditioning capability.

4. The system must be reliable and must provide a self-test capability to verify its integrity during pre-flight checkout.

5. The system must include adequate memory so that time history data may be gathered and stored for post-flight analysis.

6. The system must be built around a microprocessor of sufficient sophistication so that the flexibility that programming allows is not overshadowed by the complexity of the actual programming process. For example, the system must support high-level languages and feature an operating system that is human-oriented.

7. The system must accept standard programmable read-only memory (PROM) so that standard software can be transported and incorporated easily.

Input Capability

1. The in-flight computer must contain an interface to a standard alphanumeric terminal to be used for program development.

2. The system must allow the pilot to initialize certain predetermined parameters during pre-flight checkout and also during the flight. For example, the pilot must be able to zero his altitude gage before takeoff if he desires.

3. The system must feature an interrupt system that will allow the pilot to stop the processing of one program and begin the execution of another in flight with a minimum of effort.

4. Through the use of default parameters, the system must require a minimum of data entry during flight.

System Configuration

1. The processing and memory modules of the system must be portable and easily removed from the sailplane for post-flight analysis or program development.

2. The entire system must be small and lightweight, and must not be an obstacle in the cockpit.

3. The system must require a minimum of power, and this power supply should be separate from that required by the radio.

4. The system must be inexpensive.

A MICROPROCESSOR-BASED IN-FLIGHT COMPUTER

The proposed microprocessor-based in-flight computer system consists of three main subsystems for pressure sensing, computations, and input/output of information. A functional block diagram showing the major tasks of each subsystem is presented in figure 1.

Pressure Sensing Subsystem

The major components of the pressure sensing subsystem are two pressure transducers -- one to measure dynamic pressure and the other to measure static pressure. Transducers with adequate accuracy and reliability are very small and can easily be located at the point of measurement, thus eliminating the need for tubing and its related problems. The analog signals representing dynamic and static pressures must be conditioned either by circuitry within the pressure transducer, or by the hardware or software of the computations subsystem. A photograph of a typical pressure transducer with adequate sensitivity for sailplane applications is shown in figure 2.

Using the values of static and dynamic pressures, altitude and airspeed can easily be computed. Uncompensated and compensated rates-of-climb are merely functions of these pressures with respect to time. Because the system contains a memory and has access to stored and real-time information, the values it computes can be corrected for changing parameters, such as altitude or location on the polar curve. This flexibility will result in an output

that is far more accurate than that available from current instrumentation.

Computations Subsystem

The computations subsystem contains several important components which enable it to handle all of the processing functions of the system. The components are of two main types -- hardware, the actual circuitry that defines the capabilities of the system; and software, the programs that define how the hardware will be exercised to meet the needs of the application. The "brain" of the system is the microprocessor, the selection of which must be guided by several requirements. The microprocessor must operate at a speed sufficient to provide real-time information to the pilot, yet, at the same time, require a minimum of power. It must possess a rapid interrupt-handling feature to enable the pilot to redirect computations instantaneously. The processor word size should be of sufficient length to allow for adequate accuracy during the computations and the addressing of a sizeable memory block. Finally, the processor should be a standard, easily obtainable part that is well-supported by development and checkout software, such as high-level languages and debug packages.

A microprocessor, such as the one shown with two memory units in figure 3, would satisfy these requirements. A typical 16-bit microprocessor will allow the direct addressing of over 65,000 words of memory and the indirect addressing of many more words. The instruction set is adequate for this application and contains special instructions that allow the rapid processing of interrupts. Several 16-bit microprocessors already boast large user communities, are readily available, and are relatively inexpensive. At this writing, a typical unit price is under $25.00.

The microprocessor cannot function as a computer without supporting components. The memory requirements of the system will depend on the type and number of programs to be executed. The amount of memory can be expanded at any time up to a point depending upon the addressing scheme of the processor and the space allotted for memory on the processor board. Memory in the system will be of two types -- programmable read-only memory (PROM) containing the library of predefined programs, and random access memory (RAM) which may contain instructions or data. The cost of memory represents a large portion of the cost of the computations subsystem, and the memory will also occupy a large portion of the processor board. The cost of memory is rapidly decreasing, however, even though the capacity of each memory unit is increasing. At this writing, 1000 words of memory, packaged as one unit, cost about $10.00.

The processor board will also contain analog-to-digital hardware and some signal conditioning circuitry, depending upon how much conditioning is performed by the pressure transducers themselves, or in the software of the system.

The board may also contain special purpose hardware to perform repeatedly required functions more quickly than software can perform them.

For example, if the applications program involves the manipulation of values of very large or small magnitudes, then these values must be stored in memory as floating point numbers represented by an exponent and a mantissa. Most microprocessors available today perform computations involving floating point numbers much more slowly than those involving fixed point numbers. For this reason, hardware has been developed to perform these floating point computations very rapidly outside the microprocessor. The computations subsystem may operate more efficiently if specialized hardware to meet specific needs is included.

The system will contain a synchronizing master clock and whatever circuitry is required to drive output gages, display screens, or audio devices, and to allow input from switches or keyboards. The entire system will be driven by battery power, which must be regulated by special circuitry on the board. Figure 4 shows a processor board built for another application which illustrates the arrangement of a 16-bit processor, memory, clock, special purpose floating point hardware, and input/output circuitry on a single board.

All processing will be incorporated into a modular computations subsystem, possibly consisting of several boards that may be mounted near the panel area of the cockpit or elsewhere in the sailplane. Because the communication between each of the three subsystems is electrical, not mechanical, the location of the computations subsystem is arbitrary.

Input/Output Subsystem

System input and output will be of two types -- real-time and pre- or post-flight. The format of real-time output must meet the pilot's first requirement that information be timely and easily understood. Since standard needle-and-scale gages inform the pilot of absolute values, as well as the rate of change in these values, then this type of output display should continue to be used at least for airspeed and rate-of-climb information. Additional output desired by the pilot, such as speed-to-fly or altitude, may be displayed using a digital output device or a screen display. The choice of a proper screen display is important. A standard raster scan device, such as a small television screen, while easy to interface to the system, is heavy, cumbersome, requires a great deal of power, and does not provide adequate contrast in the cockpit environment. A liquid crystal display, however, uses ambient light to increase contrast and, therefore, is well-suited to cockpit applications. The digital display shown in figure 5(a) and the top view shown in figure 5(b) illustrate the small size of the liquid crystal display. These devices are also capable of graphic output, as shown in figure 6. A typical panel configuration, including an LCD display, is shown in figure 7.

Input to the system during flight must be minimal and uncomplicated. Select switches and a small numeric/command keyboard must be located in the cockpit where they may be accessed easily, but will not inhibit flying.

Pre- and post-flight input and output can be more complicated and time-consuming than real-time, but should be streamlined by a carefully designed human-oriented system. A functional grouping of the input and output devices would spare the pilot the task of selecting one of an array of identical pushbuttons while flying.

The entire computations subsystem is modular and portable so that it can be removed from the cockpit and connected to an alphanumeric terminal for system development. Therefore, the interface required to drive such a terminal must be included in the system.

APPLICATIONS OF THE IN-FLIGHT COMPUTER

Because of the flexibility of the system, there are as many applications of the in-flight computer as there are pilots with special interests. Two examples of possible applications are presented here.

The first example is a final glide analysis. At the time that the pilot begins his final glide, he would enter his estimated distance to destination into the system. Since the sailplane's altitude is a parameter known to the system, a display such as the one shown in figure 8 would be output to the graphic display device in the cockpit. As the pilot progresses on his final glide and recognizes a landmark, he would again enter his estimated distance to destination. The system would then update the display with this new information, and also inform the pilot of a new speed-to-fly based on his actual altitude relative to his projected altitude at this point. An updated display is shown in figure 9.

Some pilots may dispute the value of additional real-time information. The second example is one involving flight-test data acquisition. Before takeoff, the data to be gathered would be defined by the pilot and entered into the system. The data acquisition program would begin execution upon command and cause the storage of this data during the flight. After the pilot has landed, a data reduction program could be executed to display the output to the pilot in a useful format.

REMARKS

The state of electronic technology has changed drastically during recent years. Vast improvements in capability have caused electronic components to be considered for diverse applications, such as the in-flight computer discussed in this paper. In the opening address at the 1978 Conference on Man-Computer Communication in Amsterdam, W. J. Doherty of IBM stated that, "it is not facetious to say that this industry is currently rapidly approaching its infancy." (ref. 7).

The impact of this dynamic technology will continue to be felt in the years to come. At this time, it is possible to construct a microprocessor-based in-flight computer to replace current panel instrumentation and greatly improve the quality and diversity of information available to the pilot. The prototype system, however, will be much more complicated, consume more power, occupy more space, provide less capability, and be more expensive than a system built several years from now to meet the same requirements. Hardware costs and power requirements are falling, even while capability per unit is rising. Figures 10, 11, and 12 show trends in the cost of processors and the cost and density of memory that substantiate this projection.

While the capability/cost trend of the in-flight computer will probably not rise as sharply as that of more marketable items, such as hand-held calculators, the system should be within economic reach of the average soaring pilot within the next few years.

REFERENCES

1. Reichmann, Helmut: Cross-Country Soaring. (Peter Lert, Translator). Thomson Publications, 1978. German Title: Streckensegelflug.

2. Ball, Richard H.: The Altitude Derivative Variometer. Soaring, Vol. 39, No. 9, September 1975, pp. 18-19.

3. Newgard, Peter M.: Gust and Gust Filters. Soaring, Vol. 43, No. 1, January 1979, pp. 40-41.

4. Ismail, A. Raouf: Electric Variometer Systems and Developments. Motorless Flight Research, 1972. NASA CR-2315, pp. 322-334.

5. Firth, John: Experience with a Variometer-Computer. Motorless Flight Research, 1972. NASA CR-2315, pp. 315-321.

6. Foley, William M.: Are Mini-Calculators Useful in Soaring Flight? Proceeding of the Second International Symposium on the Technology and Science of Low-Speed and Motorless Flight, September 1974, pp. 39-46.

7. Doherty, W. J.: Commercial Significance of Man-Computer Interaction. Proceeding of the INFOTEC Conference on Man-Computer Communications, November 1978.

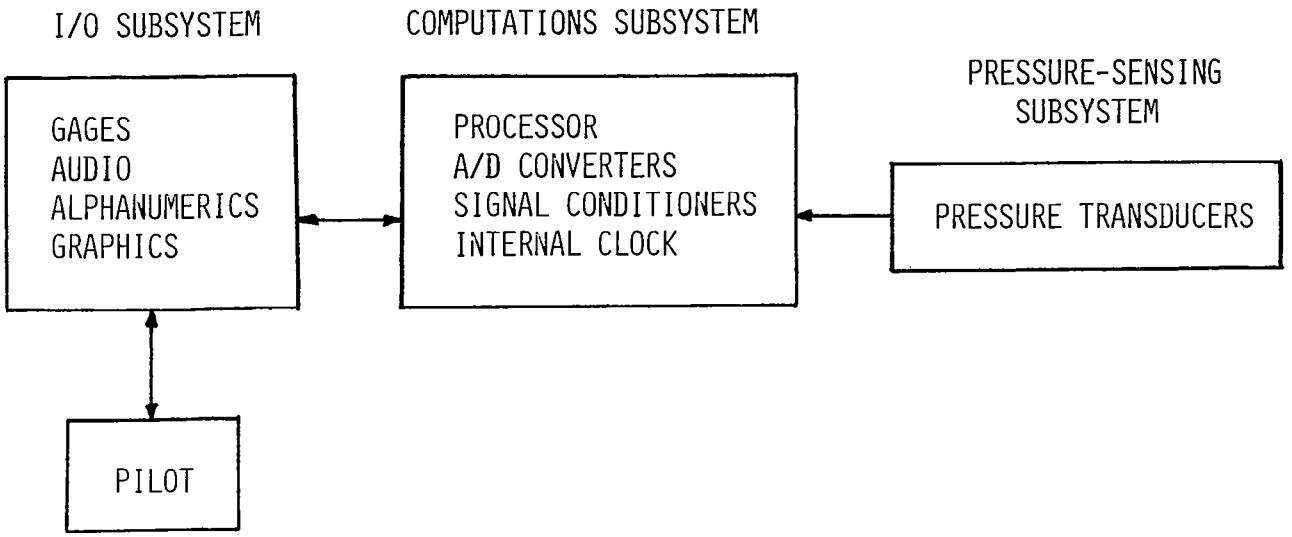

Figure 1.- Functional diagram of an in-flight computer system.

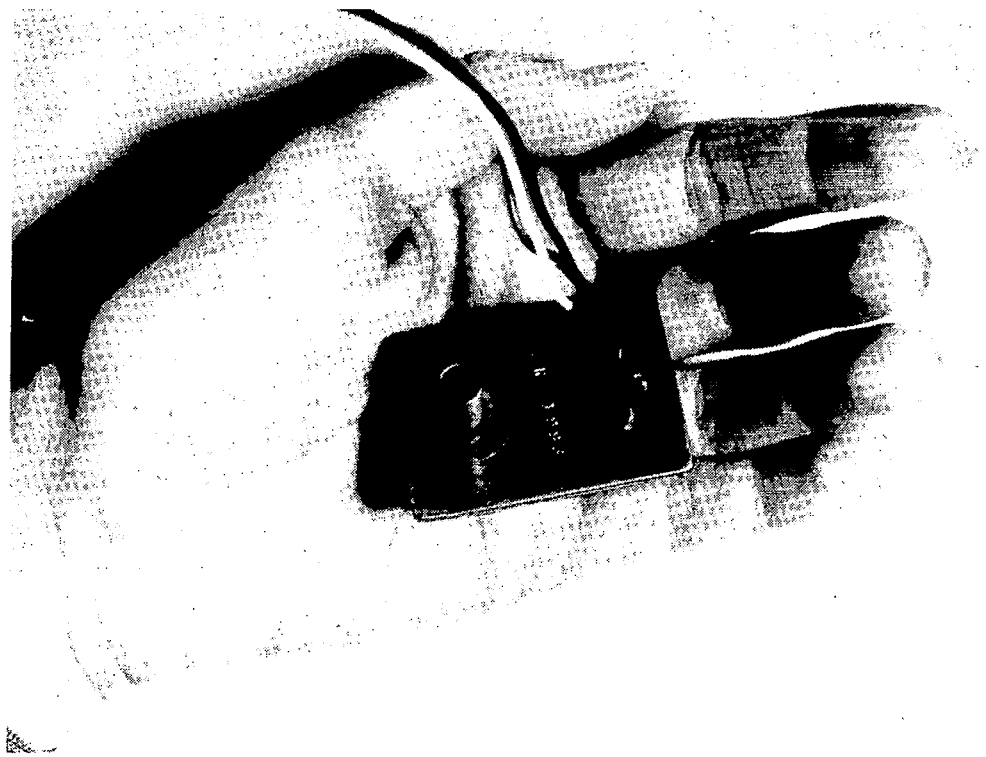

Figure 2.- Typical pressure transducer.

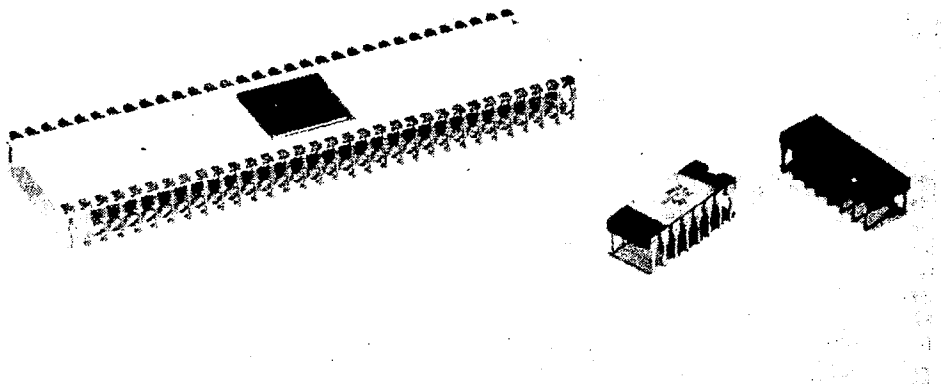

Figure 3.- Typical 16-bit microprocessor (left) and memory units (right).

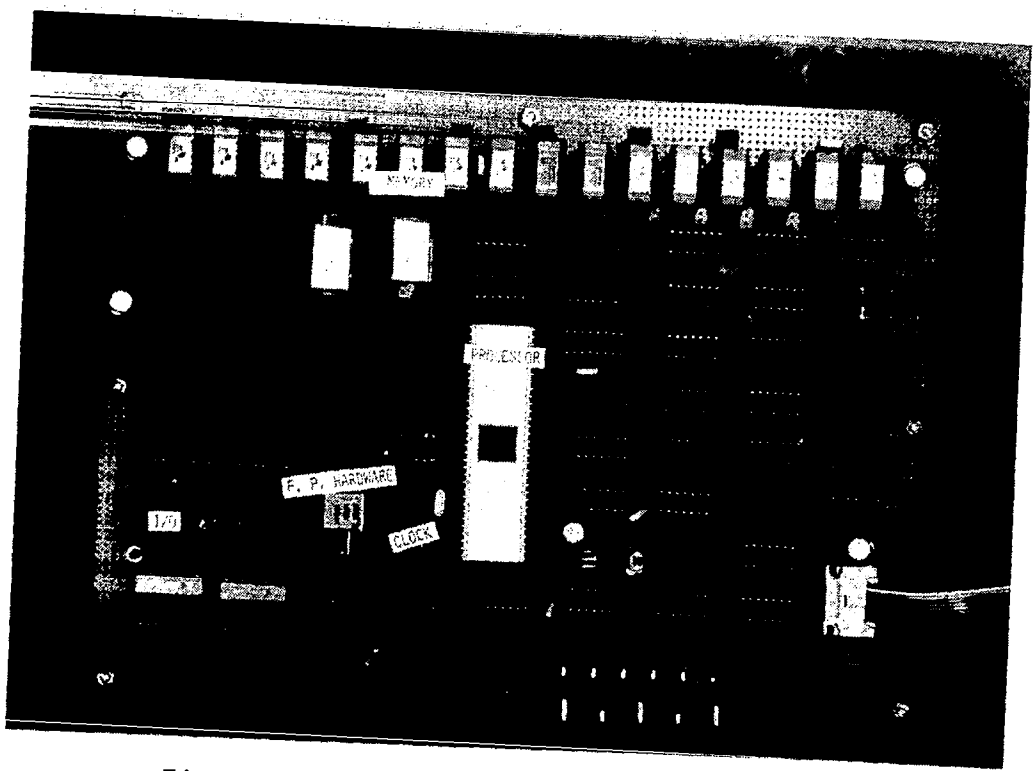

Figure 4.- Typical prototype microcomputer.

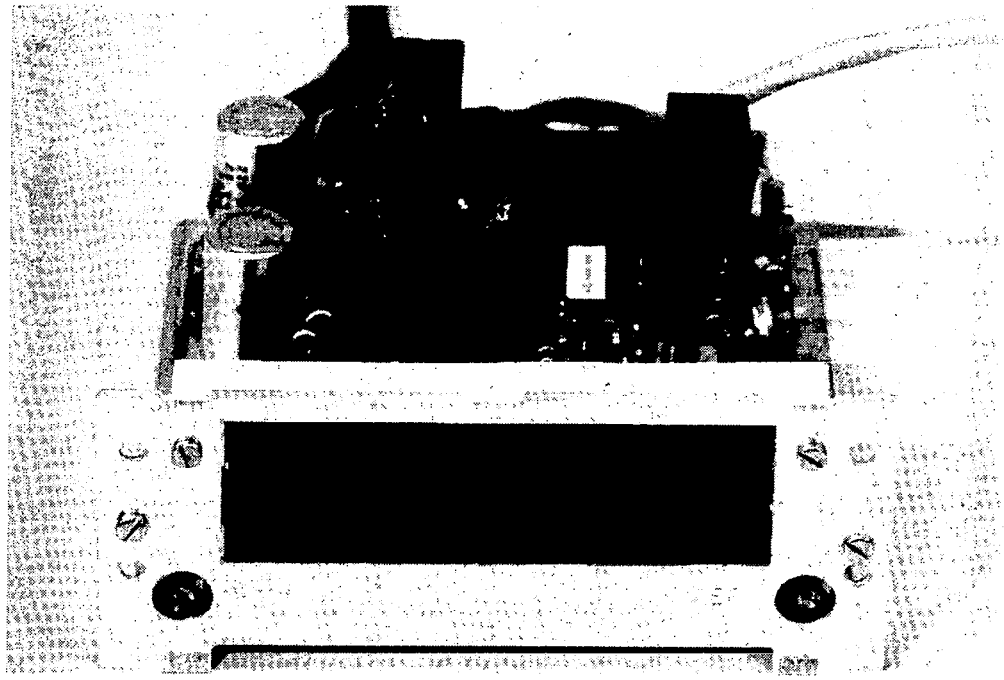

(a) Front.

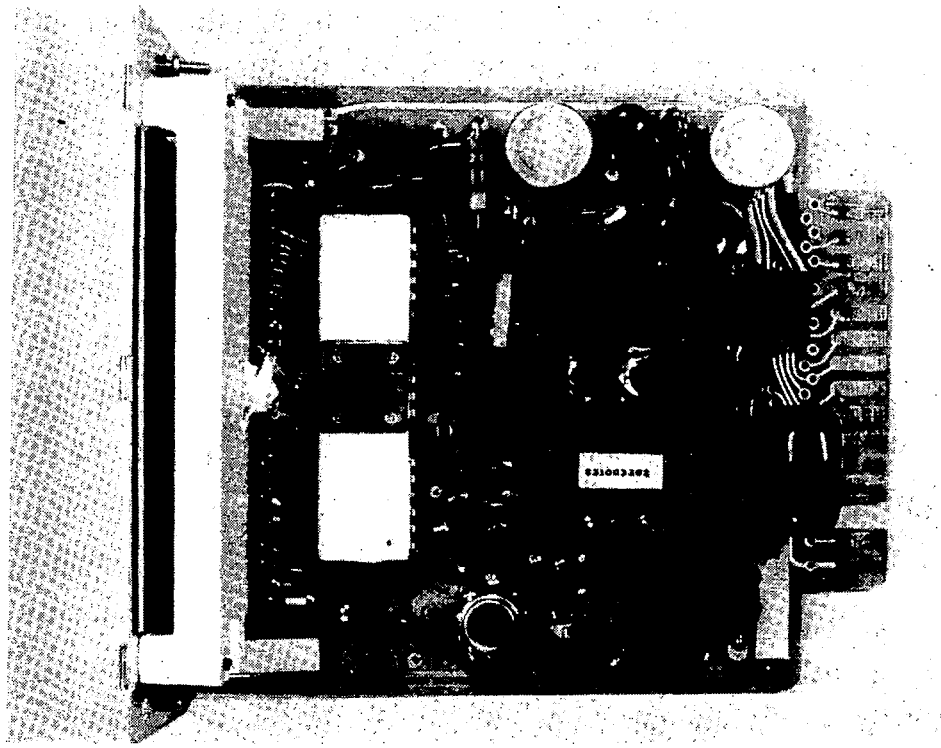

(b) Top.

Figure 5.- Typical digital liquid crystal display.

LIQUID CRYSTAL
MODULES

Figure 6.- Liquid crystal module capable of graphics output.

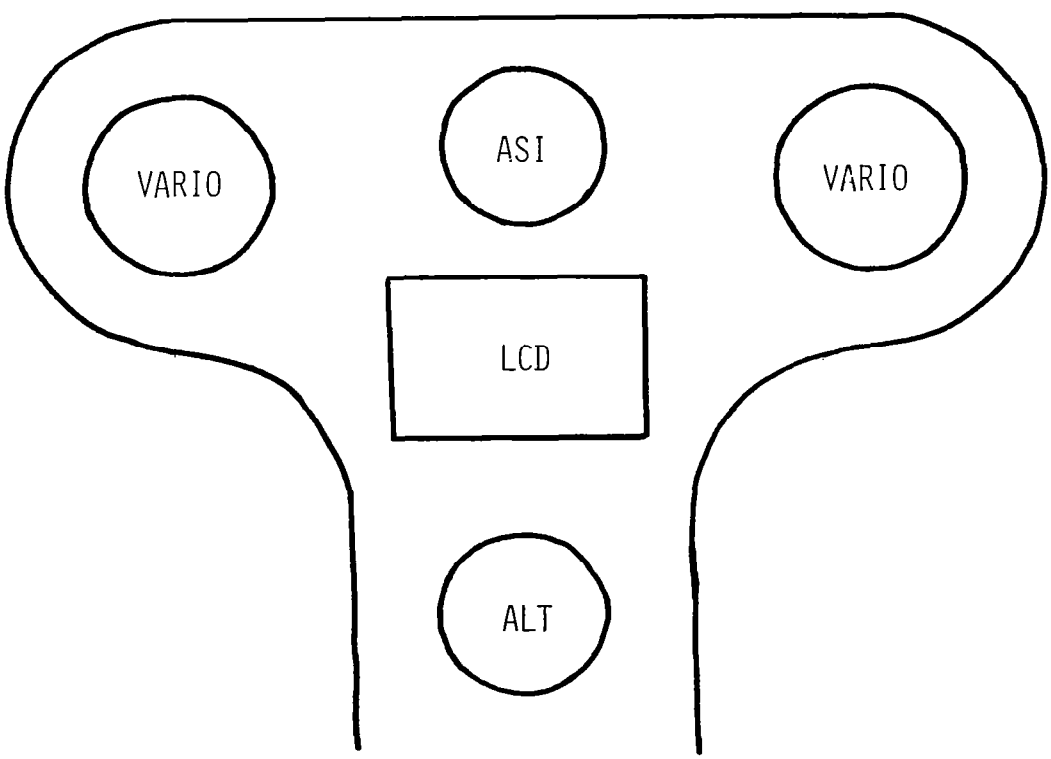

Figure 7.- Proposed minimum cockpit panel.

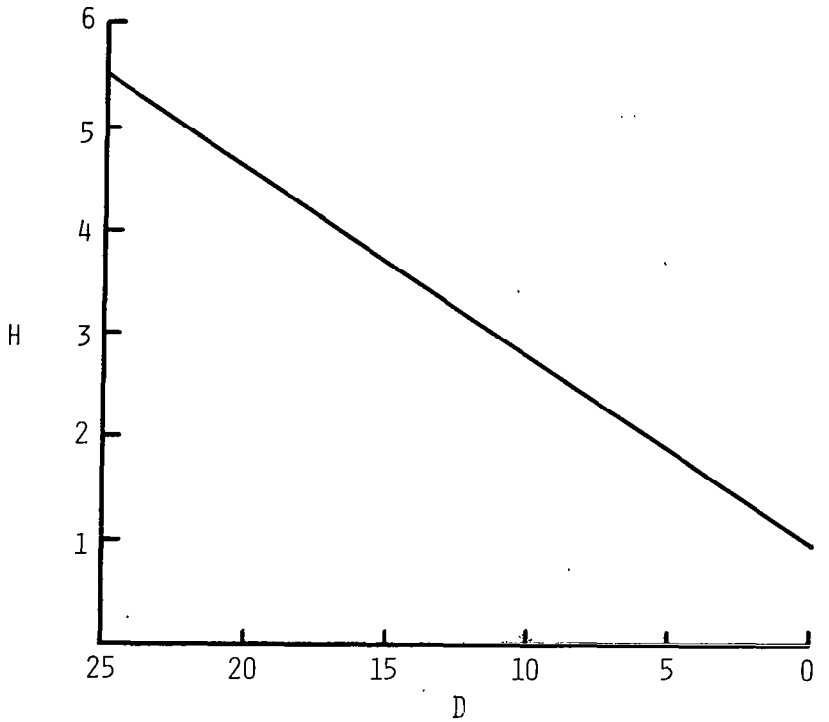

Figure 8.- Application: output display at beginning of final glide.

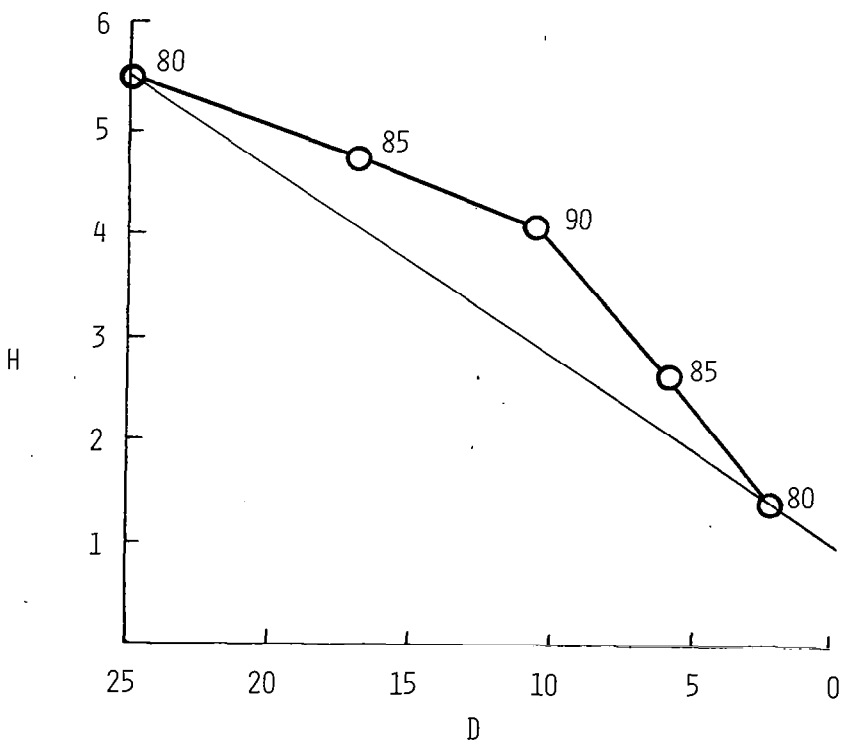

Figure 9.- Application: updated output display at landmarks during final glide.

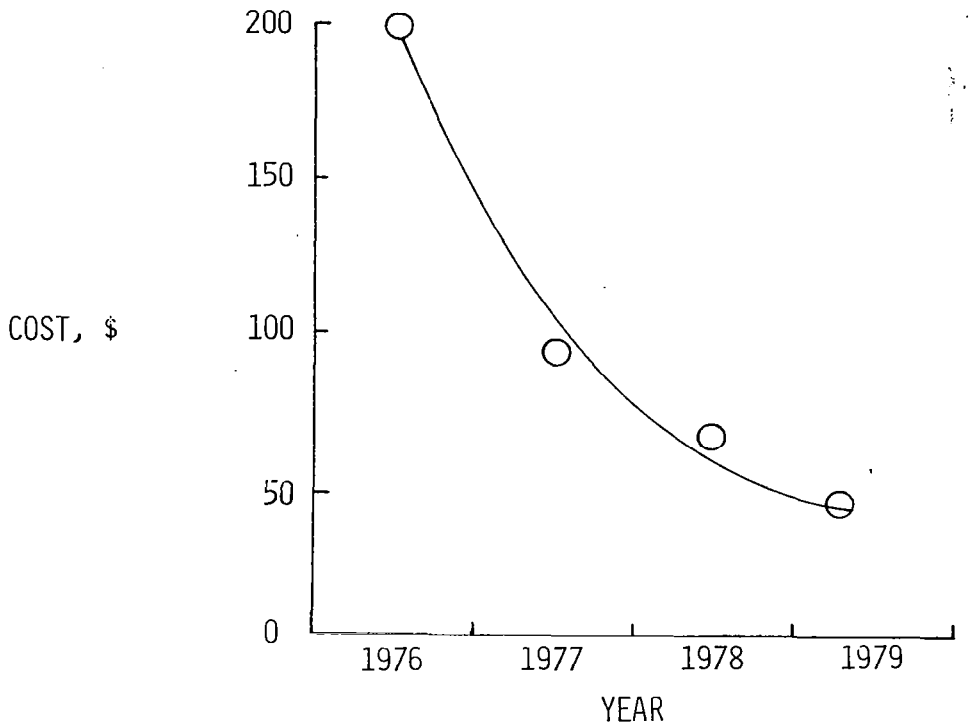

Figure 10.- Cost trend of typical 16-bit microprocessor.

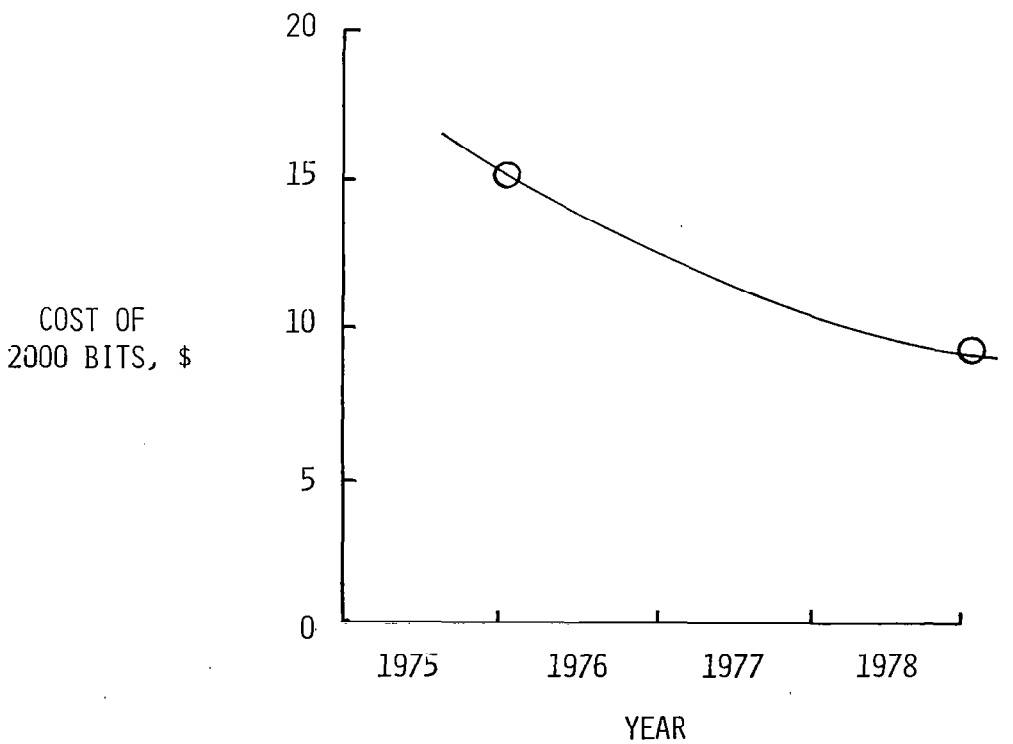

Figure 11.- Cost trend of RAM memory.

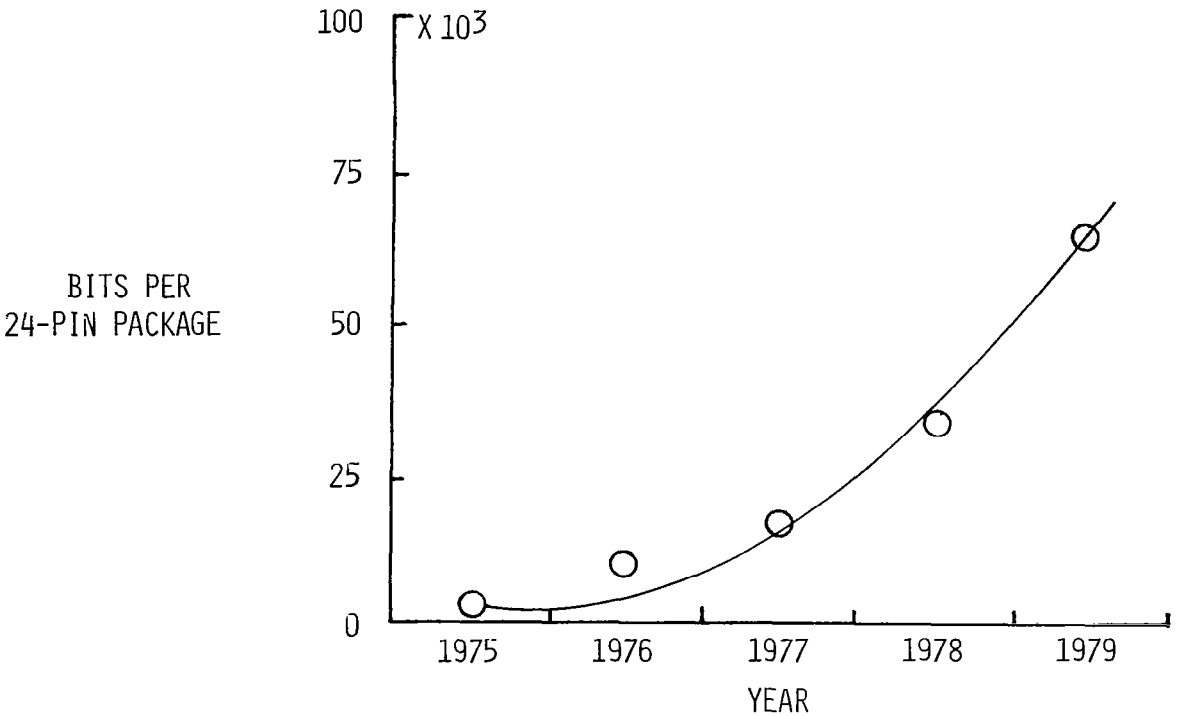

Figure 12.- Trend of amount of memory per package.

DESIGN OF PROPELLERS FOR MOTORSOARERS

E. Eugene Larrabee
Massachusetts Institute of Technology

SUMMARY

An efficient method has been developed for the design of propellers of minimum induced loss matched to an arbitrary operating point characterized by disc loading (thrust or power), air density, shaft speed, flight speed, and number of blades. A consistent procedure is outlined to predict the performance of these propellers under off-design conditions, or to predict the performance of propellers of general geometry. These procedures are particularly helpful for motorsoarer constructors and propeller builders constrained to use unusual powerplants under unusual conditions. The examples discussed include a man powered airplane, a hang glider with a 7.5 kW (10 hp) 8,000 rpm engine, and an airplane-like motorsoarer.

INTRODUCTION

For wings and propellers alike, there are spanwise or radial circulation distributions which minimize the kinetic energy loss associated with the generation of lift or thrust. These circulation distributions give rise to simple induced velocity distributions which help determine efficient wing or blade geometry. Everyone is familiar with the elliptic span loading and the corresponding uniform downwash velocity of the vortex sheet shed by a wing of minimum induced drag, but not so many are familiar with the Betz-Prandtl (ref. 1) or Goldstein (ref. 2) radial circulation functions and the corresponding uniform "displacement velocity" of the helicoidal vortex sheets shed by a propeller of minimum induced loss. The purpose of this paper is to demonstrate the application of these ideas to geometry determination and performance prediction for propellers of motorsoarers and other unusual aircraft. I have discussed some of these ideas in another paper (ref. 3). See Table I for notation used in this paper.

THE DISPLACEMENT VELOCITY

Consider an elementary helical vortex filament lying in an helicoidal vortex sheet which forms part of the slipstream of a propeller, as shown in figure 1. The vortex filament is constrained to move everywhere perpendicular to itself with a velocity w_s, which is the same as the local slipstream velocity. If the filament helix angle is ϕ_s, the axial velocity of the filament is $w_s \cos \phi_s$ and its angular velocity is $w_s \sin \phi_s / r_s$, where r_s is the helix radius. If we were unaware of the helix angular velocity, however, we would

suppose that it had only a <u>displacement velocity</u> $v' = w_s/\cos\phi_s$, in the same way that a rotating barber pole has a displacement velocity even though it has no axial velocity.

Betz, in reference 1, was the first to show that the condition for minimum induced loss operation of a propeller (or a windmill, for that matter) corresponds to radially constant displacement velocity. The axial and swirl components of the vortex sheet motion are then given by

$$w_{axial} = v' \cos^2 \phi_s \tag{1}$$

$$w_{swirl} = v' \cos \phi_s \sin \phi_s \tag{2}$$

MOTION OF THE ENTIRE SLIPSTREAM

Prandtl, in an appendix to reference 1, pointed out that the slipstream fluid between the vortex sheets moves at a fraction F of the sheet velocity, which he evaluated by analogy with the known solution for the flow about an infinite array of semi-infinite plates moving perpendicular to themselves with velocity v, as shown in figure 2. The plate solution spacing parameter, f, is recalculated according to the helicoidal vortex sheet spacing and the radial distance from the outer edges of the sheets:

$$f = \frac{B}{2} \frac{\sqrt{\lambda^2 + 1}}{\lambda} \left(1 - \frac{r}{R}\right) \tag{3}$$

Here λ is the advance ratio

$$\lambda \equiv V/\Omega R = (V/nD)/\pi \tag{4}$$

and B is the number of blades; slipstream distortion is neglected. The corresponding <u>average</u> axial and swirl velocities at a certain radius in the slipstream are then

$$\bar{w}_{axial} = F\, v' \cos^2 \phi_s \tag{1a}$$

$$\bar{w}_{swirl} = F\, v' \cos \phi_s \sin \phi_s \tag{2a}$$

$$F = (2/\pi) \cos^{-1} (e^{-f}) \tag{5}$$

THE RADIAL CIRCULATION DISTRIBUTION

The radial circulation function corresponding to this minimum induced loss slipstream motion is found by setting the circulation about a slipstream tube equal to the total vorticity trailed by the blades at the corresponding radius, and introducing "light loading" approximations:

$$B\Gamma = 2\pi\, r_s\, F\, v' \cos\phi_s \sin\phi_s \tag{6}$$

$$r_s \cong r \tag{7}$$

$$\phi_s \cong \phi \tag{8}$$

$$\phi \cong \tan^{-1}(V/\Omega r) \tag{9}$$

The resulting circulation function is conveniently written in a normalized form

$$\frac{B\Omega\Gamma}{2\pi V v'} = \frac{F\, x^2}{x^2 + 1} \equiv G \tag{10}$$

(G for Goldstein or Glauert) where

$$x \equiv \Omega r/V = (r/R)/\lambda \tag{11}$$

Equation 10 seems too simple to be true. Goldstein, in his doctor's thesis (ref. 2), verified its essential correctness, however, for propellers operating at low advance ratios or with many blades, where the vortex sheets are nearly flat, parallel, and closely spaced. The Prandtl-Betz and Goldstein circulation functions are compared in figure 3. It should be noted that a radial plot of G is identical with a radial plot of the ratio of the average axial slipstream velocity (increment) to the displacement velocity.

DETERMINATION OF THE DISPLACEMENT VELOCITY

Following Goldstein (ref. 2) we relate the displacement velocity to the disc loading (thrust or torque) by resolving Joukowsky's law into two orthogonal components:

$$\left(\frac{dT}{dr}\right)_L = \rho\Omega r\,(1 - a')\,\Gamma B \tag{12a}$$

$$\left(\frac{1}{r}\frac{dQ}{dr}\right)_L = \rho V\,(1 + a)\,\Gamma B \tag{12b}$$

Here the subscript "L" means that only the lift forces are being considered,

and a' and a are the swirl and axial components of the induced velocity at the lifting lines. Retaining the light loading assumptions, and taking the induced velocities to be half the vortex sheet velocities in the developed slipstream, we obtain:

$$a' = \frac{1}{2}\frac{v'}{\Omega r}\cos\phi_s \sin\phi_s \cong \frac{1}{2}\left(\frac{v'}{V}\right)\frac{1}{x^2+1} \tag{13a}$$

$$a = \frac{1}{2}\frac{v'}{V}\cos^2\phi_s \cong \frac{1}{2}\left(\frac{v'}{V}\right)\frac{x^2}{x^2+1} \tag{13b}$$

The circulation is given by the Betz-Prandtl approximation:

$$\Gamma = \left(\frac{2\pi V v'}{B\Omega}\right)G \qquad \text{(10 restated)}$$

The blade profile drag contributions to thrust and torque are given by

$$\left(\frac{dT}{dr}\right)_D = -\left(\frac{D}{L}\right)\frac{dL}{dr}\sin\phi \cong -\frac{D}{L}\left(\frac{dT}{dr}\right)_L\frac{1}{x} \tag{14a}$$

$$\left(\frac{1}{r}\frac{dQ}{dr}\right)_D = +\left(\frac{D}{L}\right)\frac{dL}{dr}\cos\phi \cong +\frac{D}{L}\left(\frac{1}{r}\frac{dQ}{dr}\right)_L x \tag{14b}$$

The radial gradients of thrust coefficient, $T_c \equiv 2T/\rho V^2\pi R^2$, and power coefficient, $P_c \equiv 2P/\rho V^3\pi R^2$, finally may be written as

$$\frac{dT_c}{d\xi} = \frac{dI_1}{d\xi}\zeta - \frac{dI_2}{d\xi}\zeta^2 \tag{15a}$$

$$\frac{dP_c}{d\xi} = \frac{dJ_1}{d\xi} + \frac{dJ_2}{d\xi}\zeta^2 \tag{15b}$$

where $\xi \equiv r/R$, $\zeta = v'/V$, and

$$\frac{dI_1}{d\xi} = 4\,\xi\,G\left(1 - \frac{D/L}{x}\right) \tag{16}$$

$$\frac{dI_2}{d\xi} = 2\,\xi\,G\left(1 - \frac{D/L}{x}\right)\left(\frac{1}{x^2+1}\right) \tag{17}$$

$$\frac{dJ_1}{d\xi} = 4\,\xi\,G\left(1 + \frac{D}{L}x\right) \tag{18}$$

$$\frac{dJ_2}{d\xi} = 2\,\xi\,G\left(1 + \frac{D}{L}x\right)\left(\frac{x^2}{x^2+1}\right) \tag{19}$$

Equations 16, 17, 18, and 19 can be numerically integrated radially to give four integrals I_1, I_2, J_1, and J_2 which depend only on λ and B and the presumed radial distribution of profile D/L ratio. The displacement velocity ratio is then easily found with these integrals and the propeller disc loading:

$$\zeta = \frac{I_1}{2I_2}\left(1 - \sqrt{1 - \frac{4T_c I_2}{I_1^2}}\right) \quad \text{(thrust)} \tag{20a}$$

$$\zeta = \frac{J_1}{2J_2}\left(\sqrt{1 + \frac{4P_c J_2}{J_1^2}} - 1\right) \quad \text{(power)} \tag{20b}$$

Equations 20a and 20b are the propeller counterpart of the induced angle of attack of an elliptically loaded wing, $C_L/\pi(b^2/S)$.

If the propeller is to absorb a given amount of power, one calculates the power coefficient, P_c, and the displacement velocity ratio, ζ, from equation 20b; the thrust coefficient and the efficiency are then given by $T_c = I_1\zeta - I_2\zeta^2$ and $\eta = T_c/P_c$, respectively. The alternate procedure, when the thrust is specified, is obvious.

For moderately loaded propellers operating at low advance ratios, equations 20a or 20b may give values of ζ which are large compared to λ. In this case a second approximation of the radial gradients of thrust and power coefficient is given by

$$\frac{dT_c}{d\xi} = 4\,\zeta\,\lambda\,G\left(\frac{W}{V}\right)\left(\cos\phi - \frac{D}{L}\sin\phi\right) \tag{21}$$

$$\frac{dP_c}{d\xi} = 4\,\zeta\,\xi\,G\left(\frac{W}{V}\right)\left(\sin\phi + \frac{D}{L}\cos\phi\right) \tag{22}$$

where

$$\phi = \tan^{-1}\left[\frac{\lambda}{\xi}\left(1 + \frac{\zeta}{2}\right)\right] \tag{23}$$

and

$$\frac{W}{V} = \sqrt{x^2 + 1 - \left(\frac{1}{2}\zeta\cos\phi\right)^2} \tag{24}$$

Equations 21 and 22 can then be integrated radially to find better values of T_c and P_c appropriate to the value of ζ obtained from equation 20a or 20b. Following Theodorsen (ref. 4), one might consider a third level approximation in which $G(\lambda,B)$ is recalculated with a "vortex advance ratio", $\lambda_v = \lambda(1+\zeta/2)$, to account for slipstream distortion.

DETERMINATION OF THE PROPELLER GEOMETRY

The propeller chord distribution is controlled by the choice of lift coefficient for the required circulation:

$$\frac{1}{2}\rho\ W^2\ c\ c_\ell = \rho\ W\ \Gamma = \rho\ W\ \frac{2\pi V v'}{B\Omega}\ (G) \tag{25}$$

This can be written as $\frac{c}{R} = \frac{4\pi\lambda}{B}\ \frac{G}{(W/V)}\ \frac{\zeta}{c_\ell} \cong \frac{4\pi\lambda}{B}\ \frac{G}{\sqrt{x^2+1}}\ \frac{\zeta}{c_\ell}$ (26)

Lift coefficients must be chosen with regard to structural constraints on thickness-to-chord ratios at inner radii and local Mach numbers at outer radii; also they must be consistent with the D/L ratios that have been used to find ζ. Some consideration must be given to off-design conditions as well; for example, a propeller designed for cruise can be expected to develop larger lift coefficient increases at inner radii than at outer radii when it is operated at lower advance ratios, as in climbing flight.

Traditionally propellers have been built with flat bottom airfoil sections such as the Clark Y. Considering the large thickness-to-chord ratios needed structurally at the inner radii, and the inherent variation of lift coefficient with camber (proportional to thickness-to-chord ratio), one can design the propeller to operate with radially constant zero angle of attack. In this case the propeller will have constant "true geometric pitch", given by:

$$\frac{P_{geometric}}{Diameter} = \pi\lambda\left(1 + \frac{1}{2}\zeta\right),\ \alpha = 0 \tag{27}$$

Modern computational airfoil theory (ref. 5) shows that the lift coefficient for Clark Y airfoils of varying thickness-to-chord ratio is given by

$$c_\ell = 0.062 + 4.21(t/c) + 0.0971\ \alpha^\circ;\ 0.07 < \frac{t}{c} < 0.19$$

when they are operated at a Reynolds number of 1×10^6 and a Mach number of 0.2.

The theory presented so far has assumed uniform flow at flight velocity V through the propeller disc at vanishingly small values of ζ. This is not a realistic assumption for propellers turned by direct drive piston engines which are often quite large compared to the propeller radius. If the axial velocity distribution, averaged around the propeller disc at radius r, is given by $\bar{u}V$, it is customary to "depitch the propeller" ($\bar{u}(\xi)<1$) so that the blade angle is given by

$$\beta = \tan^{-1}\left(\frac{\bar{u}\lambda}{\xi}\left(1 + \frac{\zeta}{2}\right)\right) + \alpha \tag{28}$$

This has the effect of preserving the prescribed circulation function. The performance consequences of propeller-fuselage interaction are considered in the next section.

PERFORMANCE OF ARBITRARY PROPELLERS

Unlike an untwisted elliptical planform wing, which has elliptic loading over a range of angles of attack, a minimum-induced loss propeller has minimum induced loss loading only at its design advance ratio. An arbitrary propeller theory is needed to calculate its off-design point performance, or the performance of any general propeller. The theory given here is a radially graded momentum theory like Glauert's (refs. 6 and 7), but it will return the design performance of a minimum induced loss propeller when applied to the design conditions and geometry calculated by the methods described before.

The axial and swirl components of the induced velocity at the blade elements are found by setting the changes of axial and swirl momentum within a given annulus of the slipstream equal to the axial and torque loading of the corresponding blade elements as shown in figure 4:

$$\frac{dT}{dr} = 2\pi r\rho V\ (\bar{u} + a)\ 2FaV$$
$$= \frac{\rho}{2} V^2 \left(\frac{\bar{u} + a}{\sin\phi}\right)^2 \left(\frac{Bc}{2\pi r}\right) 2\pi r\ C_y \tag{29}$$

$$\frac{1}{r}\frac{dQ}{dr} = 2\pi r\rho V\ (\bar{u} + a)\ 2F\Omega r a'$$
$$= \frac{\rho}{2} V^2 \left(\frac{\bar{u} + a}{\sin\phi}\right)^2 \left(\frac{Bc}{2\pi r}\right) 2\pi r\ C_x \tag{30}$$

where (see figure 4)

$$\phi = \tan^{-1}\left(\frac{V}{\Omega r}\ \frac{(\bar{u} + a)}{(1 - a')}\right) \tag{31}$$

$$C_y = c_\ell \cos\phi - c_d \sin\phi \tag{32}$$

$$C_x = c_\ell \sin\phi + c_d \cos\phi \tag{33}$$

In the absence of the propeller, the velocity in the flow field about the fuselage or nacelle is assumed to be given by an average axial component u and an average radial component v at a distance r from the propeller shaft. We account for only the axial component

$$\bar{u} = u/V \tag{34}$$

Equations 29 and 30 can be solved for the induced velocity components in terms of the dimensionless thrust and torque loading:

$$\frac{a}{\bar{u} + a} = \frac{1}{4}\ \frac{\sigma C_y}{\sin^2\phi}\ \frac{1}{F}\ ;\ \sigma \equiv \frac{Bc}{2\pi r} \tag{35}$$

$$\frac{a'}{1 - a'} = \frac{1}{4}\ \frac{\sigma C_x}{\sin\phi\ \cos\phi}\ \frac{1}{F} \tag{36}$$

Equations similiar to these appear in Glauert's article in Durand's "Aerodynamic Theory" (ref. 7), with the vortex spacing factor F in the numerator instead of the denominator, just as his widow and R. McKinnon Wood left them.

The induced velocity components are evaluated at each radial station by an iterative process outlined below:

At each value of ξ the following are known:

ξ, λ, F, σ, β, $\bar{u}$; $c_\ell = c_\ell(\alpha)$, $c_d = c_d(c_\ell)$

Choose α_1

Calculate $\phi_{\alpha_1} = \beta - \alpha_1$

Calculate c_ℓ, c_d

Calculate C_y, C_x (eqs. 32 and 33)

Calculate a and a' (eqs. 35 and 36)

Calculate $\phi_{a_1} = \tan^{-1}\left(\frac{\lambda}{\xi}\frac{(\bar{u} + a)}{(1 - a')}\right)$

Calculate $\phi_{\alpha_1} - \phi_{a_1}$

if $\phi_{\alpha_1} - \phi_{a_1} > 0$, $\alpha_2 < \alpha_1$

if $\phi_{\alpha_1} - \phi_{a_1} < 0$, $\alpha_2 > \alpha_1$

Iterate until $|\phi_{\alpha_n} - \phi_{a_n}|$ is less than some small quantity.

Retain ϕ_n, C_{y_n}, C_{x_n}, a_n, a'_n

The wing theory analog of this computation is to suppose that the induced angle of attack at any spanwise station y of a non-elliptically loaded wing of span b is given by

$$\alpha_{induced} = \frac{1}{4}\frac{(c/b)c_\ell}{\sqrt{1 - (2y/b)^2}} \tag{37}$$

where c and c_ℓ are the chord and section lift coefficient at the same station. The quantity $\sqrt{1 - (2y/b)^2}$ vanishes at y = b/2 in the same way that F vanishes at r = R, and it may be shown that equation 37 yields $\alpha_{induced} = C_L/\pi(b^2/S)$ for an elliptically loaded wing of elliptic planform.

The values of ϕ, C_y, C_x, and a' are then integrated radially to find the thrust load and the power absorption of the propeller in the fuselage (or nacelle) flow field. These may be conveniently written in terms of coefficients based on the shaft speed n (revolutions/sec)

$$C_T = \frac{T}{\rho n^2 D^4} \quad (D = 2R) \tag{38}$$

$$C_P = \frac{P}{\rho n^3 D^5} \tag{39}$$

$$\frac{dC_T}{d\xi} = \frac{\pi^3}{4}\left(\frac{1 - a'}{\cos\phi}\right)^2 \xi^3 \sigma C_y \tag{40}$$

$$\frac{dC_P}{d\xi} = \frac{\pi^4}{4}\left(\frac{1 - a'}{\cos\phi}\right)^2 \xi^4 \sigma C_x \tag{41}$$

The a', cos ϕ choice is preferred for numerical precision over the a, sin ϕ, $\bar{u}$ choice.

The thrusting propeller is surrounded by a static pressure field with an appreciable axial variation, both upstream and downstream. Koning (ref. 8) has estimated its value:

$$\frac{\Delta P}{\frac{\rho}{2}V^2} = + \frac{T_c}{2}\left(1 - \frac{x/R}{\sqrt{(x/R)^2 + 1}}\right) \quad \text{downstream; tractor propeller} \tag{42}$$

$$\frac{\Delta P}{\frac{\rho}{2}V^2} = - \frac{T_c}{2}\left(1 + \frac{x/R}{\sqrt{(x/R)^2 + 1}}\right) \quad \text{upstream; pusher propeller} \tag{43}$$

Here x is distance downstream from the propeller. This axial pressure gradient causes the propeller-bearing-fuselage or nacelle to have a buoyancy drag given by

$$\Delta C_{D_{buoyancy}} = \frac{1}{S_{ref}} \int_0^{\ell} \left(\frac{\Delta P}{\frac{\rho}{2}V^2}\right)\left(\frac{dS_b}{dx_b}\right) dx_b \tag{44}$$

where S_{ref} is the reference area for drag coefficients, ℓ is the body length, and S_b is the body cross section area at the distance x_b behind the body nose. The net thrust of the propeller-body combination is then given by,

$$C_{T_n} = C_T\left(1 - \frac{S_{ref}\,\Delta C_{D_{buoyancy}}}{\pi R^2}\right) \tag{45}$$

while the installed efficiency of the propeller becomes

$$\eta = \frac{C_{T_n}(\pi\lambda)}{C_P} = \frac{C_{T_n}(V/nD)}{C_P} \tag{46}$$

Figure 5 shows an application of the arbitrary propeller theory just described to the prediction of the performance of a scale model of a light airplane propeller when tested as an "isolated" propeller, and when run at the nose of a representative fuselage. This theory is computationally more demanding than the design theory presented in the previous section since it requires extensive estimates of the propeller airfoil section properties at several radii, a good estimate of the three dimensional flow field surrounding the

fuselage (or nacelle) at the propeller location, an iteration procedure to determine the induced velocities, and numerical integrations to determine blade loading and body buoyancy drag in the propeller pressure field. Limited experience with it at M.I.T. shows that it gives reasonable results, and these are being experimentally confirmed (1979). In common with other radially graded momentum theories it fails to take account of the effect of circulation at every radial station on the downwash (or "inflow") at a particular station, but it is made to be consistent with the induced velocity pattern for a minimum induced loss propeller through Prandtl's analytic vortex spacing velocity fraction F rather than through tabulated values of Goldstein's circulation function. The next step up to a "prescribed" or "free" discrete vortex model of the "rotor" and its "wake" is much more diffcult.

APPLICATIONS

(1) Man powered airplane. Here we redesign the "Gossamer Condor" propeller. The design conditions, summarized in figure 6, correspond to climbing flight in ground effect at an angle of 1°; approximately 30% of the 53.3 N (11.8 lbs) of thrust is required to overcome the component of airplane weight along the flight path. The figure shows the radial variation of profile D/L ratio and the radial gradients of the integrals I_1, I_2, J_1, and J_2. The design thrust coefficient, $T_c = 0.3175$, requires a displacement velocity ratio, $\zeta = 0.2671$, which corresponds to a power coefficient, $P_c = 0.3914$, and an efficiency, $\eta = 0.8113$. The powerplant output required is 328 watts (0.44 hp).

Since the displacement velocity ratio is moderately large, it is worthwhile to recalculate the thrust coefficient and the power coefficient using eqs. 21-24. The results are summarized in figure 7, which also compares the propeller geometry determined by the methods of this paper with the geometry actually employed. The agreement of blade angles is very good, especially when one takes into account the difference between the zero lift angles of the Clark Y airfoils assumed in the design calculations and the Stratford pressure recovery airfoils used on the "Gossamer Condor". In my opinion the propeller calculated here would be more efficient than the one actually flown.

(2) Powered hang glider. Soarmaster, Inc. supplies a powerpack consisting of a West Bend (Chrysler) two stroke, single cylinder engine developing 7.46 kW (10 hp) at 10,000 rpm, a centrifugal clutch, a chain and sprocket reduction gear, and an extension shaft turning a pusher propeller. This is a suitable powerplant for hang gliders of 12 m (40 ft) span; figure 8 presents the options available for propellers intended to absorb the engine power at a flight speed of 13 m/sec (30 mph). The diameter of the direct drive propeller is limited to 690 mm (27 in) by a tip Mach number of 0.85; its efficiency is very poor because of the excessive disc loading. Gear reductions and larger propellers lead to progressive improvements in performance. Figure 9 gives the geometry of the largest propeller considered, a 1372 mm (54 in) diameter propeller turned at 1946 rpm by a 9:37 sprocket pair driven at 8000 rpm. It has 617 mm (24 in) nominal pitch, and the typical wide root chord - narrow tip chord geometry of a propeller matched to a low advance ratio; this is in spite of a

design lift coefficient of 1 near the hub and 0.5 at the tip. Soarmaster supplies two propeller options: a 1067 x 483 mm (42 x 19 in) or an 1118 x 356 mm (44 x 14 in) "laminar" airscrew, both of fiber reinforced plastic.

Table 2 summarizes the propeller parameters covered in this study: when two values are given for T_c, P_c, and η, the second set corresponds to the improved velocity polygon geometry corresponding to eqs. 21-24; note the relatively good agreement, even for ζ values of more than 1. Examination of figure 9 and Table 2 suggests that still larger propellers and larger reduction ratios would improve climbing performance; this has to be balanced against the weight penalty and the reduction of ground clearance at the tail.

(3) Motorsoarer. The Ryson ST-100 is a 17.58 m (57.67 ft) span two seated aircraft, with a flying mass of 748.4 kg (1650 lbs), fitted with a Hoffmann HO-V-62 propeller of 1.7 m (67 in) diameter. This propeller has a low pitch setting, a high pitch setting, and can be feathered for glider mode operation. Figure 10 shows three design points which might be considered in the selection of such a propeller: sea level climbing performance at 40 m/sec (90 mph); sea level top speed at about 68 m/sec (152 mph); and cruise at 75% power at full throttle at 1981 m (6500 ft) altitude and 65 m/sec (145 mph). The circled points show the performance that may reasonably be expected from minimum induced loss propellers designed for each of these flight conditions by the methods of the paper.

Figure 11 shows how a compromise propeller may be designed which will give nearly this performance at two of these points. The displacement velocities are calculated assuming minimum induced loss loading and a somewhat pessimistic radial distribution of D/L ratio. Blade lift coefficients are assigned at $\xi = 0.3$ and $\xi = 0.7$ so that the blade chord to radius ratio, c/R, as given by equation 26, is the same for both flight conditions. The c/R ratio is then calculated at other radii, assuming a linear radial variation of c_ℓ. Reasonable assumptions are then made about the radial variation of thickness to chord ratio, t/c, to give the radial variation of blade angle (eq. 28). The compromise c/R ratio and blade twist, $\Delta\beta$, are then chosen to minimize differences between the two conditions. In general, highly loaded, low advance ratio flight conditions demand high lift coefficients near the hub Betz (ref. 9) was of the opinion that Coriolis forces within the rotating blade boundary layer favored such a distribution.

REFERENCES

1. Betz, Albert (with an appendix by Ludwig Prandtl): Schraubenpropeller mit geringstem Energieverlust (Screw propellers with Minimum Energy Loss). Goettingen Reports, 1919.

2. Goldstein, Sidney: On the Vortex Theory of Screw Propellers. Proceedings of the Royal Society, 1929 (his doctor's thesis).

3. Larrabee, E. Eugune: Practical Design of Minimum Induced Loss Propellers. SAE preprint for the April 1979 Business Aircraft Meeting and Exposition, Wichita, Kansas.

4. Theodorsen, Theodore: Theory of Propellers. McGraw-Hill Book Company, Inc. 1948.

5. Smetana, Frederick O., et al.: Light Aircraft Lift, Drag, and Moment Prediction - A Review and Analysis. NASA Contractor's Report CR-2523.

6. Glauert, H.: Elements of Aerofoil and Airscrew Theory. Cambridge, 1926.

7. Glauert, H.: Airplane Propellers. Div. L, Vol IV of Durand's "Aerodynamic Theory" Springer Verlag 1935; also Dover reprint.

8. Koning, C.: Influence of the Propeller on Other Parts of the Airplane Structure. Division M, Vol IV ibid.

9. Betz, Albert: Hoechsauftrieb von Fluegeln an umlaufenden Raedern (Maximum Lift of Blades on Running Rotors). Flugwissenschaft 9 (1961) Heft 4/5 Seiten 97-99.

TABLE I

SYMBOLS AND NOTATION (follows Glauert; ref. 8)

aV	axial component of induced velocity (m/sec)
$a'\Omega r$	rotational (swirl) component of induced velocity (m/sec)
B	number of blades
b	wing span (m)
c	blade chord (m)
c_d	section (profile) drag coefficient
c_ℓ	section (profile) lift coefficient
C_L	wing lift coefficient
C_P	power coefficient ($C_P \equiv P/\rho n^3 D^5$)
C_T	thrust coefficient ($C_T \equiv T/\rho n^2 D^4$)
C_x	blade element torque load coefficient
C_y	blade element thrust load coefficient
D	drag; also propeller diameter (m)
F	slipstream velocity fraction (eq. 5)
f	vortex sheet spacing parameter (eq. 3)
G	circulation radial distribution function (eqs. 10,11)
I_1, I_2	thrust loading integrals (eqs. 16,17)
J_1, J_2	power loading integrals (eqs. 18,19)
L	lift
n	revolutions per second
P	shaft power (kW)

P_c power coefficient ($P_c \equiv 2P/\rho V^3 \pi R^2$)
Q propeller shaft torque (Nm)
R propeller tip radius (m)
r propeller general radius (m)
S wing plan or fuselage cross section area (m^2)
T thrust (N)
T_c thrust coefficient ($T_c \equiv 2T/\rho V^2 \pi R^2$)
u axial velocity of fuselage flow field at r (m/sec)
$\bar{u}V$ average axial velocity at r (m/sec)
V flight velocity (m/sec)
v radial velocity of fuselage flow field at r (m/sec)
v' displacement velocity (m/sec); see fig. 1
W resultant velocity at blade element ($\vec{W} = \vec{V} + \vec{\Omega r} + \vec{w}$)(m/sec)
w induced velocity at blade element ($\vec{w} = a\vec{V} + a'\vec{\Omega r}$)(m/sec)
w_s slipstream velocity (incremental)(m/sec)
x velocity ratio ($x \equiv \Omega r/V$)
y spanwise location (m)

α section angle of attack (rad); $\alpha°$ (degrees)
β section blade setting angle (rad); $\beta°$ (degrees)
Γ circulation (m^2/sec)
ζ displacement velocity ratio ($\zeta \equiv v'/V$)
η efficiency ($\eta = T_c/P_c \equiv (V/nD)C_T/C_P$)
λ advance ratio ($\lambda \equiv V/\Omega R$)
ξ radius ratio ($\xi \equiv r/R$)
ρ air density (kg/m^3)
σ blade solidity ($\sigma \equiv Bc/2\pi r$)
ϕ helix angle (rad); $\phi = \beta - \alpha$
Ω shaft speed (rad/sec)

TABLE 2

POWERED HANG GLIDER PROPELLERS
V = 13.41 m/sec (30 mph)
7.457 kW (10 hp) @ 8000 engine rpm
ρ = 1.225 kg/m^3 (760 mm Hg, 15°C)

Gear Ratio	2R m	P_c	ζ	T_c	η	pitch / diameter	$\pi\lambda$
1:1	0.690	13.500	2.544	4.650	0.344	0.356	0.146
9:27	1.000	6.426	1.778	2.888	0.449	0.507	0.288
9:27	1.219	4.323 3.881	1.283 -----	2.179 2.103	0.504 0.541	0.361	0.220
9:37	1.372	3.348 3.145	1.151 -----	1.840 1.821	0.550 0.579	0.450	0.301

FIG. 1 VORTEX SHEET MOTION
MINIMUM INDUCED LOSS PROPELLER

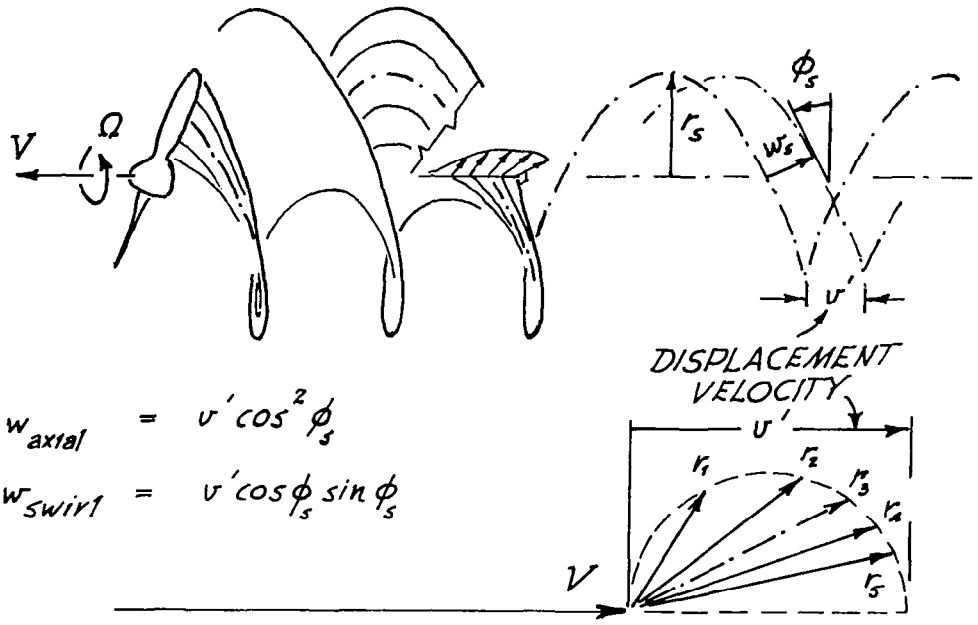

$$w_{axial} = v' \cos^2 \phi_s$$

$$w_{swirl} = v' \cos \phi_s \sin \phi_s$$

FIG. 2 PRANDTL'S VELOCITY FACTOR, F

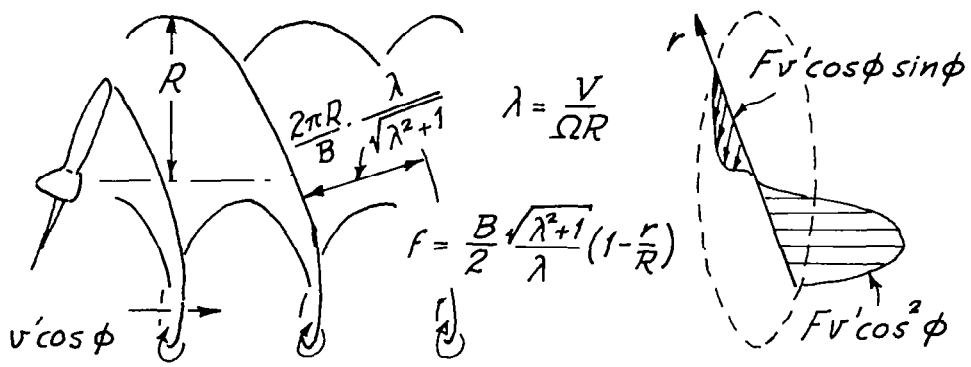

$$\lambda = \frac{V}{\Omega R}$$

$$f = \frac{B}{2} \frac{\sqrt{\lambda^2+1}}{\lambda} \left(1 - \frac{r}{R}\right)$$

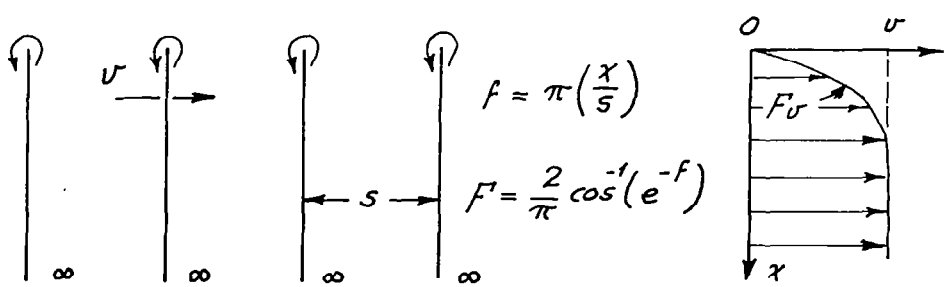

$$f = \pi \left(\frac{x}{s}\right)$$

$$F = \frac{2}{\pi} \cos^{-1}\left(e^{-f}\right)$$

FIG. 3 RADIAL CIRCULATION DISTRIBUTIONS
MINIMUM INDUCED LOSS PROPELLERS

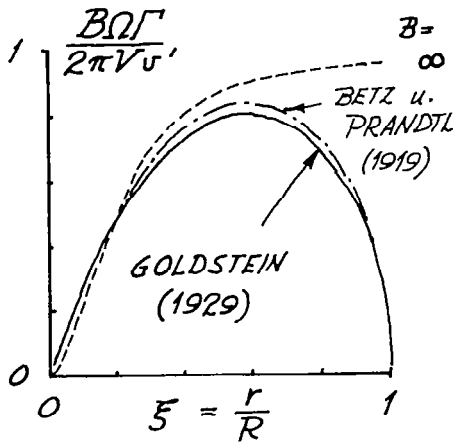

$\lambda = 0.2$
$B = 2$

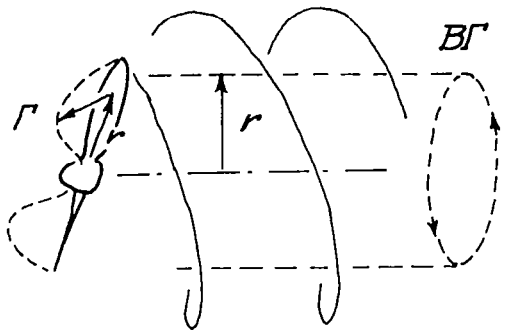

$$B\Gamma = 2\pi r F v' \cos\phi \sin\phi$$

$$\frac{B\Omega\Gamma}{2\pi V v'} = \frac{F x^2}{x^2+1} \; ; \; x \equiv \frac{\Omega r}{V}$$

BETZ u. PRANDTL

FIG. 4 RADIALLY GRADED MOMENTUM THEORY
INDUCED VELOCITY CALCULATION

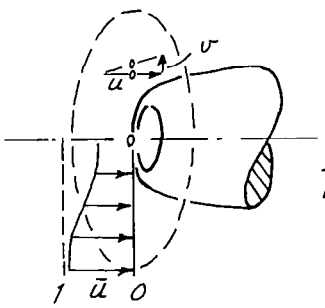

$$\frac{dT}{dr} \rightarrow \frac{a}{\bar{u}+a} = \frac{1}{4} \cdot \frac{\sigma C_y}{\sin^2\phi} \cdot \frac{1}{F}$$

$$\frac{1}{r} \cdot \frac{dQ}{dr} \rightarrow \frac{a'}{1-a'} = \frac{1}{4} \cdot \frac{\sigma C_x}{\sin\phi \cos\phi} \cdot \frac{1}{F}$$

$$\bar{u} \equiv \frac{u}{V} \; ; \; \sigma = \frac{Bc}{2\pi r}$$

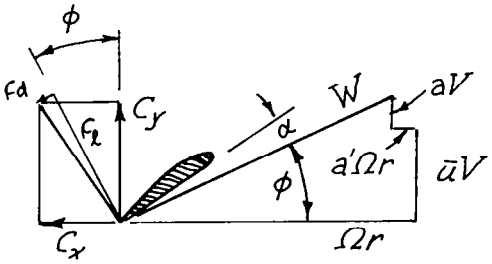

$$\phi = \beta - \alpha = \tan^{-1}\left[\frac{\bar{u}\lambda}{\xi} \cdot \frac{1+a}{1-a'}\right]$$

$$C_y = F_l \cos\phi - F_d \sin\phi$$

$$C_x = F_l \sin\phi + F_d \cos\phi$$

FIG. 5 RADIALLY GRADED MOMENTUM THEORY
$\frac{1}{4}$ SCALE MCCAULEY 1C160

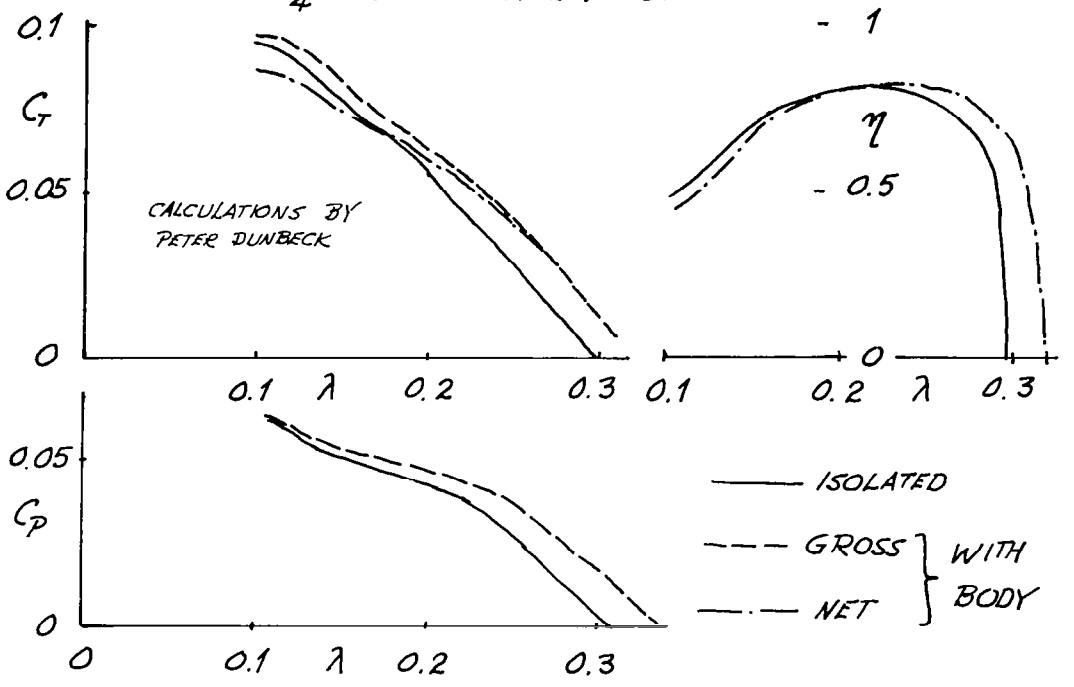

FIG. 6 PROPELLER DESIGN FUNCTIONS
MAN POWERED AIRPLANE

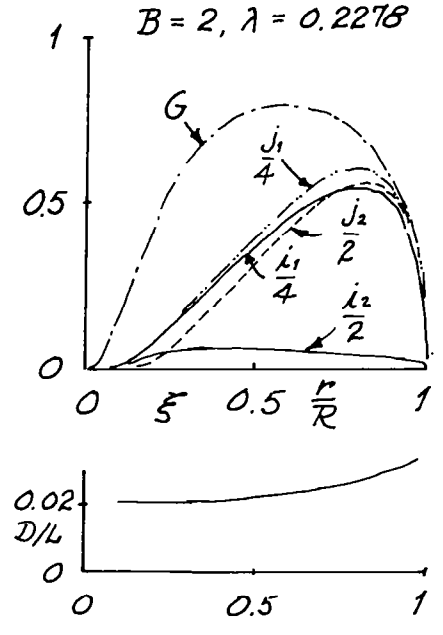

$R = 1.905\ m\ (6.25\ ft)$
$V = 5\ m/sec\ (11.2\ mph)$
$\Omega = 11.52\ rad/sec\ (110\ rpm)$
$T = 53.3\ N\ (11.8\ lbs;\ 1°\ climb)$
$\rho = 1.178\ kg/m^3$

$i_1 = dI_1/d\xi \quad I_1 = 1.2125$
$i_2 = dI_2/d\xi \quad I_2 = 0.0888$

$j_1 = dJ_1/d\xi \quad J_1 = 1.3151$
$j_2 = dJ_2/d\xi \quad J_2 = 0.5626$

$T_c = 0.3175 \rightarrow \xi = 0.2671$
$P_c = 0.3914 \rightarrow \eta = 0.8113$

$\pi\lambda\left[1 + \frac{\xi}{2}\right] = 0.8114$

FIG. 7 PROPELLER GEOMETRY
MAN POWERED AIRPLANE

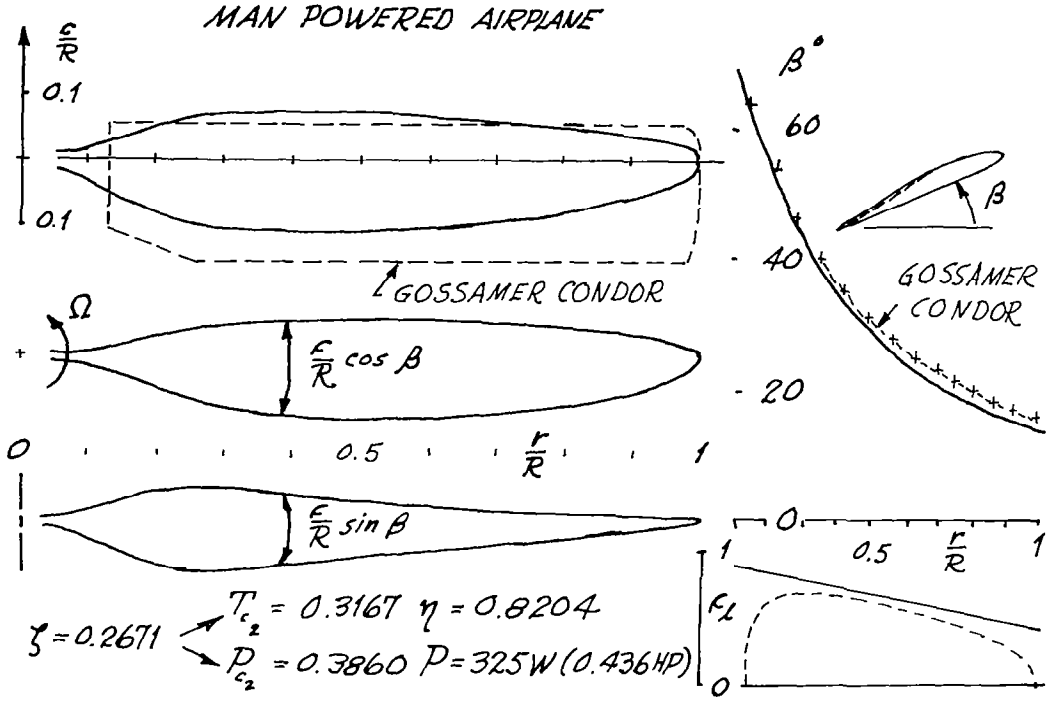

FIG. 8 POWERED HANG GLIDER PROPELLER OPTIONS

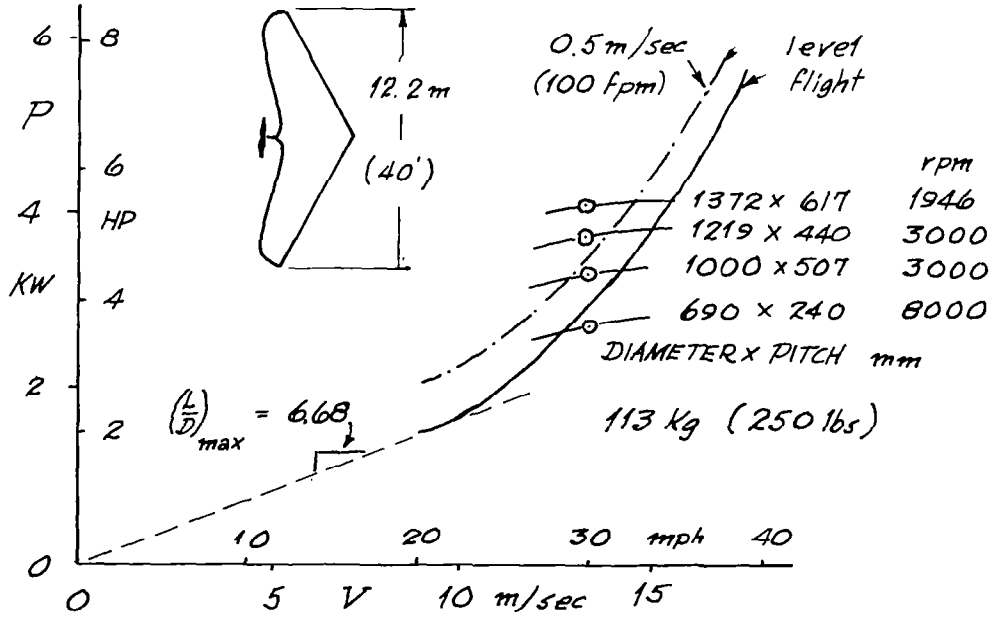

FIG. 9 PROPELLER GEOMETRY
POWERED HANG GLIDER

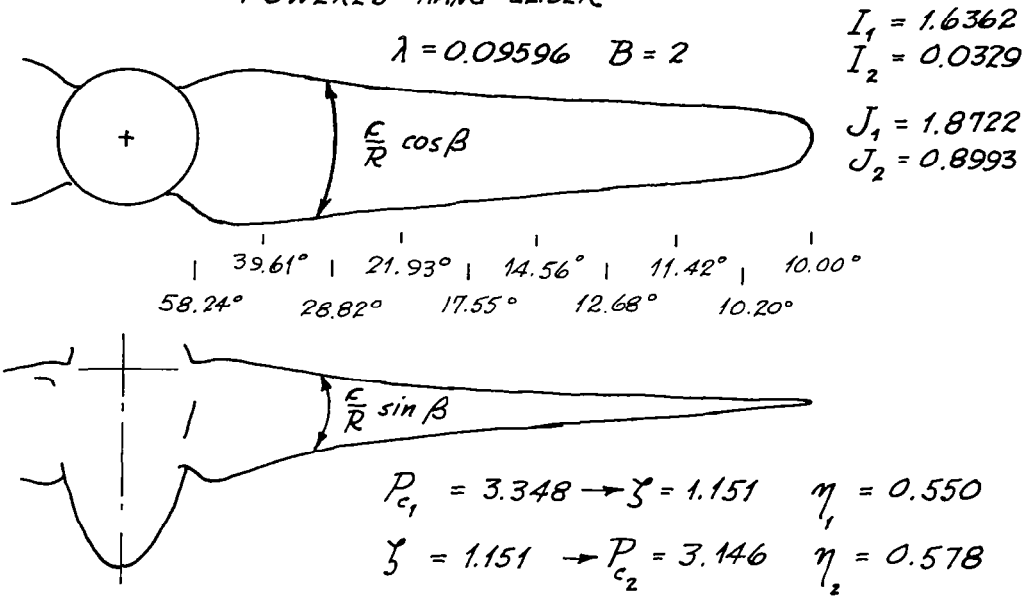

1372 mm DIAMETER x 617 mm PITCH

FIG. 10 POSSIBLE DESIGN POINT PERFORMANCE
RYSON ST-100 MOTORSOARER

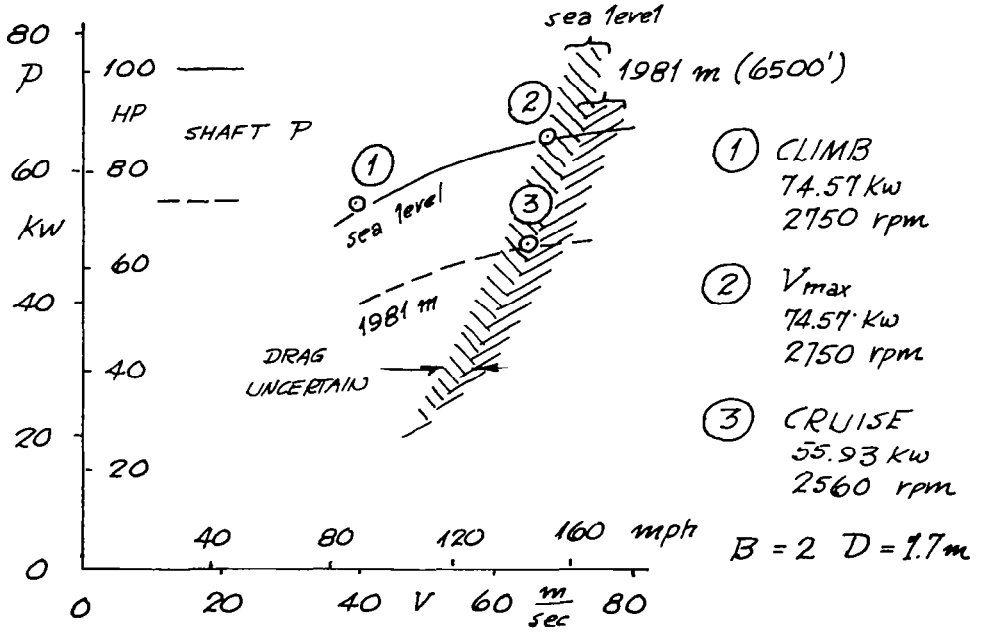

FIG. 11 COMPROMISE PROPELLER GEOMETRY
RYSON ST-100 MOTORSOARER

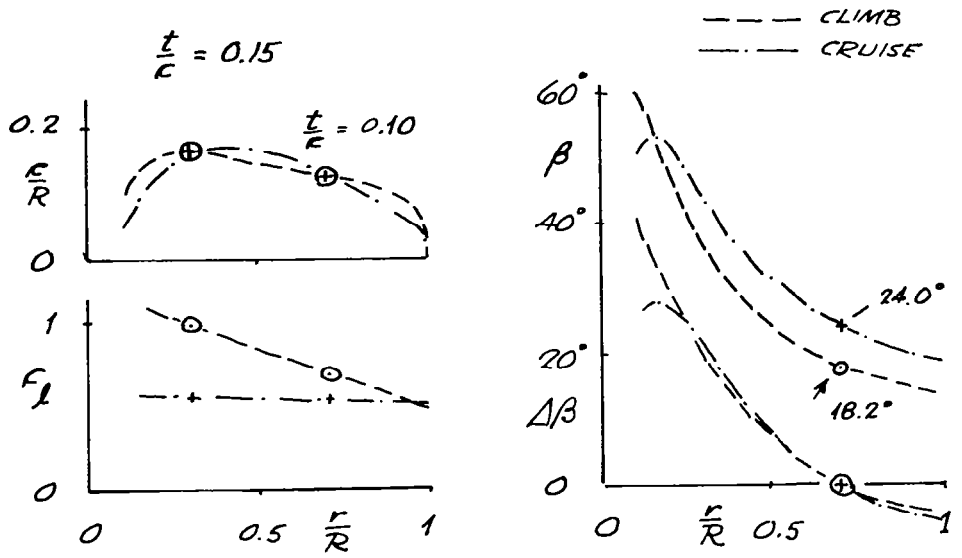

1. Report No.	2. Government Accession No.	3. Recipient's Catalog No.
NASA CP-2085, Part I		

4. Title and Subtitle	5. Report Date
THE SCIENCE AND TECHNOLOGY OF LOW SPEED AND MOTORLESS FLIGHT	June 1979
	6. Performing Organization Code
7. Author(s)	8. Performing Organization Report No.
Perry W. Hanson, compiler	L-12973
9. Performing Organization Name and Address	10. Work Unit No.
NASA Langley Research Center Hampton, VA 23665	505-02-23-01
	11. Contract or Grant No.
12. Sponsoring Agency Name and Address	13. Type of Report and Period Covered
National Aeronautics and Space Administration Washington, DC 20546	Conference Publication
	14. Sponsoring Agency Code

15. Supplementary Notes

16. Abstract

The Third International Symposium on the Science and Technology of Low Speed and Motorless Flight was held at the NASA Langley Research Center, March 29-30, 1979. The NASA Langley Research Center sponsored the symposium in cooperation with the Soaring Society of America (SSA). The symposium provided a forum for the interchange of information on recent progress in the science and technologies associated with low speed and motorless flight. This conference publication includes 28 papers presented at the symposium and 1 additional paper. The papers deal with low speed aerodynamics, new materials applications and structural concepts, advanced flight instrumentation, sailplane optimal flight techniques, motorsoarers, and ultralight sailplanes and hang gliders.

17. Key Words (Suggested by Author(s))		18. Distribution Statement
Low speed aerodynamics	Composite materials	Unclassified - Unlimited
Optimum design	Ultralight sailplanes	
Low drag airfoils	Hang gliders	
Advanced instrumentation		
Structural analysis		Subject Category 01

19. Security Classif. (of this report)	20. Security Classif. (of this page)	21. No. of Pages	22. Price*
Unclassified	Unclassified	309	$11.75

*For sale by the National Technical Information Service, Springfield, Virginia 22161

NASA-Langley, 1979